STATIC CHARACTERISTICS AND ROTORDYNAMIC COEFFICIENTS OF A FOUR-PAD TILTING-PAD JOURNAL BEARING WITH BALL-IN-SOCKET PIVOTS IN LOAD-BETWEEN-PAD CONFIGURATION

A Thesis

by

JOEL MARK HARRIS

Submitted to the Office of Graduate Studies of
Texas A&M University
in partial fulfillment of the requirements for the degree of

MASTER OF SCIENCE

December 2008

Major Subject: Mechanical Engineering

STATIC CHARACTERISTICS AND ROTORDYNAMIC COEFFICIENTS OF A FOUR-PAD TILTING-PAD JOURNAL BEARING WITH BALL-IN-SOCKET PIVOTS IN LOAD-BETWEEN-PAD CONFIGURATION

A Thesis

by

JOEL MARK HARRIS

Submitted to the Office of Graduate Studies of
Texas A&M University
in partial fulfillment of the requirements for the degree of

MASTER OF SCIENCE

Approved by:

Chair of Committee,	Dara W. Childs
Committee Members,	Bart Childs
	Luís San Andrés
Head of Department,	Dennis O'Neal

December 2008

Major Subject: Mechanical Engineering

ABSTRACT

Static Characteristics and Rotordynamic Coefficients of a Four-Pad Tilting-Pad Journal Bearing with Ball-In-Socket Pivots in Load-Between-Pad Configuration.

(December 2008)

Joel Mark Harris, B.S., University of Central Arkansas

Chair of Advisory Committee: Dr. Dara W. Childs

Static characteristics and rotordynamic coefficients were experimentally determined for a four-pad tilting-pad journal bearing with ball-in-socket pivots in load-between-pad configuration. A frequency-independent [M]-[C]-[K] model fit the measurements reasonably well, except for the cross-coupled damping coefficients. Test conditions included speeds from 4,000 to 12,000 rpm and unit loads from 0 to 1896 kPa (0 to 275 psi).

The test bearing was manufactured by Rotating Machinery Technology (RMT), Inc. Though it has a nominal diameter of 101.78 mm (4.0070 in.), measurements indicated significant bearing crush with radial bearing clearances of 99.6 μm (3.92 mils) and 54.6 μm (2.15 mils) in the axes 45º counterclockwise and 45º clockwise from the loaded axis, respectively. The pad length is 101.6 mm (4.00 in.), giving L/D = 1.00. The pad arc angle is 73º, and the pivot offset ratio is 65%. The preloads of the loaded and unloaded pads are 0.37 and 0.58, respectively.

A bulk-flow Navier-Stokes model was used for predictions, using adiabatic conditions for the bearing fluid. Because the model assumes constant nominal clearances at all pads, the average of the measured clearances was used as an estimate. Eccentricities and attitude angles were markedly under predicted while power loss was under predicted at low speeds and very well predicted at high speeds. The maximum

detected pad temperature was 71ºC (160ºF) and the rise from inlet to maximum bearing temperature was over predicted by 10-40%.

Multiple-frequency force inputs were used to excite the bearing. Direct stiffness and damping coefficients were significantly over predicted, but addition of a simple stiffness-in-series model substantially improved the agreement between theory and experiment. Direct added masses were zero or negative at low speeds and increased with speed up to a maximum of about 50 kg; they were normally greater in the unloaded direction. Although significant cross-coupled stiffness terms were present, they always had the same sign. The bearing had zero whirl frequency ratio netting unconditional stability over all test conditions. Static stiffness in the *y* direction (obtained from steady-state loading) matched the rotordynamic stiffness K_{yy} (obtained from multiple-frequency excitation) reasonably at low loads but poorly at the maximum test load.

DEDICATION

To Papaw

ACKNOWLEDGEMENTS

I thank and praise God for blessing me with the ability, means, and support to accomplish this goal; may I seek His will in all future endeavors.

I extend sincere gratitude to Dr. Childs for choosing me as a research assistant. As a boss, professor, and mentor, Dr. Childs has shown patience, knowledge, and teaching ability worthy of any student's respect and admiration. I would also like to thank Dr. Luís San Andrés for his guidance both as a committee member and as a professor. There are few professors' lectures that I have enjoyed quite as much as his. I also thank Dr. Bart Childs for serving as a committee member and Dr. Sai Lau for choosing me as a graduate student at Texas A&M.

I would like to thank the Turbomachinery Research Consortium for their support of this project and to RMT for providing the test bearing. Thanks to Andy Schaible for his assistance in learning how to assemble, disassemble, troubleshoot, and acquire data from the test apparatus and his assistance in meeting goals set forth by Dr. Childs. I greatly appreciate Stephen Phillips and Eddie Denk for providing the technical expertise to get me through much of my work. I also thank Bader Al-Jughaiman, Clint Carter, and Eric Hensley for providing some of my initial training. I have made great friends at the Turbolab and drew strength from their camaraderie; I would especially like to thank José Baker, Adolfo Delgado, Ahmed Gamal, and Arun Suryanarayanan—our good times in Aggieland will not soon be forgotten.

I thank my parents and grandparents for their support and guidance. Without them, much of what it took to get a bachelor's degree, let alone a master's degree, would not have been possible. I especially thank my wife, Leslie, for her love, patience, and support.

TABLE OF CONTENTS

Page

LIST OF FIGURES

Page

Page

LIST OF TABLES

Page

NOMENCLATURE

Units of the defined symbols are indicated in brackets following their description using the SI designation of mass (M), length (L), time (T), and temperature (Θ) as base units. A "-" symbol is used to designate a pure number.

$\boldsymbol{A}_i$	Fourier transform of the stator acceleration in the *i* direction [L/T^2]
$\boldsymbol{A}_{ij}$	Fourier transform of the measured stator acceleration in the *j* direction due to forced excitation (a shake) in the *i* direction [L/T^2]
b	*y*-intercept of a least squares linear regression [units depend on application]
C_{ave}	Average radial clearance used for prediction model [L]
C_b	Radial bearing clearance [L]
$C_{ii,\text{base}}$	Baseline direct damping coefficients [M/T]
$C_{ii,\text{eq}}$	Equivalent direct damping coefficients [M/T]
c_{ij}	Dimensionless damping coefficients [-]
C_{ij}	Direct and cross-coupled damping coefficients (force in the *i* direction due to velocity in the *j* direction) [M/T]
$\tilde{C}_{ij}$	Frequency-dependent damping coefficients output by XLTFPBrg [M/T]
c_p	Specific heat at constant pressure [$L^2/(T^2 \cdot \Theta)$]
C_p	Pad radius [L]
C_{pad}	Damping of a single pad [M/T]
$C_{\text{pad,eq}}$	Equivalent damping of a single pad with pivot stiffness considered [M/T]
C_r	Radial clearance [L]

C_x	Radial bearing clearance about the x axis [L]
$C_{x'}$	Radial bearing clearance about the x' axis [L]
C_y	Radial bearing clearance about the y axis [L]
$C_{y'}$	Radial bearing clearance about the y' axis [L]
D	Bearing diameter [L]
D_b	Ball diameter [L]
$\boldsymbol{D}_i$	Fourier transform of stator relative motion in the i direction [L]
$\boldsymbol{D}_{ij}$	Fourier transform for the measured stator relative motion in the j direction due to forced excitation (a shake) in the i direction [L]
D_s	Socket diameter [L]
$\boldsymbol{e}$	Resultant eccentricity [L]
E_b	Young's modulus for the ball [$M/(L\cdot T^2)$]
$\boldsymbol{e}_i$	Journal eccentricity in the i direction [L]
E_s	Young's modulus for the socket [$M/(L\cdot T^2)$]
f	Excitation frequency of stator in Hz [1/T]
f_{bi}	Bearing reaction force component in the i direction [$M\cdot L/T^2$]
f_i	Excitation force component in the i directions [$M\cdot L/T^2$]
$\boldsymbol{F}_i$	Fourier transform of the excitation force in the i direction [$M\cdot L/T^2$]
$\boldsymbol{F}_{ij}$	Fourier transform of the measured stator force in the j direction due to forced excitation (a shake) in the i direction [$M\cdot L/T^2$]
F_s	Bearing static load (applied in the y direction) [$M\cdot L/T^2$]
$\boldsymbol{H}_{ij}$	Direct and cross-coupled dynamic-stiffness coefficients [M/T^2]
$\boldsymbol{H}_{ij,\text{base}}$	Baseline dynamic-stiffness coefficients [M/T^2]

$\boldsymbol{H}_{ij,\text{test}}$	Raw value of dynamic-stiffness coefficients without baseline subtracted [M/T^2]
K_{eq}	Equivalent dimensionless stiffness used in WFR calculation [-]
$K_{ii,\text{base}}$	Baseline direct stiffness coefficients [M/T^2]
$K_{ii,\text{eq}}$	Equivalent direct stiffness coefficients [M/T^2]
k_{ij}	Dimensionless stiffness coefficients [-]
K_{ij}	Direct and cross-coupled stiffness coefficients (force in the *i* direction due to displacement in the *j* direction) [M/T^2]
$\tilde{K}_{ij}$	Frequency-dependent stiffness coefficients output by XLTFPBrg [M/T^2]
K_p	Pivot stiffness [M/T^2]
K_{pad}	Stiffness of a single pad [M/T^2]
$K_{\text{pad,eq}}$	Equivalent stiffness of a single pad with pivot stiffness considered [M/T^2]
K_{ps}	Pad support structure stiffness [M/T^2]
$K_{ps,\text{eff}}$	Effective pad support structure stiffness value used to modify predicted stiffness and damping terms $K_{ps,\text{eff}} = 2K_{ps}$ [M/T^2]
$K_{ps,\text{test}}$	Raw value of pad support structure stiffness without baseline subtracted [M/T^2]
$K_{yy,\text{base}}$	Baseline direct stiffness in the *y* direction [M/T^2]
$K_{yy,\text{s}}$	Static stiffness in the *y* direction [M/T^2]
L	Effective bearing length (pad length for TPJB) [L]
m	Slope of a least squares linear regression [units depend on application]
M	Number of data points [-]
M_{eq}	Equivalent dimensionless added mass used in WFR calculation [-]

$M_{ii,\mathrm{eq}}$	Equivalent direct stiffness added mass coefficients [M]
m_{ij}	Dimensionless added mass coefficients [-]
M_{ij}	Direct and cross-coupled added mass coefficients (force in the *i* direction due to acceleration in the *j* direction) [M]
M_p	Preload factor [-]
$M_{p,\mathrm{eff}}$	Effective preload factor used in the theoretical model [-]
$M_{p,\mathrm{loaded}}$	Preload factor of the loaded pads [-]
$M_{p,\mathrm{unloaded}}$	Preload factor of the unloaded pads [-]
M_s	Stator Mass [M]
N	Running speed of rotor in Hz or rpm [1/T]
N_{pad}	Number of pads [-]
P	Bearing unit load (F_s/LD) [M/(L·T^2)]
P	Power loss imposed by the bearing [M·L^2/T^3]
Q	Volumetric flow rate [L^3/T]
r	Pearson product moment correlation coefficient [-]
R	Bearing radius [L]
R_b	Nominal bearing radius [L]
R_p	Pad radius [L]
R_s	Shaft radius [L]
S	Sommerfeld number, $\mu NLD/F_s(R/C_r)^2 = \mu N/P(R/C_r)^2$ [-]
$S_{\chi\chi}$	Independent variable uncertainty parameter used in uncertainty analysis of least squares linear regression [units depend on application]
t	Confidence interval weighting factor for uncertainty analysis [-]

T	Temperature [Θ]
T_{in}, T_{out}	Inlet, outlet lubricant temperature [Θ]
T_{max}	Maximum detected bearing temperature, approximated experimentally as the maximum trailing-edge pad temperature [Θ]
W	Static load imposed on pivot [M·L/T^2]
$\ddot{x}_s, \ddot{y}_s$	Stator acceleration components in the x, y directions [L/T^2]
α_b	Coefficient of thermal expansion for the ball [1/Θ]
α_s	Coefficient of thermal expansion for the scoket [1/Θ]
β	Instability factor ($\omega_{onset} = \beta\omega_{n1}$)
γ	Dependent variable in a least squares linear regression [units depend on application]
$\bar{\gamma}$	Average of dependent variable data used to calculate a least squares linear regression or uncertainty of average [units depend on application]
δ	Pivot deflection [L]
Δb	Uncertainty in the y-intercept of a least squares linear regression [units depend on application]
ΔC_{ij}	Uncertainty of damping coefficients [M/T]
$\Delta \boldsymbol{H}_{ij}$	Uncertainty of dynamic-stiffness coefficients [M/T^2]
$\Delta \boldsymbol{H}_{ij,base}$	Uncertainty of baseline dynamic-stiffness coefficients [M/T^2]
$\Delta \boldsymbol{H}_{ij,test}$	Uncertainty of raw value of dynamic-stiffness coefficients without baseline subtracted [M/T^2]
ΔK_{ij}	Uncertainty of stiffness coefficients [M/T^2]
ΔK_p	Uncertainty of pivot stiffness [M/T^2]

$\Delta K_{p,\text{test}}$	Uncertainty of raw value of pivot stiffness without baseline subtracted [M/T^2]
$\Delta K_{yy,\text{base}}$	Uncertainty of baseline direct stiffness in y direction [M/T^2]
Δm	Uncertainty in the slope of a least squares linear regression [units depend on application]
ΔM_{ij}	Uncertainty of added mass coefficients [M]
$\Delta T_{\max}$	Maximum temperature rise [Θ]
$\Delta x, \Delta y$	Relative displacement components between the rotor and the stator in the x, y directions [L]
$\Delta \dot{x}, \Delta \dot{y}$	Relative velocity components between the rotor and the stator in the x, y directions [L]
$\Delta \ddot{x}, \Delta \ddot{y}$	Relative acceleration components between the rotor and the stator in the x, y directions [L]
θ_{pad}	Pad arc angle [-]
θ_{pivot}	Pivot arc angle [-]
μ	Lubricant viscosity [M/(L·T)]
ν_b	Poisson's ratio for the ball [-]
ν_s	Poisson's ratio for the socket [-]
ρ	Lubricant density [M/L^3]
$\hat{\sigma}^2$	Mean squared error of a least squares linear regression [units depend on application]
ϕ	Attitude angle [-]
χ	Independent variable in a least squares linear regression [units depend on application]

$\bar{\chi}$	Average of independent variable data used to calculate a least squares linear regression [units depend on application]
ω	Running speed of rotor in rad/sec [1/T]
ω_{n1}	Natural frequency of rotor-bearing or rotor seal system [1/T]
ω_{onset}	Onset speed of instability [1/T]
Ω	Excitation frequency of stator or rotor in rad/sec [1/T]

Abbreviations

DE	Drive end
FP	Flexure-pivot
gpm	Gallons per minute
LBP	Load-between-pad
LOP	Load-on-pad
MSE	Mean squared error
NDE	Non-drive end
rpm	Revolutions per minute
TPJB	Tilting-pad journal bearing
WFR	Whirl frequency ratio

INTRODUCTION

Introduction to Tilting-Pad Journal Bearings

The rising demands of modern turbomachinery have led to the development of fluid-film bearings with high load and speed capacities and better stability characteristics. Resonant whip, or oil whip, which is a condition of instability in compressors, turbines, and pumps, is most likely to occur in high-speed, lightly loaded bearings. Lund [1] notes that tilting-pad journal bearings (TPJB's) eliminate this instability due to their ability to direct the load component of each pad through the journal center, if the effects of pad inertia and pivot friction are neglected. Because of this characteristic, TPJB's have become popular in the area of turbomachinery.

A TPJB uses multiple pads, or shoes, to support the journal. Each of these pads is supported by a pivot. There are three basic types of pivots used in TPJB's: cylindrical, spherical, and flexure-pivot. A cylindrical, or rocker-back, pivot utilizes rocking motion of the pad against the housing by machining a curvature into the back of the pad that is greater than that of the housing. This profile is constant along the length of the pivot such that the pad is only able to tilt about the axial length of the bearing. This geometry is depicted in Fig. 1.

This thesis follows the style of the ASME Journal of Tribology.

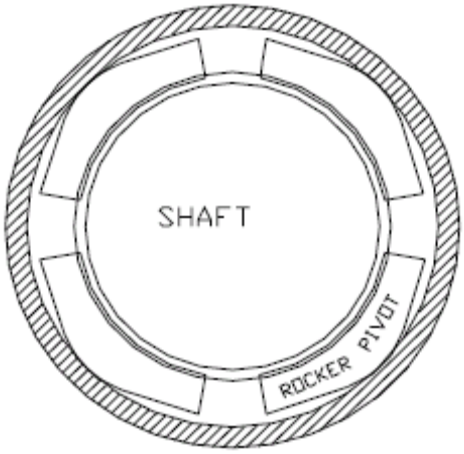

Fig. 1 Cylindrical pivot TPJB [2]

Spherical pivots add a degree of freedom to the pads, allowing them to pitch perpendicular to the bearing's axial length and thus tolerate shaft misalignment. Spherical pivots can be further divided into sphere-in-cylinder and ball-in-socket types. Sphere-in-cylinder pivots, like the one portrayed in Fig. 2, have an insert attached to the back of the pad of which the portion protruding outside the back of the pad is a partial sphere with a higher degree of curvature than that of the cylindrical housing. Thus the pad is allowed to roll without slipping about the housing.

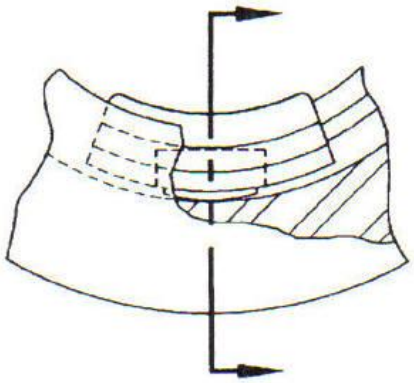

Fig. 2 Sphere-in-cylinder pivot [3]

Ball-in-socket pivots, such those in the test bearing, have a steel partial sphere (ball) affixed to the bearing housing as well a matching socket of slightly lower curvature on the back of the pad. The socket can be machined into the back of the pad or affixed to it as an insert, as in the test bearing. This type of pivot is shown in Fig. 3 and described in detail by Nicholas and Wygant [3]. Ball-in-socket pivots depend on slipping motion between the ball and socket to rotate the pads to their equilibrium angle.

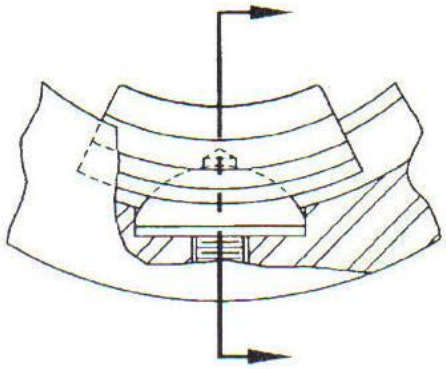

Fig. 3 Ball-in-socket pivot [3]

A flexure-pivot (FP) bearing design is described by Kepple et al. [4] and is claimed to eliminate the effects of pivot wear caused by relative motion between the pad and housing. The FP bearing is a one-piece design that uses electron discharge machining (EDM) to cut a pad with a flexural web as a pivot into the bearing housing. This type of pivot is depicted in Fig. 4.

As noted above, the current project investigates the behavior of a TPJB with a ball-in-socket pivot. Since the behavior of cylindrical and spherical pivot TPJB's is quite similar, the review of previous work herein will focus on both types.

Some of the important geometrical parameters of the TPJB are shown in Fig. 5. In Fig. 5(a), R_s, R_b, and R_p represent the respective radii of the shaft, bearing, and pad. The bearing clearance is defined as $C_b = R_b - R_s$ while the pad clearance is defined as $C_p = R_p - R_s$. These clearances combine to give the preload factor, $M_p = 1 - C_b/C_p$.

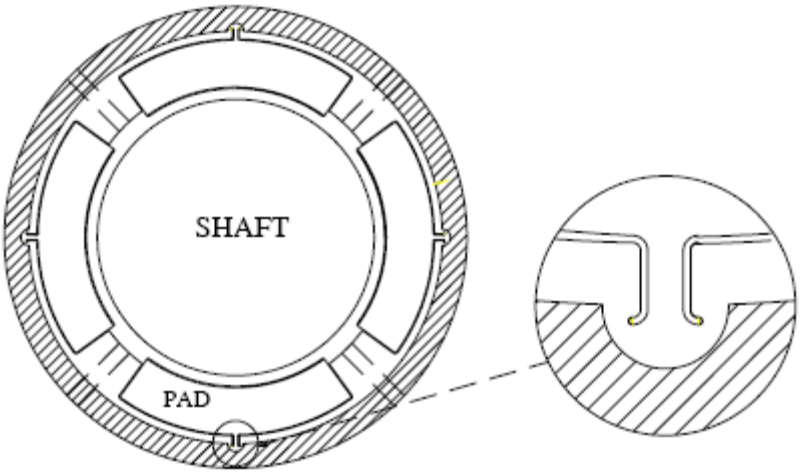

Fig. 4 Flexure-pivot bearing [2]

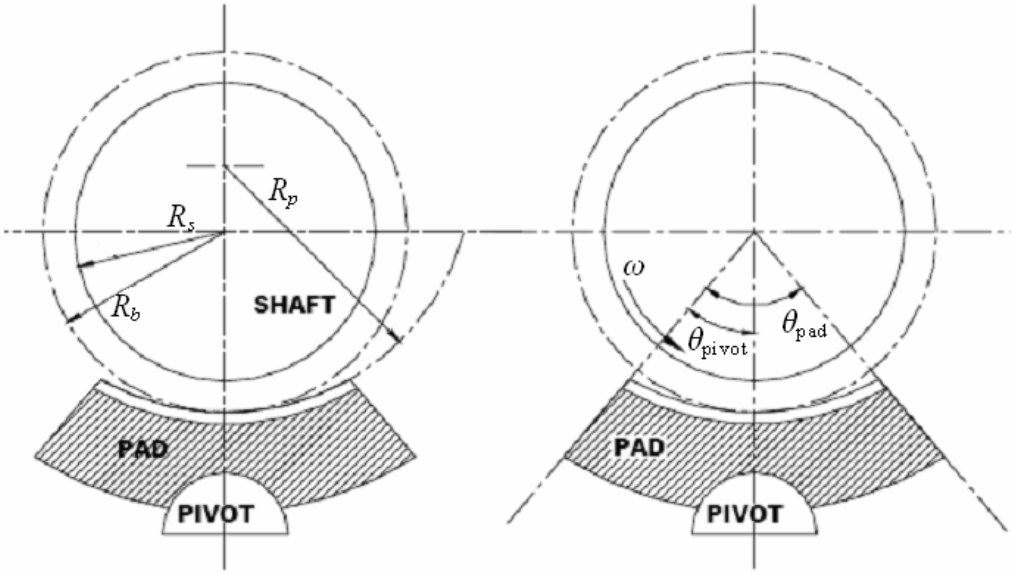

Fig. 5 (a) Radial and (b) angular geometrical parameters of the TPJB [5]

Zero preload would imply that the pad is concentric with the shaft while non-zero positive preload implies a larger pad than shaft radius and vice versa for a negative preload. Negative preloads are not machined in practice but can occur during operation due to thermal and elastic deformation. Figure 5(b) shows the pad arc angle, or

circumferential pad length, θ_{pad}, and the pivot arc angle, θ_{pivot}. The pivot offset is defined as $\theta_{pivot}/\theta_{pad}$. Typical pivot offsets are between 50-70% while the highest load capacity is achieved with a 60% offset [5]. Two additional parameters of interest are the length-to-diameter (L/D) ratio and the clearance-to-radius (C_r/R) ratio. The L/D ratio defines the ratio of the effective axial length of the bearing (axial pad length for TPJB's) to the nominal bore diameter while the C_r/R ratio defines the ratio of the nominal radial bearing clearance to nominal bearing radius. For TPJB's, $C_r = C_b$ and $R = R_b$. Additionally, the static load, F_s, imposed on a bearing can be normalized by dividing it by the projected area, LD, to produce the unit load, P. Unit load is reported in units of pressure, but does not represent an actual pressure value.

Two dimensionless numbers that are widely used in characterizing flow and stability of lubrication systems are the Reynolds number (Re) and Sommerfeld number (S). Reynolds number is a ratio of inertial forces to viscous forces for a fluid flow and is defined by Eq. (1) for fluid flow in a journal bearing:

$$\mathrm{Re} = \frac{\rho \omega R C_r}{\mu} \tag{1}$$

Equation (1) requires knowledge of the density (ρ) and the viscosity (μ) of the fluid. The symbol ω represents the running speed of the rotor in units of rad/sec. When Re $\geq$ 2,000, inertial forces in the fluid film begin to dominate and flow can be considered turbulent. While the Reynolds number is a dimensionless quantity that is useful in many areas of fluid mechanics, the Sommerfeld number is one that is specifically applicable to boundary lubrication. The Sommerfeld number, defined in Eq. (2), has historically been used as the abscissa for plots of many characteristics of journal bearings, both static and dynamic:

$$S = \frac{\mu N L D}{F_s}\left(\frac{R}{C_r}\right)^2 = \frac{\mu N}{P}\left(\frac{R}{C_r}\right)^2 \tag{2}$$

N denotes the running speed of the rotor and must carry units of Hz in this calculation. Throughout this paper, N is also used to denote running speed in units of revolutions per minute (rpm). As can be deduced from Eq. (2), the Sommerfeld number has smaller values for heavily loaded bearings with slow journal rotation speeds and larger values for lightly loaded bearings with fast journal rotation speeds. A bearing may be considered lightly loaded when $S \geq 0.5$. A shaft rotating within a plain journal bearing approaches optimum stability as $S \rightarrow 0$ but is in danger of instability as $S \rightarrow \infty$, or as $F_s \rightarrow 0$. This instability, known as oil whip, is most often realized in high-speed vertical machines.

Previous Work

To predict the static and dynamic characteristics of bearings as well as other rotordynamic elements such as seals and dampers, the pressure distribution of the fluid in them must first be formulated. This derivation was first performed by Osbourne Reynolds in 1886 [6]. The aptly named Reynolds equation, a reduction of the Navier-Stokes equation with temporal and convective acceleration terms neglected, laid the foundation for the theory of hydrodynamic lubrication. From the Reynolds equation ensued calculation of static characteristics such as static journal position and rotordynamic coefficients. Rotordynamic coefficients are analogous to stiffness, damping, and inertia terms in structural systems and are calculated via gradients of a given pressure distribution. Accurate determination of rotordynamic coefficients is imperative in predicting imbalance responses, critical speeds, and stability thresholds of rotating machines.

Equation (3) is a widely accepted force-displacement model for a bearing:

$$-\begin{bmatrix} f_{bx} \\ f_{by} \end{bmatrix} = \begin{bmatrix} K_{xx} & K_{xy} \\ K_{yx} & K_{yy} \end{bmatrix} \begin{bmatrix} \Delta x \\ \Delta y \end{bmatrix} + \begin{bmatrix} C_{xx} & C_{xy} \\ C_{yx} & C_{yy} \end{bmatrix} \begin{bmatrix} \Delta \dot{x} \\ \Delta \dot{y} \end{bmatrix} + \begin{bmatrix} M_{xx} & M_{xy} \\ M_{yx} & M_{yy} \end{bmatrix} \begin{bmatrix} \Delta \ddot{x} \\ \Delta \ddot{y} \end{bmatrix} \tag{3}$$

Δx and Δy define the relative motion between the rotor and the stator; x customarily represents the statically unloaded direction while y represents the loaded direction. The coefficients K_{ij}, C_{ij}, and M_{ij} indicate the respective stiffness, damping, and added mass coefficients. Note that Eq. (3) is an "[M]-[C]-[K]" model, meaning that added mass terms are included as acceleration-reaction force coefficients. Many analysts use only stiffness and damping terms, producing a "[C]-[K]" model.

Lund [1] used a [C]-[K] model in his 1964 paper, the first known publication to predict rotordynamic coefficients for a TPJB. Using the "Pad Assembly Method," he calculated the gradient of the fluid force for each pad independently and made a summation of the results over all the pads to obtain their net effect. The coefficients were predicted to be frequency-independent since Lund neglected fluid inertia while assuming that the pad precession frequency was synchronous with the journal running speed. Lund calculated direct stiffness and damping coefficients for 4-pad, 5-pad, and 6-pad TPJB's with no preload and varying L/D ratios in both load-on-pad (LOP) and load-between-pad (LBP) configurations. Pad inertia was initially neglected and therefore cross-coupled coefficients were predicted to be zero. For all of the 4-pad bearing geometries, the coefficients were isotropic ($K_{xx} = K_{yy}$, $C_{xx} = C_{yy}$) regardless of the load configuration. For the 5-pad and 6-pad geometries, coefficients were orthotropic ($K_{xx} \neq K_{yy}$, $C_{xx} \neq C_{yy}$) to a higher degree for LOP configuration. For one of the 4-pad geometries, Lund showed the effect of considering pad inertia by retaining its value in the equations of motion for the pads and rotor and once again assuming their motion to be synchronous. An increase in pad inertia caused a decrease in the direct coefficients (above a certain Sommerfeld number) while bringing about equal and opposite cross-coupled stiffness and damping coefficients. As the value of the pad mass was increased, the direct coefficients continued to decrease while the cross-coupled coefficients increased. However, the cross-coupled coefficients were typically less than 1% of their direct counterparts. Lund also gave an equation for the maximum allowable pad inertia, or "critical mass," above which resonant vibration of the pads is predicted. This condition is known is "pad flutter," and is an undesirable vibrational motion that can

occur in TPJB's, most likely in the unload pads as opposed to the loaded pads. However, Lund notes that pad flutter is predicted to occur at high Sommefeld numbers where the minimum film thickness and damping are high such that the resonant pad vibration "may not be too serious [1]." Typical measures taken to reduce pad flutter in unloaded pads include increasing preload and machining a Rayleigh step or chamfer into the leading edge of the pads. The test bearing uses a larger preload for the unloaded pads (compared to the loaded pads) and has the aforementioned chamfers in them.

Lund compared his predictions to results from Hagg and Sankey [7,8] as a function of Sommerfeld number for one each of the 4-pad and 6-pad geometries in LBP configuration. For the 6-pad bearing, (i) K_{xx} was over predicted for $S < 1$ and under predicted for $S > 1$, (ii) K_{yy} was generally under predicted but began to converge as S approached 0, (iii) C_{xx} was over predicted but began to converge for $S > 1$, and (iv) C_{yy} was generally under predicted. For the 4-pad bearing, Hagg and Sankey obtained direct coefficients in both the x and y directions but plotted only one curve as their values were nearly equal. Furthermore, since Hagg and Sankey did not test for cross-coupled coefficients, Lund was able to compare his calculated direct stiffness and damping coefficients to one experimental curve apiece. Stiffness was predicted very well up to $S = 0.5$ and divergently under predicted beyond that value. Damping was over predicted, strikingly so for $S < 0.5$.

While Lund did not consider the effect of fluid inertia in his 1964 paper [1], acknowledgement of its influence on fluid films would proceed in the following decade. Hirs [9] presented a "bulk-flow" model in 1973 that modified the Reynolds equation to include shear turbulence factors that predict a net increase in effective viscosity for turbulent flows ($\mathrm{Re} \geq 2{,}000$). This model analyzes a control volume that extends from the journal to bearing surface and is "based on the empirical finding that the relationship between wall-shear stress and mean flow velocity relative to the wall at which the shear stress is exerted can be expressed by a common simple formula for pressure flow, shear flow, or a combination of these two basic types of flow." Additionally, a 1975 study by Reinhardt and Lund [10] found that the convective and temporal acceleration terms

discarded from the more general Navier-Stokes equation can become significant at Reynolds numbers as low as 100 and have a profound effect at the transition to turbulence. These terms can be included in the bulk-flow model, predicting addition of added mass terms to the linear rotordynamic coefficients due to stiffness coefficients that decrease quadratically with increasing excitation frequency. Reinhardt and Lund predict a linear increase of damping coefficients with increasing excitation frequency.

As mentioned above, Lund's method reduces the rotor-bearing model to two degrees of freedom and produces "synchronously reduced" coefficients since the pad rotational frequency is assumed to be synchronous with the shaft speed. However, Lund's pad assembly method is "general enough to accept non-synchronous excitation frequencies without additional complexities [11]." Parsell et al. [12] extended Lund's original model [1] to include non-synchronous excitation frequencies. Pad rotation was included, rendering $(2+N_{pad})$ degrees of freedom in the model, where N_{pad} denotes the total number of pads. Assuming the pads' rotational frequencies to equal excitation frequency and reducing the model to two degrees of freedom for vertical and horizontal journal motion yielded frequency-dependent formulas for stiffness and damping coefficients. The frequency-dependency imposed by these equations is present even upon assumption of zero pad inertia. In fact, Parsell et al. note that the moment on the pads due to their inertia is typically small compared to the moment due to the fluid film and is normally neglected for industrial bearings. However, as Lund noted [1], Parsell mentions that the pad mass can become large enough to cause pad flutter. In the remainder of this thesis, the term "model reduction" shall denote the process of condensing the multiple-degree-of-freedom TPJB dynamic system into a two-degree-of-freedom system. Parsell et al. predicted the effect of this model reduction on the reduced stiffness and damping coefficients of a 5-pad TPJB with preloads ranging from null to 0.5 and Sommerfeld numbers ranging from 0.1 to 10, loaded in both LOP and LBP configurations. Pad inertia was neglected and the frequency ratio (excitation frequency to running speed) was varied from 0 to 1 in each of six cases. Stiffness consistently showed a quadratic decrease while damping increased with increasing excitation

frequency, and these effects became more pronounced with increasing Sommerfeld number and decreasing preload. In the two cases where S = 10 and there was no preload, the damping became negative below 0.5 frequency ratio (½x).

Using the formulas of Parsell et al. [12], White and Chan [13] performed an analysis in 1991, once again reducing the model from $2(5N_{\text{pad}} + 4)$ to 8 total coefficients (assuming a [C]-[K] model). White and Chan used a finite element analysis of the Reynolds equation to predict direct stiffness and damping coefficients for a 5-pad, LOP TPJB over a span of preloads from null to 0.5 and offsets from 0.50 to 0.59. Results for direct stiffness and damping for synchronous (1x) and half speed (½x) excitation are shown. Stiffness is predicted to be higher at ½x than 1x while damping is predicted to be lower, this effect being more pronounced at higher Sommerfeld numbers, i.e. higher speeds and lower loads.

In the analyses performed in [1,12,13], translational motion of the pads was neglected. In 1988, Kirk and Reedy [14] developed equations to predict the effect of this additional degree of freedom on TPJB coefficients, modeling an individual pad as a point mass connected to ground by the pivot's stiffness and damping and connected to the rotor by the stiffness and damping of the fluid film. Also note that rotational motion was ignored in the model, making it a two-degree-of-freedom system. Setting the pad inertia and pivot damping to zero resulted in the following formulas:

$$
\begin{aligned}
K_{\text{pad,eq}}\left(\Omega\right) &= \frac{K_{\text{pad}}K_p\left(K_{\text{pad}}+K_p\right)+K_pC_{\text{pad}}^2\Omega^2}{\left(K_{\text{pad}}+K_p\right)^2+C_{\text{pad}}^2\Omega^2} \\
C_{\text{pad,eq}}\left(\Omega\right) &= \frac{C_{\text{pad}}K_p^2}{\left(K_{\text{pad}}+K_p\right)^2+C_{\text{pad}}^2\Omega^2}
\end{aligned}
\tag{4}
$$

Here, $K_{\text{pad,eq}}$ and $C_{\text{pad,eq}}$ denote the equivalent stiffness and damping of a single pad with pivot stiffness considered, K_{pad} and C_{pad} are the calculated bearing stiffness and damping of a single pad without pivot stiffness considered, K_p is the pivot stiffness, and Ω is the

excitation frequency. Childs [15] also arrived at Eq. (4), starting with a model of a spring, representing the pivot, in series with a parallel spring and damper, representing the fluid film. However, to show the effect of zeroth and second order frequency terms on the equivalent stiffness and damping, Childs calculated a Taylor series of his result about $\Omega = 0$:

$$\begin{aligned} K_{\text{pad,eq}}(\Omega) &= \frac{K_{\text{pad}}K_p}{K_{\text{pad}}+K_p} + \frac{K_p^2 C_{\text{pad}}^2}{\left(K_{\text{pad}}+K_p\right)^3}\Omega^2 + O\left(\Omega^4\right) \\ C_{\text{pad,eq}}(\Omega) &= \frac{C_{\text{pad}}K_p^2}{\left(K_{\text{pad}}+K_p\right)^2} - \frac{C_{\text{pad}}^3 K_p^2}{\left(K_{\text{pad}}+K_p\right)^4}\Omega^2 + O\left(\Omega^4\right) \end{aligned} \tag{5}$$

Equation (5) predicts that inclusion of pivot stiffness in a TPJB model has four main effects, which become more pronounced as pivot stiffness decreases: (i) a decrease in the zero-frequency stiffness value, (ii) an increase in stiffness proportional (primarily) to the square of excitation frequency, (iii) a decrease in the zero-frequency damping value, and (iv) a decrease in damping proportional (primarily) to the square of excitation frequency.

Kirk and Reedy [14] also used Hertzian contact formulas to evaluate pivot stiffness for several different types of pivot designs. The geometries considered are (i) sphere-on-a-flat-plate, (ii) sphere-in-a-sphere, (iii) sphere-in-a-cylinder, (iv) cylinder-in-a-cylinder, (v) and general curvature. A ball-in-socket is a sphere-in-a-sphere pivot. In all cases, deflection is a non-linear function of load. The inverse of the derivative of the deflection with respect to load is defined as the stiffness. Evaluating the pivot stiffness in this manner results in a load-dependent formula, which is more useful in bearing formulation than a deflection-dependent formula since static load values are typically more readily available. When applied to calculations of fluid-film bearing coefficients for several geometries (also provided by Kirk and Reedy [14]), the outlined formulation of pivot stiffness has the following effects on the effective dynamic coefficients: (i) the damping is decreased by as much as 72% while (ii) the stiffness can be either increased or decreased but does not typically change appreciably for “operation near design speed

[14]." In the specific interest of this thesis, the equations for sphere-in-a-sphere formulation are cited from Kirk and Reedy's paper. Equation (6) gives the deflection, δ, as a function of static load, W:

$$\begin{aligned}
&\delta = 1.040\sqrt[3]{\frac{W^2 C_E^2}{C_D}}, \\
&C_E = \frac{1-\nu_b^2}{E_b} + \frac{1-\nu_s^2}{E_s},\ C_D = \frac{D_b D_s}{\left(D_s - D_b\right)} \\
&E_b = 205 \text{ GPa} = 29700 \text{ ksi},\quad E_s = 76 \text{ GPa} = 11000 \text{ ksi} \\
&\nu_b = 0.29,\quad \nu_s = 0.325
\end{aligned} \tag{6}$$

Evaluation of the parameters C_E and C_D require specific knowledge of Young's modulus and Poisson's ratio, E and ν, for the ball and socket as well as their diameters (the subscripts b and s denote the ball and socket, respectively). In Eq. (6), E and ν are provided for bronze and 4140 steel since these are the materials used for the test bearing. The inverse of the derivative of this equation with respect to W gives the load-dependent pivot stiffness shown in Eq. (7):

$$K_p\left(W\right) = 1.442\sqrt[3]{\frac{C_D W}{C_E^2}} \tag{7}$$

The pivot stiffness is sensitive to the differential diameter, $D_s - D_b$, and decreases exponentially as it increases. The theoretical value of the pivot stiffness is infinity when the differential diameter is zero, meaning that the pivot would have no flexibility and no effect on the overall stiffness and damping of the bearing.

Nicholas and Wygant [3] revisited pivot modeling in 1995, adding design considerations to their study. They used Kirk and Reedy's [14] formulas for sphere-in-a-sphere, sphere-in-a-cylinder, and cylinder-in-a-cylinder geometries. The importance of differential diameter is emphasized. For sphere-in-a-sphere (ball-in-socket) geometry,

the housing is typically steel while the pivot is bronze. While temperature does not have an appreciable effect on the differential diameter of sphere-in-a-cylinder and cylinder-in-a-cylinder (rocker-back) geometries, it can cause an exponential decrease in pivot stiffness for a ball-in-socket pivot since the bronze housing has a higher thermal expansion coefficient than steel. Nicholas and Wygant [3] give the following equation for the "differential thermal growth" of a ball-in-socket pivot with a steel ball and bronze socket:

$$\begin{aligned} &\Delta\left(D_s - D_b\right) = \left(\alpha_s - \alpha_b\right)\cdot\Delta T\cdot D_b \\ &\alpha_b = 12.2\times10^{-6}\ \text{mm/}\left(\text{mm}\cdot^{\text{o}}\text{C}\right) = 6.8\times10^{-6}\ \text{in/}\left(\text{in}\cdot^{\text{o}}\text{F}\right) \\ &\alpha_s = 18.0\times10^{-6}\ \text{mm/}\left(\text{mm}\cdot^{\text{o}}\text{C}\right) = 10.0\times10^{-6}\ \text{in/}\left(\text{in}\cdot^{\text{o}}\text{F}\right) \end{aligned} \tag{8}$$

Here, α_b and α_s represent the respective coefficients of thermal expansion of the ball and socket while ΔT is the change in temperature from ambient to operating conditions. This increase in differential diameter can be added to the differential diameter used in Eqs. (6,7), thus correcting these formulas to account for the temperature change. As a specific example, Nicholas and Wygant consider a ball-in-socket pivot loaded to 24.6 kN (5520 lbs.) with a ball diameter varying from 25 to 100 mm (1 to 4 in.). Assuming line-to-line contact at ambient temperature and ΔT = 56ºC (100ºF), they predict a decrease in pivot stiffness of about 10-40% as ball diameter increases. The formulas for equivalent stiffness and damping are derived and presented, once again predicting frequency-dependency due to the pivot. While Kirk and Reedy [14] report that stiffness will increase or decrease, Nicholas and Wygant predict only a decrease of up to 56% in equivalent stiffness for a sphere-in-a-cylinder type pivot. Results for damping are similar, with Nicholas and Wygant predicting up to an 82% decrease in effective damping. Note that while Kirk and Reedy performed calculations for a single pad, Nicholas and Wygant did the same calculations for an entire 5-pad, LBP TPJB. Nicholas and Wygant go on to state that local yielding at the pivot can decrease a bearing's stiffness and damping by increasing the clearance.

From the late 1980's up to the present day, a wealth of papers documenting experimental examinations of TPJB's became available. While the field was still concerned with static performance characteristics, rotordynamic coefficients and stability has drawn more interest during this time. At the forefront of this era in scientific testing was a book published in 1989 by Someya [16] that, among test results for several other fluid-film bearings, presented rotordynamic coefficients for three TPJB's. Parameters of these three TPJB's are given in Table 1. Someya's data book compared experimental results to calculations from an isoviscous hydrodynamic (HD) code. The experimental results were reported as dimensionless coefficients with stiffness non-dimensionalized using clearance over load and damping non-dimensionalized using rotational speed times clearance over load. Only one of the bearings was excited with multiple frequencies but frequency-dependent results were not available. The bearings were denoted, respectively, as test bearing numbers 9, 10, and 11. Bearing 9 was excited simultaneously in two directions with a compound sinusoid containing frequencies of 15.0 and 30.0 Hz. The results for bearing 9 confirmed Lund's predictions [1] by showing approximately isotropic stiffness and damping. The theoretical curve for the direct stiffnesses shows a decreasing trend while the experimental curve shows an increasing trend such that the stiffnesses are over predicted at low Sommerfeld numbers and under predicted at high Sommerfeld numbers. The cross-coupling forces were small and were always of the same sign for the damping, but the K_{yx} stiffness term showed a negative value with a magnitude of about 25% of the direct terms at Sommerfeld numbers above 0.5. The K_{xy} term for these cases was near zero but positive. The increasing trend of the theoretical damping curve matches that of the experimental curve for the direct damping terms. The damping is, however, over predicted at lower Sommerfeld numbers by a factor of about 3 while it is only over predicted by 5-10% above Sommerfeld numbers of 0.5. Bearings 10 and 11 were

Table 1 Parameters for bearings in [16]

Parameter	Bearing Number (Given by Author)		
	9	10	11
Number of Pads	4	5	5
Load Configuration	LBP	LOP	LOP
Nominal Diameter	140 mm (5.51 in.)	100 mm (3.94 in.)	76.4 mm (3.01 in.)
Axial Length	95 mm (3.74 in.)	50 mm (1.97 in.)	31.6 mm (1.24 in.)
Pad Clearance	0.175 mm (6.89 mil)	0.216 mm (8.50 mil)	0.086 mm (3.39 mil)
Preload Factor	null	0.51	null
Pad Arc Angle	73.7°	60°	58°
Pivot Offset	0.5	0.5	0.5
Running Speeds	3,000 rpm, 6,000 rpm	3,000 rpm, 6,000 rpm	3,000 rpm, 6,000 rpm

excited in the same manner as bearing 9, but with only a single frequency. Bearing 10 was excited at 190 Hz for all test conditions while bearing 11 was excited at about 45 Hz when the speed was 3,000 rpm and 100 Hz when the speed was 6,000 rpm, such that the excitation was roughly synchronous. The results from bearing 10 show much higher direct stiffnesses and much more rapidly increasing trends in the stiffnesses than either bearing 9 or 11 (ranging from 1 to 15 and 9 to 18 dimensionless stiffness in the x and y directions, resectively). However, the cross-coupled stiffnesses were significant, reaching magnitudes near around 40% of K_{yy}, and had opposite signs when $S \geq 0.2$. The experimental and theoretical stiffness K_{xx} showed the same discrepancy as in the direct stiffnesses of bearing 9 while K_{yy} was under predicted with the under prediction becoming more pronounced at higher Sommerfeld numbers. Both stiffnesses increased with Sommerfeld number. The direct damping terms were approximately isotropic, which was not predicted, and C_{xx} was largely over predicted at lower Sommerfeld numbers. The direct damping increased with Sommerfeld number. The cross-coupled damping terms were about 30% of the direct damping terms and opposite in sign,

increasing in magnitude with Sommerfeld number. The magnitudes of the coefficients for bearing 10 had more dependence on load than on speed. However, all coefficients except C_{yy} showed a strong dependence on speed at low loads where they increased with speed. All stiffness terms for bearing number 11 were roughly independent of Sommerfeld number. The cross-coupled stiffnesses were near zero. The code predicted K_{yy} very well while it over predicted K_{xx} at lower Sommerfeld numbers and seemed to converge with experimental results at around $S = 0.5$. All these features were the same for the damping, except that the direct terms showed a slight increase with Sommerfeld number. The direct damping coefficients for bearing 11 seemed to have slightly more dependence on load than on speed, increasing more for a given decrease in load than for an increase in speed. Bearing 11 seemed to be the most stable with a high degree of orthotropy and negligible cross-coupling while bearing 10 easily had the highest direct stiffness and damping terms (by a factor of 3 to 6 as compared to bearing 9 and 11) but also had the highest degree of cross-coupling and was likely the least stable.

While most papers discussing pivot effects considered that of pivot flexibility, a two-part series written by Wygant et al. [17,18] in 1999 presented their investigation on the effect of pivot friction. Wygant et al. tested two 5-pad TPJB's with identical geometry aside from one having a rocker-back pivot and one having a ball-in-socket pivot. Both had an L/D ratio of 0.75, offset ratio of 0.50, radial bearing clearance of 113.0 μm (4.45 mils), preload of 0.320, and diameter of 70 mm (2.756 in.). Testing speeds ranged from 900 to 2250 rpm while unit loads, directed on the pivot, ranged from 60.7 to 727 kPa (8.80 to 105 psi). This combination of speeds and loads resulted in Sommerfeld numbers from 0.1 to 2. Synchronous frequency excitations of 15, 27.5, and 37.5 Hz were used to extract dynamic coefficients. While roughly zero cross-coupled stiffness was found for the rocker-back design, a significant amount was found for the ball-in-socket design. The cross-coupled terms became opposite in sign at a Sommerfeld number of about 0.8. These terms, as with all others, showed little dependence on speed; the coefficients became noticeably more divergent as load was decreased. The uncertainty in the coefficients ranged from 5-45% for the direct stiffness, 9-28% for C_{xx},

6-82% for C_{yy}, and 25-272% for cross-coupled stiffnesses (which were small). Wygant et al. note that there is a much larger friction coefficient for sliding motion of the ball-in-socket pivot (0.4) than for that of rolling without slipping of the rocker-back pivot (0.006). They noted that theory and testing by Kostrzewsky et al. [19] showed that high cross-coupling stiffnesses are present for fixed geometry bearings and compared the resistance of motion due to the high friction coefficient for the ball-in-socket design to fixed geometry to arrive at an explanation for the cross-coupled stiffness terms encountered in his experiment. Wygant et al. provide the same reasoning in [17] to explain the difference in attitude angles between the two bearings. The results for the rocker-back bearing showed a straight-line path from low to high eccentricity with nearly zero attitude angle, while the ball-in-socket bearing showed a curved path with attitude angles ranging from 13°-33° as load increased. The attitude angle increased with speed.

Ikeda et al. [20] tested a 4-pad, 580 mm (22.8 in.) diameter TPJB in 2004. The bearing had an L/D ratio of 0.55, a C_r/R ratio of 0.0026, a 60% pivot offset, a 72° pad arc angle, and a null preload. Though the authors do not explicitly state the type of pivot, figures in the paper seem to indicate that it is a rocker-back type. The authors state that direct lubrication, in which oil at supply temperature is injected directly into the fluid film at the leading edge of each pad, increases the load capacity while decreasing the power loss. Ikeda et al. also state that the addition of a Rayleigh step to the leading edge of the unloaded pads decreases pad flutter by introducing a load onto these pads; this reduction in vibration is confirmed by their test results. Dynamic data were compared to theoretical results from [21] wherein finite difference methods are used to solve the Reynolds equation with turbulence considered but thermal and elastic effects ignored. Stiffness and damping coefficients were extracted using synchronous, single frequencies of 40, 50, and 60 Hz. As expected, very little orthotropy is seen in the experimental rotordynamic coefficients. The cross-coupled stiffnesses are near zero and are always of the same sign. The direct stiffnesses increase approximately linearly with Sommerfeld number and are predicted well at lower Sommerfeld numbers but greatly over predicted

beginning at Sommerfeld numbers of about 0.4. This over prediction becomes quadratically more pronounced as Sommerfeld number increases and reaches a percent difference of about 100% at a S = 0.6. The cross-coupled damping terms are close to zero but have opposite signs at most Sommerfeld numbers. The direct terms are nearly isotropic and increase slightly with Sommerfeld number. These dimensionless terms range from about 0.15 to 0.35 and are even further over predicted by theory with percent differences ranging from about 230% at the lowest Sommerfeld number to 270% at the highest. Ikeda et al. attribute this discrepancy to fluid inertia effects that were likely present during testing but not accounted for in the analysis.

Revisiting pivot flexibility effects, Dmochowski [22] analyzed two TPJB's in 2005 for which parameters are tabulated in Table 2. The pivot-types are not specified, but the reader might assume that the bearings have a rocker-back pivot based on a figure in the paper. For Case A, dynamic coefficients for frequencies ranging from 0 to 300 Hz were obtained using the Power Spectral Density Method, explained by Rouvas and Childs [23] (the reader is referred to the "Rotordynamic Coefficient Identification" subsection of this paper for a brief explanation of this method). However, while Eq. (17) defines the rotordynamic coefficients in terms of a frequency-independent [M]-[C]-[K] model, Dmochowski sets the added mass equal to zero and defines the real parts of the "dynamic-stiffness" coefficients (see Eq. (15)) as frequency-dependent stiffness terms. For Case A, the stiffness terms remained approximately constant up to synchronous frequency (150 Hz) and decreased beyond that value while the direct damping terms were fairly constant. According to the "well-defined" [22] trends of the coefficients, the real and imaginary parts of the dynamic-stiffnesses (impedances) are fit to quadratic and linear curves, respectively, and thus could have been used to determine the twelve coefficients for a frequency-independent [M]-[C]-[K] model. For Case B, calculations

Table 2 Parameters for bearings in [22]

Parameter	Case A	Case B
Number of Pads	5	5
Load Configuration	LBP	LOP
Nominal Diameter	98.5 mm (3.88 in.)	100 mm (4.0 in.)
Length-to-Diameter Ratio	0.4	1
Preload	0.3	0.3
Applied Load	4.0 kN (900 lbs.)	4.45 kN (1000 lbs.)
Unit Load	1.0 Mpa (150 psi)	0.45 Mpa (65 psi)
Shaft Speed	9,000 rpm	9,000 rpm

from a thermoelastohydrodynamic (TEHD) algorithm developed by Brockwell et al. [24] are provided. TEHD refers to the code's consideration of temperature variations (via the energy equation), elastic deflection of solid parts, and hydrodynamic effects (via Reynolds' equation). The author notes that this code accounts for turbulence by using the "Reynolds number effect." Initially, elastic deflection is analyzed for the pads only. Then a comparison is shown between theoretical results assuming a rigid pivot and those assuming a flexible pivot as formulated by Kirk and Reedy [14]. Figure 6 is an excerpt from Dmochowski's paper showing what he declares is a pivot stiffness versus static load curve for a "typical 100 mm [3.94 in.] TPJB" which is presumably what was used to calculate effective rotordynamic coefficients. If a rigid pivot is assumed, the

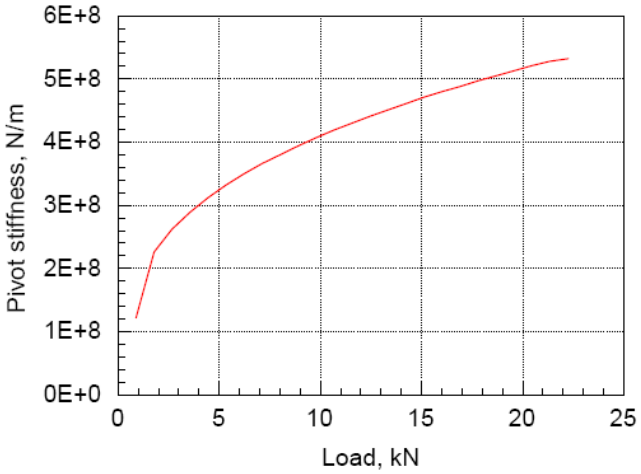

Fig. 6 Calculated pivot stiffness versus load of a "typical 100 mm TPJB" [22]

coefficients are not predicted to be appreciably frequency-dependent. On the other hand, calculations for this case show that the direct stiffness terms increase with excitation frequency if the pivots are modeled as flexible. Dmochowski attributed this stiffening effect to the bearing being lightly loaded (because of the higher L/D ratio). The direct damping for this case is predicted to be strongly dependent on excitation frequency, "leveling out" well before the synchronous frequency. The code predicts zero cross-coupling forces for both stiffness and damping regardless of the pivot model.

In 2005, Al-Ghasem [2] reported test results for a FP bearing in LBP configuration with D = 116.8 mm (4.6 in.) using the test rig described in the "Test Rig and Instrumentation" subsection of this paper. The bearing was tested at speeds from 4,000-12,000 rpm and excited at frequencies up to 300 Hz. Results were compared to theoretical predictions from a bulk-flow Navier-Stokes (NS) model developed by San Andrés and based on [25]. The computer code, fully described in the "Prediction Model" section of this paper, can use either the NS or Reynolds equation (user's choice) and can also use either isothermal—which was used in this case—or adiabatic conditions for the fluid between the journal and bearing. It does not account for translational pivot flexibility but does use the model reduction technique described by Parsell et al. [12] to account for non-synchronous, rotational pad excitation and includes the discrete value of flexural web moment stiffness for FP bearings. However, the routine used in Al-Ghasem's case retains pad inertia in the equations for the reduced rotordynamic coefficients. Test results showed frequency-dependent stiffnesses, with the real parts of the direct dynamic-stiffness coefficients decreasing rapidly with excitation frequency as predicted by both the Navier-Stokes and Reynolds models. The imaginary parts of the direct dynamic-stiffness coefficients were predicted to be approximately linear—indicating frequency-independent damping—and little change was seen in these coefficients between the NS and Reynolds models, indicating negligible fluid inertia effects. Experimental results also indicated frequency-independent damping and were accordingly modeled with frequency-independent [M]-[C]-[K] matrices. The decrease

in the direct stiffnesses with excitation frequency produced effective added mass terms of approximately 32 kg.

In 2006, Rodriguez and Childs [26] reported test results for the same bearing in LOP configuration. Similar results were found, with direct added masses around 40 kg. The real direct dynamic-stiffness coefficients were well-predicted using either the Reynolds equation or the bulk-flow NS equation solution for frequencies up to 1x. Both the NS and the Reynolds Equation models began to modestly diverge from measurements above 1x, predicting lower added mass terms than measured. However, the bulk-flow NS equation predicted the decrease in direct dynamic-stiffnesses at frequencies above the 1x frequency more accurately because it accounts for fluid inertia terms. In both [2] and [26], there is close agreement in the real parts of the dynamic-stiffnesses between the NS and Reynolds equations out to 1x, indicating that fluid inertia has little effect on the frequency-dependency of these coefficients. Rodriguez and Childs also note that pad inertia has a negligible effect on the frequency-dependency of the predicted coefficients and that model reduction is the primary cause.

Carter [27], also using the test rig described in the "Test Rig and Instrumentation" subsection, tested a 5-pad TPJB in both LOP and LBP configurations and reported results in 2007. The bearing and rotor had the following geometrical parameters: 0.282 preload, 60% offset, 57.87º pad arc angle, 101.587 mm (3.9995 in.) rotor diameter, 157.5 μm (6.20 mils) diametrical clearance, and 60.325 mm (2.375 in.) pad length. Static and dynamic characteristics were reported at speeds from 4,000-13,000 rpm and loads from 345-3101 kPa (50-450 psi). Hydraulic shakers were used to excite the stator (bearing and housing) at frequencies from 20-320 Hz. A frequency-independent [M]-[C]-[K] model fit the data accurately, as real parts of the dynamic-stiffnesses showed a quadratic dependence on excitation frequency while the imaginary parts were approximately linear. A stability analysis showed a whirl frequency ratio of zero, meaning infinite stability, for all test conditions. Stiffness orthotropy was measured and predicted for both loading configurations, but was more prevalent for LOP. The direct stiffness coefficients were highly dependent on load, increasing linearly with increasing load.

They were also dependent on speed, but to a much lower degree. K_{xx} slightly increased with speed at all loads while K_{yy} did the same for low loads but began to decrease with speed at higher loads. Direct stiffnesses were slightly over predicted and uncertainties were low, most being less than 10%. Cross-coupled stiffnesses were low, normally 10% or less of the direct terms and only had opposite signs at high speeds for the LBP case. Added mass terms increased with speed and were as high as 60 kg. These terms were significantly higher in the loaded direction and were over predicted at low speeds and under predicted at high speeds. At some test conditions, the added masses were negative, meaning that stiffness was increasing with excitation frequency. This effect was most noticeable at the lowest speed, 4,000 rpm. XLTFPBrg™ (used in [2,26]), assuming an adiabatic model, did not predict this but rather predicted small positive added mass at these conditions. Uncertainties in the added masses varied from about 5-40%, increasing with speed. Direct damping did not vary appreciably with speed or load and was consequently over predicted at low speeds and high loads. The uncertainties were low, typically less than 5%. Cross-coupled damping coefficients were also small, ranging from 5-20% of the direct terms but not showing a discernable pattern with speed or load. Comparison of static stiffness in the *y* direction and the rotordynamic coefficient K_{yy} showed that K_{yy} values were generally only slightly higher at low loads but significantly higher at high loads. "Static stiffness" refers to the slope of the load versus deflection curve at a given load; note that this can only be calculated in the *y* direction since that is the only loaded axis. Attitude angles were significant at low loads, but decreased to very low values at the highest loads. Pad temperatures typically did not exceed 80ºC (175ºF) aside from those measured near the trailing edge of the loaded pads at loads above 1034 kPa (150 psi); the maximum temperature detected during testing was 100ºC (212ºF) and occurred at the maximum unit load, 3103 kPa (450 psi). The maximum bearing temperature rose approximately linearly with speed. The trend of these curves was exceptionally well predicted, but the theoretical curves were 10-15ºC (18-27ºF) lower than the measured curves. Power loss was estimated by measuring the flow rate and inlet and outlet oil temperatures and assuming that all heat generated by

journal rotation was carried away by the lubricant. Power loss was minutely influenced by load, but increased significantly with speed. The maximum reported power loss was 14 kW (19 hp). While power loss was very accurately predicted for LOP, there was little basis for comparison for the LBP configuration as the data were obviously erroneous (negative power loss was reported as low speeds). Carter also monitored pad vibration by installing a thermocouple behind one loaded and one unloaded pad. The prevalent frequencies observed were running speed and its harmonics and vibration of the unloaded pads was typically 2-3 times higher than that of the loaded pads. However, waveforms of the pad vibration indicated negligibly small magnitudes.

The literature described in this introduction describes advancements in theory and testing of TPJB's through over four decades, beginning with the first published theoretical work by Lund [1] and concluding with more recent studies such as Dmochowksi [22] and Carter [27]. A common question that the authors sought to answer is that of whether or not rotordynamic coefficients for TPJB's are frequency-dependent. Table 3 summarizes the predictions of authors in this literature review with respect frequency-dependency of TPJBs' rotordynamic coefficients. Kirk and Reedy [14] and Nicholas and Wygant [3] present the effects of considering pivot flexibility in a model of the TPJB, reporting its general effect on direct stiffness and damping coefficients. These results are summarized in Table 4. While it is difficult to distinguish between the causes listed in Table 3 in testing, results of Dmochowski [22], Al-Ghasem [2], Rodriguez and Childs [26], and Carter [27] all demonstrate stiffness coefficients that have quadratic dependence on excitation frequency, and damping coefficients can be effectively modeled as frequency-independent due to the linear nature of the imaginary parts of the dynamic-stiffnesses. Table 5 presents a summary of comparison of theory to

Table 3 Predicted effect of discussed model attributes on frequency-dependent rotordynamic coefficients of TPJB's

Model Attribute	Effect on Coefficients w/ Increasing Frequency	
	Stiffness	Damping
Model Reduction	Quadratic decrease	Increase
Pad Inertia	Negligible	Negligible
Fluid Inertia	Quadratic decrease (according to [10]) Negligible (according to [2,26])	Linear increase (according to [10]) Negligible (according to [2,26])
Pivot Flexibility	Quadratic increase	Quadratic decrease

Table 4 Predicted effect of including pivot flexibility in model on synchronously reduced stiffness and damping of TPJB's

Direct Coefficients	Authors' Reported Effect Due to Pivot Flex.	
	Kirk and Reedy [14]	Nicholas and Wygant [3]
Stiffness	Increase or Decrease	Decrease up to 56%
Damping	Decrease up to 72%	Decrease up to 82%

experiment for four of the works in the literature review. While the works listed in Table 5 varied in most other attributes of their models, none of them accounted for pivot flexibility. While the prediction of stiffness varies from case to case, damping is generally over predicted. This fact begs the following question: if Kirk and Reedy [14]

Table 5 Comparison of theory and experiment for works in the literature review

Author	Prediction of Coefficients	
	Stiffness	Damping
Lund [1]	Varies	Over predicted in most cases
Someya [16]	Varies	Over predicted
Ikeda [20]	Heavily over predicted	Heavily over predicted
Carter [27]	Slightly over predicted	Heavily over predicted

are correct that predicted stiffness coefficients will increase or decrease and damping coefficients will decrease (up to 72%) due to considering pivot flexibility in the model, would adding pivot flexibility into the model help correct the discrepancies seen in Table 5?

This thesis is not only an addition to Table 5, but a supplement to the previous work of Wygant et al. [17,18] as it contains results for the less commonly tested ball-in-socket TPJB. Furthermore, as was done by Al-Ghasem [2], Rodriguez and Childs [26], and Carter [27], comparison will be made to XLTFPBrg code within the XLTRC^2 rotordynamics software suite (described in the proceeding "Prediction Model" section). Additionally, a somewhat elementary approach is taken to modify the results of the code by placing the measured stiffness of the pad support structures—one of which is measured by loading the rotor directly on top of one of the pads above the pivot location (see the "Pad Support Structure Stiffness Measurement" subsection)—in series with the calculated bearing stiffness and damping using the zeroth-order terms of Eq. (5).

In this modification, the pivot stiffness term, K_p, in the zeroth-order terms of Eq. (5) is replaced with the net stiffness of all "springs" from the top of the pad to the base of the ball—this includes the pad and its Babbitt layer, the ball-in-socket pivot, and the support shims for the ball and socket and is denoted as K_{ps}. The validity of using this measurement in Eq. (5) is realized by noting that the net contribution of all these elements is the effective stiffness that is in series with the bearing stiffness and damping during operation—though it is likely that the contact area between the rotor and pad Babbitt layer are more flexible for dry, stationary contact than when in moving contact and separated by an oil film during operation. Also, Kirk and Reedy's formulas—Eqs. (6,7) [14]—are used and corrected via Eq. (8) [3] to calculate pivot stiffness. Since the author presumes that the pivot is significantly more flexible than the rest of the pad support structure, the result of the pad support structure stiffness measurement is compared to the predicted pivot stiffness.

Objectives

The main objectives of this study are summarized in the list below:

(i) Measure static operating characteristics and rotordynamic coefficients for a 4-pad TPJB with ball-in-socket pivots in LBP configuration over a range of unit loads and shaft speeds.

(ii) Compare results to XLTFPBrg™ [25] predictions.

Secondary objectives are as follows:

(i) Measure stiffness of one of the test bearing's pad support structures.

(ii) Compare the result to pivot stiffness calculations using Eqs. (6,7,8) [3,14].

(iii) Modify the direct stiffness and damping predicted by XLTFPBrg using only the zeroth-order terms in Eq. (5) and the measured pad support structure stiffness value.

EXPERIMENTAL PROCEDURE

Test Rig and Instrumentation

Figure 7 illustrates the test rig that was originally designed by Kaul [28] for oil seals and has been modified for testing hydrodynamic bearings. The rotor is supported

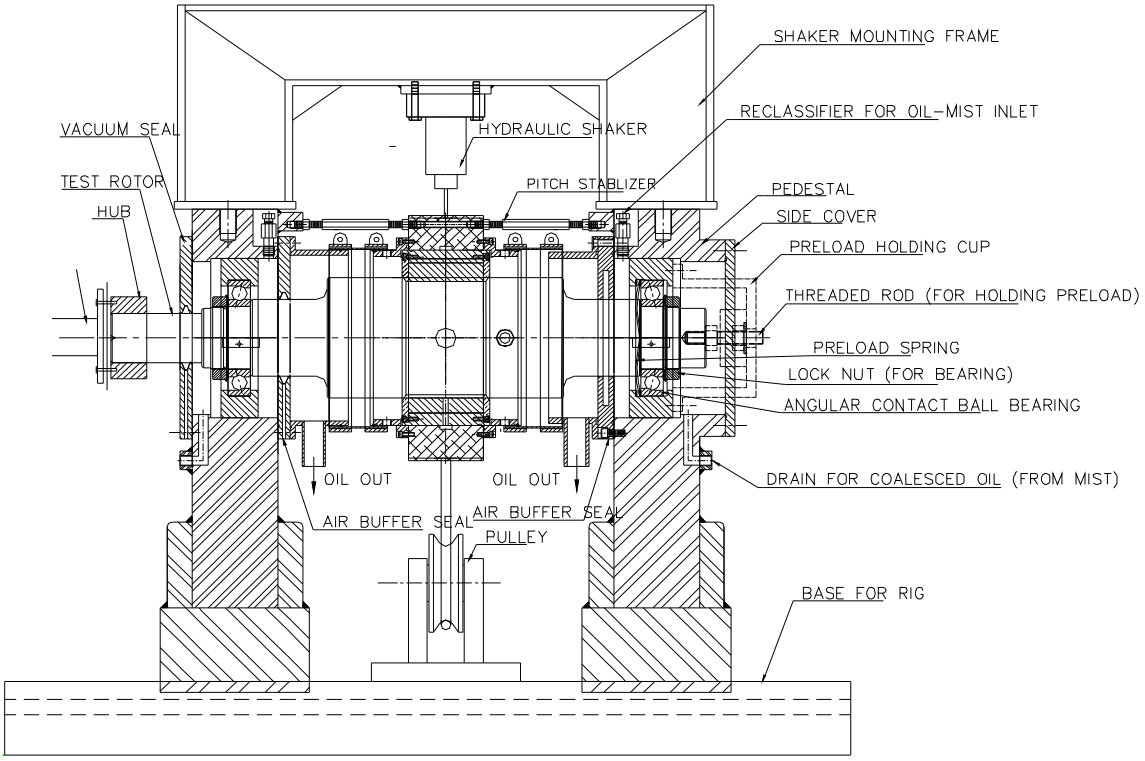

Fig. 7 Test section of test rig [29]

by two pedestals spaced approximately 381 mm (15 in.) apart, where it sits on two ball bearings. An oil-mist system supplies lubricant to the ball bearings during operation. Lubricant is supplied to the test bearing via a closed-loop pump system, for which flow rate is measured with a flow meter downstream of the pump and upstream of the bearing inlet. An air turbine is coupled to the rotor by a high-speed flexible coupling, and it can

provide 67 kW (90 hp) to drive the rotor up to 17,000 rpm. The rotor diameter is measured as 101.587 mm (3.9995 in.).

The stator houses the bearing and the non-contacting eddy current proximity probes that measure the relative stator-to-rotor position in two orthogonal directions at two planes. The planes are located orthogonally to the rotor's axis at the drive end (DE) and non-drive end (NDE). The absolute stator acceleration is measured with piezoelectric accelerometers, which are also located on the stator. Figure 8 shows the static loader assembly as viewed from the NDE of the test rig. A yoke is used to affix a pneumatic static loader to the stator. The static loader can provide up to 20 kN (4500 lbs.), and the applied load is measured using a load cell mounted as in Fig. 8.

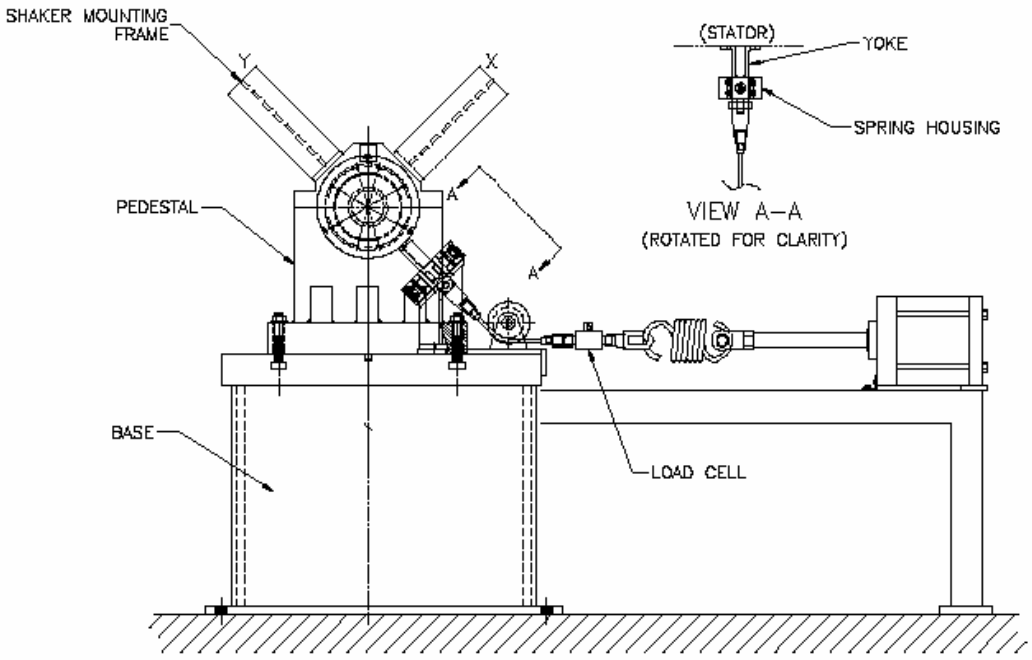

Fig. 8 Static loader configuration [29]

Shaft speed is measured with an eddy current tachometer at the NDE while inlet oil pressure is measured with a pressure probe attached to the stator. Inlet and outlet temperatures are measure via K-type thermocouples that are also installed in the stator. The shakers can provide dynamic forces with amplitudes approaching 4.45 kN

(1000 lbs.) at excitation frequencies up to 1 kHz; these forces are measured with load cells affixed between the shakers and the stingers that attach the shakers to the stator. Figure 9 shows the shaker-stinger configuration as viewed from the NDE.

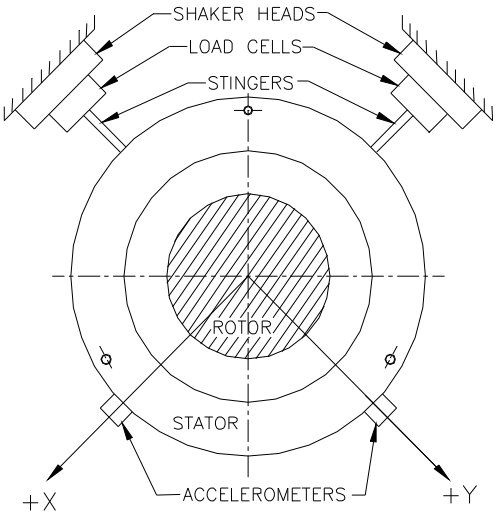

Fig. 9 Shaker-stinger configuration view from non-drive end [29]

Table 6 provides a summary of the instrumentation used. Though lubricant flow rate and pressure were not needed to report any of the static or dynamic data, they were needed to set the set the position of the oil pump valve so that specified inlet conditions of the lubricant could be met. In addition to the two K-type thermocouples used for inlet and outlet oil temperature, eight J-type thermocouples were used to measure trailing-edge pad temperatures.

Table 6 Instrumentation and measured data

Instrumentation	Measured Data
Load cells (3)	Static load, Dynamic loads
Flow Meter	Lubricant flow rate
Pressure probe	Inlet pressure
Thermocouples (10)	Inlet/Outlet and pad temperatures
Proximity probes (4)	Relative displacement (shaft↔stator)
Accelerometers (2)	Absolute stator acceleration
Eddy current tachometer	Shaft rotational speed

Test Bearing

The test bearing is a 4-pad TPJB with ball-in-socket type pivots and was manufactured by Rotating Machinery Technology (RMT), Inc. An engineering drawing is provided in Fig. 52 of Appendix A. Pictures of the bearing viewed from the DE and NDE are given in Figs. 10 and 11. Although the nominal diameter reported by the manufacturer was 101.78 mm (4.0070 in.), which would produce a radial bearing clearance of 95.3 μm (3.75 mils) for the test rotor, measurements indicated significant bearing crush with a radial bearing clearance of 99.6 μm (3.92 mils) in the axis 45º counterclockwise from the loaded axis (as viewed from the DE) and 54.6 μm (2.15 mils) in the axis 45º clockwise from the loaded axis. The bearing crush may have been due to press-fitting the instrumentation housing onto the outer diameter of the bearing. Other bearing parameters are given in Table 7. The pads are made from C18200 chromium

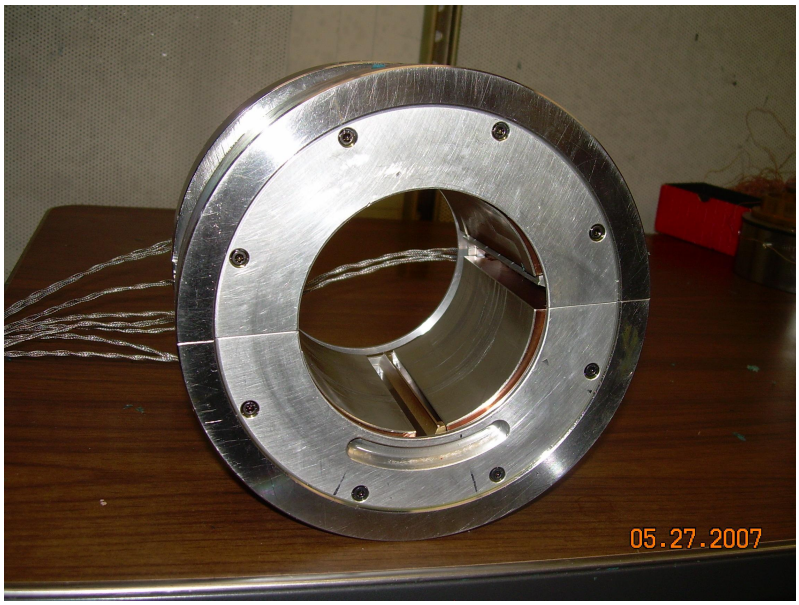

Fig. 10 Picture of test bearing from DE

copper alloy with a Babbitt metal lining. Pictures of the split halves of the test bearing are given in Figs. 12 and 13. Leading edge chamfers, one of which is pointed out in Fig. 13, are used to decrease flutter of the unloaded pads.

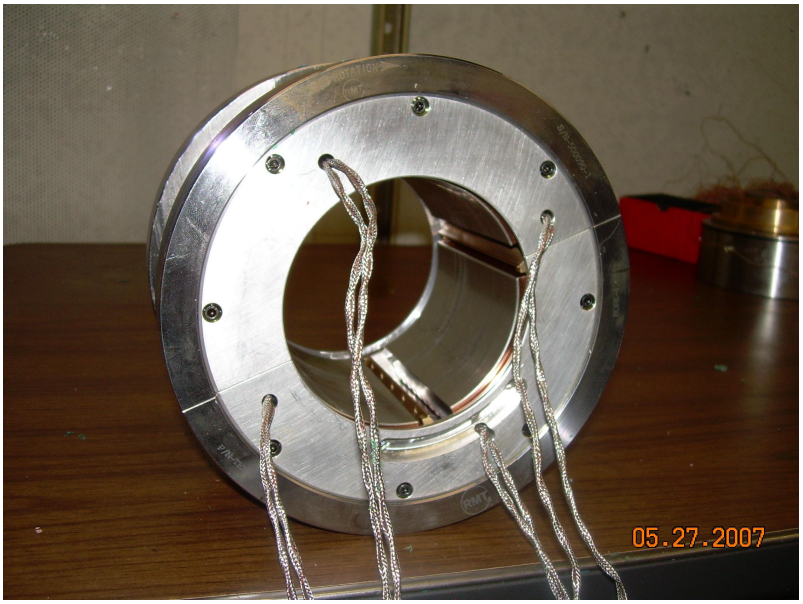

Fig. 11 Picture of test bearing from NDE

Table 7 Bearing parameters

Number of pads	4
Configuration	LBP
Pad arc angle	73^{o}
Pivot offset	65%
Rotor diameter	101.59 ± 0.01 mm (3.9995 ± 0.0005 in.)
Pad axial length	101.60 ± 0.03 mm (4.000 ± 0.001 in.)
Manufacturer-reported radial bearing clearance (C_b)	95.3 μm (3.75 mils)
Measured radial bearing clearance about x' axis (C_b)	99.6 ± 0.2 μm (3.92 ± 0.01 mils)
Measured radial bearing clearance about y' axis (C_b)	54.6 ± 4.5 μm (2.15 ± 0.18 mils)
Mean Loaded Pad Preload	0.37
Mean Unloaded Pad Preload	0.58
Ball Radius of Curvature (Design)	3.175 + 0.0008 - 0 cm (1.25 + 0.0003 - 0 in.)
Ball Material	4140 Rc 52 Steel w/ 12L14 Steel Support Shim
Socket Radius of Curvature (Design)	3.175 ± 0.013 cm (1.25 + 0.005 in.)
Socket Material	Bronze
Lubricant type	ISO VG32

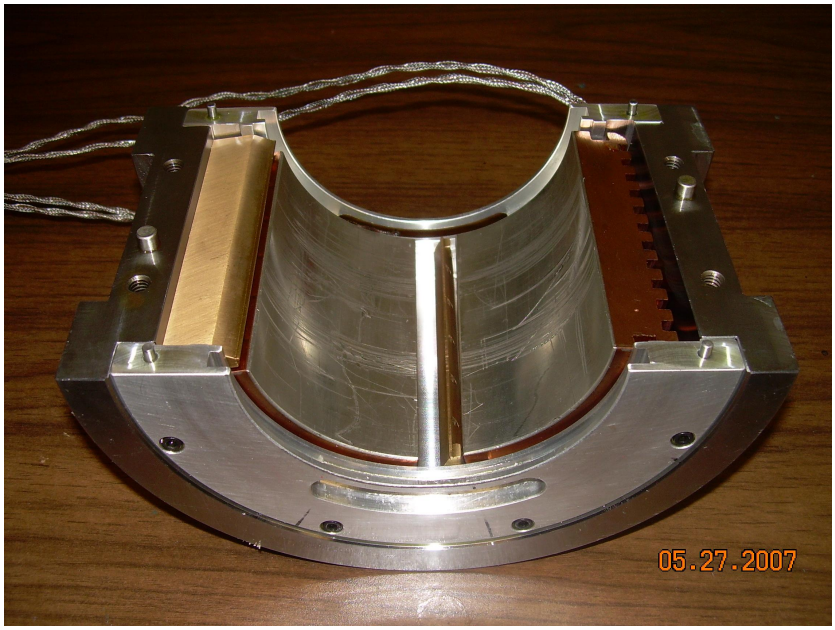

Fig. 12 Lower (loaded) half of test bearing

Fig. 13 Upper (unloaded) half of test bearing

The bearing uses patented Spray-Bar Blockers® and By-Pass Cooling®, described by Nicholas [32]. These technologies aim to increase load capacity and stability by keeping the oil temperature as close to the inlet temperature as possible. In a conventional "flooded" bearing, hot oil carried over from upstream pads is directed onto downstream pads such that the oil temperature increases from pad to pad. Spray-bar blockers are wall-like barriers located just upstream of the pads that reduce this development by blocking hot oil carry-over and spraying cool inlet oil onto the pads through tapped holes that extend from the bearing's outer diameter to just outside the radial location of the pads' leading edges. By-pass cooling uses circumferential cooling chambers that direct cool inlet oil through the outside of the pad, cooling the pad metal and decreasing thermal deformation and degradation as well as assisting oil-film cooling on the pad. The supply outlets of both the spray-bar blockers and by-pass cooling are shown in Fig. 14.

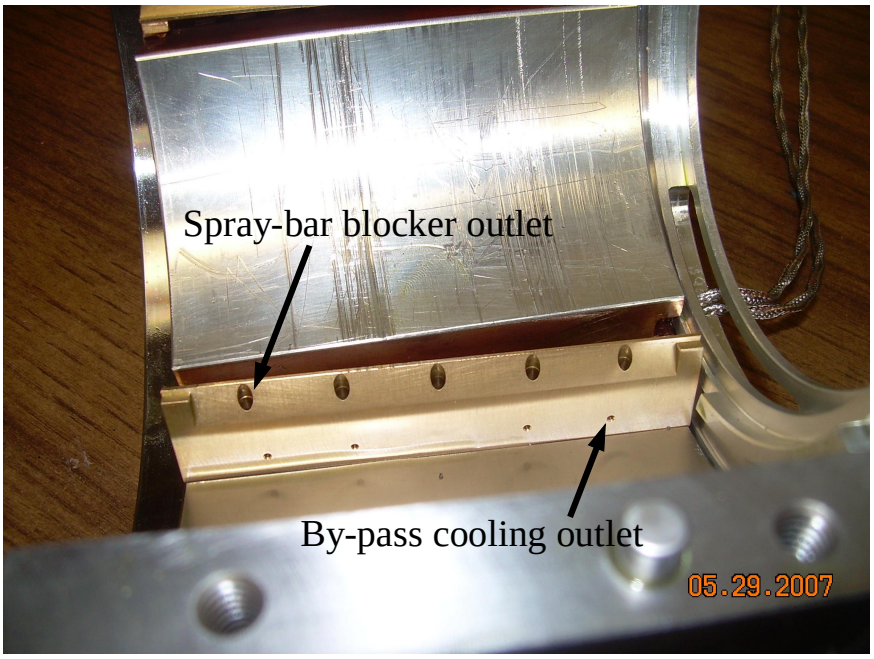

Fig. 14 Picture of spay-bar blocker with downstream pad removed

The ball and socket and one of the cooling chambers are shown in Fig. 15. The ball and socket are steel and bronze, respectively. The ball is bolted to the pad housing and has a support shim beneath it. The socket is inserted into a milled slot in the back of the pad. Annular retaining rings prevent the pads from floating out of position or falling out the housing during removal, installation, and transportation while still allowing them freedom to pitch and tilt during operation.

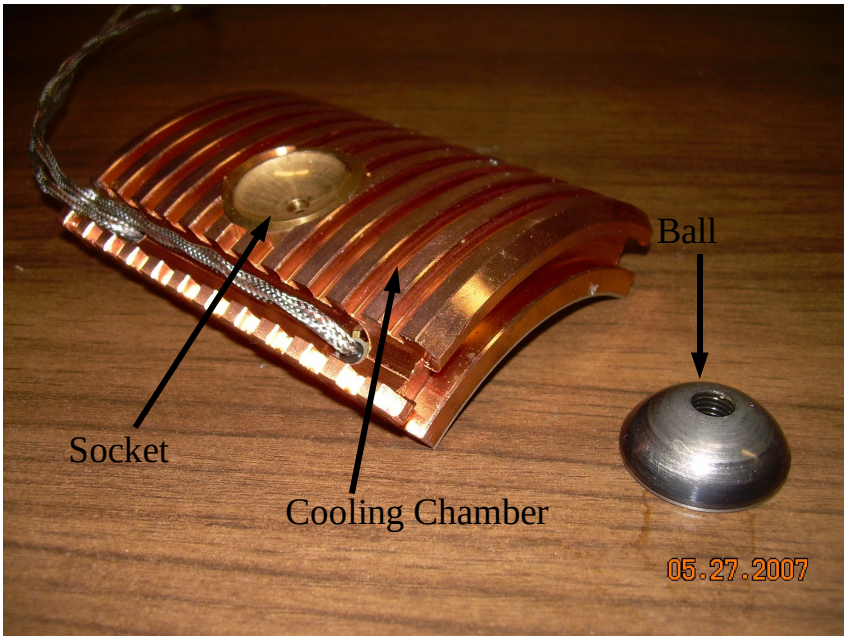

Fig. 15 Ball and back of pad

Test Conditions

A fan-cooled heat exchanger and PID controller were set to hold the inlet oil temperature between 37.8-43.3ºC (100-110ºF), though inlet temperatures were occasionally slightly above the upper bound (the maximum detected inlet temperature was 43.8ºC). Manual control of the pump valve was used to hold the flow rate and inlet pressure at roughly 1 L/s (16 gpm) and 97 kPa (14 psig). Exact values for inlet temperature, flow rate, and inlet pressure are recorded in Table 10 in Appendix A. Inlet temperature, pressure, and flow rate of the oil all affect the static and dynamic

characteristics of hydrodynamic bearings and typically have optimal or threshold values provided by the manufacturer. However, shaft speed and unit load are the driving independent variables behind bearing performance and dynamics and are easily controlled by experimenters. While shaft speed and unit load have customarily been used as control variables by experimenters, most have used Sommerfeld number as the abscissa for both static and dynamic data plotting. However, this study analyzes the independent effects of speed and load by plotting data as a function of load at fixed speeds and vice versa. Table 8 shows the speed and load combinations at which data were acquired. "s" denotes a test point at which static performance characteristics (static data) were collected while "d" denotes a test point at which rotordynamic coefficients (dynamic data) were collected.

Table 8 Speed and load conditions for data collection

Rotational Speed, rpm	Bearing Unit Load, kPa (psi)						
	0 (0)	345 (50)	689 (100)	1034 (150)	1379 (200)	1724 (250)	1896 (275)
4,000	s,d	s	s,d	s	s,d	s	s,d
6,000	s,d	s	s,d	s	s,d	s	s,d
8,000	s,d	s	s,d	s	s,d	s	s,d
10,000	s,d	s	s,d	s	s,d	s	s,d
12,000	s,d	s	s,d	s	s,d	s	s,d

Bearing Coordinate System

As previously noted, the *y* axis typically represents the loaded axis for journal bearings while the *x* axis is the unloaded axis; the same convention is used in this study. However, while some examinations define the positive *y* axis to be removed 90º in the direction of rotation from the positive *x* axis, the coordinate system for experiment in this research defines the positive *y* axis as being 90º removed from the positive *x* axis against the direction of rotation. Figure 16 depicts the bearing coordinate system, showing the (i) *x* and *y* axes, (ii) *x*' and *y*' axes about which bearing clearances were measured, (iii) static load (F_s) direction, (iv) circumferential coordinate θ, (v) shaft rotation (ω) direction, (vi) oil inlet location, and (vii) pad numbering convention.

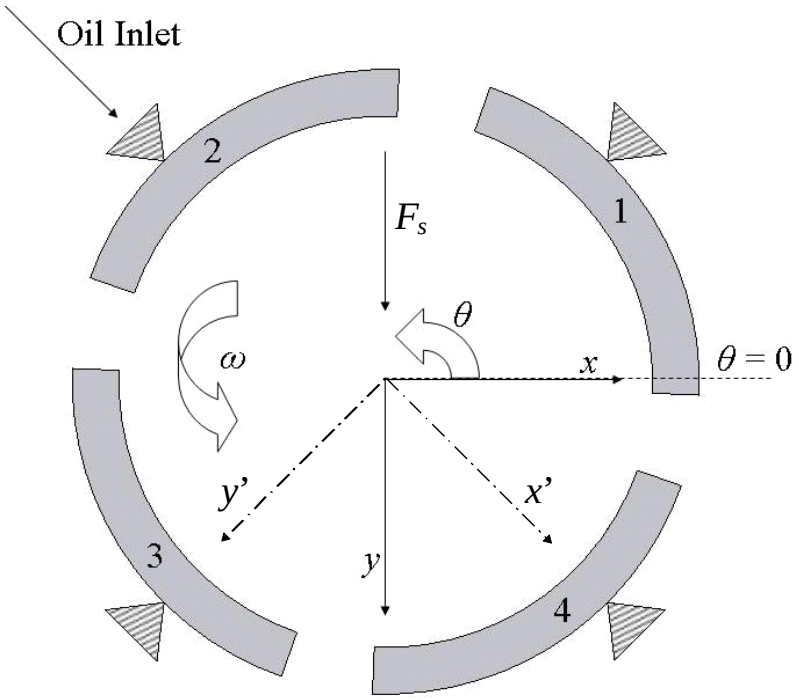

Fig. 16 Bearing coordinate system

Collection and Calculation of Static Data

The static data that are reported as dependent variables include the following: (i) journal position relative to the stator (eccentricity and attitude angle), (ii) estimated power loss, (iii) trailing-edge pad temperatures and maximum temperature rise, and (iv) static stiffness. This subsection describes how the necessary raw data for each were acquired and how the final data were calculated. The subsection begins with a description of the process for locating the bearing center and describes how this process was used to determine bearing clearances in the *x*' and *y*' directions.

Locating the Bearing Center

Before taking static or dynamic data, the center of the bearing had to be located; this subsection describes that process and Fig. 17 shows a schematic of it. This process is executed at ambient conditions prior to oil flow.

Step 1 – The journal center starts at an arbitrary position. The hydraulic shakers are used to pull the stator in the $-y$' direction such that journal center is displaced in the $+y$' direction relative to the stator until contact with the pad is made. Contact is assumed when the load cells connected to the stingers register a reading of about 110 N (25 lbs.) or more. A voltage reading of the proximity probes is taken. The journal is then displaced (relative to the stator) in the $-y$' direction until contact is made and a voltage reading is taken once again. The median voltage values at both the DE and NDE proximity probes are taken as $y' = 0$.

Step 2 – The same process is executed to find $x' = 0$.

Step 3 – The accuracy of the zero for the y' axis is checked by pulling the stator in both directions and ensuring equal readings of the proximity probes at both extremes. If readings are equal within a tolerance of about 1.3 μm (0.05 mils), the bearing center is defined. Otherwise, the experimenter reverts to step 1.

Step 4 (if necessary) – If step 1 is performed again, the accuracy of the zero for the x' axis is checked in the same manner as for the y' axis in step 3. If necessary, the experimenter reverts to step 2.

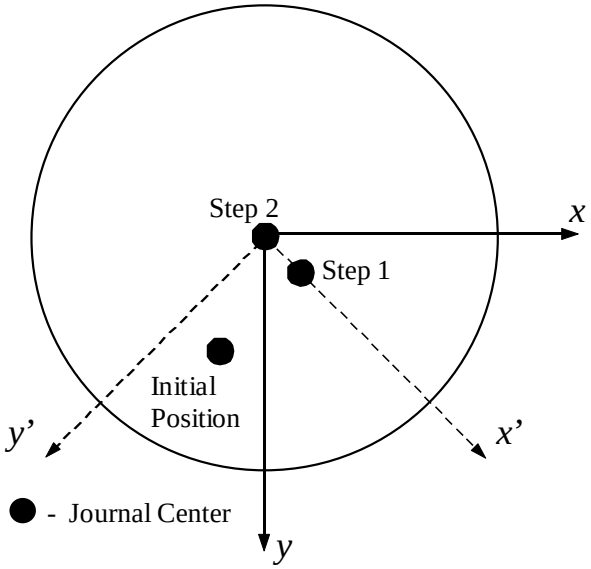

Fig. 17 Schematic of the process for locating the bearing center

While locating the center can be an iterative process, it could typically be completed in practice by step 3. Note that the *x*' and *y*' axes are used to find the bearing center since there are pivots at either end of these axes, allowing for a solid contact foundation.

Clearance Measurement

In the process of finding the bearing center, described in the previous subsection, readings from the proximity probes were taken at each extreme of the *x*' and *y*' axes. Once the bearing center was found, absolute values of these readings were averaged in each axis to obtain their radial clearances. As mentioned in the previous section, this process was performed at ambient conditions before oil circulation.

Journal Position

Note that in actuality the "stator," while not a rotating part, was the piece of the test rig that was pulled statically and shaken dynamically. However, journal position relative to the stator was recorded since a load in one direction on the stator is equivalent to a load in the opposite direction on the rotor according to Newton's third law. Two proximity probes in each axis were used to record journal position in both axes, in both the DE and NDE planes. The pitch stabilizers were tightened and adjusted prior to measurement such that the stator and rotor centerlines were approximately parallel. During operation, maximum pitch and yaw of 0.1 milliradians were allowed, which translates to a difference of 11 μm (0.4 mils) between the relative displacements at the ends of the bearing. The average of the proximity probe readings at the DE and NDE planes were taken as relative displacements from center in each axis.

The eccentricity is reported in a locus plot showing the displacement from center in both the *x* and *y* axes. Figure 18 gives a graphical representation of the eccentricity vectors $\boldsymbol{e}_x$ and $\boldsymbol{e}_y$ as well as the resultant eccentricity $\boldsymbol{e}$ and the attitude angle ϕ. The radial clearances shown in Fig. 18 are based on the ad hoc definitions $C_x = C_{y'}$ and $C_y = C_{x'}$ because, if the pad preload is disregarded and the pad are not tilted, the diametrical clearance between pads 1 and 3 about the *x* axis is taken as the measured clearance about the *y*' axis while that between pads 2 and 4 about the *y* axis is taken as the measured

clearance about the *x*' axis. In actuality, there is a preload and the pads tilt and deflect, all of which increase the clearance. Accordingly, eccentricities greater than the defined clearances about the coordinate axes are possible without dry rubbing. The equation for magnitude of the resultant eccentricity is shown in Eq. (9):

$$e = \sqrt{e_x^2 + e_y^2} \tag{9}$$

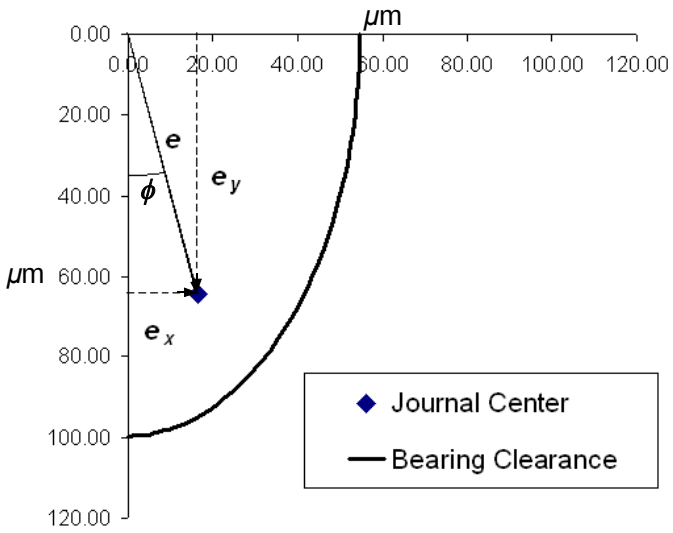

Fig. 18 Graphical representation of eccentricity and attitude angle

Typically, one would define the eccentricity ratio in either direction as the ratio of eccentricity to bearing clearance, but that definition is invalid here due to the high degree of bearing crush.

The attitude angle is defined as the angle between the positive *y* axis and the eccentricity vector ***e*** and is defined in Eq. (10):

$$\phi = \tan^{-1}\left(\frac{e_x}{e_y}\right) \tag{10}$$

In cases where the clearances are equal about both axes, the attitude angle could also be defined as the angle between the *y* axis and the resultant eccentricity ratio vector. However, since the clearance is tighter about the *x* axis for the test bearing, the attitude angle would appear larger using this method of calculation than if using the eccentricity vector. As explained in the "Prediction Model" section, the average clearance had to be used for predictions since XLTFPBrg does not accept differing clearances about the main coordinate axes.

Estimated Power Loss

The raw data used to estimate the power loss imposed by the bearing are the inlet and outlet oil temperatures measured just downstream of the oil inlet and just outside the axial length of the bearing where the oil exits out the NDE side along with the oil flow rate measured upstream of the bearing supply inlet. The test rig was designed to measure temperatures at both ends of the bearing, but unknown errors caused poor readings at the DE exit thermocouple during this test. These temperature readings were direct oil temperature measurements as the probe tips were immersed in the lubricant.

To estimate the power loss, the difference in thermal energy per unit volume of the inlet and exit oil is multiplied by the volumetric flow rate, *Q*, as in Eq. (11):

$$\mathsf{P} = Q\rho\left(T_{\text{ave}}\right)c_p\left(T_{\text{ave}}\right)\left(T_{\text{out}} - T_{\text{in}}\right) \tag{11}$$

Here, T_{ave} is the average of the inlet and outlet temperatures, T_{in} and T_{out}. The density and specific heat (ρ, c_p) are linear functions of absolute temperature. Vendor data for the slopes and *y*-intercepts of these functions are given in Eq. (12) for ISO VG 32:

$$\begin{aligned} c_p\left(T\right) &= 3.627T + 811.75, \left[\text{J}/\left(\text{kg}\cdot\text{K}\right)\right] \\ \rho\left(T\right) &= -0.6616T + 1064, \left[\text{kg}/\text{m}^3\right] \end{aligned} \tag{12}$$

The use of T_{ave} in Eq. (11) is justified by the fact that the percent differences (between inlet and exit values) in both ρ and c_p were less than 3% even for the largest temperature

increase. Note that some heat is conducted to the stator and shaft metal and radiated away to the environment, so this approximation slightly underestimates the power loss.

Trailing-Edge Pad Temperatures and Maximum Temperature Rise

As mentioned in the "Test Rig and Instrumentation" subsection, eight thermocouples were used to measure trailing-edge pad temperatures. The bearing manufacturer provided thermocouples, tapped into the back of the pads, at identical circumferential locations of 68º (offset ratio of 93%). Both were displaced roughly 3.18 cm (1.25 in.) from the axial bearing center. Figure 19 depicts the (a) circumferential and (b) axial locations of the thermocouples. The assumed intent of the manufacturer was to

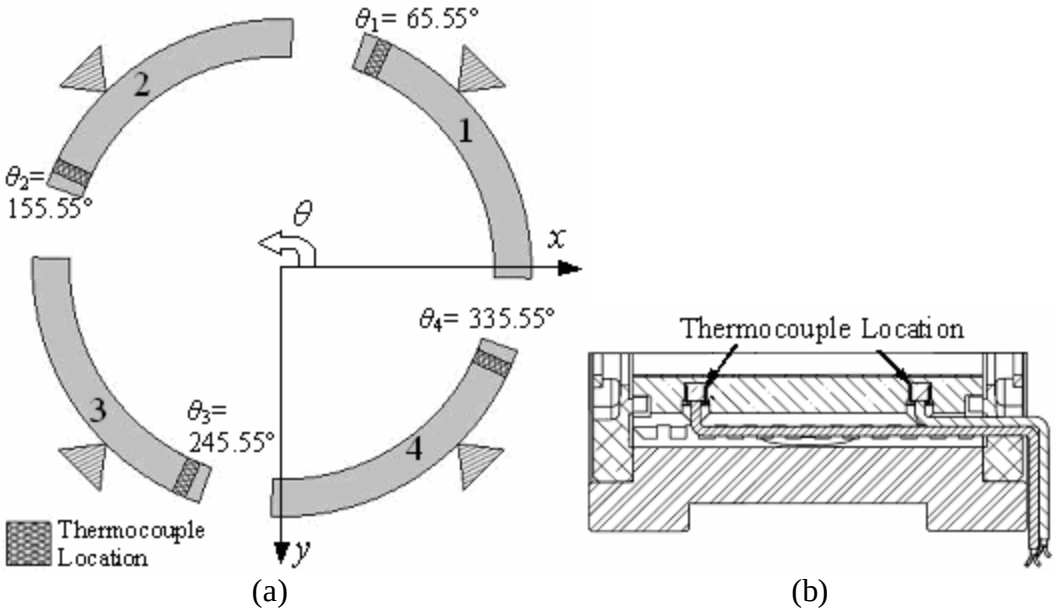

Fig. 19 (a) Circumferential and (b) axial thermocouple locations for trailing-edge pad temperature measurements

allow the experimenters to obtain an approximation of the maximum oil film temperature for each pad and to obtain an average or observe variation by taking measurements at separate axial locations. Test results of Al-Ghasem [2] and Carter [27] show pad temperatures that increase with pad angle to a maximum temperature at the highest offset thermocouple location, which was 95% for all but pad 1 in Carter's

bearing (in this case there was no thermocouple past 75% offset, but the maximum temperature was still recorded at this highest offset thermocouple). Though fluid film temperatures were not directly measured, the thermocouple probe-tips were only roughly 0.28 cm (0.11 in.) from the pad surface and the system was allowed to reach a steady state aside from oscillation of the temperature control system. Since variation in recorded temperature between the two axial locations averaged only 1.2ºC (2.2ºF), the average of the two thermocouple readings at each pad was taken as the trailing-edge pad temperature for each of the pads.

Maximum oil film temperatures are also of interest. Since T_{in} varied by up to 5ºC (9ºF), reporting the maximum temperature rise from the inlet to the location of the maximum trailing-edge pad temperature served as a better basis of comparison to theory. The maximum temperature rise, ΔT_{max}, is simply the difference in temperature between the maximum detected bearing temperature, T_{max}, and inlet oil temperature, T_{in}, as shown in Eq. (13):

$$\Delta T_{\text{max}} = T_{\text{max}} - T_{\text{in}} \tag{13}$$

Static Stiffness

At each test speed, the static loader was used to impose several successively increasing known loads (measured by the load cell) on the stator. Each load, F_s, caused the eccentricity about the y axis to increase. Measuring e_y at each load using the proximity probes, a load versus deflection graph in the y direction was obtained for each speed. The static stiffness is defined as the slope of this load versus deflection plot at a given point and is denoted symbolically as $K_{yy,s}$. Figure 20(a) shows the load versus deflection plot at 12,000 rpm. To calculate the static stiffness, a second order polynomial is first fit to a set of three adjacent points using the least squares method. For the first point on the plot, the second and third points are used as the adjacent points. For the last point, the previous two points are used as the adjacent points. And for points in between the first and last, the surrounding points are used as adjacent points. The

derivative of this function is then evaluated at the point of interest. Figure 20(b) shows the Excel plot that was used to calculate the static stiffness at 1896 kPa (275 psi) and 12,000 rpm. On the plot, one can see the can see the output of Excel's curve-fitting function for which the derivative was calculated at the measured value of e_y. Since the results of this

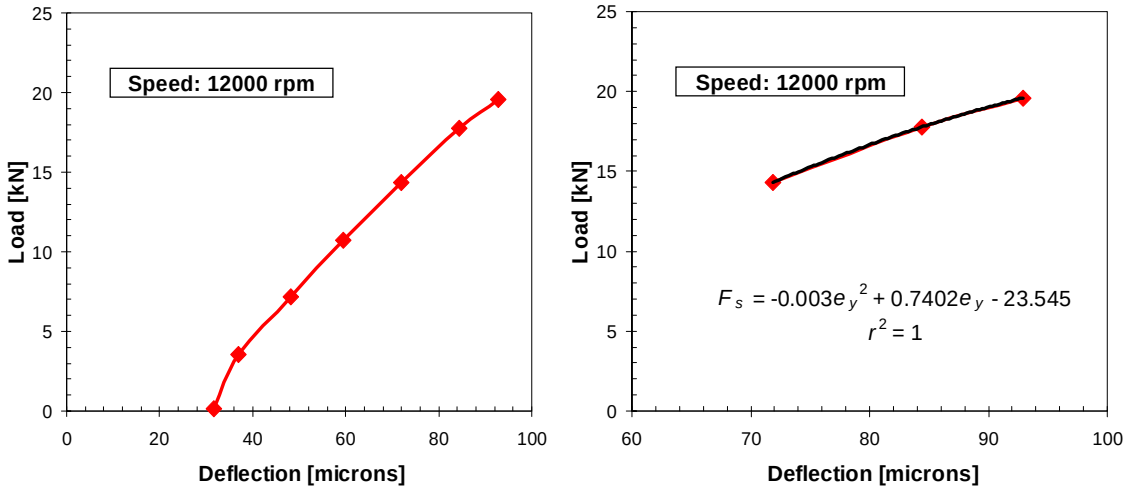

(a) (b)

Fig. 20 Load versus deflection plots: (a) overall, (b) at three adjacent points at 12,000 rpm

measurement are compared to dynamic data, the graphs are provided in a "Static Stiffness Versus K_{yy}" subsection that is separate to the "Static Data" and "Dynamic Data" subsections of the "Results" section.

Collection and Calculation of Dynamic Data

Rotordynamic Coefficient Identification

Childs and Hale [30] explain how rotordynamic coefficients are estimated from measurements. The following discussion describes how this method was utilized to obtain the coefficients presented in this thesis. The equations of motion for the stator mass M_s are given in Eq. (14),

$$M_s \begin{bmatrix} \ddot{x}_s \\ \ddot{y}_s \end{bmatrix} = \begin{bmatrix} f_x \\ f_y \end{bmatrix} - \begin{bmatrix} f_{bx} \\ f_{by} \end{bmatrix} \tag{14}$$

where $\ddot{x}_s$, $\ddot{y}_s$ are the stator acceleration components measured with the accelerometers; f_x, f_y are the force components induced by the hydraulic shakers and measured with dynamic load cells; and f_{bx}, f_{by} are the bearing reaction force components. M_s is obtained by simply weighing the entire bearing and accompanying instrumentation housing. The housing assembly is treated as a rigid body, neglecting the relative motion of the pads. This simplification is based on the assumption that the pads' natural frequencies are significantly higher than the excitation frequencies. Present and previous testing has shown no evidence that the relative pad motion has any perceivable influence on housing acceleration measurements.

Substituting Eq. (3) into Eq. (14) and applying an FFT nets

$$\begin{bmatrix} \boldsymbol{F}_x - M_s \boldsymbol{A}_x \\ \boldsymbol{F}_y - M_s \boldsymbol{A}_y \end{bmatrix} = -\begin{bmatrix} \boldsymbol{H}_{xx} & \boldsymbol{H}_{xy} \\ \boldsymbol{H}_{yx} & \boldsymbol{H}_{yy} \end{bmatrix} \begin{bmatrix} \boldsymbol{D}_x \\ \boldsymbol{D}_y \end{bmatrix} \tag{15}$$

$\boldsymbol{D}_i$ denotes the Fourier transform of the measured displacement in the i (x or y) direction. $\boldsymbol{H}_{ij}$ coefficients are the direct and cross-coupled dynamic-stiffness coefficients for the bearing. $\boldsymbol{F}_i$ and $\boldsymbol{A}_i$ are the complex Fourier transformed values for the measured force and acceleration components, respectively. The four dynamic-stiffness coefficients $\boldsymbol{H}_{ij}$ in Eq. (15) are the unknowns, but there are only two equations. Independent excitation in the x and y directions produces the following four independent equations:

$$\begin{bmatrix} \boldsymbol{F}_{xx} - M_s \boldsymbol{A}_{xx} & \boldsymbol{F}_{xy} - M_s \boldsymbol{A}_{xy} \\ \boldsymbol{F}_{yx} - M_s \boldsymbol{A}_{yx} & \boldsymbol{F}_{yy} - M_s \boldsymbol{A}_{yy} \end{bmatrix} = -\begin{bmatrix} \boldsymbol{H}_{xx} & \boldsymbol{H}_{xy} \\ \boldsymbol{H}_{yx} & \boldsymbol{H}_{yy} \end{bmatrix} \begin{bmatrix} \boldsymbol{D}_{xx} & \boldsymbol{D}_{xy} \\ \boldsymbol{D}_{yx} & \boldsymbol{D}_{yy} \end{bmatrix} \tag{16}$$

The stator was shaken alternately in the x and y directions with force versus time waveforms containing components with discrete frequency values ranging from 20 to

260 Hz at intervals of 10 Hz. The waveform is repeated 32 times and the resulting force, displacement, and acceleration data are averaged in the frequency domain. Ten separate "shakes" are performed at each test condition to get uncertainties of the dynamic-stiffness coefficients at each frequency. Relationships between the dynamic-stiffness $\boldsymbol{H}_{ij}$ coefficients and the rotordynamic coefficients are defined in Eq. (17):

$$\begin{aligned} &\boldsymbol{H}_{ij} = (K_{ij} - \Omega^2 M_{ij}) + \boldsymbol{j}(\Omega C_{ij}), \\ &\mathrm{Re}\left(\boldsymbol{H}_{ij}\right) = K_{ij} - \Omega^2 M_{ij}, \;\; \mathrm{Im}(\boldsymbol{H}_{ij}) = \Omega C_{ij} \end{aligned} \tag{17}$$

The averages of the FFT values at each of the discrete frequencies provide a dynamic-stiffness versus frequency plot for the real and imaginary parts of each of the four dynamic-stiffness coefficients, netting eight total plots. Equation (17) provides the equations for the real and imaginary dynamic-stiffness coefficients based on a frequency-independent [M]-[C]-[K] model. To extract the rotordynamic coefficients, a least squares linear regression fits a line in the form of the real and imaginary parts of Eq. (17) to data from each of the eight dynamic-stiffness curves. Equation (18) formulates a least squares regression, where *m* is the slope and *b* is the *y*-intercept:

$$\begin{aligned} &b = \bar{\gamma} - m\bar{\chi}, \;\; \bar{\chi} = \frac{1}{M}\sum_{l=1}^{M}\chi_l, \;\; \bar{\gamma} = \frac{1}{M}\sum_{l=1}^{M}\gamma_l \\ &m = \frac{M\sum_{l=1}^{M}\chi_l\gamma_l - \bar{\chi}\,\bar{\gamma}}{M\sum_{l=1}^{M}\left(\chi_l\right)^2 - \bar{\chi}^2} \end{aligned} \tag{18}$$

γ and χ are the dependent and independent variables, respectively, while $\bar{\gamma}$ and $\bar{\chi}$ are their averages. M is the number of data points and l is an indexing subscript. Equation (19) defines the variables in Eq. (18) for the two cases in which it was used to extract rotordynamic coefficients:

$$\chi = \begin{cases} \Omega^2 \text{ if } \gamma = \mathrm{Re}\left(\boldsymbol{H}_{ij}\right) \\ \Omega \text{ if } \gamma = \mathrm{Im}\left(\boldsymbol{H}_{ij}\right) \end{cases}, \quad m = \begin{cases} -M_{ij} \text{ if } \gamma = \mathrm{Re}\left(\boldsymbol{H}_{ij}\right) \\ C_{ij} \quad \text{if } \gamma = \mathrm{Im}\left(\boldsymbol{H}_{ij}\right) \end{cases}$$
$$b = \begin{cases} K_{ij} \text{ if } \gamma = \mathrm{Re}\left(\boldsymbol{H}_{ij}\right) \\ 0 \quad \text{if } \gamma = \mathrm{Im}\left(\boldsymbol{H}_{ij}\right) \end{cases} \tag{19}$$

While $b = 0$ when $\gamma = \mathrm{Im}(\boldsymbol{H}_{ij})$ in theory, the linear regressions of the imaginary parts of the dynamic-stiffness data were allowed to have a *y*-intercept so that the regression could capture the slope of the curve when the intercept of such data varied from zero. In most cases, these *y*-intercepts were small and were not reported as they are physically meaningless to the [M]-[C]-[K] model that was used.

In cases where $\mathrm{Re}(\boldsymbol{H}_{ij})$ was poorly fit with a linear curve, there was low uncertainty in the average of these dynamic-stiffnesses (see Eq. (23) in the next subsection, "Uncertainty of Dynamic-Stiffnesses and Rotordynamic Coefficients"). Accordingly, M_{ij} was omitted from the model and K_{ij} was defined as the average of $\mathrm{Re}(\boldsymbol{H}_{ij})$ over the span of excitation frequencies. In practice, M_{ij} omitted if its uncertainty (see Eqs. (21,22)) was 35% or more.

While 25 discrete frequencies were included in the dynamic-stiffness data, a point was removed and not included in the linear regression calculation if the uncertainty of the average of the data from the ten separate shakes was excessive. The uncertainty of these points was based on a 95% confidence interval, or two standard deviations. The following list provides the frequency of points that were typically omitted:

- Electrical noise: 60 Hz.
- The natural frequency of the stator system: 170-180 Hz.
- The running frequency: 60-70 Hz for 4,000 rpm; 100 Hz for 6,000 rpm; 130-140 Hz for 8,000 rpm; 160-170 Hz for 10,000 rpm; and 200 Hz for 12,000 rpm.

Note that this is not an exhaustive list nor are the points in this list omitted a priori as the points occasionally had acceptable uncertainties. Figures 21(a) and (b) depict examples of the data and the corresponding curve-fits for sets of real and imaginary dynamic-

stiffnesses while (c) shows a case where an average was fit to a set of real dynamic-stiffness data at 12,000 rpm and 689 kPa (100 psi). In the cases of Fig. 21, one can extract K_{xx} = 417.98 MN/m and M_{xx} = 29.31 kg from (a), C_{yy} = 166.22 kN·s/m from (b), and K_{yy} = 331.03 MN/m from (c).

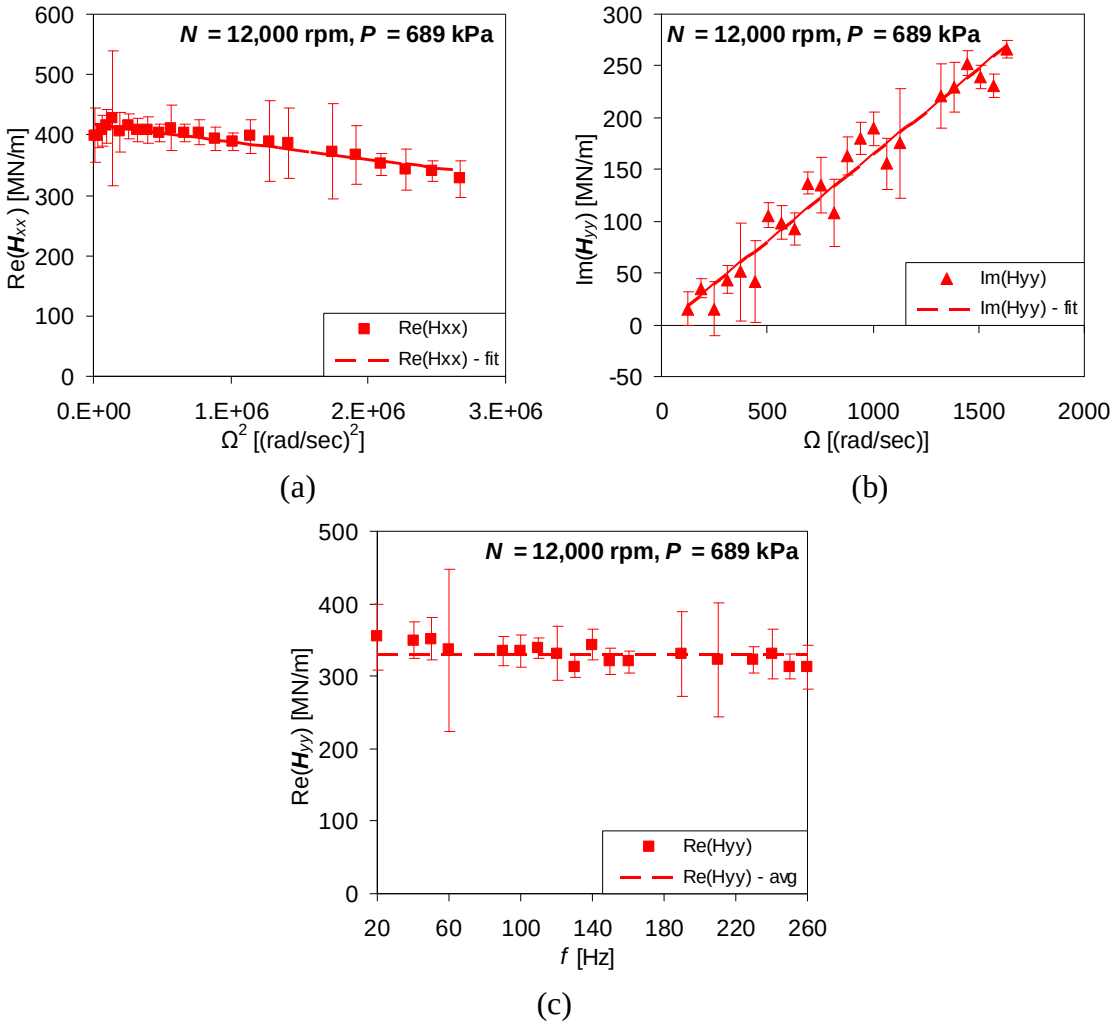

Fig. 21 Curve-fits of (a) Re($\boldsymbol{H}_{xx}$) and (b) Im($\boldsymbol{H}_{yy}$) and (c) average of Re($\boldsymbol{H}_{yy}$) at 12,000 rpm, 689 kPa (100 psi)

Uncertainty of Dynamic-Stiffnesses and Rotordynamic Coefficients

The uncertainty of the dynamic-stiffnesses, as mentioned, is merely twice the standard deviation of the mean of the ten samples, or shakes. Using Eq. (20) provides a 95% confidence interval assuming a normal distribution of data:

$$\Delta \boldsymbol{H}_{ij} = 2\sqrt{\frac{\sum_{l=1}^{10}\left(\boldsymbol{H}_{ij}^{l} - \bar{\boldsymbol{H}}_{ij}\right)^2}{9}} \tag{20}$$

Here, $\Delta \boldsymbol{H}_{ij}$ is the uncertainty of the average of the dynamic-stiffnesses deduced from the ten shakes, $\bar{\boldsymbol{H}}_{ij}$ (in the rest of the study the $\bar{\boldsymbol{H}}_{ij}$ nomenclature is dropped and it is assumed that $\boldsymbol{H}_{ij}$ denotes the average), and $\boldsymbol{H}_{ij}^{l}$ is one particular sample of the ten shakes (e.g. $\boldsymbol{H}_{ij}^{3}$ is the dynamic-stiffness deduced from the third shake).

The uncertainty of the rotordynamic coefficients themselves are calculated based on the correlation of the linear regression to the dynamic-stiffness data. A series of equations is presented that ultimately leads to an expression for the uncertainty of the slope and *y*-intercept of a least squares curve-fit. Equation (21) presents the mean squared error (MSE) and the quantity $S_{\chi\chi}$:

$$\hat{\sigma}^2 = \frac{\sum_{l=1}^{M}\left(\hat{\gamma}_l - \gamma_l\right)^2}{M-2}, \quad S_{\chi\chi} = \sum_{l=1}^{M}\chi_l^2 - M\,\bar{\chi}^2 \tag{21}$$

Here, $\hat{\gamma}_l$ represents the curve-fit values of the dependent variable. The quantities in Eq. (21) are used to calculate the uncertainty of the slope, Δm, and of the *y*-intercept, Δb, as shown in Eq. (22):

$$\Delta m = t\sqrt{\frac{\hat{\sigma}^2}{S_{\chi\chi}}},\ \ \Delta b = t\sqrt{\hat{\sigma}^2\left(\frac{1}{M}+\frac{\overline{\chi}^2}{S_{\chi\chi}}\right)} \tag{22}$$

The variable t is a weighting variable that determines the size of the confidence interval; t is set to 1.96 to obtain a 95% confidence interval. Again using the examples in Fig. 21(a) and 21(b), the corresponding uncertainties of the rotordynamic-coefficients are ΔK_{xx} = 5.71 MN/m, ΔM_{xx} = 4.53 kg, and ΔC_{yy} = 16.12 kN·s/m.

Using the same formulation as Al-Jughaiman [31], the uncertainty in K_{ij} is calculated using the Eq. (23) in the case that M_{ij} is omitted and K_{ij} is the average of the dynamic-stiffnesses:

$$\Delta K_{ij} = t\frac{\sqrt{\frac{\left(\overline{\gamma}-\gamma_l\right)^2}{M-1}}}{\sqrt{M}} \tag{23}$$

In this case, $\overline{\gamma}$ still represents the average value while γ_l still represents the discrete values of the dependent variable (dynamic-stiffness). As in Eq. (22), t = 1.96. Application of Eq. (23) to the data in Fig. 21(c) results in ΔK_{xx} = 7.14 MN/m.

Another value that is presented for each of the pair of sets of dynamic stiffness data (γ and χ variables) is the square of the Pearson product moment correlation coefficient, r. The square of this coefficient is well-known as the "r-squared" value. It should not be confused with the upper case R that denotes bearing radius. Equation (24) gives its definition:

$$r = \frac{M\left(\sum_{l=1}^{M}\chi_l\gamma_l\right)-\left(\sum_{l=1}^{M}\chi_l\right)\left(\sum_{l=1}^{M}\gamma_l\right)}{\sqrt{\left[M\left(\sum_{l=1}^{M}\chi_l^2\right)-\left(\sum_{l=1}^{M}\chi_l\right)^2\right]\left[M\left(\sum_{l=1}^{M}\gamma_l^2\right)-\left(\sum_{l=1}^{M}\gamma_l\right)^2\right]}} \tag{24}$$

r gauges the linearity of the two data sets and can vary from -1 to 1. The closer r^2 is to 1, the better a linear regression can be fit to it. As r^2 approaches zero, the linear correlation is degraded.

Baseline Dynamic-Stiffness Measurement

There is some degree of stiffness and damping imposed by the structure surrounding the stator via the soft connection to the oil collection chambers, inlet oil hose, etc. A "baseline" dynamic-stiffness measurement is made to establish that which is not due to bearing reaction forces or stator inertia. Upon assembly of the test rig, prior to running any oil through the bearing and without rotation of the shaft, the stator is shaken with a peak-to-peak acceleration amplitude of at least 5 m/s^2 (0.5 g's) in each direction while ensuring no contact between the rotor and bearing pads. This may also be referred to as a "dry-shake." The dynamic-stiffnesses obtained from the dry-shake are simply subtracted from those deduced at the test conditions while their uncertainties are added, as in Eq. (25):

$$\begin{aligned} \boldsymbol{H}_{ij} &= \boldsymbol{H}_{ij,\text{test}} - \boldsymbol{H}_{ij,\text{base}} \\ \Delta\boldsymbol{H}_{ij} &= \Delta\boldsymbol{H}_{ij,\text{test}} + \Delta\boldsymbol{H}_{ij,\text{base}} \end{aligned} \tag{25}$$

Here, $\boldsymbol{H}_{ij}$, $\boldsymbol{H}_{ij,\text{test}}$, and $\boldsymbol{H}_{ij,\text{base}}$ represent the resultant (reported), test condition, and baseline dynamic-stiffnesses, respectively, while Δ denotes uncertainty.

Whirl Frequency Ratio

The whirl frequency ratio (WFR) of a bearing or seal is defined as the ratio of the natural frequency of the rotor-bearing or rotor-seal system (ω_{n1}) to the onset speed of instability of the rotor, as shown in Eq. (26):

$$\text{WFR} = \frac{\omega_{\text{n1}}}{\omega_{\text{onset}}} \tag{26}$$

Lund [33] describes how to evaluate the WFR for a rigid shaft supported by plain journal bearings modeled without added mass terms. Equation (27) is the result of Lund's analysis:

$$\begin{aligned} \mathrm{WFR} &= \sqrt{\frac{\left(K_{eq}-k_{xx}\right)\left(K_{eq}-k_{yy}\right)-k_{xy}k_{yx}}{c_{xx}c_{yy}-c_{xy}c_{yx}}} \\ K_{eq} &= \frac{c_{xx}k_{yy}+c_{yy}k_{xx}-c_{yx}k_{xy}-c_{xy}k_{yx}}{c_{xx}+c_{yy}} \\ k_{ij} &= \frac{C_r}{W}K_{ij}, \quad c_{ij} = \frac{C_r\omega}{W}C_{ij} \end{aligned} \tag{27}$$

Though WFR depends on static load and shaft speed, a plot of WFR versus Sommerfeld number typically shows the WFR "leveling out" above a certain value of *S*; this value is typically quoted as the WFR for the bearing. For example, a plain journal bearing has a WFR of 0.5. It is obvious from Eq. (26) that if the natural frequency of the rotor-bearing system is known, the WFR can also be used to calculate a value for the onset speed of instability for the system. The inverse of the WFR equals the factor by which the natural frequency is multiplied to obtain the onset speed of instability. This factor is denoted as β in Eq. (28):

$$\beta = \frac{1}{\mathrm{WFR}}, \quad \omega_{\mathrm{onset}} = \beta\,\omega_{\mathrm{n1}} \tag{28}$$

For example, $\beta = 2$ for a plain journal bearing, so the onset speed of instability would be twice the natural frequency. San Andrés [34] presents equations that can be utilized to calculate the WFR for a bearing or seal that is modeled with added mass terms. The roots of Eq. (29) are solved using the definitions of Eq. (30):

$$a + b\left(\mathrm{WFR}\right)^2 + c\left(\mathrm{WFR}\right)^4 = 0 \tag{29}$$

$$
\begin{aligned}
a &= k_{xx}k_{yy} - k_{xy}k_{yx} + K_{eq}^2 - \left(k_{xx} + k_{yy}\right)K_{eq} \\
b &= \left(k_{xx} + k_{yy}\right)M_{eq} + \left(m_{xx} + m_{yy}\right)K_{eq} - 2K_{eq}M_{eq} - \tau \\
\tau &= k_{xx}m_{yy} + k_{yy}m_{xx} + c_{xx}c_{yy} - k_{xy}m_{yx} - k_{yx}m_{xy} - c_{xy}c_{yx} \\
c &= M_{eq}^2 + \left(m_{xx}m_{yy} - m_{xy}m_{yx}\right) - \left(m_{xx} + m_{yy}\right)M_{eq} \\
m_{ij} &= \frac{C_r\omega^2}{W}M_{ij} \\
M_{eq} &= \frac{c_{yy}m_{xx} + c_{xx}m_{yy} - c_{xy}m_{yx} - c_{yx}m_{xy}}{c_{xx} + c_{yy}}
\end{aligned}
\tag{30}
$$

Although Eqs. (29,30) were developed to evaluate WFR when added mass is present, these equations coincidently reduce to Eq. (27) when $M_{xy} = M_{yx} = 0$. Equation (29) will have four roots, but only one will be either a non-negative real or a pure imaginary number. If the number is non-negative real, then its value is the WFR. If it is pure imaginary, WFR = 0, implying that the onset speed of instability is infinite. Ertras and Vance [35] note that direct damping and cross-coupled stiffness coefficients have the most profound effect on stability of a rotor-bearing or rotor-seal system. Indeed, WFR decreases as direct damping terms increase while skew-symmetric cross-coupled stiffness terms increase the WFR, augmenting it further as they diverge from the zero axis. The WFR will become positive when the cross-coupled coefficients take on opposite signs, but having same-sign cross-coupled stiffness coefficients does not guarantee unconditional stability. Analysis of the WFR equations also indicates that orthotropy in the direct stiffness terms enhances stability by decreasing the WFR. Stiffness orthotropy typically increases from LBP to LOP configuration of a TPJB and for this reason LOP is a more stable configuration, though it normally has a lower load capacity. The effect of added mass terms on stability is more easily realized by considering the implication of the added mass terms on real parts of the dynamic-stiffnesses. For example, if the cross-coupled stiffness terms are already skew-symmetric, then skew-symmetric cross-coupled added mass terms could either degrade

or enhance stability by causing the cross-coupled dynamic-stiffnesses to either diverge from or converge toward the zero axis with increasing excitation frequency. The WFR of this bearing was evaluated at each dynamic test condition.

Pad Support Structure Stiffness Measurement

A secondary objective of this research was to investigate the effect of pivot stiffness on the predicted direct stiffness and damping coefficients of the bearing. Though a testing apparatus capable of acquiring the necessary data to deduce the stiffness of the pivot by itself was not available, the test rig described above was used to obtain such data for the entire pad support structure by loading the rotor directly on atop one of the loaded pads above its pivot axis at several loads and measuring the resulting displacement. This is done at ambient conditions with no oil flow and before any oil has been introduced into the clearance space. The "pad support structure" includes every "spring" that is in series with the bearing stiffness and damping during operation including the pad and its Babbitt layer, the ball-in-socket pivot, and the support shims for the ball and socket. Because of the testing conditions, the Babbitt layer may be less flexible during operation since there is no Hertzian contact between it and the rotor during this time. Even so, it is likely—though not certain—that the contact area between the ball and socket is significantly more flexible than rest of these elements. This presumption is based on the much larger contact area between the rotor and pad and the support shims and their contact surfaces.

The bearing was rotated to the LOP configuration such that the load axis of the static loader passed directly through the pivot of one of the loaded pads (pad 4), as shown in Fig. 22. The *y* direction stinger was disconnected from the stator while the *x* direction stinger remained connected. The static loader was used to pull the stator until contact was made between the rotor and pad—establishing this initial contact required only a small amount force. The resulting values of load and deflection were set as the zeroes for both data sets and were subtracted from all subsequent points. The *x* direction stinger was used to secure the stator position such that the static load vector passed through the center of the pivot at all loads. The targets for load values were the

components of the static load, F_s, that would be imposed on the pivots during testing. Since the load would be directed at approximately a 45º-angle to the pivots during testing (since the ratio of eccentricity to the line connecting the journal center and contact point between the ball and socket is on the order of 0.001), the experimenter sought loads of $(\sqrt{2}/2)F_s$ for the pad support structure stiffness measurement. Outputs

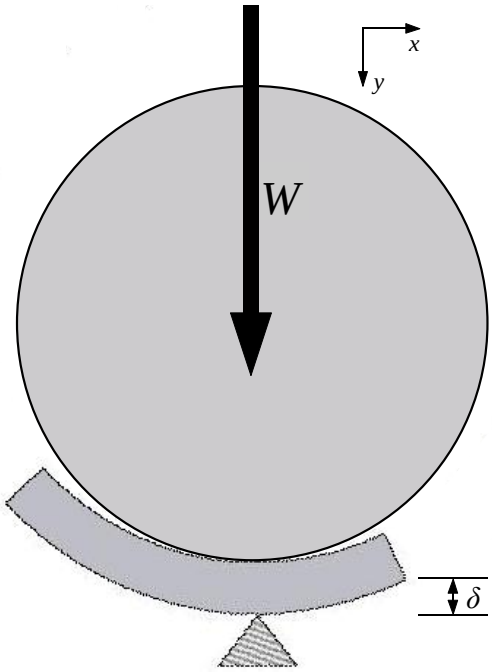

Fig. 22 Illustration of pad support structure stiffness measurement

from the static load cell and y direction proximity probes were used to create a static load (W) versus deflection (δ) plot. According to Kirk and Reedy's formulas, the plot should be non-linear—slope increasing with the input load—if the pivot dominates this measurement. However, the slope was approximately constant over the range of test loads. Accordingly, the pad support structure stiffness was assumed constant over these loads and was calculated by evaluating the slope of the load versus deflection plot via a linear regression as was done to calculate the rotordynamic coefficients—see Eq. (18). In this case $\gamma = W$ and $\chi = \delta$. The uncertainty of the pad support structure stiffness was

calculated in the same manner as that of the rotordynamic coefficients, using Eqs. (21,22). Since there was a small degree of structural stiffness of the test rig—as described in the "Baseline Dynamic-Stiffness Measurement" subsection—in parallel with the pad support structure stiffness, the value of $K_{yy,\text{base}}$ found in the dry-shake was subtracted from the measured pad support structure stiffness, $K_{ps,\text{test}}$, to obtain the resultant value, K_{ps}, as shown in Eq. (31):

$$K_{ps} = K_{ps,\text{test}} - K_{yy,\text{base}}, \quad \Delta K_{ps} = \Delta K_{ps,\text{test}} + \Delta K_{yy,\text{base}} \tag{31}$$

Their uncertainties were added to obtain the total uncertainty in the pad support structure stiffness measurement. The resulting values of K_{ps} and ΔK_{ps} are given in the "Pad Support Structure Stiffness Measurement and Pivot Stiffness Calculations" subsection of the "Results" section.

PREDICTION MODEL

XLTFPBrg™ Predictions

XLTFPBrg™, a program developed under the direction of Luís San Andrés at Texas A&M University and based on the theoretical model described in [25], was used to predict the static and dynamic values measured in this study. This code was also utilized in [2,26,27]. Although [25] describes the analysis in terms of the bulk-flow NS equation, the user can also specify the Reynolds equation. An isothermal or adiabatic model can be designated; the latter was used in this study. The code is not designed to model the thermal effects of the Spray-Bar Blockers® or By-Pass Cooling®. A CFD control-volume algorithm is used to solve the bulk-flow NS equations, and a perturbation analysis is applied to determine the stiffness and damping coefficients for each pad.

Following Lund [1] and Parsell et al. [12], the code includes pad rotation—but not translation—for each pad as a degree of freedom, thus initially yielding $2(4+5N_{pad})$ total stiffness and damping coefficients. Then, based on the user's input, it will either synchronously reduce the coefficients (as in [1]) or reduce them at any number of specified frequencies (as in [12]) and add them to obtain the resultant reduced stiffness and damping coefficients for the entire bearing. Unlike the analyses in [12,13], the value of pad inertia is retained in the equations of motion; herein, it was set to the value given by the manufacturer (7.91 $kg \cdot cm^2$). Multiple frequencies equal to the excitation frequencies used in testing were input at each load-speed condition. Figure 23(a) shows a screenshot of a sample load-speed condition. As shown in Fig. 23(b), the output contains the needed data to calculate static characteristics, but the output dynamic data are based on a frequency-dependent [C]-[K] model, so steps must be taken to convert the data to a frequency-independent [M]-[C]-[K] model.

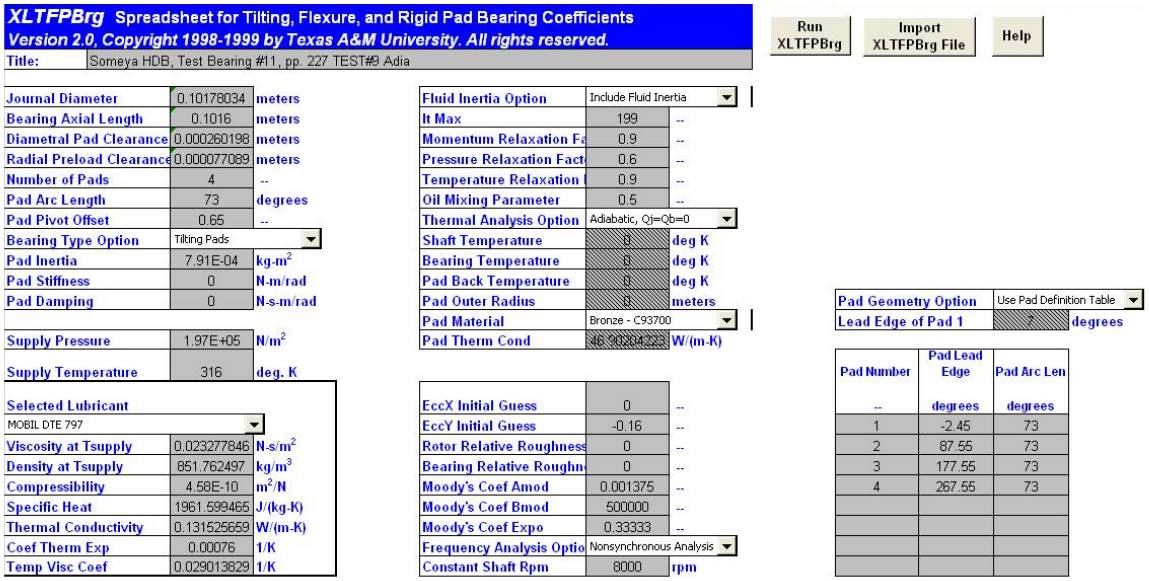

XLTFPBrg Spreadsheet for Tilting, Flexure, and Rigid Pad Bearing Coefficients
Version 2.0, Copyright 1998-1999 by Texas A&M University. All rights reserved.

Run XLTFPBrg | Import XLTFPBrg File | Help

Title: Someya HDB, Test Bearing #11, pp. 227 TEST#9 Adia

Journal Diameter	0.10178034	meters
Bearing Axial Length	0.1016	meters
Diametral Pad Clearance	0.000260198	meters
Radial Preload Clearance	0.000077089	meters
Number of Pads	4	--
Pad Arc Length	73	degrees
Pad Pivot Offset	0.65	--
Bearing Type Option	Tilting Pads	
Pad Inertia	7.91E-04	kg-m^2
Pad Stiffness	0	N-m/rad
Pad Damping	0	N-s-m/rad
Supply Pressure	1.97E+05	N/m^2
Supply Temperature	316	deg. K

Selected Lubricant	MOBIL DTE 797	
Viscosity at Tsupply	0.023277846	N-s/m^2
Density at Tsupply	851.762497	kg/m^3
Compressibility	4.58E-10	m^2/N
Specific Heat	1961.599465	J/(kg-K)
Thermal Conductivity	0.131525659	W/(m-K)
Coef Therm Exp	0.00076	1/K
Temp Visc Coef	0.029013829	1/K

Fluid Inertia Option	Include Fluid Inertia	
It Max	199	--
Momentum Relaxation Fa	0.9	--
Pressure Relaxation Fact	0.6	--
Temperature Relaxation I	0.9	--
Oil Mixing Parameter	0.5	--
Thermal Analysis Option	Adiabatic, Qi=Qb=0	
Shaft Temperature	0	deg K
Bearing Temperature	0	deg K
Pad Back Temperature	0	deg K
Pad Outer Radius	0	meters
Pad Material	Bronze - C93700	
Pad Therm Cond	46.90204233	W/(m-K)
EccX Initial Guess	0	--
EccY Initial Guess	-0.16	--
Rotor Relative Roughness	0	--
Bearing Relative Roughn	0	--
Moody's Coef Amod	0.001375	--
Moody's Coef Bmod	500000	--
Moody's Coef Expo	0.33333	--
Frequency Analysis Optio	Nonsynchronous Analysis	
Constant Shaft Rpm	8000	rpm

Pad Geometry Option	Use Pad Definition Table	
Lead Edge of Pad 1	7	degrees

Pad Number	Pad Lead Edge	Pad Arc Len
--	degrees	degrees
1	-2.45	73
2	87.55	73
3	177.55	73
4	267.55	73

(a)

X Load Newtons	Y Load Newtons	Speed rpm	Kxx N/m	Kxy N/m	Kyx N/m	Kyy N/m	Cxx N-s/m	Cxy N-s/m	Cyx N-s/m	Cyy N-s/m
0	-14234	1200	7.77E+08	-1.77E+06	-1.63E+06	7.77E+08	8.87E+05	-1.37E+03	-1.39E+03	8.87E+05
0	-14234	1800	7.75E+08	-1.81E+06	-1.64E+06	7.75E+08	8.89E+05	-1.36E+03	-1.41E+03	8.89E+05
0	-14234	2400	7.73E+08	-1.87E+06	-1.57E+06	7.73E+08	8.91E+05	-1.35E+03	-1.43E+03	8.91E+05
0	-14234	3000	7.70E+08	-1.94E+06	-1.48E+06	7.70E+08	8.93E+05	-1.33E+03	-1.47E+03	8.93E+05
0	-14234	3600	7.67E+08	-2.04E+06	-1.36E+06	7.67E+08	8.95E+05	-1.31E+03	-1.50E+03	8.95E+05
0	-14234	4200	7.63E+08	-2.14E+06	-1.23E+06	7.63E+08	8.98E+05	-1.28E+03	-1.55E+03	8.98E+05
0	-14234	4800	7.59E+08	-2.27E+06	-1.09E+06	7.59E+08	9.01E+05	-1.25E+03	-1.59E+03	9.01E+05
0	-14234	5400	7.54E+08	-2.41E+06	-9.20E+05	7.54E+08	9.04E+05	-1.21E+03	-1.65E+03	9.04E+05
0	-14234	6000	7.50E+08	-2.57E+06	-7.41E+05	7.50E+08	9.07E+05	-1.17E+03	-1.71E+03	9.07E+05
0	-14234	6600	7.45E+08	-2.75E+06	-5.47E+05	7.45E+08	9.10E+05	-1.12E+03	-1.77E+03	9.10E+05
0	-14234	7200	7.41E+08	-2.93E+06	-3.41E+05	7.41E+08	9.13E+05	-1.06E+03	-1.84E+03	9.13E+05
0	-14234	7800	7.36E+08	-3.13E+06	-1.13E+05	7.36E+08	9.16E+05	-1.00E+03	-1.91E+03	9.16E+05
0	-14234	8400	7.32E+08	-3.35E+06	1.13E+05	7.32E+08	9.19E+05	-9.37E+02	-1.98E+03	9.19E+05
0	-14234	9000	7.28E+08	-3.57E+06	3.57E+05	7.28E+08	9.21E+05	-8.68E+02	-2.05E+03	9.21E+05
0	-14234	9600	7.23E+08	-3.81E+06	6.11E+05	7.23E+08	9.23E+05	-7.96E+02	-2.12E+03	9.23E+05
0	-14234	10200	7.20E+08	-4.05E+06	8.76E+05	7.20E+08	9.25E+05	-7.20E+02	-2.20E+03	9.25E+05
0	-14234	10800	7.16E+08	-4.31E+06	1.15E+06	7.16E+08	9.27E+05	-6.42E+02	-2.27E+03	9.27E+05
0	-14234	11400	7.12E+08	-4.57E+06	1.44E+06	7.12E+08	9.28E+05	-5.62E+02	-2.35E+03	9.28E+05
0	-14234	12000	7.08E+08	-4.83E+06	1.74E+06	7.08E+08	9.29E+05	-4.80E+02	-2.42E+03	9.29E+05
0	-14234	12600	7.04E+08	-5.14E+06	2.01E+06	7.04E+08	9.29E+05	-2.63E+02	-2.37E+03	9.29E+05
0	-14234	13200	7.00E+08	-5.39E+06	2.36E+06	7.00E+08	9.30E+05	-3.13E+02	-2.58E+03	9.30E+05
0	-14234	13800	6.96E+08	-5.68E+06	2.68E+06	6.96E+08	9.30E+05	-2.27E+02	-2.66E+03	9.30E+05
0	-14234	14400	6.92E+08	-5.97E+06	3.02E+06	6.92E+08	9.30E+05	-1.40E+02	-2.74E+03	9.30E+05
0	-14234	15000	6.87E+08	-6.27E+06	3.37E+06	6.87E+08	9.29E+05	-5.23E+01	-2.82E+03	9.29E+05
0	-14234	15600	6.82E+08	-6.57E+06	3.72E+06	6.82E+08	9.29E+05	3.64E+01	-2.90E+03	9.29E+05

Speed rpm	Somm Number --	Reynolds Number --	Loading N/m2	Ecc X --	Ecc Y --	Min P N/m2	Max P N/m2	Min T Deg. K	Max T Deg. K	Power Loss kw
1200	0.35	173.82	1.38E+06	0.0043	-0.1546	1.97E+05	9.79E+06	319.9	340.9	12.628
1800	0.35	173.82	1.38E+06	0.0043	-0.1546	1.97E+05	9.79E+06	319.9	340.9	12.628
2400	0.35	173.82	1.38E+06	0.0043	-0.1546	1.97E+05	9.79E+06	319.9	340.9	12.628
3000	0.35	173.82	1.38E+06	0.0043	-0.1546	1.97E+05	9.79E+06	319.9	340.9	12.628
3600	0.35	173.82	1.38E+06	0.0043	-0.1546	1.97E+05	9.79E+06	319.9	340.9	12.628
4200	0.35	173.82	1.38E+06	0.0043	-0.1546	1.97E+05	9.79E+06	319.9	340.9	12.628
4800	0.35	173.82	1.38E+06	0.0043	-0.1546	1.97E+05	9.79E+06	319.9	340.9	12.628
5400	0.35	173.82	1.38E+06	0.0043	-0.1546	1.97E+05	9.79E+06	319.9	340.9	12.628
6000	0.35	173.82	1.38E+06	0.0043	-0.1546	1.97E+05	9.79E+06	319.9	340.9	12.628
6600	0.35	173.82	1.38E+06	0.0043	-0.1546	1.97E+05	9.79E+06	319.9	340.9	12.628
7200	0.35	173.82	1.38E+06	0.0043	-0.1546	1.97E+05	9.79E+06	319.9	340.9	12.628
7800	0.35	173.82	1.38E+06	0.0043	-0.1546	1.97E+05	9.79E+06	319.9	340.9	12.628
8400	0.35	173.82	1.38E+06	0.0043	-0.1546	1.97E+05	9.79E+06	319.9	340.9	12.628
9000	0.35	173.82	1.38E+06	0.0043	-0.1546	1.97E+05	9.79E+06	319.9	340.9	12.628
9600	0.35	173.82	1.38E+06	0.0043	-0.1546	1.97E+05	9.79E+06	319.9	340.9	12.628
10200	0.35	173.82	1.38E+06	0.0043	-0.1546	1.97E+05	9.79E+06	319.9	340.9	12.628
10800	0.35	173.82	1.38E+06	0.0043	-0.1546	1.97E+05	9.79E+06	319.9	340.9	12.628
11400	0.35	173.82	1.38E+06	0.0043	-0.1546	1.97E+05	9.79E+06	319.9	340.9	12.628
12000	0.35	173.82	1.38E+06	0.0043	-0.1546	1.97E+05	9.79E+06	319.9	340.9	12.628
12600	0.35	173.82	1.38E+06	0.0043	-0.1546	1.97E+05	9.79E+06	319.9	340.9	12.628
13200	0.35	173.82	1.38E+06	0.0043	-0.1546	1.97E+05	9.79E+06	319.9	340.9	12.628
13800	0.35	173.82	1.38E+06	0.0043	-0.1546	1.97E+05	9.79E+06	319.9	340.9	12.628
14400	0.35	173.82	1.38E+06	0.0043	-0.1546	1.97E+05	9.79E+06	319.9	340.9	12.628
15000	0.35	173.82	1.38E+06	0.0043	-0.1546	1.97E+05	9.79E+06	319.9	340.9	12.628
15600	0.35	173.82	1.38E+06	0.0043	-0.1546	1.97E+05	9.79E+06	319.9	340.9	12.628

(b)

Fig. 23 (a) Input and (b) output XLTFPBrg™ screens

Equation (32) contains the definitions necessary to perform this conversion, where $\tilde{K}_{ij}(\Omega)$, $\tilde{C}_{ij}(\Omega)$ represent the output (frequency-dependent) stiffness and damping values:

$$\mathrm{Re}\left(\boldsymbol{H}_{ij}\right)=\tilde{K}_{ij}(\Omega),\ \ \mathrm{Im}\left(\boldsymbol{H}_{ij}\right)=\tilde{C}_{ij}(\Omega)\Omega \tag{32}$$

The second part of this equation is based on the "secant" definition of damping, i.e. damping at a given frequency is equal to the slope of the line that connects 0 to Im($\boldsymbol{H}_{ij}$) at that frequency. The resulting dynamic-stiffness versus excitation frequency plots were used to calculate the rotordynamic coefficients based on a frequency-independent [M]-[C]-[K] model in the same manner as for the experimental plots, using Eq. (18). In most cases, the linear regressions fit the predicted data very well, but there was still some uncertainty associated with the slopes and *y*-intercepts of the curve-fits as $r^2 < 1$ for all the plots. The uncertainty and r^2 values of these curve-fits were also calculated in the same way as the uncertainty of the experimental coefficients, using Eqs. (21,22,24). In cases where Re($\boldsymbol{H}_{ij}$) could not be effectively with frequency-independent stiffness and added mass terms, its average over the span of frequencies was defined as K_{ij} and the uncertainty was calculated using Eq. (23).

Certain limitations of XLTFPBrg prevented the user from modeling the exact geometrical parameters of the test bearing. First, as noted in Table 7 as well as the "Clearance" subsection of the "Results" section, the bearing has clearances that differ substantially about the pivot axes and coordinate axes. But since XLTFPBrg only accepts a single bearing clearance value, the average bearing clearance of 77.1 μm (3.04 mils) based on clearance measurements was input into the code. XLTFPBrg also only accepts a single pad preload value, but the test bearing has unequal values of the said parameter for the loaded (3 and 4) and unloaded (1 and 2) pads. A weighted average of the preload values was used such that the single preload value input into the code

decreased toward the preload of the loaded pads as the experimental value of e_y increased. Equation (33) shows that the limiting cases for this calculation govern that $M_{p,\text{eff}} = ½(M_{p,\text{loaded}} + M_{p,\text{unloaded}})$ when $e_y = 0$ and $M_{p,\text{eff}} = M_{p,\text{loaded}}$ when $e_y = C_y$:

$$M_{p,\text{eff}} = \frac{1}{2}\left[\left(1+\frac{e_y}{C_y}\right)M_{p,\text{loaded}} + \left(1-\frac{e_y}{C_y}\right)M_{p,\text{unloaded}}\right] \tag{33}$$

Pivot Stiffness Calculations

While Table 7 gives design values for the radii of the ball and socket, the range of differential diameters according to the tolerances of these values could possibly vary from -15.2 μm (-0.6 mils) to 238.8 μm (9.4 mils). The range of values results in a large range of pivot stiffnesses. Accordingly, the pivot stiffness is calculated at several values over the range of possible differential diameters, excluding negative values (since this would result in a negative result from Eq. (7)). The ball diameter is held constant at 6.35000 cm (2.5000 in.) while the socket diameter is allowed to vary from 6.35254 cm (2.5010 in.) to its highest value within design tolerance of 6.37388 cm (2.5094 in.). While Eq. (7) gives pivot stiffness as a function of load, use of Eq. (6) produced load versus deflection plots that could be fit to a linear curve with r^2 values in excess of 0.95 for all assumed values of differential diameter of the range of test loads. While this would not only simplify computation if one were to use a theoretical value of pivot stiffness, it also served as a better basis of comparison to the measured value in this study.

Equation (8) was also used to correct the differential diameter for the change in temperature, using 21ºC (70ºF) as the ambient temperature and the average of the trailing-edge pad temperatures in Table 12 of Appendix A as the operating temperature. While the temperature at the pivots is most likely lower than that of the trailing-edges of the pads, such a conservative estimate would provide a “built-in” safety factor in the design stage. Also note that the pivot stiffness values calculated using the corrected

differential diameters are not suitable to compare to the measured value since the pivot stiffness was measured at ambient temperature.

Modification of Predictions Using Equivalent Stiffness and Damping Formulas

The code does not model the effect of any translational (radial) stiffness in series with the bearing stiffness and damping, but the result of the measurement given in the "Pad Support Structure Stiffness Measurement and Pivot Stiffness Calculations" subsection of the "Results" section was placed in series with the predicted direct stiffness and damping terms using only the zeroth-order terms of Eq. (5). As noted, Eqs. (4,5) are valid for this modification since the pad support structure stiffness represents the net stiffness that is in series with the oil film during operation, though the Babbitt layer may be slightly stiffer during operation than at dry, ambient conditions. Since the predicted cross-coupled coefficients were very small in magnitude, placing this stiffness in series with them had an insignificant effect. Accordingly, results are only reported for the direct coefficients.

It is important to note that Eq. (5) modifies the stiffness and damping of a single pad by placing the stiffness of a single pad support structure in series with it. Since the user of XLTFPBrg does not have access to the individual pad coefficients, use of the aforementioned equations required deduction of a stiffness value that could be added in series to K_{xx} and K_{yy} and produce approximately the same result as placing the stiffness of each pad support structure in series with the coefficients for each pad then summing the components of the individual pads in the directions of the coordinate axes. Figure 24 provides a visual description of the required transformation while Appendix B shows that the effective value of pad support structure stiffness is the value given in Eq. (34):

$$K_{ps,\text{eff}} = 2K_{ps} \tag{34}$$

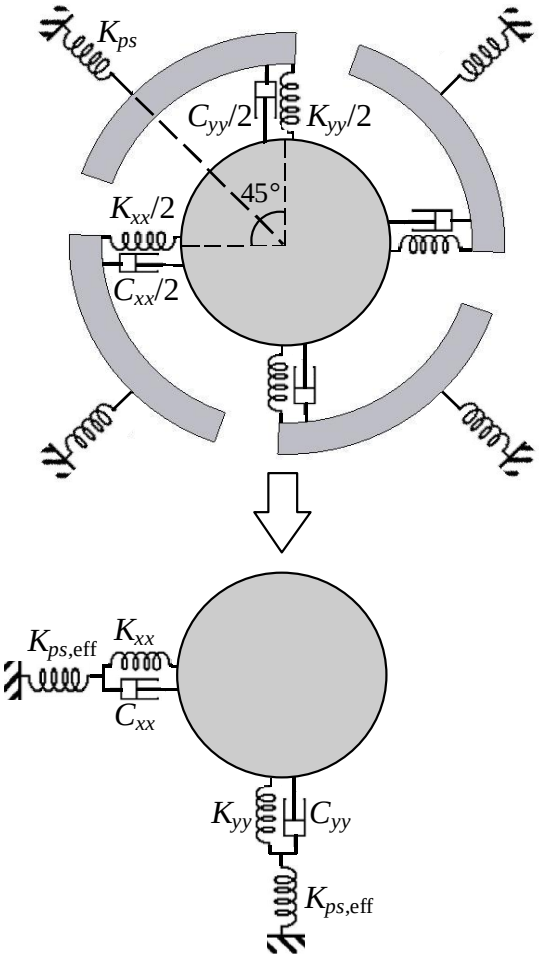

Fig. 24 Illustration of effective pad support structure stiffness

Making the substitutions $K_{\mathrm{pad}} \rightarrow K_{ii}$, $K_{\mathrm{pad,eq}} \rightarrow K_{ii,\mathrm{eq}}$, and $K_p \rightarrow K_{ps,\mathrm{eff}}$, the zeroth-order term in the first line of Eq. (5) is used to modify the predicted direct stiffness as shown in Eq. (35) (note that the "→" symbol only denotes substitution in this case, not equality):

$$K_{ii,\mathrm{eq}} = \frac{K_{ii} K_{ps,\mathrm{eff}}}{K_{ii} + K_{ps,\mathrm{eff}}} \tag{35}$$

Making the substitutions $C_{\text{pad}} \rightarrow C_{ii}$, $C_{\text{pad,eq}} \rightarrow C_{ii,\text{eq}}$, and $K_p \rightarrow K_{ps,\text{eff}}$, the zeroth-order term in the second line of Eq. (5) is used to modify the predicted damping as in Eq. (36):

$$C_{ii,\text{eq}} = \frac{C_{ii} K_{ps,\text{eff}}^2}{\left(K_{ii} + K_{ps,\text{eff}}\right)^2} \tag{36}$$

While the error of the pad support structure stiffness measurement (see Eq. (37)) caused a small additional uncertainty in the calculation of the modified bearing stiffness and damping coefficients, the additional uncertainty was negligible and thus is not reported.

RESULTS

In most cases, both experimental and theoretical results are given as a comparison. In some cases (e.g. clearance and trailing-edge pad temperatures) theoretical values were either inapplicable or could not be calculated with the XLTFPBrg. Exhaustive spreadsheets of test data are included in Appendix A, while a select amount of data deserving greater emphasis is listed and/or plotted in the body of this paper. Table 10 of Appendix A provides the raw static operating data that are not reported in plots.

Pad Support Structure Stiffness Measurement and Pivot Stiffness Calculations

Since the measured pad support structure stiffness will be referred to early on in this section, the result of the measurement is accordingly presented first in this section (although the method for determining this value was presented last in the "Experimental Procedure" section). Figure 25 shows the measured load versus deflection plot recorded during measurement while Table 9 in Appendix A provides the measured values.

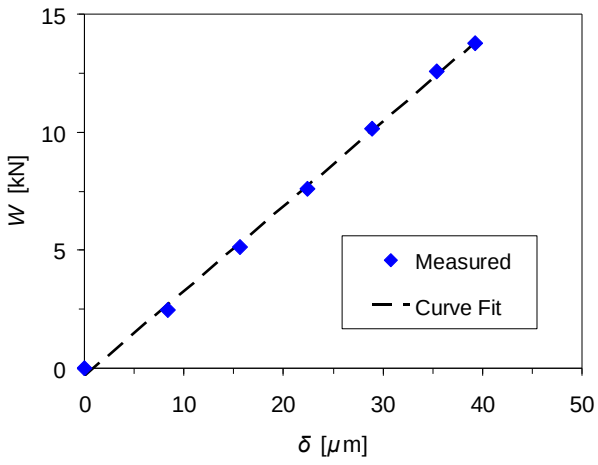

Fig. 25 Load versus deflection plot used to calculate the pad support structure stiffness

As explained in the "Experimental Procedure" section, the unexpected linearity of this plot (r^2 = 1.00) facilitated the experimenter's ability to fit a linear curve to the data points. Upon calculation of this slope, the baseline dynamic-stiffness in the *y* direction (presented in the "Baseline Dynamic-Stiffness Coefficients" subsection of the "Results" section) was subtracted from the slope while its uncertainty was added, resulting in the value presented in Eq. (37):

$$\begin{aligned} K_{ps} &= 350 \pm 13 \text{ MN/m} \\ &= 2000 \pm 75 \text{ lbs/mil} \end{aligned} \tag{37}$$

Theoretical load versus deflection plots for the ball-in-socket pivots, based on Eq. (6) for six values of differential diameter are shown in Fig. 26. As expected,

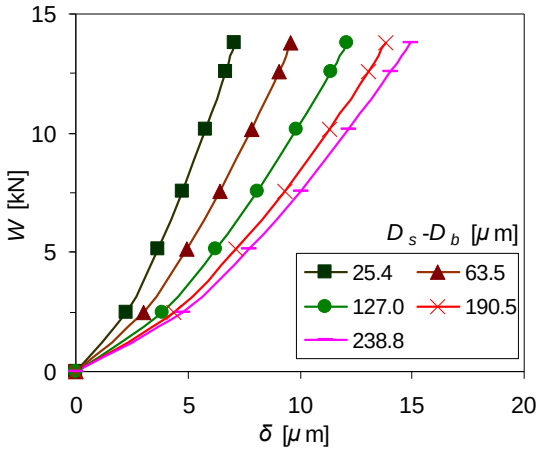

Fig. 26 Theoretical load versus deflection plots for several differential diameter values

deflection increases with differential diameter. However, the surprising characteristic of these plots is their degree of linearity over the range of test loads. All of the data sets were fit to linear curves, resulting in r^2 = 0.97 for every set, which is similar to the measured pad support structure load versus deflection curves. However, the deflection in these plots is considerably less than that of the measured pad support structure values.

The estimates of pivot stiffness values resulting from these curve-fits are plotted versus differential diameter in Fig. 27. Also in this figure is a black dashed line indicating the measured value of pad support structure stiffness. As can be seen from the shape of the

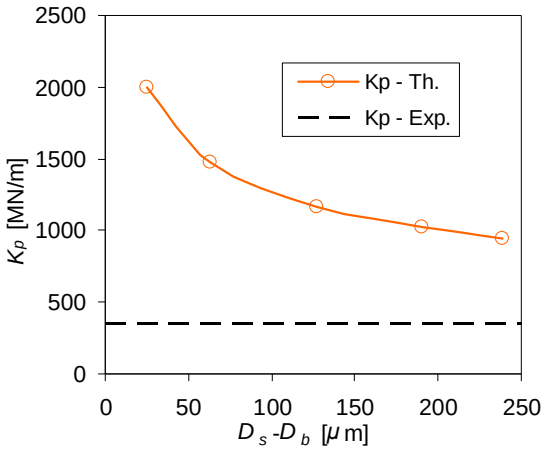

Fig. 27 Theoretical pivot stiffness versus differential diameter

plot, the fact that the load versus deflection data sets were fit to linear curves—as opposed to calculating them directly for each load via Eq. (7)—does not alter the prediction that pivot stiffness will decrease exponentially with differential diameter. However, the theoretical, linear estimates of pivot stiffness are obviously much higher than the measured value of pad support structure stiffness, even for the higher values of differential diameter.

Equation (8) was used to calculate the differential thermal growth based on an ambient temperature of 21ºC. The average of the recorded trailing-edge pad temperatures shown in Table 12 was taken as the operating temperature, resulting in ΔT = 35ºC (as explained in the "Pivot Stiffness Calculations" subsection, this is a conservative estimate). Since D_s = 63.5 mm (2.5 in.), the differential thermal growth equates to 13 μm (0.51 mils). Figure 28 includes a graph of the corrected pivot stiffness values. While this makes an appreciable difference (13%) in the pivot stiffness for the

lowest value of differential diameter, the change decreases to less than 5% as the differential diameter is increased.

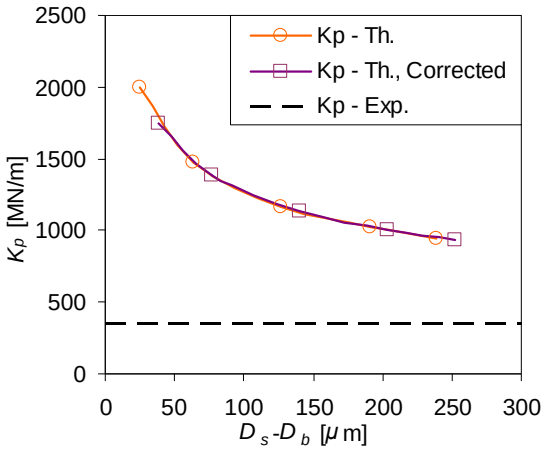

Fig. 28 Theoretical pivot stiffness versus differential diameter with corrected curve

Static Data

Clearance

The measured clearances about the *x*' and *y*' axes are given in Table 7 and are also reported below in Eq. (38):

$$\begin{aligned} C_{x'} &= 99.6 \pm 0.2 \ \mu\text{m} \ \left(3.92 \pm 0.01 \text{ mils}\right) \\ C_{y'} &= 54.6 \pm 4.5 \ \mu\text{m} \ \left(2.15 \pm 0.18 \text{ mils}\right) \end{aligned} \tag{38}$$

The uncertainties in these measurements are based on the standard deviation of ten samples, five each from two different proximity probes. It was previously noted that $C_{x'}$ was defined as the clearance about the *y* axis and $C_{y'}$ as the clearance about the *x* axis of the test bearing coordinate system.

As a first pass at defining a single clearance value to input into XLTFPBrg, an effective clearance defined as the maximum vertical and horizontal space between the

bounds of a 45º skewed ellipse, as shown in Fig. 29, was used. Here, the major and

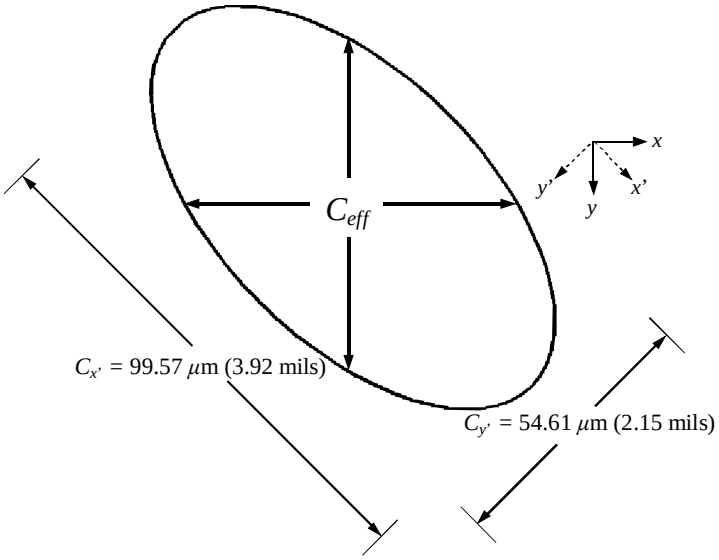

Fig. 29 **"**Effective" clearance depiction

minor axes are the measured values of the clearance spaces between the pivot axes. A calculation of this clearance produced a value of 67.8 μm (2.67 mils). However, this clearance produced unreasonably high values for the direct stiffness and damping and unreasonably low values for the eccentricity. This clearance did, however, produce reasonable results for the power loss and over predicted the maximum bearing temperature in most cases by about 8ºC (14ºF).

To obtain more reasonable values for the direct coefficients and eccentricity, the average clearance between the pivot axes, C_{ave} = 77.1 μm (3.04 mils), was used in XLTFPBrg code. While direct rotordynamic coefficients were still over predicted and eccentricity was still under predicted, using this clearance gave results that were closer to experimental values than with the effective clearance used above, for which the theoretical values of the direct coefficients were up to four to five times the experimental values.

Journal Position

The eccentricities are reported in locus plots in Fig. 30, showing both the experimental values overlaid on the clearances of the coordinate axes and the theoretical values overlaid on the average clearance circle. Note that $-e_y$ is reported in the plots due to the coordinate sign convention of the plotting utility. Figure 31 shows the magnitude of the resultant eccentricity (e) as a function of unit load.

The most striking feature of these plots is the stark difference between the theoretical predictions and measurements. First of all, the eccentricity in the y direction is grossly under predicted. At the speed of 4,000 rpm, the measured eccentricity is even outside of the nominal bearing clearance of the coordinate axes. At first glance, one might assume that a rub had occurred. However once must recall that (i) the pads are allowed to tilt, (ii) the pad clearance is greater than the bearing clearance at locations away from the pivot, and (iii) the pads and (more notably) the pivots will deflect under load. All three of these factors act to increase the clearance space about the location of the journal center. In fact, according to the measured pad support structure stiffness, the maximum load of 19.57 kN (4400 lbs.) would increase the clearance of the loaded pads about the pivot axes by 39.1 μm (1.54 mils), which is a substantial fraction of the measured clearances.

Also note that while there is a significant attitude angle displayed in the experimental plots, that of the theoretical plots is practically null (between 1°-2°). This result is also readily discerned from Fig. 32, where the attitude angle is plotted versus unit load. The theoretical attitude angle is not plotted at zero load due to the high fluctuation in values, which can be seen in Table 11 of Appendix A. Since the theoretical values of e_y are very small at zero load, small fluctuation in the value of e_x (which occurred frequently due to iterative error) caused this high fluctuation in the theoretical attitude angle. Conversely, the experimental attitude angles at zero load did not show a high degree of fluctuation and were all within the range of 20°-40° aside from the lone negative value at 12,000 rpm.

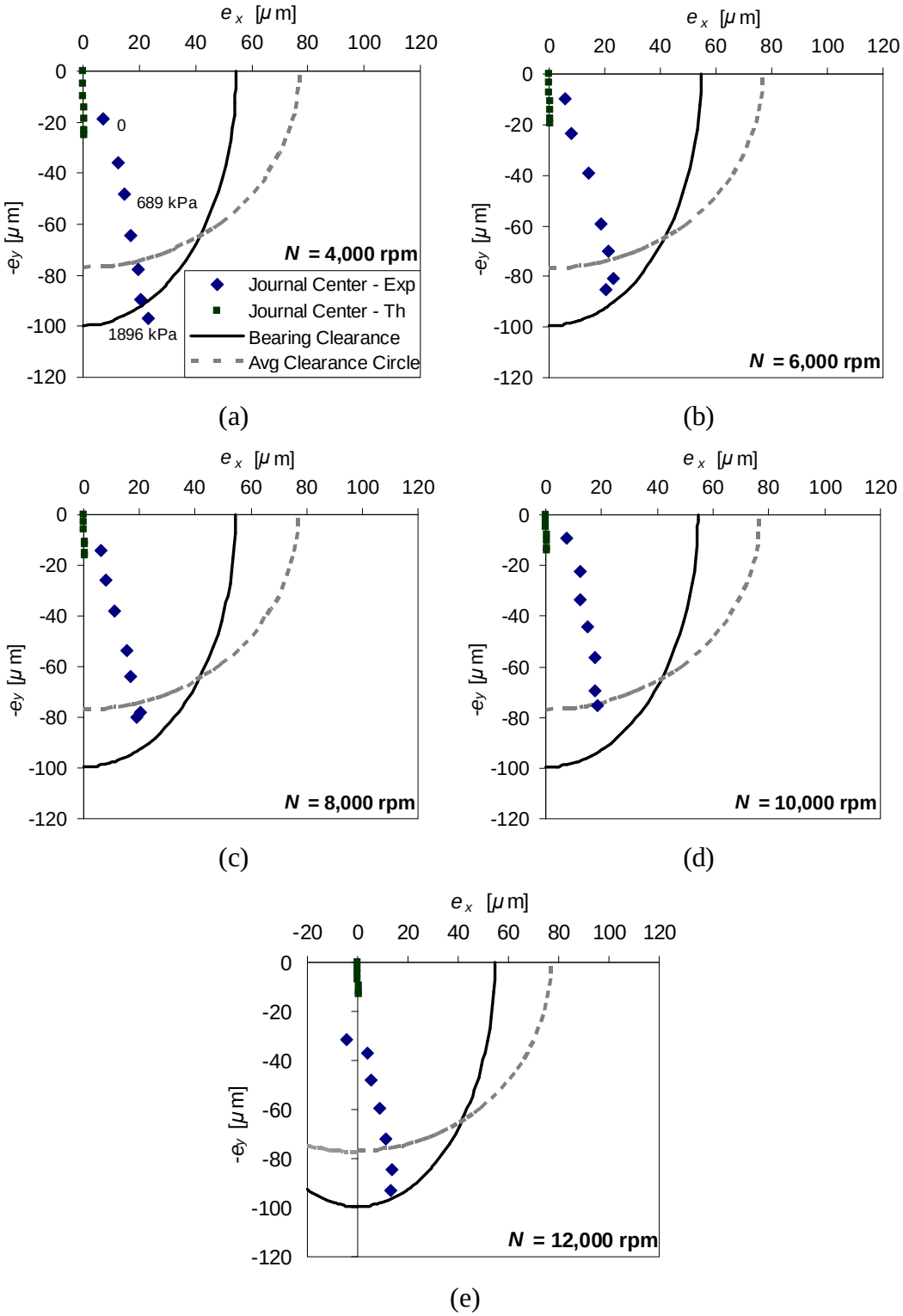

Fig. 30 Journal centerline locus plots at (a) 4,000 rpm, (b) 6,000 rpm, (c) 8,000 rpm, (d) 10,000 rpm, and (e) 12,000 rpm

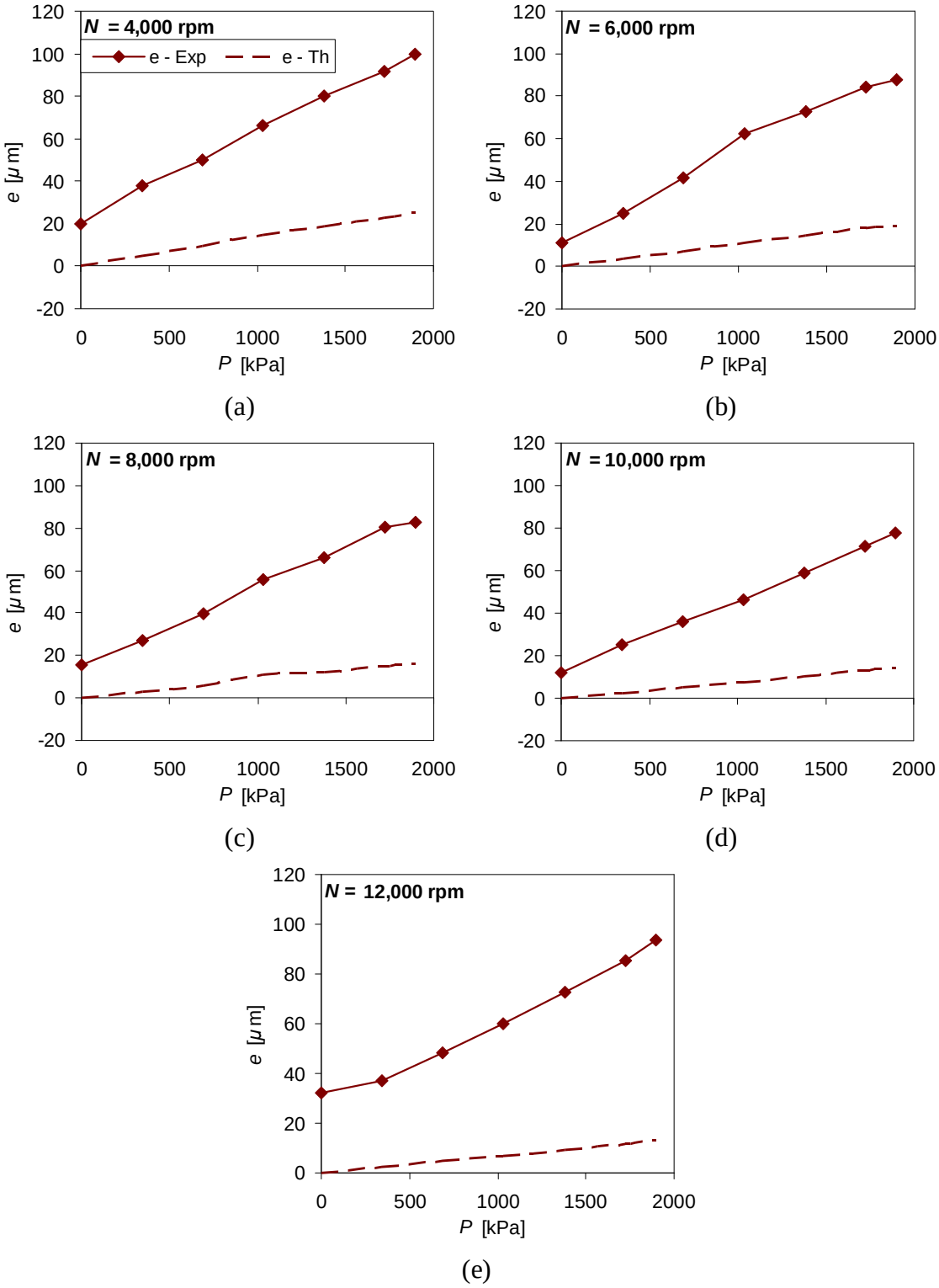

Fig. 31 Eccentricities versus unit load at (a) 4,000 rpm, (b) 6,000 rpm, (c) 8,000 rpm, (d) 10,000 rpm, and (e) 12,000 rpm

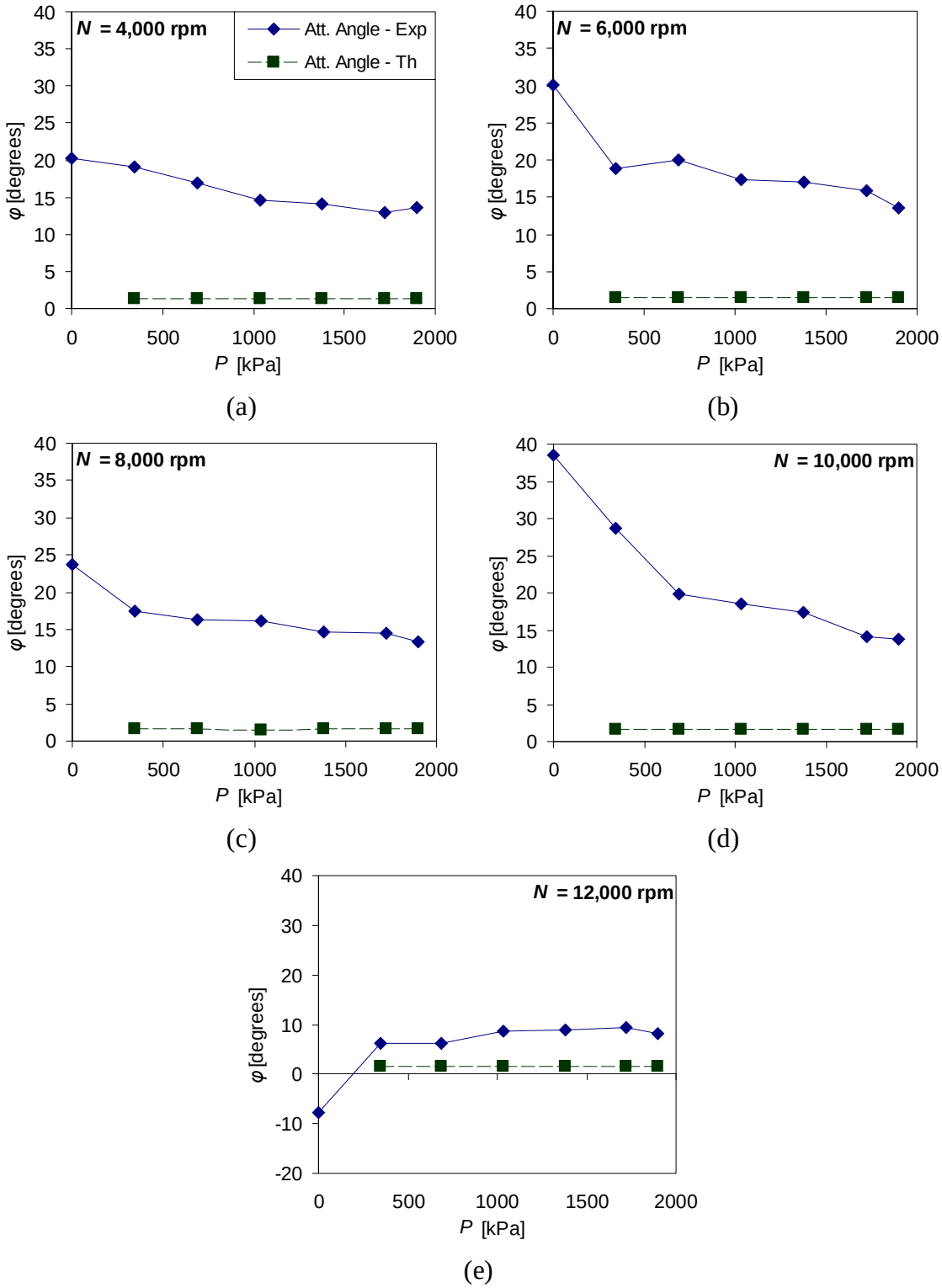

Fig. 32 Attitude angle versus unit load at (a) 4,000 rpm, (b) 6,000 rpm, (c) 8,000 rpm, (d) 10,000 rpm, and (e) 12,000 rpm

At non-zero loads, the experimental attitude angle decreased with load, varying from 6°-29° and typically settling at around 15° except at 12,000 rpm where it settled around 8°. The eccentricities and attitude angles are fully documented in Table 11 of Appendix A. These data include both theoretical and experimental values.

Estimated Power Loss

The maximum value of experimental estimated power loss occurred at the maximum unit load for most speed conditions and even when it did not, the value at the maximum load was within 8% or less of the maximum value. In theory, the maximum power loss always occurred at the maximum load for a given speed. For this reason, one plot of estimated power loss at maximum load versus speed is shown in Fig. 33. Note

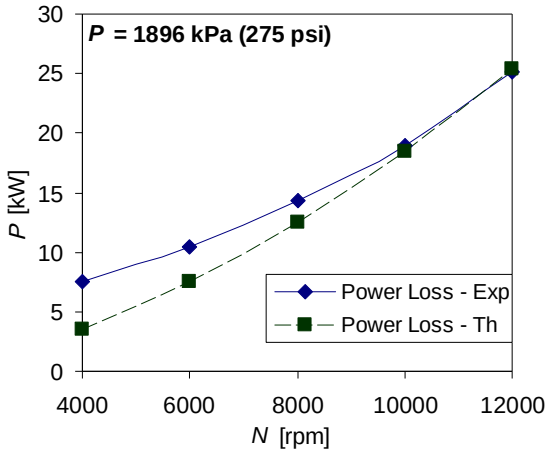

Fig. 33 Estimated power loss at the maximum load,1896 kPa (275 psi)

that neither the approximation model used for experiment nor the code model accounts for heat removed by the By-Pass Cooling chambers. At low speeds, the power loss is under predicted by as much as 50%, but the values converge as the speed increases until they are nearly identical at 12,000 rpm. The maximum measured value is about 25 kW (34 hp). A full list of the experimental and theoretical values is provided in Table 11 of Appendix A.

Trailing-Edge Pad Temperatures and Maximum Temperature Rise

As noted in the "Experimental Procedure" section, trailing-edge pad temperatures were recorded at each load-speed condition where static data were collected. For the sake of brevity, plots for only the four loads at which dynamic data were recorded are shown in Fig. 34, which shows a separate plot for each load and, within each plot, a curve representing temperature versus circumferential location (θ coordinate in Fig. 16) at each of the five speeds. The common feature of nearly all the trailing-edge temperatures is that they increase with speed. However, the temperatures at pads 1 and 2 tend to decrease with load while those at pads 3 and 4 increase. Pads 1 and 4 have the maximum and minimum temperatures, respectively, when the bearing is lightly loaded while pads 3 and 2 have the respective maximum and minimum temperatures when the bearing is heavily loaded.

The data for the maximum temperature rise from inlet to maximum bearing temperature are given fully in Table 12 of Appendix A; the cells that are bordered in with diagonal stripes indicate the highest maximum temperature rise for a given speed. As one can see from Table 12 the highest maximum temperature rise almost always occurs at the highest unit load for a given speed. The only speed that this is not the case is 4,000 rpm, at which the maximum temperature rise of 15.4°C (27.7°F) occurs at 1724 kPa (250 psi) and the maximum temperature rise at 1896 kPa (275 psi) is 15.1°C (27.2°F), only 2% less than the highest value. Accordingly, maximum load is seen as a critical condition for maximum temperature rise and is compared to predictions versus shaft speed in Fig. 35. The maximum temperature rise is over predicted by about 40% at 4,000 rpm and 10-20% above this speed.

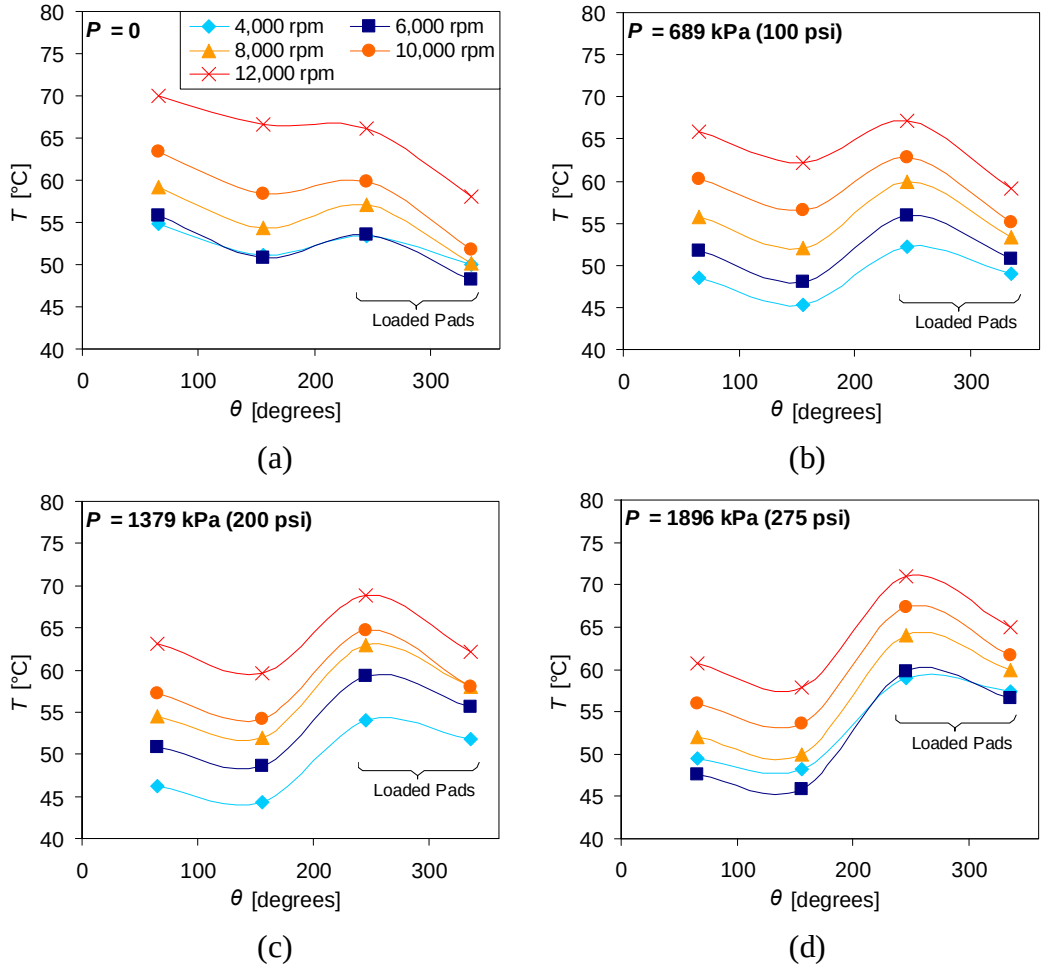

Fig. 34 Trailing-edge pad temperature versus circumferential location at (a) 0 kPa, (b) 689 kPa, (c) 1379 kPa, and (d) 1896 kPa

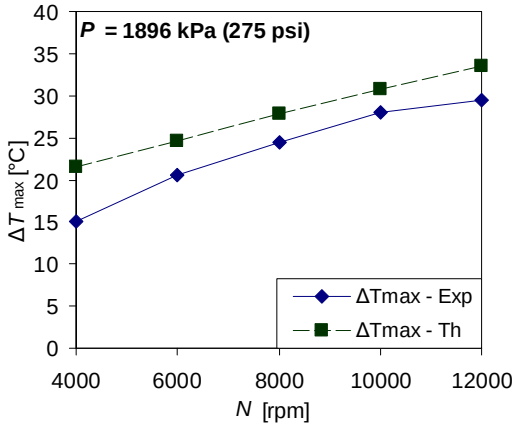

Fig. 35 Maximum temperature rise versus speed at 1896 kPa (275 psi)

Dynamic Data

Since the baseline dynamic-stiffness measurements were needed to net the dynamic-stiffnesses at the test conditions, this section begins by presenting the baseline data. In this subsection, the symbols $\boldsymbol{H_{ii}}$ and $\boldsymbol{H_{ik}}$ are used to denote direct and cross-coupled dynamic-stiffness coefficients, respectively. This notation is most useful in the case of the theoretical data as the direct dynamic-stiffness coefficients were predicted to be isotropic.

Baseline Dynamic-Stiffness Coefficients

Plots of the baseline dynamic-stiffness coefficients are provided in Fig. 36. Figures 36(a) and (c) show a baseline dynamic-stiffness for which the average over the frequencies indicates stiffness coefficients of $K_{xx,\text{base}}$ = 7.02 MN/m and $K_{yy,\text{base}}$ = 9.40 MN/m. Here, the average of the real parts of the dynamic-stiffnesses represent the stiffness since lack of a fluid film implies that there is no added mass; this is also evident from the lack of a discernable trend in the plots. The baseline stiffness is probably due mostly to the pitch stabilizers while $K_{yy,\text{base}}$ is likely slightly higher due to the connection of the static loader in the y axis. Lack of a discernable trend indicates frequency-independency, as is expected for structural stiffness. The coefficients Im($\boldsymbol{H}_{xx,\text{base}}$) and Im($\boldsymbol{H}_{yy,\text{base}}$) show a linear trend and can be fit to a linear curve as described in the "Rotordynamic Coefficient Identification" subsection, giving values of $C_{xx,\text{base}}$ = 11.72 kN·s/m and $C_{yy,\text{base}}$ = 17.45 kN·s/m. The majority of the baseline damping is most likely from the soft connections from the stator to the oil collection chambers and in part to the hoses and cables. The measured values of $\boldsymbol{H}_{xy,\text{base}}$ and $\boldsymbol{H}_{yx,\text{base}}$ are small, indicating that there is little cross-coupling exhibited by the structure.

Editor's note: Subsequent to publication, the author has noted the experimental dynamic-stiffness data, which are the basis for the rotordynamic coefficients, to be unreliable. To the author's knowledge, all static data (both experimental and theoretical) and the theoretical dynamic data are valid. Please reference the Texas A&M University Master's thesis of David M. Coghlan (Static, Rotordynamic, and Thermal Characteristics of a Four Pad Spherical-Seat Tilting Pad Journal Bearing with Four Methods of Directed Lubrication) for valid dynamic data for a spherical-seat tilting pad journal bearing. (2014)

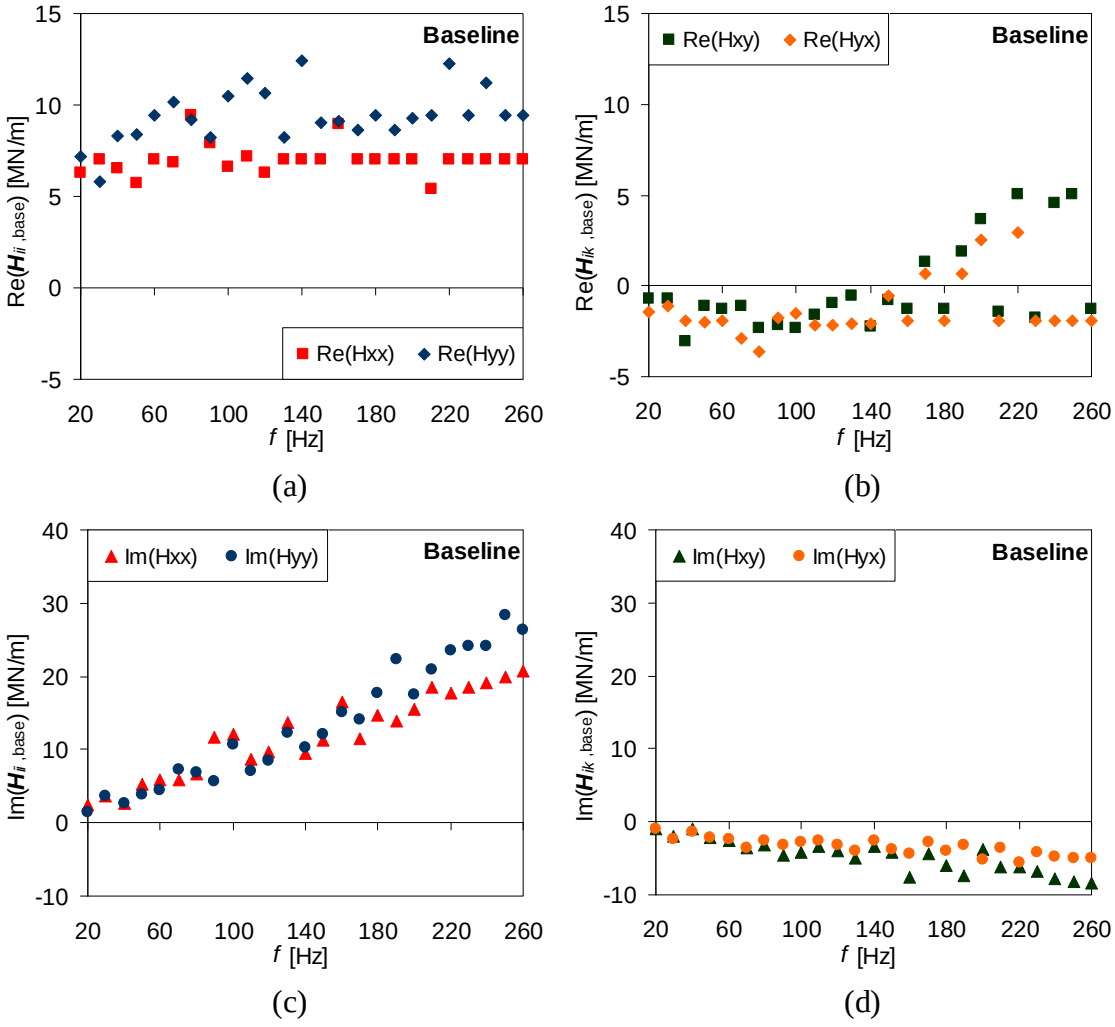

Fig. 36 Baseline dynamic-stiffnesses (a) Re($\boldsymbol{H}_{ii,\text{base}}$), (b) Re($\boldsymbol{H}_{ik,\text{base}}$), (c) Im($\boldsymbol{H}_{ii,\text{base}}$), and (d) Im($\boldsymbol{H}_{ik,\text{base}}$)

Dynamic-Stiffness Coefficients

Tables 13-32 of Appendix A provide full lists of the experimental dynamic-stiffness data at each frequency. In the experimental tables, a cell with a dotted background indicates that the point was omitted due to excessive uncertainty.

Figure 37 shows plots of the real and imaginary parts of the direct dynamic-stiffness data at N = 12,000 rpm, P = 689 kPa. As previously noted, added mass coefficients were omitted if their uncertainties were 35% or more, which typically

corresponded to $r^2 < 0.7$. This was the case for 6 conditions for Re($\boldsymbol{H}_{xx}$) and 10 conditions for Re($\boldsymbol{H}_{yy}$) (out of 20 total test conditions for each). Of the remaining test points where added mass terms were utilized, the r^2 values averaged 0.80. The average uncertainty was 25% for the direct added mass terms and 2% for the direct stiffness terms.

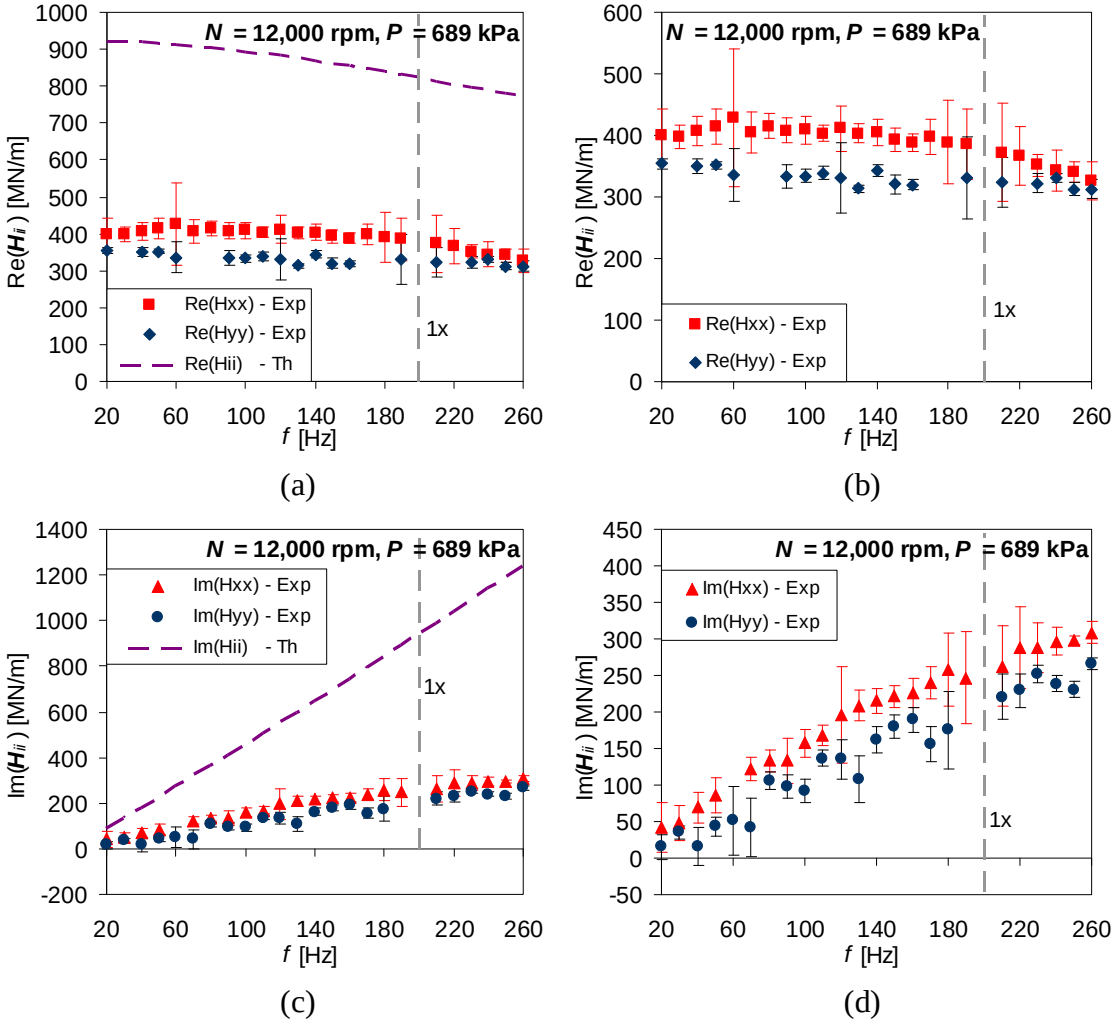

Fig. 37 $\boldsymbol{H}_{ii}$ plots (a,c) containing all data sets and (b,d) zoomed in to only experimental data at 12,000 rpm, 689 kPa

Im($\boldsymbol{H}_{xx}$), Im($\boldsymbol{H}_{yy}$) were very well-fitted by the linear model of Eq. (17), having an average r^2 value of 0.96; these curve-fits resulted in direct damping coefficients with

uncertainties averaging only 10%. While there is a noticeable curvature to these plots, it does not highly affect the goodness of fit of a linear curve to the data at the frequencies considered. Additionally (as will be explained in the "Rotordynamic Coefficients" subsection of this section), uncertainties for the frequency-dependent damping values calculated from these data were too high at low frequencies—which is where most deviation from a constant value occurred—to make a firm conclusion as to a specific trend that either damping curve follows.

Figure 38 shows plots of the real and imaginary parts of the cross-coupled dynamic-stiffness data at N = 12,000 rpm, P = 689 kPa. There were only 5 cases for Re($\boldsymbol{H}_{xy}$) and 3 cases Re($\boldsymbol{H}_{yx}$) where the data could be fit to a linear curve and modeled with added mass coefficients. Of these leftover cases, r^2 was 0.75 on average and ΔM_{ik} was 29% on average; ΔK_{ik} averaged 10% over all test conditions.

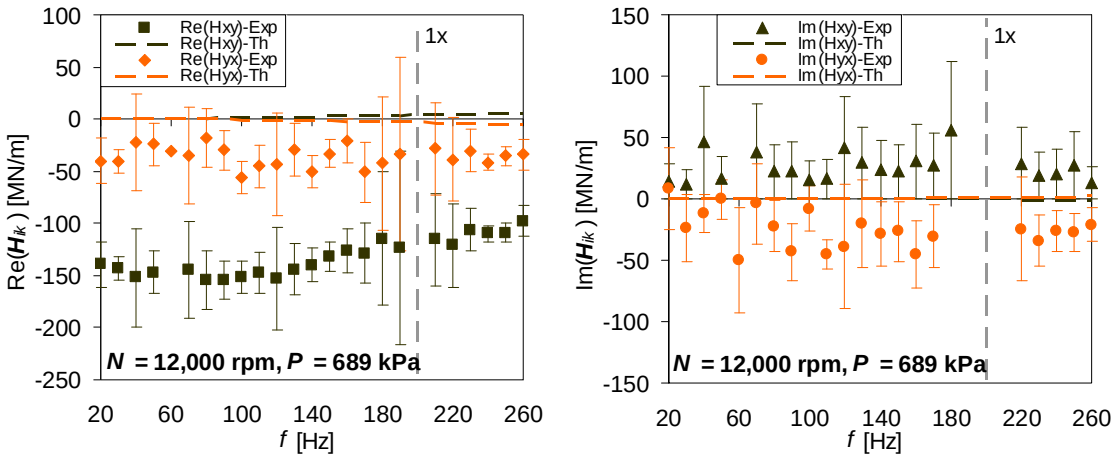

(a) (b)

Fig. 38 $\boldsymbol{H}_{ik}$ plots at 12,000 rpm, 689 kPa

There were only 3 total cases where Im($\boldsymbol{H}_{xy}$), Im($\boldsymbol{H}_{yx}$) could be modeled with frequency-independent damping values with less than 35% uncertainty. The cross-coupled damping is most likely frequency-dependent, but there is too much scatter in the dynamic-stiffness data to deduce a trend in the values. The magnitudes of Im($\boldsymbol{H}_{xy}$),

Im($\boldsymbol{H}_{yx}$) are low compared to the direct terms so they likely would have a small effect on dynamics.

The r^2 values for the theoretical dynamic-stiffness curve-fits were generally high but were lower than desirable in some cases. As with the experimental data, if there was greater than 35% uncertainty in an added mass or damping term it was omitted. This was the case for 1 direct and 16 cross-coupled real dynamic-stiffness data sets and 4 cross-coupled imaginary dynamic-stiffness data sets.

Rotordynamic Coefficients

The following section presents the experimental and theoretical rotordynamic coefficients. For the direct stiffness and damping, plots of (i) experiment, (ii) predictions taken directly from XLTFPBrg code, and (iii) modified theory (using Eqs. (35,36)) are all shown. All of the cross-coupled coefficients and the direct added masses are presented in the same way, with only experimental and theoretical curves directly from XLTFPBrg on the same plot since these coefficients did not have a modified theoretical case to present. Tables 33-36 document the experimental and theoretical rotordynamic coefficients and their respective uncertainties.

Figure 39 shows the experimental and theoretical direct stiffness coefficients at each test speed as a function of load while Fig. 40 shows the same plots zoomed in to experiment and modified theory only such that the reader can better view the load-dependency of these coefficients. Figures 41 and 42 show the direct stiffness coefficients at each test load as a function of speed, once again with the second figure zoomed in to experiment and modified theory only. Note that in the plot legends, the labels “Exp,” “Th,” and “Mod Th” refer to experiment, theory, and modified theory, respectively.

First note that there is only one curve for each of the theoretical cases as the bearing is predicted to be isotropic. It is clear that the raw output from XLTFPBrg markedly over predicts the direct stiffnesses; the degree of over prediction increases with speed. The addition of the simple stiffness-in-series model (Eq. (35)) vastly improves the agreement of theory and experiment, giving average percent differences of less than

5% for K_{xx} and 10% for K_{yy}. While K_{yy} is typically slightly lower than K_{xx}, the coefficients show the same trends. The direct stiffnesses generally increase with load only at lower speeds. As speed is increased, they begin to display a trend of dropping slightly then rising back up to the starting value at the highest load. The direct stiffnesses show greater dependence on speed than on load, rising more briskly as shaft speed is increased. The slopes of the direct stiffness coefficients are generally well-predicted by theory (especially with respect to load), though the raw XLTFPBrg plots have a higher slope than both experimental and modified theoretical data as a function of speed and load.

Figure 43 shows the cross-coupled stiffness coefficients as a function of load. While theory predicts the cross-coupled stiffnesses to be insignificant in magnitude (though normally having a non-zero positive value), K_{xy} and K_{yx} exhibit magnitudes of about 35% and 15% of the direct coefficients, respectively. However, while their magnitudes are relatively large, the cross-coupled stiffnesses exhibit same-sign values at all test conditions. Since there is no consistent trend with load or speed, these coefficients are only plotted versus load.

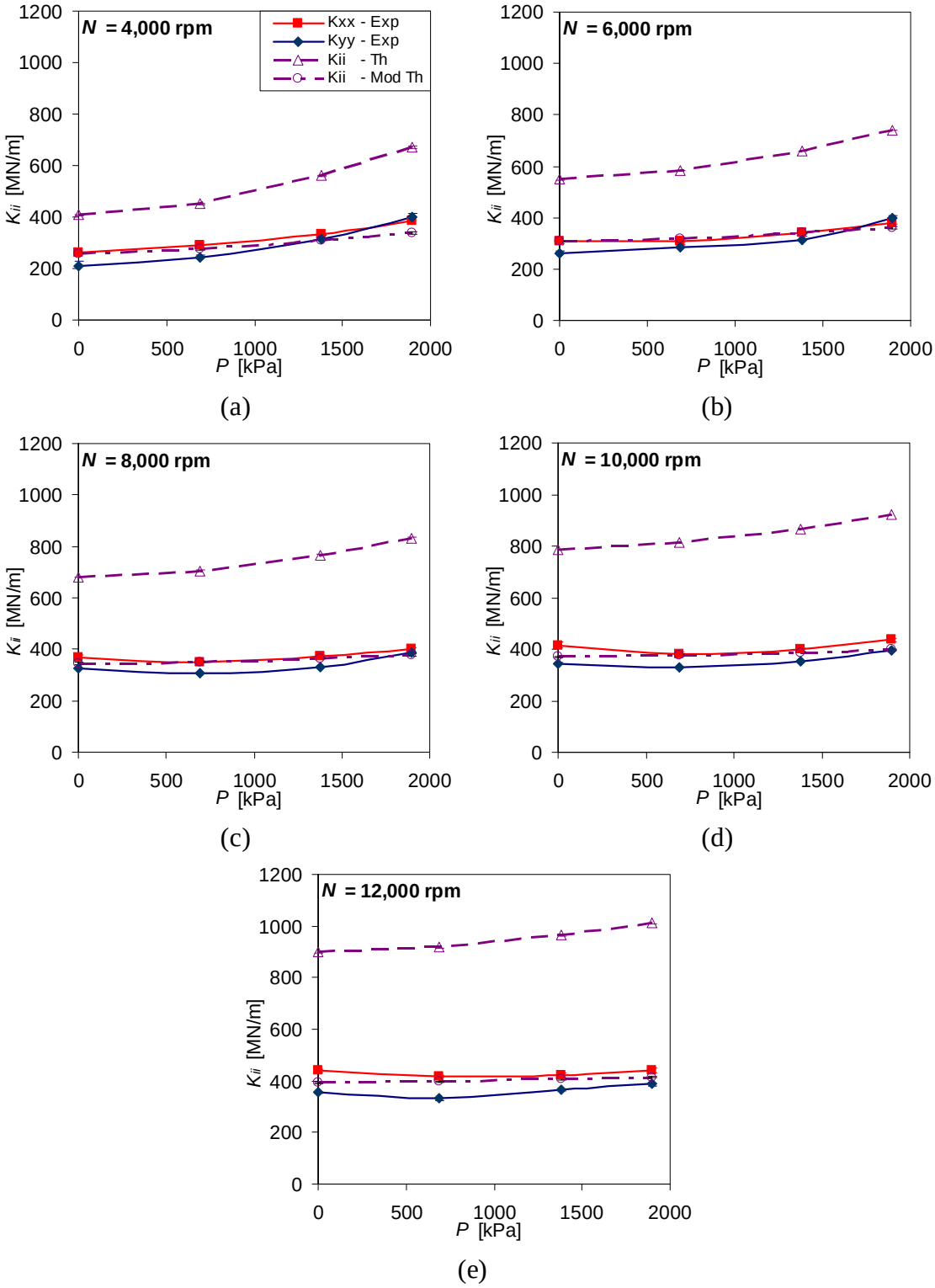

Fig. 39 Direct stiffness coefficients versus load at (a) 4,000 rpm, (b) 6,000 rpm, (c) 8,000 rpm, (d) 10,000 rpm, and (e) 12,000 rpm

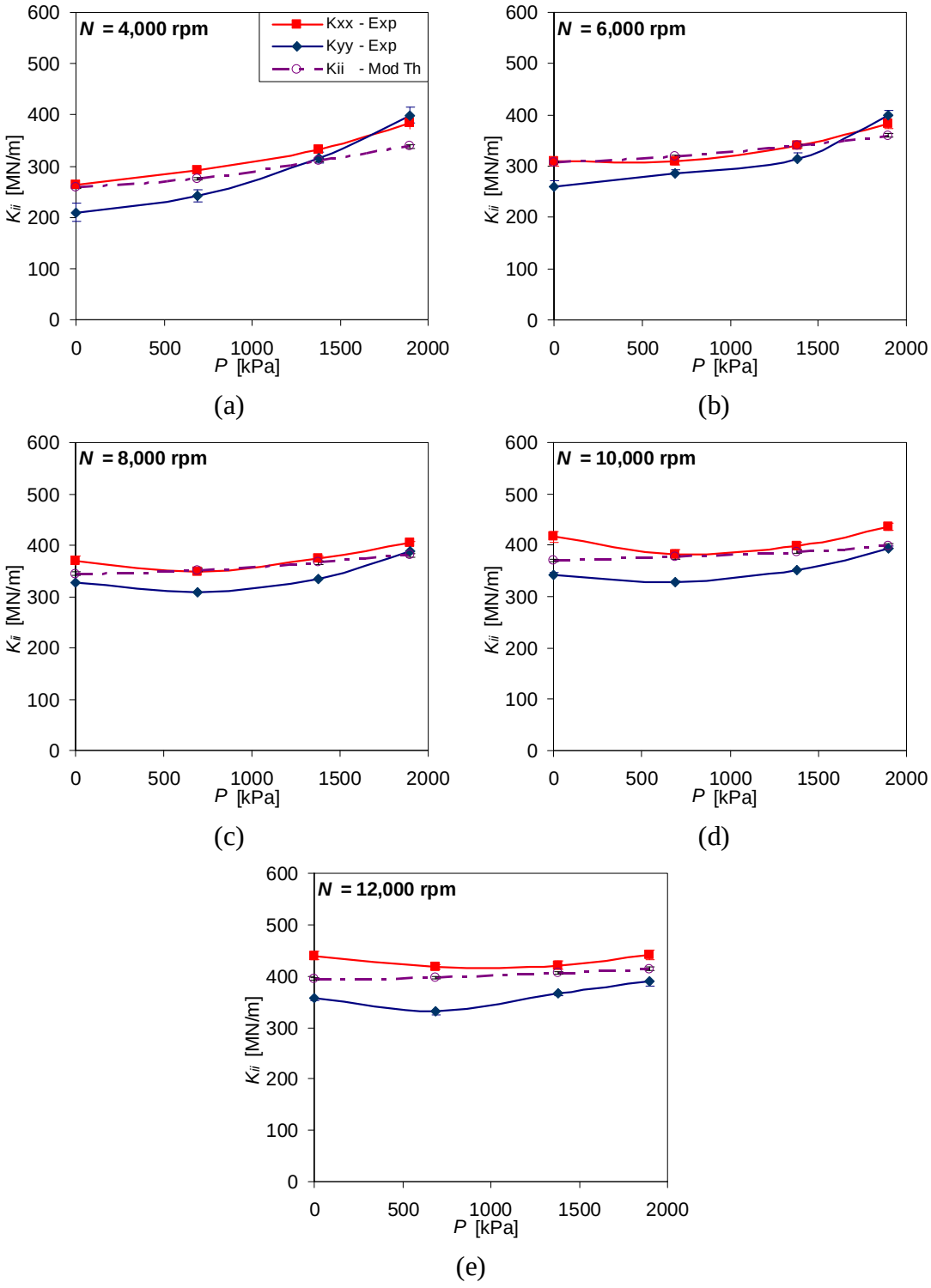

Fig. 40 Direct stiffness coefficients versus load at (a) 4,000 rpm, (b) 6,000 rpm, (c) 8,000 rpm, (d) 10,000 rpm, and (e) 12,000 rpm zoomed to show experiment and modified theory only

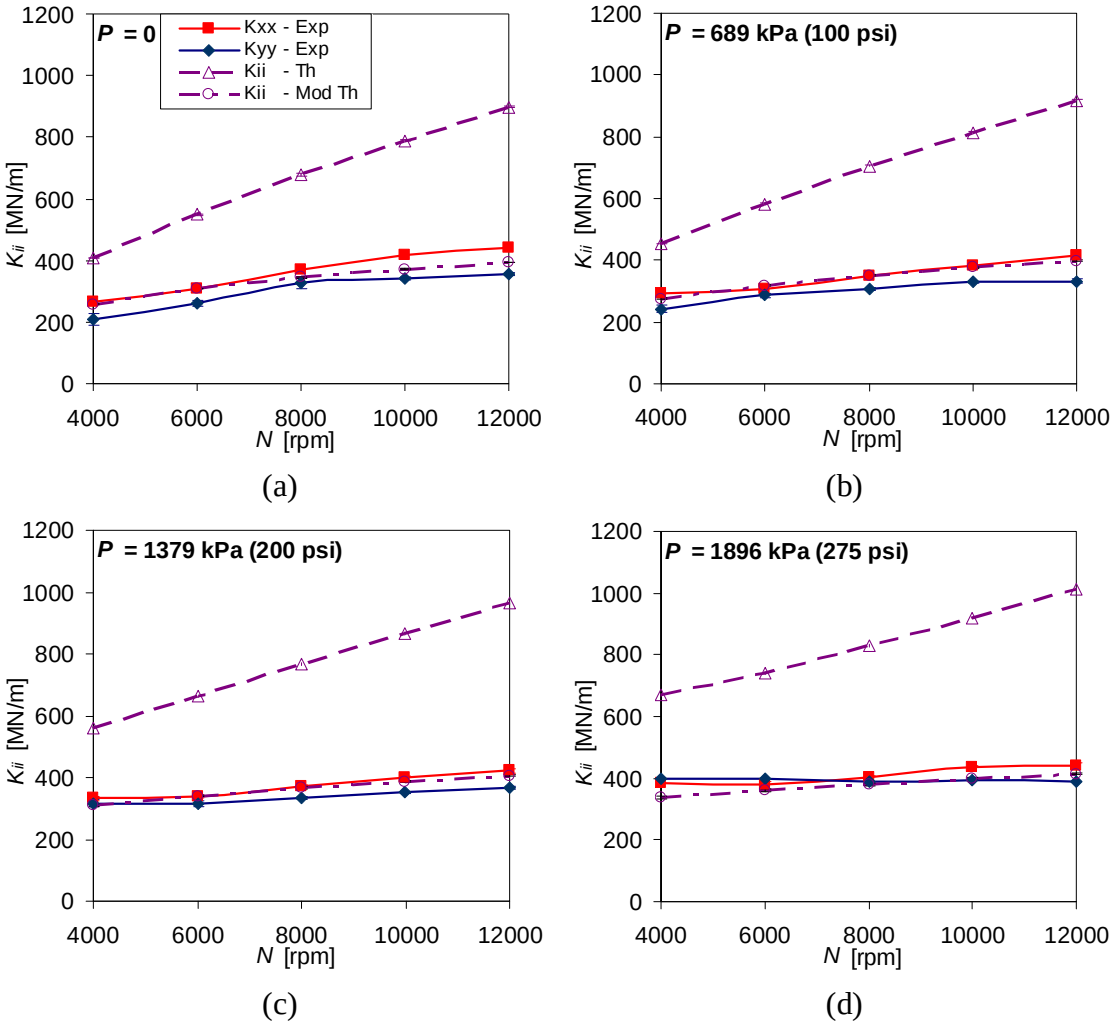

Fig. 41 Direct stiffness coefficients versus speed at (a) 0 kPa, (b) 689 kPa, (c) 1379 kPa, (d) and 1896 kPa

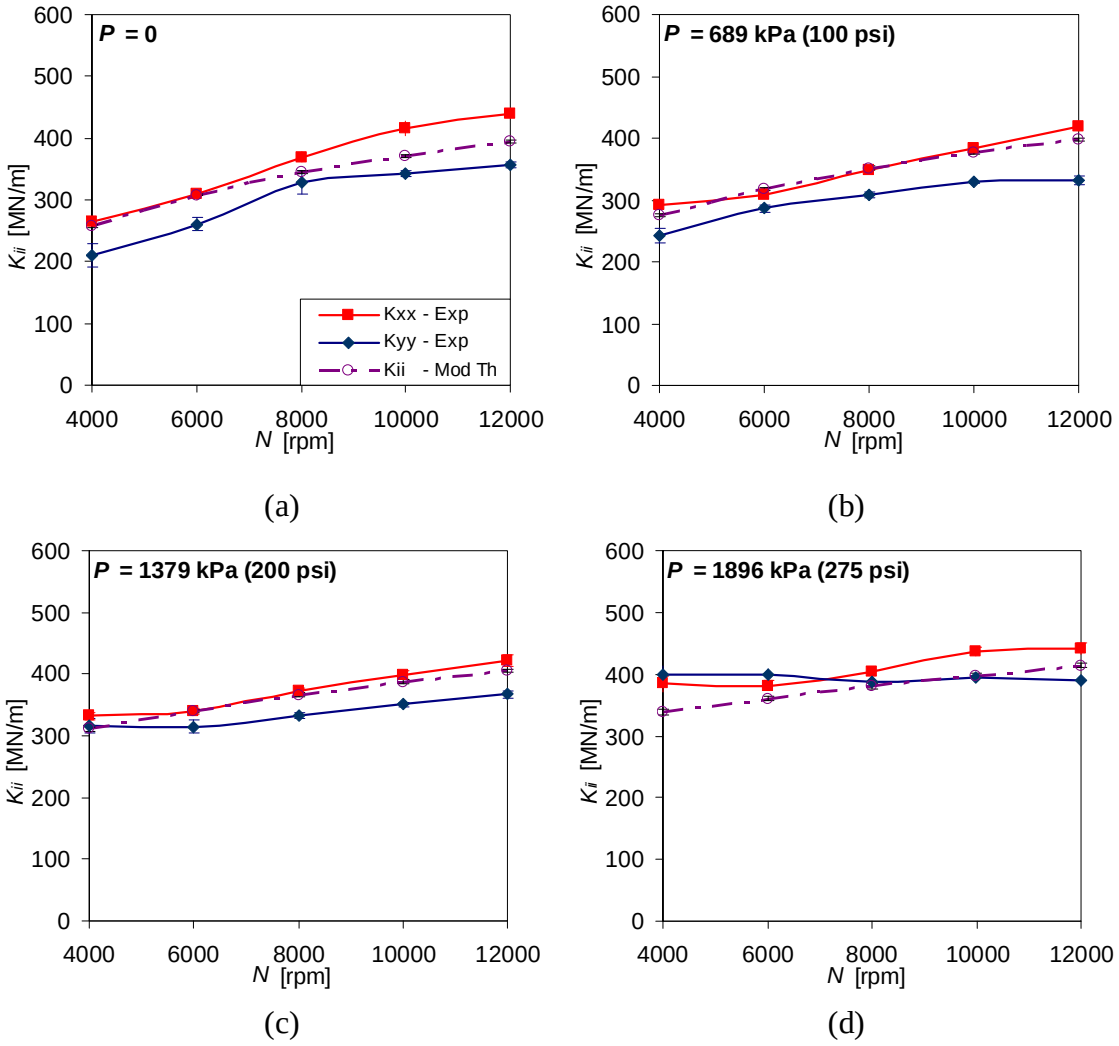

Fig. 42 Direct stiffness coefficients versus speed at (a) 0 kPa, (b) 689 kPa, (c) 1379 kPa, (d) and 1896 kPa zoomed to show experiment and modified theory only

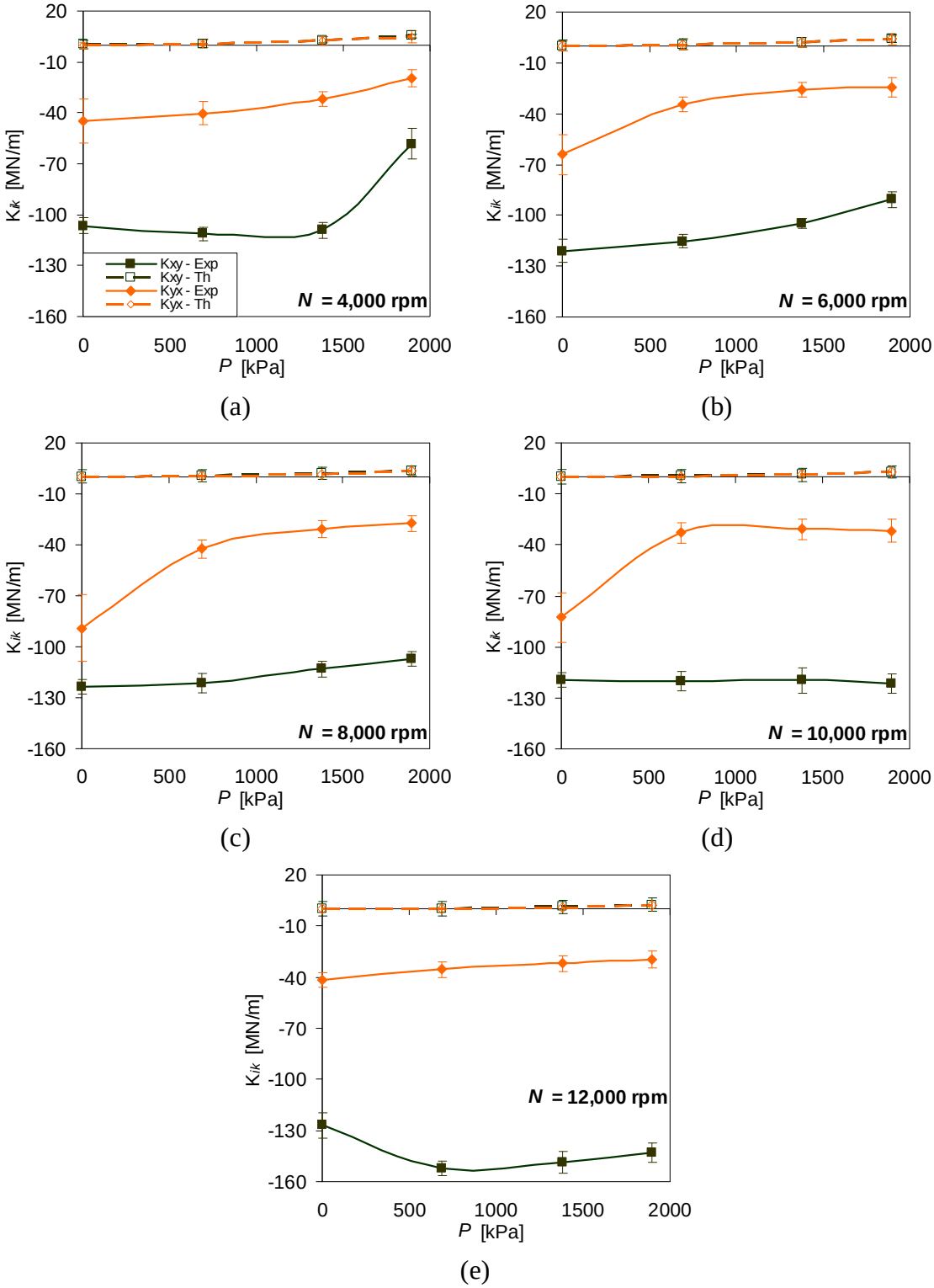

Fig. 43 Cross-coupled stiffness coefficients versus load at (a) 4,000 rpm, (b) 6,000 rpm, (c) 8,000 rpm, (d) 10,000 rpm, and (e) 12,000 rpm

Figures 44-47 present the direct damping coefficients in the same manner that the direct stiffness coefficients were presented. Once again, since the bearing is predicted to isotropic, only one curve is presented for each case of the theoretical values. Within the bounds of uncertainty, this attribute is duplicated by experiment. As with the direct stiffness coefficients, the direct damping coefficients are strongly over predicted. But in the case of the damping, the over prediction improves as speed is increased. The direct damping slightly decreases with speed but is approximately independent of load. Like the direct stiffnesses, accounting for the pad support structure using Eq. (35) extensively improves agreement between theory and experiment though there is still a significant degree of over prediction at low speeds.

Once again note that while this discussion presents the damping as frequency-independent (justified by high r^2 values), there was a noticeable curvature in the imaginary parts of the dynamic-stiffness coefficients as seen in Fig. 37(d) (page 77). Figure 48 shows a plot of the experimental frequency-dependent damping calculated using the secant method (described in the "XLTFPBrg™ Predictions" subsection). Both curves are fairly constant past 100 Hz, but the averages of the $C_{xx}(\Omega)$ values show a decreasing trend over the range of excitation frequencies. There is no significant trend in $C_{yy}(\Omega)$ below 100 Hz although some of the averaged points are lower than the rest below this frequency. At any rate, the uncertainties become too large make a solid conclusion on the trend of either plot below 100 Hz. The described characteristics were displayed at most test conditions, though more prevalent at higher speeds. The uncertainty in damping is exacerbated at low frequency values since the denominator is the frequency value. It is also likely that the same damage caused by press-fitting the housing onto the bearing, scratches on the pad surfaces, and imbalance in the test rig rotor contributed.

The cross-coupled damping curves are not plotted since there were few cases where they could be modeled as frequency-independent. Rough linear curve-fits of $\mathrm{Im}(\boldsymbol{H}_{xy})$, $\mathrm{Im}(\boldsymbol{H}_{yx})$ resulted in cross-coupled damping values that were typically only 10% or less of the direct values.

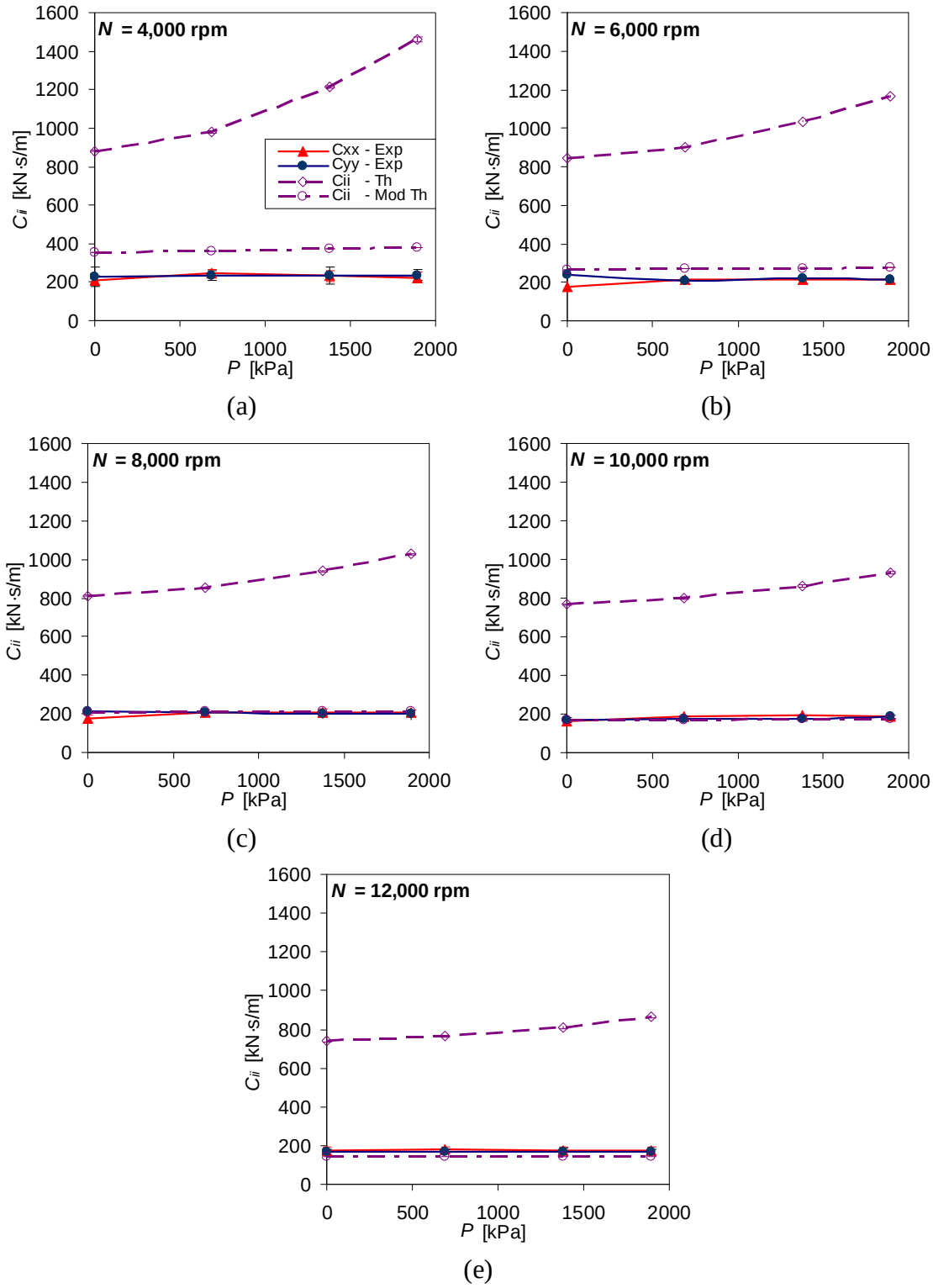

Fig. 44 Direct damping coefficients versus load at (a) 4,000 rpm, (b) 6,000 rpm, (c) 8,000 rpm, (d) 10,000 rpm, and (e) 12,000 rpm

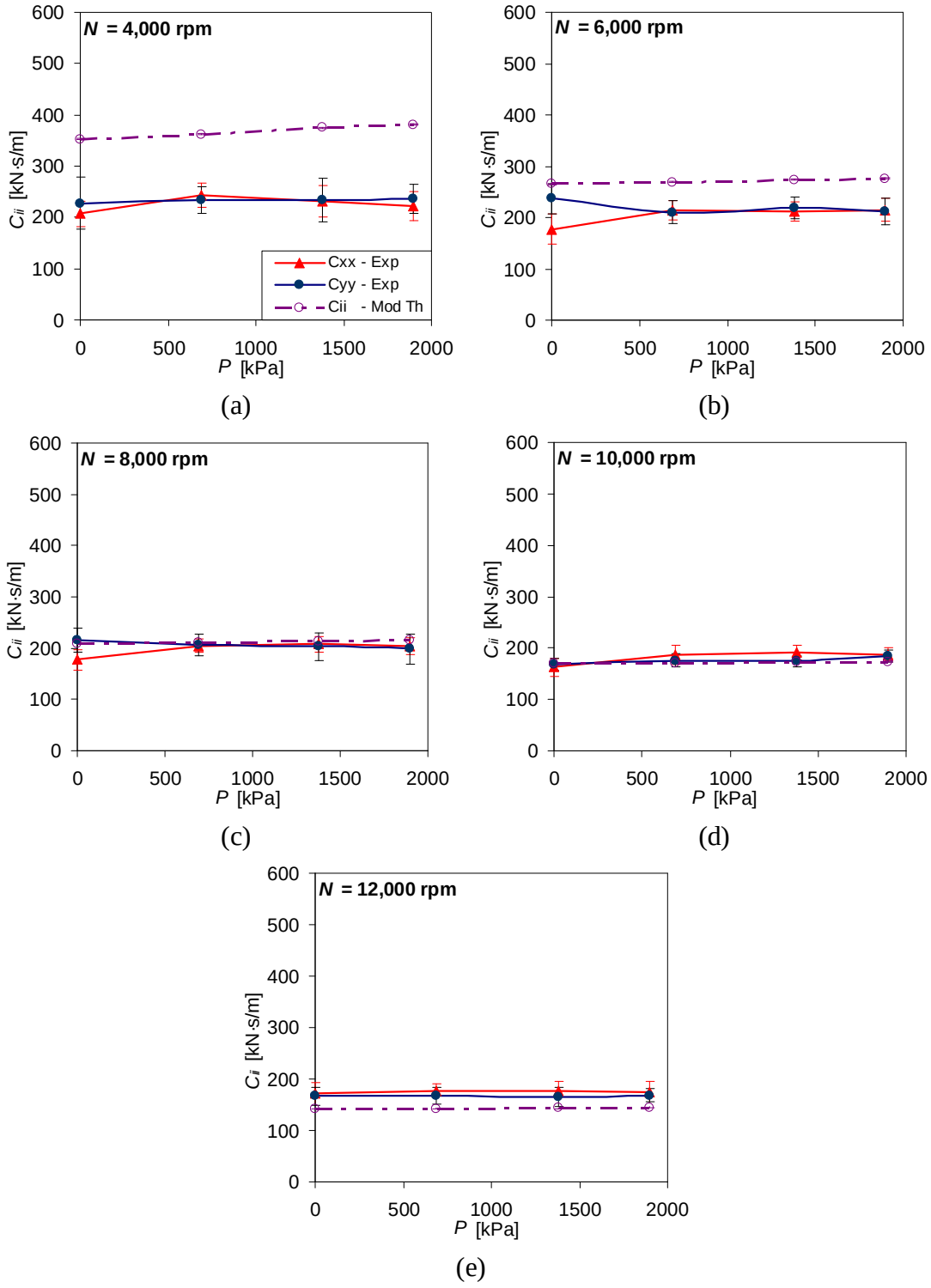

Fig. 45 Direct damping coefficients versus load at (a) 4,000 rpm, (b) 6,000 rpm, (c) 8,000 rpm, (d) 10,000 rpm, and (e) 12,000 rpm zoomed to show experiment and modified theory only

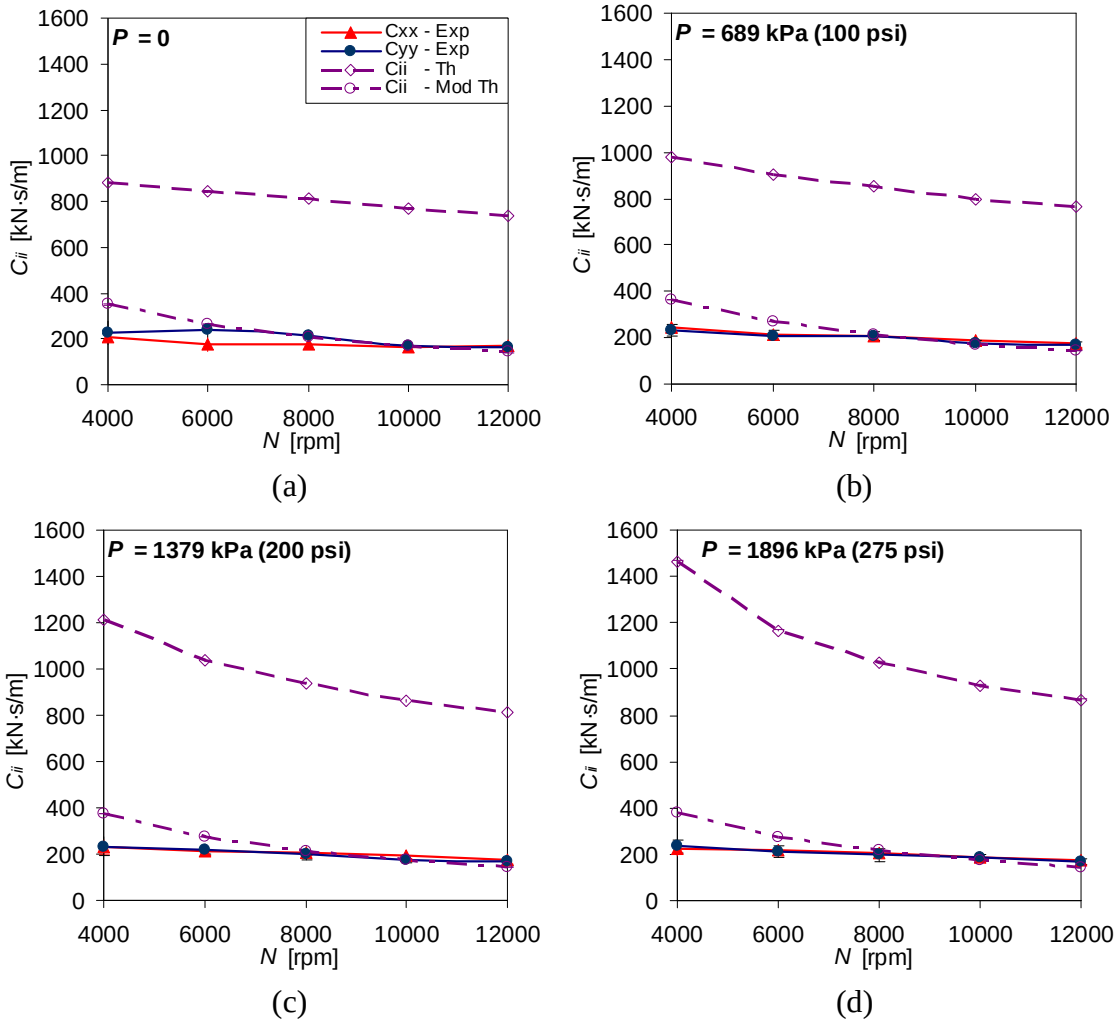

Fig. 46 Direct damping coefficients versus speed at (a) 0 kPa, (b) 689 kPa, (c) 1379 kPa, (d) and 1896 kPa

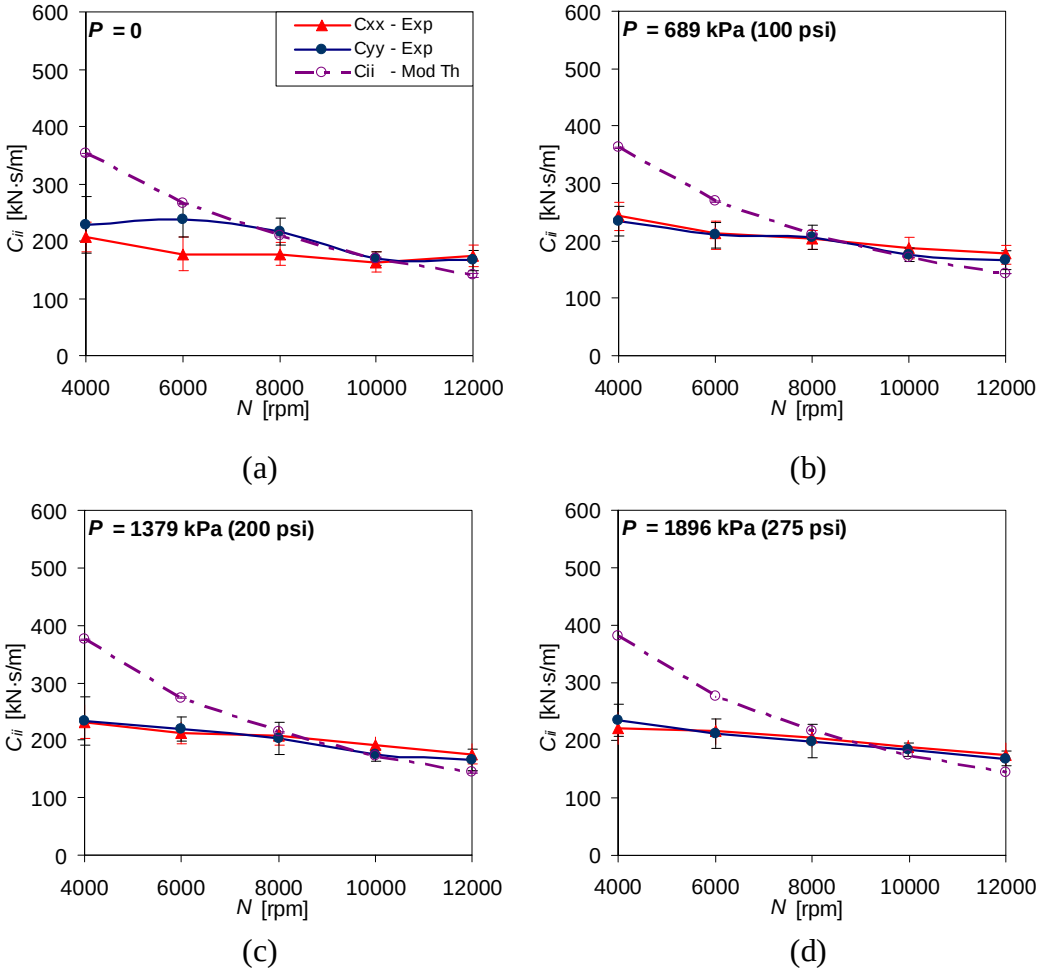

Fig. 47 Direct damping coefficients versus speed at (a) 0 kPa, (b) 689 kPa, (c) 1379 kPa, (d) and 1896 kPa zoomed to show experiment and modified theory only

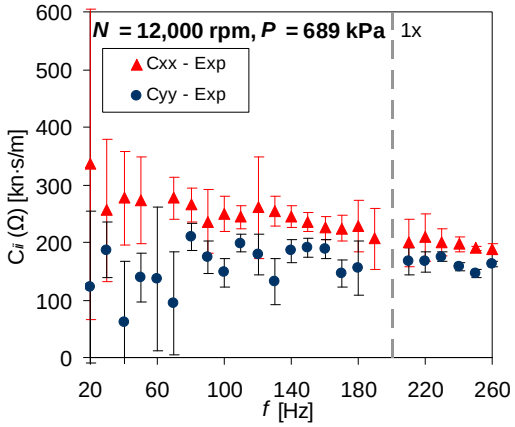

Fig. 48 Experimental frequency-dependent damping at 12,000 rpm, 689 kPa

The direct added mass coefficients are shown versus speed in Fig. 49 but are not shown versus load since they did not show a consistent trend with respect to load. First note that there are 5 cases where the direct added masses are negative, indicating an increase in the real parts of the corresponding direct dynamic-stiffness coefficients with frequency. This effect is most pronounced at low speeds and low loads and normally only occurs for M_{yy} as M_{xx} is typically zero at low speeds. In general, M_{yy} is lower than M_{xx}, but they tend to converge as the bearing is loaded. Both coefficients increase notably with speed at every load value. Just as in the case of the direct stiffness and damping, these coefficients are predicted isotropic. While theory over predicts the added masses and does not predict the negative values, it tends to match the trend of their curves with respect to speed quite well.

The cross-coupled real dynamic-stiffnesses were only modeled with added mass coefficients in 8 cases. The most common two conditions for this to occur were maximum speed and zero load, which are shown in Figs. 50(a) and (b), respectively. At the maximum speed (N = 12,000 rpm), M_{xy} is around -20 kg above zero load while M_{yx} is around -40 kg at intermediate speeds at zero load. In both of these cases, the negative added mass caused the corresponding dynamic-stiffness coefficient to increase with frequency, but did not cause Re($\boldsymbol{H}_{xy}$), Re($\boldsymbol{H}_{xy}$) become opposite in sign at or below 1x frequency.

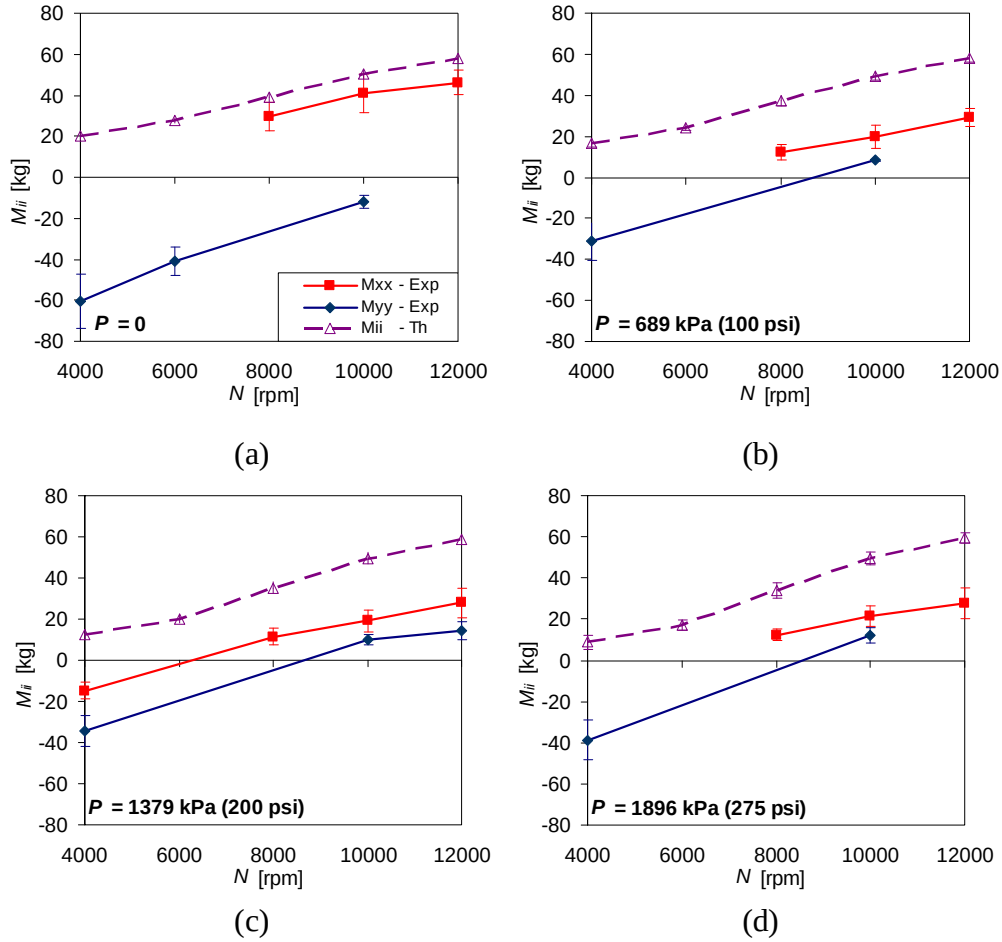

Fig. 49 Direct added mass coefficients versus speed at (a) 0 kPa, (b) 689 kPa, (c) 1379 kPa, (d) and 1896 kPa

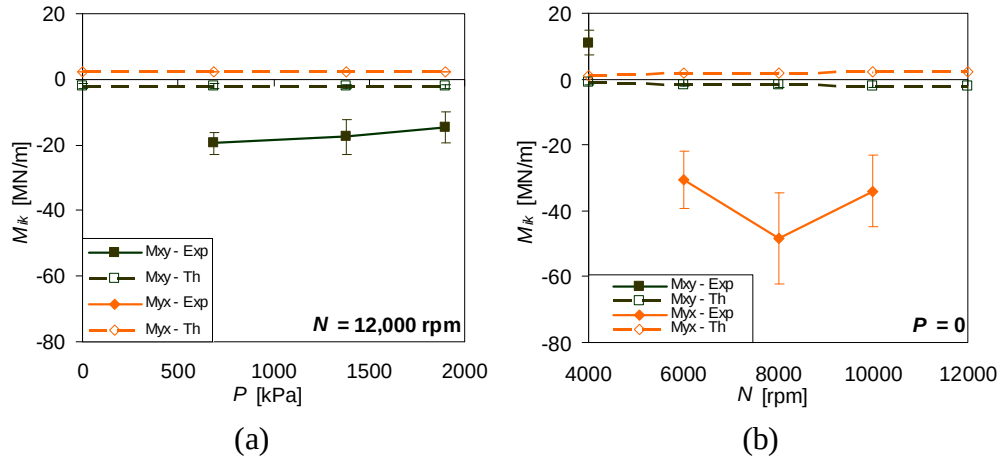

Fig. 50 Cross-coupled added mass coefficients at (a) 12,000 rpm and (b) $P = 0$

Static Stiffness Versus K_{yy}

Plots of static stiffness in the *y* direction versus the rotordynamic stiffness K_{yy} are presented above are shown below in Fig. 51. $K_{yy,s}$ and K_{yy} typically coincide reasonably well at the first three test loads, aside from N = 12,000 rpm at P = 0 (Fig. 51(a)). However, at P = 1896 kPa as seen in Fig. 51(d), they compare poorly.

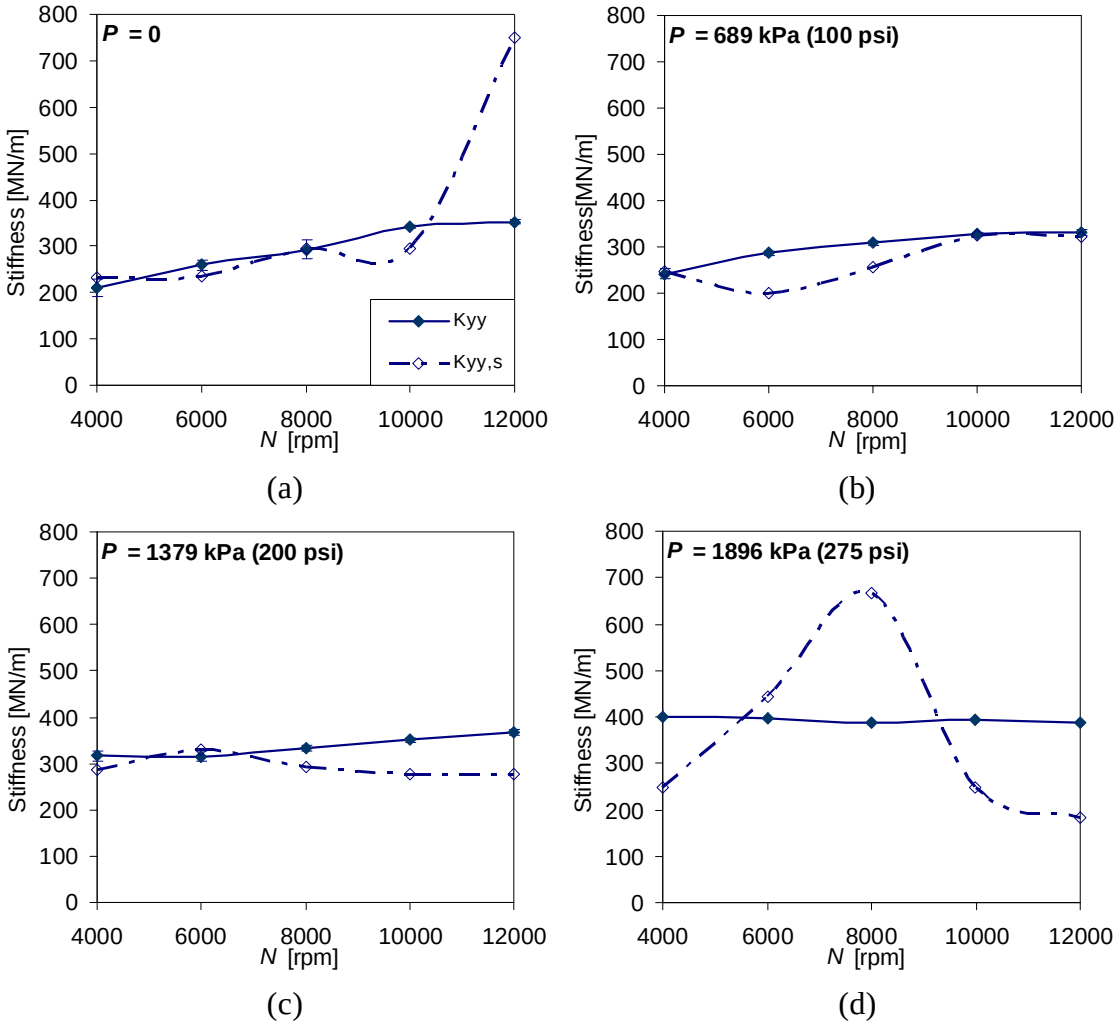

Fig. 51 $K_{yy,s}$ and K_{yy} versus speed at (a) 0 kPa, (b) 689 kPa, (c) 1379 kPa, (d) and 1896 kPa

Whirl Frequency Ratio

Evaluation of Eq. (30) always led to an imaginary number, netting WFR = 0 for all test conditions. Though Eq. (30) requires values for cross-coupled damping coefficients, Im(H_{xy}), Im(H_{yx}) were poorly modeled by a linear regression. As an estimate, linear regressions were initially used to provide cross-coupled damping values for calculation of the WFR. But setting them to zero in the calculation netted approximately the same result for the square of the WFR.

XLTFPBrg predicted very small positive values for the WFR only at zero load, the largest of these values being on the order of 0.001. This result may be effectively interpreted as WFR = 0 as well since this implies that a rotor spinning inside the bearing would have to reach a rotational speed of $1{,}000\omega_{n1}$ in order to become unstable.

SUMMARY AND CONCLUSIONS

Though predictions were compared to experiment throughout the paper, the reader must remain aware that the code for predictions was not designed to model TPJB's with (i) clearances differing in separate axes, (ii) multiple preload values, (iii) leading edge chamfers, or (iv) oil temperature control mechanisms such as Spray-Bar Blockers® and By-Pass® Cooling chambers. While no effort was made to compensate for the effects of (iii) and (iv), the author accounted for (i) and (ii) by using the average clearance of 77.1 μm (3.04 mils) and defining an effective preload (Eq. (33)). Since these approximations have not been shown accurate, note that the following conclusions pertaining to theory versus experiment would be less refutable if the above characteristics could be modeled or if the test bearing did not have them.

Pivot Stiffness

Kirk and Reedy [14] predict pivot stiffness values that vary with load. Accordingly, load versus deflection plots predicted by Eq. (6) are non-linear in contrast to the linear experimental load versus deflection data in Fig. 25. However, the theoretical load versus deflection plots shown in Fig. 26 were fit to linear curves with $r^2 > 0.97$ in every case. While the linearity of these curves would most likely degrade if the curve-fits were carried out over a larger domain of differential diameter values, this finding—coupled with the fact that the experimental pad support structure stiffness was approximately constant with load—suggests that pivot stiffness can be considered constant to within a reasonable margin of error over a sufficiently small range of applied loads. This could simplify bearing codes by preventing the coder from having to evaluate the pivot stiffness separately for each pivot based on the resultant force vector for each one.

While plots produced by Eq. (6) do agree with experiment in that they can be approximated as linear, Fig. 27 showed an experimental value for pad support structure

stiffness that is well below the calculated values for pivot stiffness, even in the case of the largest possible differential diameter. The author presents the following explanations: (i) the differential diameter is greater largest possible design value, (ii) the elements of the pad support structure other than the pivot have stiffness values on the order of the pivot stiffness, or (iii) a combination of (i) and (ii).

Figure 28 shows that a change in differential diameter due to differential thermal growth of the ball and socket is predicted to have a significant effect on the pivot stiffness at lower ambient-condition values of differential diameter. Assuming an initial differential diameter of 25.4 μm (1 mil, i.e. near flush), the predicted pivot stiffness drops by about 13% due to a 35ºC (63ºF) temperature increase. This is similar to Nicholas and Wygant's results [3] though they assumed a temperature increase of 55ºC (100ºF). This is a significant prediction since it is desirable to have a socket that is nearly flush to the ball to avoid excessive pivot flexibility.

Journal Position

Figures 30-32 show that the eccentricities and attitude angles were acutely under predicted. This result agrees with the facts that the direct and cross-coupled stiffness coefficients were largely over predicted and under predicted, respectively. Under prediction of the eccentricities is the first indication that pivot stiffness could have a notable influence on the characteristics of the bearing. The fact that eccentricity was once outside of the nominal clearance may also suggest that the clearance space became larger during operation due to deflection of the loaded pivots. As indicated in the "Results" section, the clearance space could increase up to 39.1 μm (1.54 mils) at the maximum test load according to the pad support structure stiffness measurement. Comparison of the low attitude angles in Carter's test results [27] for a rocker-back pivot and those herein that varied from 6°-29° away from zero load for a ball-in-socket design seem to parallel Wygant et al.'s results [17] in that attitude angle increases when changing from a rocker-back to a ball-in-socket design—Wygant et al. measured low attitude angles for the rocker-back bearing and 13°-33° attitude angles for the ball-in-socket bearing.

Power Loss and Temperature Data

The estimated power loss was under predicted by as much as 50% at low speeds but theoretical and experimental values converged until they were almost exactly the same as speed was increased. The fact that maximum temperature rise from the bearing inlet was over predicted by as much as 40% suggests that the special design features to minimize temperature rise are effective in reducing bearing pad temperatures.

Dynamic Stiffness Coeffficients

Similar to the results in [2,22,26,27], the frequency-independent [M]-[C]-[K] model did a good job of fitting the experimental dynamic-stiffness coefficients both in theory and experiment for all coefficients other than the cross-coupled imaginary dynamic-stiffnesses—this fact indicates that cross-coupled damping is likely frequency-dependent. In several cases, a linear regression did not fit the real dynamic-stiffness coefficients well and the added mass was set to zero, netting a frequency-independent stiffness coefficient—this was more common for the cross-coupled coefficients. For these cases, it is also likely that the span of frequencies was not large enough to manifest significant curvature in Re($\boldsymbol{H}_{ij}$) as there was a slight rise or drop in this coefficient from 20 to 260 Hz. There was some evidence of frequency-dependency in the experimental direct damping particularly in the x (unloaded) direction apparent from a decreasing curvature of the imaginary parts of the direct dynamic-stiffness coefficients. Even so, these experimental data were fit to linear regressions with high r^2 values.

Rotordynamic Coefficients

A general observation of the direct rotordynamic coefficients is that they were normally close to being isotropic aside from the added masses at zero load, though K_{yy} was consistently slightly lower than K_{xx}. This feature can be conclusively attributed to the bearing's symmetrical 4-pad geometry for which Lund [1] first predicted isotropic coefficients and predictions herein follow suit. This result is also corroborated by experiment in [7,16,20]. Also note that while modification of the predicted direct stiffness and damping coefficients via Eqs. (35,36) substantially dropped their

magnitude, the values would have dropped even more had the apparent increase in clearance been accounted for [3]. The following subsections present additional observations and conclusions regarding each of the three sets of coefficients.

Stiffness Coefficients

At zero load, the identified K_{xx} and K_{yy} coefficients increase modestly with increasing speed only at low loads and vice versa; both dependencies were eliminated with an increase in the other variable. Carter's results [27] differ in that these coefficients increased modestly with speed but always increased briskly with increasing applied load. While the direct stiffness coefficients were markedly over predicted, consideration of pivot stiffness vastly improved this agreement. Modification of the direct stiffness coefficients caused them to decrease up to 59%. This outcome matches Nicholas and Wygant's assertion [3] that adding consideration of pivot stiffness to a TPJB model will decrease the coefficients up to 56% very closely (see Table 4). While Kirk and Reedy [14] predicted that damping does not change appreciably for "operation near design speed," note that they included the higher-order frequency terms—which tend to increase stiffness with increase frequency—to the calculation at a "design speed" of 200 Hz (12,000 rpm) whereas Nicholas and Wygant's calculation was for 5,000 rpm. While the authors do not state their reduction method, it is apparent that the coefficients in both papers were synchronously reduced.

The cross-coupled stiffness coefficients did not show a general trend with load or speed. These coefficients were of significant magnitude (about 35% for K_{xy} and 15% for K_{yx}) of the direct stiffness coefficients whereas the cross-coupled stiffnesses in Carter's case [27] were quite low. This comparison also parallels the results of Wygant et al. [18] and suggests that pivot friction plays a significant role in the bearing's characteristics. However, unlike Wygant et al.'s results, the cross-coupled stiffness coefficients were always of the same sign (negative). As in Lund's analysis [1], the predicted cross-coupled stiffness coefficients have a non-zero magnitude but are on the order of 1% or less of the direct coefficients even when pad inertia is considered. This prediction—along with the results of this study and those of Wygant et al. [18]—

suggests that pad inertia plays a small role in the magnitude of cross-coupled stiffness coefficients for ball-in-socket TPJB's, and the only way to predict the notable magnitude of these coefficients would be to develop formulation to model the effect of pivot friction.

Damping Coefficients

Measured C_{xx} and C_{yy} coefficients drop slightly with increasing speed but are insensitive to changes in the applied loads, which is similar to Carter's results [27]. As with the direct stiffness coefficients, the pivot stiffness modification brought the theoretical values much closer to those measured. As an addition to Table 4, accounting for pivot stiffness decreased the predicted direct damping up to 83%, which is similar to the results of both Kirk and Reedy [14] and Nicholas and Wygant [3].

It was noted that there was a discernable curvature in the imaginary parts of the direct dynamic-stiffness coefficients in the unloaded direction, as slope tended to decrease with increasing frequency for Im($\boldsymbol{H}_{xx}$). Frequency-dependent damping calculations using the secant method (i.e. $C_{ij}(\Omega)$ = Im($\boldsymbol{H}_{ij}$)/Ω) showed a decrease in C_{xx} with increasing frequency. However, the calculated uncertainties of the frequency-dependent damping coefficients were so high at low frequencies that a flat line could conceivably be drawn through a plot of them within the bounds of the uncertainty. Perhaps more reliable frequency-dependent damping coefficients could be identified if steps were taken to improve the test bearing and/or testing apparatus (e.g. resurfacing the pads, balancing the rotor). If the averages of the frequency-dependent damping values for $C_{xx}(\Omega)$ identified herein were found to be reliable, the common assertion that damping is lower at subsynchronous frequencies [12,13] could be contrasted with test results that not only show damping that can be approximated as frequency-independent but is actually higher at subsynchronous frequencies. On the other hand, if high r^2 values continue to result from curve-fits of imaginary dynamic-stiffness data (even in spite of solid evidence of slight frequency-dependency), there may be little value to breaking away from a frequency-independent [M]-[C]-[K] model since inclusion of

frequency-dependent damping terms in a rotordynamic model would require iteration for eigenvalue analysis.

The cross-coupled imaginary dynamic stiffnesses are not modeled well with a linear regression and the cross-coupled damping coefficients are likely frequency-dependent, but scatter in the data prevented the author from deducing a general trend in these coefficients—this has been common a occurrence in testing utilizing the test rig described herein [2,26,27]. However, Im($\boldsymbol{H}_{xy}$), Im($\boldsymbol{H}_{yx}$) are normally small in magnitude and rough linear estimates led to cross-coupled damping coefficients that were usually around 10% of the direct coefficients but typically had high uncertainties, especially at zero load. They, like the cross-coupled stiffness coefficients, are predicted to be too small to have a noticeable effect on the stability of the bearing.

Added Mass Coefficients

At low speeds, M_{xx} and M_{yy} were negative (more negative for M_{yy}) in many cases, indicating that the bearing "hardens" with increasing excitation frequency. This could be partly due to the higher-order frequency terms in Eq. (4), which are a function of pivot stiffness. M_{xx} and M_{yy} increased with increasing speed and were over predicted by XLTFPBrg, which predicted all positive added masses. Carter's results for a rocker-back bearing [27] showed smaller negative added masses at the lowest speed. The cross-coupled added mass coefficients had significant non-zero negative values in some cases, most notably maximum speed (12,000 rpm) and zero load. While this causes the negative value of corresponding negative cross-coupled stiffness coefficient to trend toward zero and become positive (opposite in sign of the other cross-coupled stiffness coefficient), it did not cause the cross-coupled stiffness coefficients to become opposite in sign below 1x and did not cause the bearing to have a non-zero positive WFR.

Static Stiffness Versus K_{yy}

Like Carter's results [27], the static stiffness in the *y* direction normally matched reasonably well with K_{yy} except at the highest load. However, in Carter's case K_{yy} was

generally much higher at the maximum test load, whereas it was either higher or lower depending on the speed for the test bearing considered here.

Whirl Frequency Ratio

WFR was zero for all test conditions, indicating unconditional stability (note that this was based on rough linear curve-fits for cross-coupled damping values). This was predicted by XLTFPBrg though there was a very small WFR on the order of 0.001 (at most) predicted at zero load conditions.

Closing Comments

Advocates of subsychronously reduced damping coefficients frequently state that use of these coefficients better predicts compressor stability since these coefficients are lower in magnitude. As previously mentioned, the current results repeat [2,22,26,27] in measuring largely frequency-independent damping coefficients. Table 5 documents the variance of predictions of direct stiffness and damping coefficients. Prediction for this bearing follows the results of Ikeda [21] in marked over prediction of both stiffness and damping. For the test bearing, it is quite clear that the flexibility of the pad support structure dominates its behavior and addition of a simple stiffness-in-series model vastly improves agreement between theory and experiment. This is not an outcome that can be repeated on Carter's [27] bearing where the direct stiffnesses are reasonably predicted, C_{yy} is over predicted at low speeds but only slightly over predicted at high speeds, and C_{xx} is generally over predicted by a factor of 1.5-2.

As an addition to Table 5, it remains that, in general, damping is the only coefficient that is consistently over predicted. While leaving many questions open to further investigation, the results of this study offer to further corroborate the following simple explanation for the conflict between (i) measurements that show frequency-independent damping coefficients, and (ii) stability calculation requirements for lower damping values: specifically, damping, while approximately frequency-independent, is being systematically over predicted by computer models.

REFERENCES

[1] Lund, J.W., 1964, "Spring and Damping Coefficients for the Tilting-Pad Journal Bearing," ASLE Transactions, **7**(3), pp. 342-352.

[2] Al-Ghasem, A., 2004, "Measurement of Rotordynamic Coefficients for a High Speed Flexure-Pivot Tilting-Pad Bearing (Load Between Pad Configuration)," M.S. Thesis, Texas A&M University, College Station, TX.

[3] Nicholas, J.C., and Wygant, K.D., 1995, "Tilting Pad Journal Bearing Pivot Design For High Load Applications," *Proc. 24th Turbomachinery Symposium*, Houston, TX, pp. 33-47.

[4] Kepple, W. E., Read, D. W., Zeidan, F.Y., Paraskevakos, C., and Dawson, M. P., 1998, "Experience in the Use of Flexure Pivot Tilt Pad Bearings in Boiler Feed Water Pumps," *Proc. 15th International Pump Users Symposium*, Houston, TX, pp. 77-84.

[5] Rotech Engineering Services, 2007, "Tilting Pad Journal Bearings: Principles of Operation," http://www.rotechconsulting.com/bearings_sub2.htm, accessed April 2007, Delmont, PA.

[6] Reynolds, O., 1886, "On the Theory of Lubrication and Its Application to Mr. Beauchamp Tower's Experiments Including an Experimental Determination of the Viscosity of Olive Oil," Phil. Trans., Roy. Soc. London, **177**, pp. 157-234.

[7] Hagg, A.C., and Sankey, G.O., 1956, "Some Dynamic Properties of Oil-Film Journal Bearings with Reference to the Unbalance Vibration of Rotors," ASME J. Appl. Mech., **23**, pp. 302-306.

[8] Hagg, A.C., and Sankey, G.O., 1958, "Elastic and Damping Properties of Oil-Film Bearings for Application to Unbalance Vibration Calculations," ASME J. Appl. Mech., **25**, p. 141.

[9] Hirs, G.G., 1973, "A Bulk-Flow Theory for Turbulence in Lubricant Films," ASME J. Lubr. Technol., **94**, pp. 137-146.

[10] Reinhardt, E., and Lund, L., 1975, “The Influence of Fluid Inertia on the Dynamic Properties of Journal Bearings,” ASME J. Lubr. Technol., **97**, pp. 159-167.

[11] Nicholas, J.C., 2003, “Lund’s Tilting Pad Journal Bearing Pad Assembly Method,” ASME J. Vib. Acoust., **125**(4), 448-454.

[12] Parsell, J. K., Allaire, P. E., and Barrett, L. E., 1983, ‘‘Frequency Effects in Tilting-Pad Journal Bearing Dynamic Coefficients,’’ ASLE Transactions, **26**, pp. 222–227.

[13] White, M.F., and Chan, S.H., 1992, “The Subsynchronous Dynamic Behavior of Tilting-Pad Journal Bearings,” ASME J. Tribol., **114**, pp.167-173.

[14] Kirk, R.G., and Reedy, S.W., 1988, “Evaluation of Pivot Stiffness for Typical Tilting-Pad Journal Bearing Designs,” ASME J. Vib. Acoust. Stress Reliab. Des., **110**, pp. 165-171.

[15] Childs, D., 2002, “Rotordynamics of Turbomachinery...Looking Back...Looking Forward,” *Proc. 6th IFToMM International Conference on Rotordynamics*, Sydney, Australia, pp. 25-27.

[16] Someya, T., 1989, *Journal-Bearing Databook*, Springer-Verlag Heidelberg, New York, pp. 222-229, 231, Chap. 3, 4.

[17] Wygant, K.D., Barrett, L.E., and Flack, R.D., 1999, “Influence of Pad Pivot Friction on Tilting-Pad Journal Bearing Measurements—Part I: Steady Operating Position,” STLE Tribology Transactions, **42**(1), pp. 210-215.

[18] Wygant, K.D., Barrett, L.E., and Flack, R.D., 1999, “Influence of Pad Pivot Friction on Tilting-Pad Journal Bearing Measurements—Part II: Dynamics Coefficients,” STLE Tribology Transactions, **42**(1), pp. 250-256.

[19] Kostrzewski, G.J., Taylor, D.V. and Flack, R.D., 1990, “Accuracy Evaluation of Experimentally Derived Dynamic Coefficients of Fluid Film Bearings—Part II: Case Studies,” STLE Tribology Transactions, **33**(1), pp. 115-121.

[20] Ikeda, K., Hirano, T., Yamashita, T., Mikami, M., and Sakakida, H., 2004, “An Experimental Study of Static and Dynamic Characteristics of a 580 mm (22.8 in.) Direct Lubrication Tilting Pad Journal Bearing,” *Proc. 2004 ASME/STLE*

International Joint Tribology Conference, Long Beach, California, USA, Paper No. TRIB2004-64064.

[21] Mikami, M., Kumagai, M., Uno, S., and Hashimoto, H., 1988, "Static and Dynamic Characteristics of Rolling-Pad Journal Bearings in Super-Laminar Flow Regime," ASME J. Tribol., **110**, pp. 73-79.

[22] Dmochowski, W., 2005, "Dynamic Properties of Tilting-Pad Journal Bearings: Analysis and Experiment," *Proc. 16th Symposium on Industrial Application of Gas Turbines*, Banff, Alberta, Canada, Paper No. 05-IAGT-2.8.

[23] Rouvas, C., and Childs, D.W., 1993, "A Parameter Identification Method for the Rotordynamic Coefficients of a High Reynolds Number Hydrostatic Bearing," ASME J. Vib. Acoust., **115**(3), pp.264-270.

[24] Brockwell, K., Kleinbub, D., and Dmochowski, W., 1990, "Measurement and Calculation of the Dynamic Operating Characteristics oif the Five shoe, tilting Pad Journal Bearing," STLE Tribology Transactions, **33**(4), 481-492.

[25] San Andrés, L. A., 1995, "Bulk-Flow Analysis of Flexure and Tilting Pad Fluid Film Bearings," *Research Progress Report to the Turbomachinery Research Consortium*, Turbomachinery Laboratory, Texas A&M University, College Station, Texas, Paper No. TRC-B&C-3-95.

[26] Rodriguez, L., and Childs, D., 2006, "Frequency Dependency of Measured and Predicted Rotordynamic Coefficients for a Load-on-Pad Flexible-Pivot Tiling-Pad Bearing," ASME J. Tribol., **128**, pp. 388-391.

[27] Carter, C.R., 2007, "Measured and Predicted Rotordynamic Coefficients and Static Performance of a Rocker-Pivot, Tilt Pad Bearing in Load-on-Pad and Load-Between-Pad Configurations," M.S. Thesis, Texas A&M University, College Station, TX.

[28] Kaul, A., 1999, "Design and Development of a Test Setup for the Experimental Determination of the Rotordynamic and Leakage Characteristics of Annular Bushing Oil Seals," M.S. Thesis, Texas A&M University, College Station, TX.

[29] Rodriguez, L., 2003, "Experimental Frequency-Dependent Rotordynamic Coefficients for a Load-On-Pad, High-Speed, Flexible-Pivot Tilting-Pad Bearing," M.S. Thesis, Texas A&M University, College Station, TX.

[30] Childs, D., and Hale, K., 1994, "A Test Apparatus and Facility to Identify the Rotordynamic Coefficients of High-Speed Hydrostatic Bearings," ASME J. Tribol., **116**, pp. 337-344.

[31] Al-Jughaiman, B., 2006, "Static and Dynamic Characteristics for a Two-Axial-Groove Bearing and a Pressure Dam Bearing," M.S. Thesis, Texas A&M University, College Station, TX.

[32] Nicholas, J. C., 2002, "Bearing Assembly with By-Pass Cooling," US Patent No. 6,485,182, Rotating Machinery Technology, Inc., Wellsville, New York.

[33] Lund, J., 1965, "The Stability of an Elastic Rotor in Journal Bearings with Flexible Damped Supports," ASME J. Appl. Mech., **87**, pp. 911-920.

[34] San Andrés, L. A., 1991, "Effect of Eccentricity on the Force Response of a Hybrid Bearing," STLE Tribology Transactions, **34**(4), pp. 537- 544.

[35] Ertras, B., and Vance, J., 2007, "The Influence of Same-Sign Cross-Coupled Stiffness on Rotordynamics," ASME J. Vib. Acoust., **129**, pp. 24-31.

APPENDIX A

DRAWING AND DATA TABLES

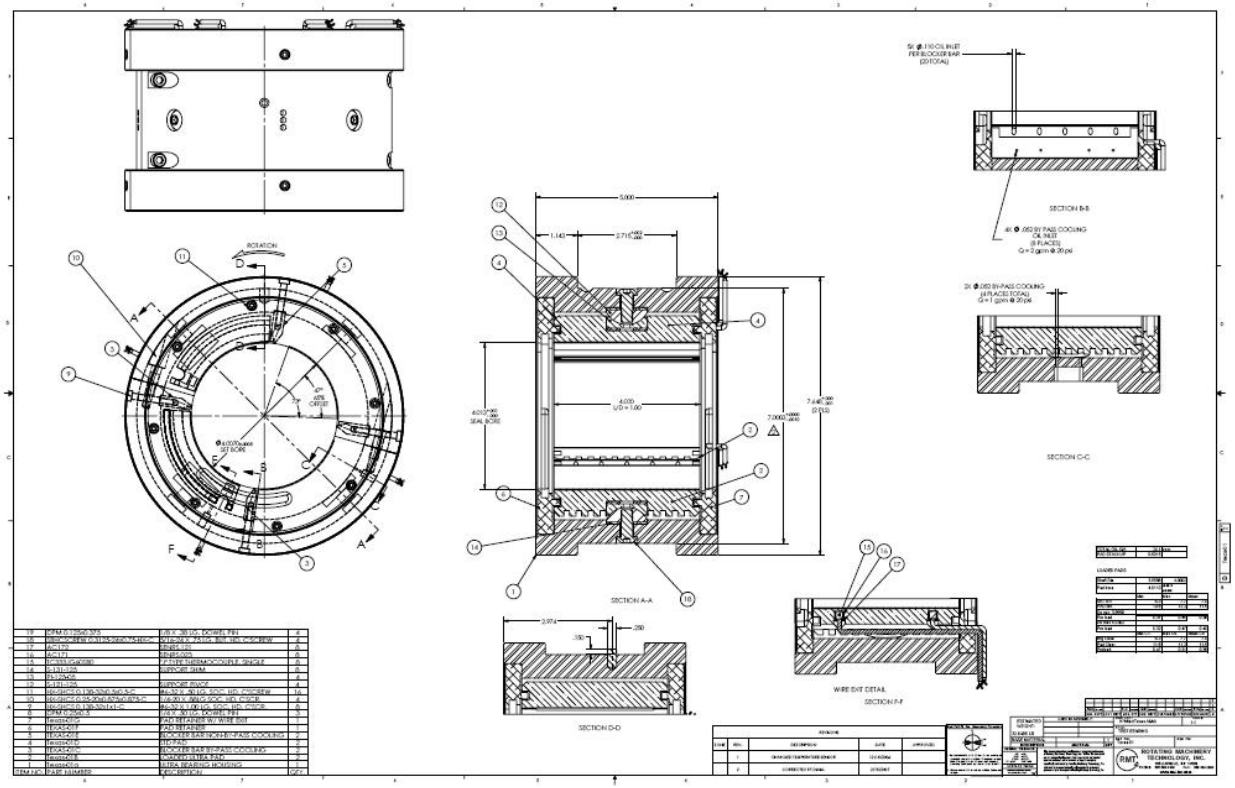

Fig. 52 Engineering drawing of the bearing

Table 9 Load versus deflection data from pad support structure stiffness measurement

W [kN]	δ [μm]
0	0
2.46	8.4
5.12	15.6
7.59	22.4
10.15	28.9
12.59	35.4
13.78	39.2

Table 10 Raw static operating data

N [rpm]	F_s (target) [kN]	F_s (actual) [kN]	Q [L/s]	P_{in} [kPa]	T_{in} [°C]	T_{out} [°C]
4,000	0	0.14	1.01	93.9	43.6	48.0
4,000	3.56	3.59	1.02	96.4	43.1	47.5
4,000	7.12	7.19	1.01	97.1	39.5	44.2
4,000	10.68	10.65	1.01	102.6	38.9	43.8
4,000	14.23	14.22	1.01	100.7	39.1	44.3
4,000	17.79	17.85	1.02	102.5	39.4	44.4
4,000	19.57	19.65	1.02	99.7	43.8	48.6
6,000	0	0.08	1.02	95.8	39.3	45.4
6,000	3.56	3.56	1.01	96.9	39.1	45.1
6,000	7.12	7.09	1.02	97.2	39.4	45.4
6,000	10.68	10.74	1.02	97.3	43.4	49.5
6,000	14.23	14.20	1.02	95.8	41.3	47.7
6,000	17.79	17.79	1.02	97.4	39.6	46.4
6,000	19.57	19.66	1.02	102.0	39.1	45.8
8,000	0	0.12	1.01	95.4	39.4	47.9
8,000	3.56	3.61	1.01	98.5	39.8	48.1
8,000	7.12	7.09	1.01	94.7	39.8	48.4
8,000	10.68	10.71	1.01	101.0	40.1	49.1
8,000	14.23	14.13	1.02	94.5	41.3	50.1
8,000	17.79	17.78	1.02	98.9	40.8	49.8
8,000	19.57	19.33	1.01	96.9	39.6	48.9
10,000	0	0.05	1.01	98.1	38.8	50.0
10,000	3.56	3.61	1.01	99.3	40.3	51.2
10,000	7.12	7.16	1.02	99.4	39.9	50.9
10,000	10.68	10.73	1.01	99.2	39.4	50.7
10,000	14.23	14.20	1.02	100.3	39.4	50.6
10,000	17.79	17.72	1.01	95.1	39.3	50.8
10,000	19.57	19.21	1.01	94.9	39.3	51.2
12,000	0	0.12	1.02	92.1	43.4	58.1
12,000	3.56	3.56	1.02	90.8	42.3	56.4
12,000	7.12	7.18	1.02	101.4	42.4	56.7
12,000	10.68	10.75	1.02	96.6	42.1	56.6
12,000	14.23	14.32	1.02	92.7	41.9	56.4
12,000	17.79	17.78	1.02	95.3	41.7	56.3
12,000	19.57	19.60	1.02	99.8	41.6	56.2

Table 11 Journal position and power loss data

		Experiment				Theory			
N [rpm]	P [kPa]	e_x [μm]	e_y [μm]	φ [degrees]	P [kW]	e_x [μm]	e_y [μm]	φ [degrees]	P [kW]
4,000	0	6.97	18.82	20.3	7.5	0.00	0.01	15.9	3.6
4,000	345	12.42	35.81	19.1	7.6	0.11	4.90	1.3	3.6
4,000	689	14.66	48.06	17.0	8.0	0.21	9.75	1.2	3.6
4,000	1034	16.73	64.24	14.6	8.3	0.32	14.47	1.3	3.7
4,000	1379	19.48	77.66	14.1	8.9	0.42	18.89	1.3	3.7
4,000	1724	20.59	89.43	13.0	8.6	0.51	22.97	1.3	3.8
4,000	1896	23.41	96.70	13.6	8.2	0.56	24.94	1.3	3.8
6,000	0	5.64	9.76	30.0	10.4	0.00	0.00	-71.6	7.5
6,000	345	8.05	23.61	18.8	10.2	0.09	3.55	1.5	7.5
6,000	689	14.31	39.19	20.1	10.2	0.19	7.18	1.5	7.5
6,000	1034	18.55	59.43	17.3	10.4	0.29	10.86	1.5	7.6
6,000	1379	21.39	69.81	17.0	11.0	0.38	14.40	1.5	7.6
6,000	1724	22.94	80.81	15.8	11.6	0.47	17.79	1.5	7.7
6,000	1896	20.59	85.06	13.6	11.4	0.51	19.41	1.5	7.7
8,000	0	6.24	14.26	23.6	14.3	0.00	0.00	-56.3	12.5
8,000	345	8.11	25.92	17.4	13.9	0.08	2.92	1.6	12.5
8,000	689	11.09	37.86	16.3	14.5	0.17	5.88	1.6	12.6
8,000	1034	15.52	53.69	16.1	15.2	0.29	10.86	1.5	12.6
8,000	1379	16.79	64.06	14.7	15.0	0.33	11.91	1.6	12.6
8,000	1724	20.23	77.91	14.6	15.3	0.42	14.90	1.6	12.7
8,000	1896	19.06	80.23	13.4	15.7	0.46	16.30	1.6	12.7
10,000	0	7.44	9.36	38.5	19.0	0.00	0.00	26.6	18.5
10,000	345	12.15	22.22	28.7	18.6	0.07	2.52	1.6	18.5
10,000	689	12.16	33.64	19.9	18.8	0.15	5.08	1.7	18.5
10,000	1034	14.80	44.14	18.5	19.1	0.22	7.68	1.7	18.6
10,000	1379	17.59	56.25	17.4	19.1	0.28	10.32	1.6	18.6
10,000	1724	17.46	69.41	14.1	19.7	0.37	12.96	1.6	18.6
10,000	1896	18.59	75.45	13.8	20.2	0.42	14.26	1.7	18.6
12,000	0	-4.37	31.68	-7.9	25.2	0.00	0.00	-45.0	25.3
12,000	345	4.04	37.01	6.2	24.2	0.06	2.30	1.6	25.4
12,000	689	5.23	48.15	6.2	24.6	0.13	4.66	1.6	25.4
12,000	1034	9.02	59.48	8.6	24.9	0.20	7.05	1.6	25.4
12,000	1379	11.14	71.87	8.8	25.0	0.26	9.48	1.6	25.4
12,000	1724	13.77	84.38	9.3	25.2	0.32	11.94	1.5	25.4
12,000	1896	13.20	92.89	8.1	25.2	0.36	13.19	1.6	25.5

Table 12 Trailing-edge pad temperatures and temperature rise data

		Exp. Trailing-Edge Pad Temp. [°C]				Exp. Temperature Rise [°C]				Theory	
N	P	Pivot Number (Circumferential Location)				Pivot Number (Circumferential Location)				T_{max}	ΔT_{max}
[rpm]	[kPa]	1 (65.55°)	2 (155.55°)	3 (245.55°)	4 (335.55°)	1 (65.55°)	2 (155.55°)	3 (245.55°)	4 (335.55°)	[°C]	[°C]
4,000	0	54.8	51.1	53.4	50.0	11.2	7.5	9.8	6.4	53.4	10.6
4,000	345	53.2	49.5	54.2	51.0	10.1	6.5	11.2	7.9	55.0	12.1
4,000	689	48.6	45.3	52.2	49.0	9.1	5.8	12.7	9.5	56.7	13.9
4,000	1034	46.9	44.3	52.7	50.0	8.1	5.4	13.9	11.1	58.7	15.9
4,000	1379	46.3	44.3	54.1	51.7	7.2	5.2	15.0	12.6	60.9	18.0
4,000	1724	45.6	44.2	54.8	53.0	6.3	4.8	15.4	13.6	63.1	20.3
4,000	1896	49.5	48.3	58.9	57.4	5.7	4.5	15.1	13.6	64.3	21.5
6,000	0	55.8	50.8	53.6	48.3	16.4	11.5	14.3	8.9	57.6	14.8
6,000	345	53.3	49.0	54.5	49.1	14.3	9.9	15.5	10.0	59.1	16.2
6,000	689	51.8	48.0	55.9	50.7	12.4	8.7	16.5	11.3	60.7	17.9
6,000	1034	54.5	51.8	60.4	56.5	11.1	8.4	16.9	13.0	62.5	19.6
6,000	1379	50.9	48.7	59.3	55.7	9.6	7.4	18.1	14.4	64.4	21.6
6,000	1724	48.8	46.8	59.7	56.4	9.2	7.2	20.1	16.7	66.5	23.6
6,000	1896	47.7	45.9	59.7	56.5	8.6	6.8	20.6	17.4	67.5	24.7
8,000	0	59.2	54.4	57.2	50.2	19.7	14.9	17.7	10.7	61.4	18.5
8,000	345	57.3	53.0	58.5	51.6	17.4	13.1	18.7	11.8	62.8	19.9
8,000	689	55.8	52.1	59.9	53.4	15.9	12.3	20.0	13.6	64.3	21.5
8,000	1034	54.7	51.7	61.3	55.5	14.6	11.6	21.1	15.4	66.0	23.1
8,000	1379	54.5	52.0	63.0	58.1	13.2	10.7	21.7	16.7	67.8	24.9
8,000	1724	53.1	51.1	63.8	59.8	12.3	10.3	22.9	19.0	69.7	26.8
8,000	1896	52.1	50.0	64.1	60.0	12.4	10.4	24.4	20.3	70.6	27.8
10,000	0	63.3	58.4	59.8	51.8	24.6	19.6	21.0	13.0	64.7	21.9
10,000	345	61.9	58.0	61.8	54.1	21.6	17.7	21.5	13.7	66.1	23.3
10,000	689	60.2	56.5	62.8	55.2	20.3	16.6	23.0	15.3	67.6	24.8
10,000	1034	58.6	55.1	63.8	56.6	19.2	15.7	24.3	17.1	69.2	26.4
10,000	1379	57.2	54.1	64.7	58.1	17.8	14.8	25.3	18.7	70.9	28.1
10,000	1724	56.2	53.6	66.3	60.3	16.9	14.3	27.0	21.0	72.7	29.8
10,000	1896	56.0	53.6	67.3	61.7	16.7	14.3	28.0	22.4	73.6	30.8
12,000	0	70.0	66.6	66.1	58.0	26.6	23.1	22.6	14.6	67.8	25.0
12,000	345	66.7	63.1	65.5	57.5	24.5	20.8	23.2	15.2	69.2	26.3
12,000	689	65.8	62.2	67.1	59.2	23.4	19.8	24.7	16.8	70.6	27.8
12,000	1034	64.4	60.8	67.8	60.5	22.3	18.7	25.7	18.4	72.2	29.3
12,000	1379	63.1	59.6	68.8	62.1	21.2	17.7	26.9	20.2	73.8	30.9
12,000	1724	61.6	58.4	70.3	63.9	19.9	16.7	28.6	22.2	75.5	32.6
12,000	1896	60.8	57.9	71.0	64.9	19.2	16.4	29.4	23.4	76.3	33.5

Table 13 Experimental dynamic-stiffness coefficients and uncertainties at N = 4,000 rpm, P = 0

N = 4,000 rpm P = 0		Experimental Dynamic-Stiffnesses								Uncertainties							
f	f/N	Re(H_{xx})	Re(H_{yy})	Re(H_{xy})	Re(H_{yx})	Im(H_{xx})	Im(H_{yy})	Im(H_{xy})	Im(H_{yx})	Re(H_{xx})	Re(H_{yy})	Re(H_{xy})	Re(H_{yx})	Im(H_{xx})	Im(H_{yy})	Im(H_{xy})	Im(H_{yx})
[Hz]	[Hz/Hz]	[MN/m]								[MN/m]							
20	0.30	257.20	234.91	-101.38	-68.42	65.3	-23.5	-25.69	165.97	25.60	23.79	5.24	27.91	29.9	51.7	5.68	172.75
30	0.45	258.87	155.70	-107.31	174.68	78.8	-98.2	-28.36	412.48	29.41	66.65	21.41	205.15	23.7	193.1	13.29	573.79
40	0.60	257.93	191.32	-108.32	43.06	93.6	-2.5	-23.79	68.72	22.21	42.47	40.69	82.84	44.9	99.4	15.95	37.82
50	0.75	256.46	341.28	-105.13	-296.12	125.3	88.4	-37.78	-38.51	36.28	153.93	22.76	258.17	51.5	102.3	21.75	159.86
60	0.90	227.04	183.68	-128.90	66.00	132.6	111.9	-15.10	-94.65	127.55	61.79	99.18	99.88	241.7	47.8	154.83	37.20
70	1.05	194.56	88.51	-29.60	9.38	96.9	15.3	276.96	-190.99	170.19	180.06	120.46	119.35	188.7	176.3	278.42	240.96
80	1.20	241.20	248.51	-94.91	-59.91	191.7	131.3	-86.34	23.15	100.81	196.02	127.17	17.02	61.7	149.6	191.28	25.52
90	1.35	270.53	236.97	-108.44	-140.24	187.8	120.4	-46.37	11.42	25.62	49.98	58.08	153.60	48.6	58.2	26.22	39.37
100	1.50	254.13	237.00	-105.62	-43.89	185.1	206.5	-47.78	-196.54	25.31	48.89	11.58	47.92	33.9	62.3	5.57	126.48
110	1.65	264.77	212.36	-113.57	-13.17	223.2	183.4	-45.32	-10.25	21.42	10.31	28.82	12.38	42.0	37.5	20.55	36.82
120	1.80	271.57	211.93	-112.28	85.78	232.2	245.6	-35.53	-173.02	106.19	106.81	59.39	110.62	115.5	32.2	47.57	126.45
130	1.95	210.62	246.38	-74.81	-8.77	138.4	144.3	20.66	7.40	368.65	294.22	384.35	333.09	171.5	562.5	595.63	165.42
140	2.10	209.03	143.91	41.60	36.90	163.2	141.8	69.44	-61.25	270.01	376.93	539.33	138.85	486.8	544.9	407.78	573.72
150	2.25	253.10	266.60	-143.12	-38.85	323.8	319.2	-96.96	-102.36	33.45	90.50	119.27	29.43	155.0	162.0	196.42	134.78
160	2.40	246.51	267.92	-116.61	-80.66	296.7	185.6	-36.17	27.92	13.86	92.48	67.53	37.08	47.5	39.1	45.58	43.08
170	2.55	269.40	288.29	-129.61	-41.89	302.4	266.3	-26.75	-50.29	20.65	37.79	25.21	43.44	20.9	88.5	98.48	25.82
180	2.70	279.08	308.99	-134.87	-25.04	336.6	360.6	-38.99	-158.07	25.96	51.84	29.61	100.70	71.9	159.3	106.68	111.54
190	2.85	270.84	313.32	-147.36	-51.74	332.6	380.5	-67.02	-90.46	35.07	189.12	141.48	18.45	42.6	145.5	142.10	28.33
200	3.00	234.43	274.44	-109.90	-2.50	358.0	325.2	-30.88	54.77	243.28	39.65	170.76	107.85	142.5	168.7	130.40	263.19
210	3.15	305.50	326.61	-137.83	-28.80	408.1	351.4	14.97	-35.12	346.53	223.15	267.39	224.89	270.7	164.8	254.20	251.33
220	3.30	271.64	321.79	-127.03	-34.61	349.4	353.2	-1.69	-36.09	33.29	36.55	35.30	23.30	64.9	41.6	19.54	12.61
230	3.45	274.01	364.11	-118.86	-35.60	337.2	327.8	-5.65	-73.67	17.61	36.38	8.96	17.80	40.9	35.1	37.21	12.73
240	3.60	273.40	332.53	-131.50	-42.95	343.4	333.8	1.00	1.68	24.41	25.57	39.38	11.77	44.6	40.5	25.80	15.53
250	3.75	267.53	357.86	-131.23	-24.34	352.9	352.5	19.31	6.14	24.10	59.11	49.16	11.23	35.8	84.0	108.39	26.49
260	3.90	203.05	280.25	-136.46	-88.66	287.7	294.5	-56.57	1.40	168.78	229.49	161.43	273.95	85.9	201.8	115.64	164.89

Editor's note: Subsequent to publication, the author has noted the experimental dynamic-stiffness data, which are the basis for the rotordynamic coefficients, to be unreliable. To the author's knowledge, all static data (both experimental and theoretical) and the theoretical dynamic data are valid. Please reference the Texas A&M University Master's thesis of David M. Coghlan (Static, Rotordynamic, and Thermal Characteristics of a Four Pad Spherical-Seat Tilting Pad Journal Bearing with Four Methods of Directed Lubrication) for valid dynamic data for a spherical-seat tilting pad journal bearing. (2014)

Table 14 Experimental dynamic-stiffness coefficients and uncertainties at N = 4,000 rpm, P = 689 kPa (100 psi)

N = 4,000 rpm P = 689 kPa		Experimental Dynamic-Stiffnesses								Uncertainties							
f	f/N	Re(H_{xx})	Re(H_{yy})	Re(H_{xy})	Re(H_{yx})	Im(H_{xx})	Im(H_{yy})	Im(H_{xy})	Im(H_{yx})	Re(H_{xx})	Re(H_{yy})	Re(H_{xy})	Re(H_{yx})	Im(H_{xx})	Im(H_{yy})	Im(H_{xy})	Im(H_{yx})
[Hz]	[Hz/Hz]	[MN/m]								[MN/m]							
20	0.30	270.00	257.58	-104.30	-43.81	50.8	34.7	-15.04	-16.15	9.95	8.21	5.83	7.29	21.7	5.2	10.21	8.00
30	0.45	272.77	259.57	-105.59	-45.23	68.4	54.1	-17.82	-23.80	17.51	4.68	10.05	15.54	9.4	4.0	5.86	7.96
40	0.60	276.05	253.44	-103.09	-32.84	91.1	32.9	-16.32	-4.97	7.67	19.22	19.88	13.97	23.1	32.1	44.36	11.81
50	0.75	287.20	251.75	-116.00	-36.04	111.7	73.9	-23.99	-3.12	21.73	19.30	19.12	25.59	39.1	17.8	25.14	26.99
60	0.90	286.29	242.55	-117.76	-26.63	101.7	84.0	-11.90	-17.92	91.05	35.31	68.19	51.46	117.0	33.7	124.09	40.38
70	1.05	318.57	5.90	-302.41	-73.97	215.0	-117.6	331.63	-14.15	383.08	189.73	622.70	426.20	512.8	485.9	326.56	211.36
80	1.20	292.48	214.65	-122.44	-17.85	164.8	105.3	-29.22	-7.54	50.76	17.25	48.93	30.59	49.6	70.5	66.39	52.35
90	1.35	295.74	248.57	-119.93	-35.24	190.4	142.1	-51.97	-20.97	30.42	34.39	34.97	39.13	35.4	20.4	33.26	38.81
100	1.50	295.84	244.16	-115.71	-36.63	208.5	164.2	-53.97	-39.28	41.20	17.17	20.91	29.20	29.8	8.0	28.19	31.43
110	1.65	296.08	248.10	-118.59	-39.09	225.5	203.4	-56.50	-43.67	33.39	11.93	14.51	28.43	24.1	12.5	25.63	23.73
120	1.80	296.32	253.03	-133.19	-48.55	282.7	230.4	-81.21	-66.38	73.40	78.55	113.56	119.21	119.0	45.7	101.03	75.01
130	1.95	254.44	197.45	-60.05	-24.30	267.6	188.0	-37.48	-35.81	126.36	129.90	213.48	90.35	152.6	81.5	108.95	109.25
140	2.10	199.71	116.14	94.31	41.10	191.9	208.9	-9.09	22.91	348.71	227.01	301.84	271.63	435.4	347.3	369.84	381.33
150	2.25	318.94	256.44	-113.34	-37.61	288.5	251.0	-18.75	-60.40	121.29	66.05	90.68	94.61	64.1	63.5	49.95	34.77
160	2.40	319.96	261.84	-151.91	-39.89	324.1	289.9	-79.32	-65.53	132.75	109.50	145.79	87.16	55.6	84.2	76.90	68.41
170	2.55	291.24	300.63	-113.66	-36.11	347.4	278.1	-83.27	-75.34	52.17	31.24	38.62	41.15	85.4	84.7	76.42	62.97
180	2.70	295.54	308.61	-111.88	-49.44	341.2	295.4	-54.80	-64.36	74.92	67.15	53.78	79.17	81.9	70.7	60.03	84.74
190	2.85	296.72	295.61	-105.89	-37.30	362.3	328.9	-44.51	-86.68	51.80	115.82	24.99	73.29	89.0	67.9	89.66	55.95
200	3.00	365.13	347.87	-145.44	-82.18	373.5	300.5	-13.44	-85.00	256.69	171.93	197.27	100.14	214.6	116.8	142.99	257.53
210	3.15	290.27	342.26	-53.28	-0.99	423.1	303.5	38.88	-66.71	456.14	495.64	307.19	531.80	518.3	359.2	614.34	323.57
220	3.30	300.27	264.02	-117.35	-29.16	404.3	339.5	-35.33	-65.29	52.42	36.22	32.19	62.38	92.5	37.1	67.17	65.90
230	3.45	303.23	314.61	-104.21	-56.60	369.7	362.2	-15.83	-73.76	27.41	20.08	20.09	33.40	36.6	50.3	21.61	34.95
240	3.60	302.93	321.54	-105.84	-57.72	385.9	343.1	-43.57	-43.37	25.64	21.28	31.24	27.56	28.7	43.2	32.82	23.35
250	3.75	322.64	323.03	-109.09	-50.06	391.6	345.9	-30.91	-56.10	11.88	26.02	21.22	16.03	22.7	76.0	32.93	18.26
260	3.90	288.82	324.87	-99.29	-69.08	411.9	337.0	-34.73	-28.34	30.52	62.07	14.30	36.16	57.2	62.4	78.14	40.69

Editor's note: Subsequent to publication, the author has noted the experimental dynamic-stiffness data, which are the basis for the rotordynamic coefficients, to be unreliable. To the author's knowledge, all static data (both experimental and theoretical) and the theoretical dynamic data are valid. Please reference the Texas A&M University Master's thesis of David M. Coghlan (Static, Rotordynamic, and Thermal Characteristics of a Four Pad Spherical-Seat Tilting Pad Journal Bearing with Four Methods of Directed Lubrication) for valid dynamic data for a spherical-seat tilting pad journal bearing. (2014)

Table 15 Experimental dynamic-stiffness coefficients and uncertainties at N = 4,000 rpm, P = 1379 kPa (200 psi)

N = 4,000 rpm P = 1379 kPa		Experimental Dynamic-Stiffnesses								Uncertainties							
f	f/N	Re(H_{xx})	Re(H_{yy})	Re(H_{xy})	Re(H_{yx})	Im(H_{xx})	Im(H_{yy})	Im(H_{xy})	Im(H_{yx})	Re(H_{xx})	Re(H_{yy})	Re(H_{xy})	Re(H_{yx})	Im(H_{xx})	Im(H_{yy})	Im(H_{xy})	Im(H_{yx})
[Hz]	[Hz/Hz]	[MN/m]								[MN/m]							
20	0.30	322.84	313.89	-104.08	-41.87	50.2	33.1	-14.24	-5.83	21.43	17.19	18.11	15.24	38.1	18.4	5.24	37.36
30	0.45	331.01	313.54	-107.16	-40.28	72.6	60.6	-16.07	-21.61	38.38	23.35	24.27	41.04	12.1	9.3	10.53	12.56
40	0.60	323.27	326.43	-96.45	-42.90	96.1	31.4	-16.35	-4.42	8.45	67.30	24.95	28.65	55.0	54.8	117.21	39.17
50	0.75	335.01	311.71	-108.44	-25.07	110.8	95.3	-23.91	-15.64	53.71	25.79	40.72	10.86	66.2	30.4	37.14	59.72
60	0.90	339.72	293.55	-90.39	-21.45	110.3	92.2	4.23	0.16	212.08	143.61	148.03	103.39	194.3	106.0	192.45	129.89
70	1.05	386.33	-89.12	-52.83	47.43	57.9	54.7	449.06	35.50	421.56	464.92	328.62	174.67	247.8	199.3	549.77	353.47
80	1.20	339.13	285.09	-147.44	-21.93	172.6	118.0	-47.45	-2.02	50.18	222.61	169.01	57.22	90.6	127.3	274.07	109.74
90	1.35	340.86	328.83	-108.00	-32.33	235.8	173.7	-57.71	-47.61	69.17	69.73	94.87	20.28	102.9	93.6	29.43	103.95
100	1.50	336.74	309.20	-108.17	-28.37	237.5	189.3	-58.93	-39.44	33.43	15.20	55.51	29.86	75.1	65.8	22.59	94.88
110	1.65	345.04	334.27	-116.34	-28.75	239.6	216.8	-47.95	-49.27	26.24	63.94	63.89	30.76	51.9	54.9	9.05	49.45
120	1.80	314.93	333.06	-108.74	-14.19	260.7	263.7	-64.46	-30.05	142.25	73.01	80.31	135.16	107.3	85.8	35.20	127.56
130	1.95	362.06	174.76	38.29	-41.38	246.4	225.9	-81.51	-18.46	265.32	316.38	499.90	213.74	347.8	259.6	354.41	228.79
140	2.10	203.67	7.06	301.88	112.22	357.4	99.4	85.07	-101.42	403.09	1002.68	1204.89	510.94	1081.4	626.0	527.52	911.60
150	2.25	333.71	286.27	-50.20	-13.96	295.4	294.1	-41.30	-38.32	33.37	117.62	100.52	16.77	130.2	116.1	143.30	85.93
160	2.40	348.32	328.72	-147.83	-31.31	302.1	290.3	-76.34	-28.39	87.36	115.76	32.93	52.92	91.5	133.9	152.06	56.15
170	2.55	355.89	388.97	-99.63	-41.82	351.9	297.5	-73.70	-53.78	25.59	69.90	68.31	10.45	100.0	124.7	25.42	62.32
180	2.70	350.04	377.72	-96.08	-37.14	345.1	303.4	-47.14	-57.62	63.08	63.43	69.51	61.04	61.5	152.0	121.26	90.66
190	2.85	365.03	350.72	-90.51	-35.80	337.7	391.0	-49.62	-66.45	70.84	161.93	100.05	18.88	66.7	118.9	127.90	25.38
200	3.00	313.69	379.24	-89.17	-26.58	358.7	278.3	-24.08	-3.12	176.26	60.85	175.17	101.57	158.0	208.7	105.49	172.59
210	3.15	274.78	385.23	-23.65	-70.54	327.3	321.1	8.23	18.16	176.49	215.48	331.63	232.78	204.6	303.0	162.87	153.51
220	3.30	377.75	352.49	-95.25	-33.21	374.4	339.1	-25.81	-72.97	53.97	41.91	16.61	68.16	109.4	60.9	116.58	74.54
230	3.45	359.52	384.65	-84.58	-32.71	392.8	379.7	-45.18	-51.15	27.29	81.06	25.18	34.49	51.0	43.3	17.85	37.18
240	3.60	366.13	393.27	-88.79	-28.98	388.1	359.3	-55.88	-58.35	44.23	28.44	38.13	27.97	29.8	77.3	17.11	30.43
250	3.75	360.30	398.27	-86.96	-46.01	380.4	338.7	-53.45	-55.50	18.40	65.44	33.22	18.66	16.7	71.9	46.03	24.84
260	3.90	359.72	409.76	-75.32	-26.37	384.0	377.1	-49.87	-46.20	44.91	90.43	44.78	48.86	52.6	88.1	22.89	54.07

Editor's note: Subsequent to publication, the author has noted the experimental dynamic-stiffness data, which are the basis for the rotordynamic coefficients, to be unreliable. To the author's knowledge, all static data (both experimental and theoretical) and the theoretical dynamic data are valid. Please reference the Texas A&M University Master's thesis of David M. Coghlan (Static, Rotordynamic, and Thermal Characteristics of a Four Pad Spherical-Seat Tilting Pad Journal Bearing with Four Methods of Directed Lubrication) for valid dynamic data for a spherical-seat tilting pad journal bearing. (2014)

Table 16 Experimental dynamic-stiffness coefficients and uncertainties at N = 4,000 rpm, P = 1896 kPa (275 psi)

N = 4,000 rpm P = 1896 kPa		Experimental Dynamic-Stiffnesses								Uncertainties							
f	f/N	Re(H_{xx})	Re(H_{yy})	Re(H_{xy})	Re(H_{yx})	Im(H_{xx})	Im(H_{yy})	Im(H_{xy})	Im(H_{yx})	Re(H_{xx})	Re(H_{yy})	Re(H_{xy})	Re(H_{yx})	Im(H_{xx})	Im(H_{yy})	Im(H_{xy})	Im(H_{yx})
[Hz]	[Hz/Hz]	[MN/m]								[MN/m]							
20	0.30	361.06	413.55	-70.54	-26.89	62.2	34.8	-8.58	-6.79	43.97	40.26	31.26	42.37	41.1	28.8	23.97	71.30
30	0.45	364.63	413.80	-74.02	-25.32	70.7	64.1	-10.55	-29.18	77.21	45.08	40.90	73.15	42.2	23.3	27.14	37.58
40	0.60	369.15	421.75	-67.30	-29.45	94.4	18.0	27.06	-7.10	44.17	195.85	210.57	79.48	37.9	298.4	178.86	71.34
50	0.75	365.05	400.32	-73.23	14.89	108.3	100.9	-17.26	-25.10	127.48	99.19	78.38	171.56	216.3	59.4	66.37	138.43
60	0.90	314.50	198.20	15.83	51.04	-21.6	106.8	244.58	-107.21	422.03	556.20	801.34	587.35	819.2	731.1	288.22	555.13
70	1.05	357.15	56.05	37.79	53.17	61.9	87.0	372.53	-52.89	45.78	377.43	819.25	272.96	342.3	578.4	427.98	51.30
80	1.20	415.60	364.45	-114.56	-17.58	194.7	110.2	-15.97	-3.69	143.49	264.34	419.64	127.29	130.6	268.3	341.27	80.01
90	1.35	410.03	444.86	-87.69	-34.04	204.7	197.7	-80.44	-35.53	254.09	296.64	210.01	139.34	84.4	169.2	372.18	27.74
100	1.50	387.88	411.29	-67.55	-17.34	243.8	207.0	-71.98	-27.32	172.19	196.91	45.28	146.92	174.4	67.0	271.35	44.95
110	1.65	409.90	451.79	-102.51	-32.14	263.0	251.7	-44.55	-79.53	171.74	389.52	417.41	184.66	240.8	248.7	204.57	210.75
120	1.80	294.26	245.75	154.74	56.45	44.3	363.2	-109.72	176.11	711.37	861.56	862.51	879.98	432.9	808.8	647.56	468.84
130	1.95	400.45	-375.95	691.66	-51.51	339.4	-17.6	77.73	-150.89	823.38	3153.72	3209.43	638.38	1660.9	1627.6	1533.14	1733.72
140	2.10	394.67	406.46	12.01	-4.67	304.7	248.0	-21.38	-80.60	138.16	197.19	169.65	149.32	146.2	243.3	256.42	183.67
150	2.25	384.06	415.11	-36.89	-6.23	268.0	255.5	-38.77	-42.73	43.78	94.01	47.82	87.04	56.0	82.0	83.28	157.52
160	2.40	396.66	418.48	-63.69	-18.28	289.0	296.6	-108.41	-33.34	103.33	51.26	64.56	113.64	61.0	44.3	218.45	55.76
170	2.55	395.05	480.79	-39.98	-47.47	336.5	284.2	-91.51	-64.80	75.90	206.73	235.29	167.60	49.4	38.8	60.12	138.10
180	2.70	398.57	443.36	14.68	-16.29	354.9	270.0	-83.50	-53.61	151.95	106.87	176.72	226.49	194.0	164.7	48.84	214.48
190	2.85	372.61	130.97	89.34	34.79	411.5	299.7	-332.70	-43.54	209.51	689.39	538.78	448.79	384.8	786.9	819.18	246.48
200	3.00	417.87	478.99	-57.17	-21.39	357.4	295.0	-40.41	-76.24	103.92	96.28	83.84	104.24	137.6	84.4	37.84	162.78
210	3.15	386.16	455.82	-54.06	-19.13	358.3	353.2	-53.88	-63.70	82.53	95.46	77.52	91.96	50.2	62.9	67.57	50.68
220	3.30	396.91	454.78	-50.98	-21.50	354.4	344.6	-48.54	-53.95	72.25	24.70	47.93	61.41	86.7	78.8	61.87	60.55
230	3.45	404.64	484.65	-47.75	-15.96	372.6	398.3	-55.73	-56.17	64.89	125.25	30.01	70.52	82.8	65.5	51.02	60.19
240	3.60	400.33	498.74	-59.10	-30.33	367.4	409.0	-48.54	-73.16	144.82	107.59	38.17	194.53	46.0	181.8	37.00	134.13
250	3.75	492.22	1792.55	1487.15	-2.49	28.4	-1158.5	-1263.46	-422.34	1017.95	8225.88	9502.14	640.71	2324.7	7514.1	5966.08	2460.62
260	3.90	401.09	512.21	-42.98	-12.93	369.2	374.5	-44.54	-57.03	51.41	108.87	69.45	93.28	54.5	100.0	66.35	30.14

Editor's note: Subsequent to publication, the author has noted the experimental dynamic-stiffness data, which are the basis for the rotordynamic coefficients, to be unreliable. To the author's knowledge, all static data (both experimental and theoretical) and the theoretical dynamic data are valid. Please reference the Texas A&M University Master's thesis of David M. Coghlan (Static, Rotordynamic, and Thermal Characteristics of a Four Pad Spherical-Seat Tilting Pad Journal Bearing with Four Methods of Directed Lubrication) for valid dynamic data for a spherical-seat tilting pad journal bearing. (2014)

Table 17 Experimental dynamic-stiffness coefficients and uncertainties at N = 6,000 rpm, P = 0

N = 6,000 rpm P = 0		Experimental Dynamic-Stiffnesses								Uncertainties							
f	f/N	Re(H_{xx})	Re(H_{yy})	Re(H_{xy})	Re(H_{yx})	Im(H_{xx})	Im(H_{yy})	Im(H_{xy})	Im(H_{yx})	Re(H_{xx})	Re(H_{yy})	Re(H_{xy})	Re(H_{yx})	Im(H_{xx})	Im(H_{yy})	Im(H_{xy})	Im(H_{yx})
[Hz]	[Hz/Hz]	[MN/m]								[MN/m]							
20	0.20	308.37	282.76	-101.51	-62.82	78.9	-19.3	-27.47	184.69	20.78	15.19	11.54	17.02	24.2	125.8	9.89	427.09
30	0.30	319.93	192.12	-110.22	232.81	68.3	-97.9	-23.14	452.12	48.09	253.52	22.23	704.13	17.4	446.3	9.19	1402.99
40	0.40	325.99	254.03	-117.93	50.65	111.7	27.2	-26.55	91.76	9.57	23.05	25.60	199.14	33.3	38.5	51.36	244.36
50	0.50	318.96	395.39	-112.69	-77.21	122.4	54.6	-37.61	22.48	22.06	287.05	26.98	32.97	45.2	31.9	25.10	24.76
60	0.60	320.64	245.62	-119.34	-29.06	104.5	105.5	-8.59	-68.33	123.03	88.31	99.40	14.35	69.1	28.7	50.83	33.61
70	0.70	317.44	261.18	-112.92	-78.97	170.5	143.6	-25.77	-200.59	77.69	106.16	135.76	20.92	49.7	178.6	104.16	557.37
80	0.80	315.81	264.67	-95.04	-47.11	180.8	129.3	-54.52	116.02	90.67	236.72	123.30	38.55	51.5	135.9	156.12	414.68
90	0.90	352.22	224.16	-102.29	-137.61	157.0	118.6	7.98	-9.76	163.89	181.76	257.30	480.52	219.8	257.5	141.72	30.54
100	1.00	-21.93	506.76	-304.60	-74.37	393.2	77.8	-105.42	-471.48	615.37	1299.88	1580.51	1380.20	1871.4	873.9	1022.65	957.69
110	1.10	364.62	270.90	-156.13	-59.98	220.3	152.8	-50.21	-25.13	150.94	206.49	113.58	106.01	104.3	127.0	212.73	48.84
120	1.20	309.00	274.67	-122.35	-16.28	208.8	255.8	-46.37	-198.18	110.25	50.77	77.05	54.57	52.5	145.5	100.54	297.02
130	1.30	304.27	277.85	-111.78	-47.81	265.2	210.1	-95.49	-93.65	49.74	108.89	105.83	42.30	94.8	132.2	123.43	200.97
140	1.40	312.09	290.60	-130.60	-25.96	257.6	240.3	-35.88	-180.48	49.52	53.23	43.06	38.74	39.0	26.2	56.31	248.93
150	1.50	316.87	292.35	-134.74	-58.75	263.0	228.4	-36.85	-39.57	36.47	57.85	39.77	30.62	46.9	54.5	54.19	56.03
160	1.60	324.92	295.71	-108.40	-44.46	296.3	179.2	-52.73	99.50	39.94	57.27	79.29	50.11	54.5	113.5	35.45	243.22
170	1.70	320.22	305.75	-117.82	-25.40	315.9	253.3	-23.28	-53.04	29.93	73.49	141.41	51.37	62.8	53.0	31.10	20.00
180	1.80	298.49	337.75	-113.61	28.71	293.1	286.5	-21.36	-73.37	68.19	142.35	133.47	187.96	87.7	124.2	118.94	47.25
190	1.90	228.66	117.91	147.61	35.97	388.3	160.7	102.21	-135.70	454.92	897.48	972.55	463.02	962.8	524.4	693.38	788.59
200	2.00	-159.77	138.80	136.24	213.62	107.5	354.2	-289.53	176.15	1048.95	758.40	986.69	529.04	700.8	811.9	1388.35	493.25
210	2.10	386.71	303.17	-146.85	-16.15	384.5	302.8	12.15	-35.25	79.67	124.25	197.09	72.54	142.7	84.2	156.87	32.85
220	2.20	301.71	328.37	-135.49	-8.35	344.3	313.8	2.37	-58.26	37.16	81.34	32.60	53.94	57.6	84.1	99.41	44.36
230	2.30	294.30	353.78	-116.77	-16.59	289.3	319.2	-3.30	-72.51	23.02	61.01	31.81	33.48	31.2	70.9	66.24	12.84
240	2.40	278.06	357.88	-134.13	9.65	320.6	329.6	18.28	-6.11	20.10	96.20	72.06	20.68	41.7	51.4	51.57	26.31
250	2.50	280.92	373.34	-132.99	15.70	337.0	338.7	30.36	-17.40	28.56	39.53	36.96	28.18	30.0	47.5	16.94	12.42
260	2.60	218.14	360.06	-128.94	31.05	311.1	425.6	27.45	59.23	21.37	45.87	39.19	50.97	91.9	70.8	140.52	242.84

Editor's note: Subsequent to publication, the author has noted the experimental dynamic-stiffness data, which are the basis for the rotordynamic coefficients, to be unreliable. To the author's knowledge, all static data (both experimental and theoretical) and the theoretical dynamic data are valid. Please reference the Texas A&M University Master's thesis of David M. Coghlan (Static, Rotordynamic, and Thermal Characteristics of a Four Pad Spherical-Seat Tilting Pad Journal Bearing with Four Methods of Directed Lubrication) for valid dynamic data for a spherical-seat tilting pad journal bearing. (2014)

Table 18 Experimental dynamic-stiffness coefficients and uncertainties at N = 6,000 rpm, P = 689 kPa (100 psi)

N = 6,000 rpm P = 689 kPa		Experimental Dynamic-Stiffnesses								Uncertainties							
f	f/N	Re(H_{xx})	Re(H_{yy})	Re(H_{xy})	Re(H_{yx})	Im(H_{xx})	Im(H_{yy})	Im(H_{xy})	Im(H_{yx})	Re(H_{xx})	Re(H_{yy})	Re(H_{xy})	Re(H_{yx})	Im(H_{xx})	Im(H_{yy})	Im(H_{xy})	Im(H_{yx})
[Hz]	[Hz/Hz]	[MN/m]								[MN/m]							
20	0.20	310.44	283.98	-109.51	-42.87	40.9	26.0	-14.01	-9.57	21.56	8.73	17.15	18.11	37.2	8.7	17.75	26.52
30	0.30	308.01	285.70	-110.16	-35.84	62.2	43.5	-18.65	-15.52	23.29	9.37	18.56	22.36	16.7	9.4	8.75	7.83
40	0.40	302.88	290.23	-110.97	-43.85	79.7	9.8	-22.65	-7.60	10.82	19.67	35.37	16.49	39.5	19.7	62.48	24.17
50	0.50	315.39	289.84	-114.40	-45.17	110.7	62.8	-33.93	-8.38	40.16	20.23	33.82	24.75	37.8	20.2	22.20	37.45
60	0.60	316.02	270.95	-126.57	-45.82	136.1	65.7	-31.65	-24.74	84.40	38.74	88.55	51.07	166.1	38.7	133.29	62.65
70	0.70	314.71	230.82	-136.58	-33.02	135.2	48.1	-11.74	-17.53	27.61	67.49	151.40	39.17	64.4	67.5	31.68	26.30
80	0.80	317.50	216.20	-117.49	-23.84	136.5	106.4	2.02	1.95	67.69	89.46	130.26	56.59	39.8	89.5	112.10	51.51
90	0.90	325.98	241.07	-153.78	-46.07	189.6	87.1	1.72	-18.61	202.79	108.12	190.30	71.18	144.0	108.1	142.29	165.82
100	1.00	335.78	82.67	-85.96	19.92	83.7	87.8	196.39	17.61	827.23	445.44	330.84	490.07	588.3	445.4	545.59	640.58
110	1.10	277.49	325.42	-135.19	-20.29	207.7	189.1	-111.50	-68.63	227.64	177.72	319.10	199.07	249.0	177.7	263.14	196.17
120	1.20	377.59	279.43	-152.09	-35.14	205.0	167.5	-68.04	-42.37	167.72	56.20	185.07	118.51	219.9	56.2	157.97	169.28
130	1.30	306.84	255.94	-70.09	-38.08	279.6	198.2	-79.47	-49.48	162.24	137.18	172.09	33.51	104.8	137.2	204.80	135.73
140	1.40	328.67	279.81	-119.83	-36.13	254.7	198.8	-40.34	-35.18	44.39	44.77	45.64	36.71	85.0	44.8	39.30	67.92
150	1.50	313.82	273.61	-116.83	-35.19	270.9	227.0	-51.33	-52.33	41.33	21.31	75.74	35.29	91.4	21.3	31.87	74.14
160	1.60	309.17	239.64	-117.44	-30.25	261.0	225.9	-43.29	-29.25	42.83	59.46	29.83	23.15	60.5	59.5	65.15	41.89
170	1.70	314.45	291.49	-122.52	-34.63	283.6	207.2	-49.48	-34.78	41.29	61.24	117.13	31.67	89.0	61.2	108.05	76.30
180	1.80	309.89	327.84	-129.03	-32.77	345.4	252.9	-53.76	-66.99	67.86	124.55	123.34	43.66	148.4	124.6	147.27	124.12
190	1.90	324.31	277.97	-79.49	-42.89	271.6	269.4	-9.62	-17.11	212.84	225.80	283.43	197.32	121.5	225.8	327.20	100.92
200	2.00	160.99	256.95	-73.25	81.12	206.8	242.7	-33.73	51.90	525.82	198.36	290.45	400.27	301.7	198.4	327.69	232.83
210	2.10	329.85	388.67	-219.68	-68.12	143.2	256.2	37.01	111.88	484.73	624.55	715.36	461.21	657.1	624.5	377.33	508.04
220	2.20	314.77	232.67	-113.68	-20.03	400.6	325.6	-64.52	-89.68	155.80	113.54	145.49	132.15	307.0	113.5	179.33	200.83
230	2.30	289.74	289.68	-119.44	-21.97	343.2	324.4	-31.18	-53.60	51.79	82.57	72.12	32.60	72.7	82.6	53.48	100.05
240	2.40	294.82	292.37	-117.70	-23.57	354.4	303.1	-31.66	-62.75	77.99	36.92	69.14	58.76	41.7	36.9	49.52	29.05
250	2.50	300.60	299.16	-113.51	-27.39	345.7	302.7	-22.61	-44.92	34.85	47.04	45.47	22.30	31.1	47.0	55.45	18.42
260	2.60	290.99	298.33	-107.53	-26.24	368.9	319.4	-3.84	-56.88	35.02	34.33	41.48	23.41	66.3	34.3	31.68	39.71

Editor's note: Subsequent to publication, the author has noted the experimental dynamic-stiffness data, which are the basis for the rotordynamic coefficients, to be unreliable. To the author's knowledge, all static data (both experimental and theoretical) and the theoretical dynamic data are valid. Please reference the Texas A&M University Master's thesis of David M. Coghlan (Static, Rotordynamic, and Thermal Characteristics of a Four Pad Spherical-Seat Tilting Pad Journal Bearing with Four Methods of Directed Lubrication) for valid dynamic data for a spherical-seat tilting pad journal bearing. (2014)

Table 19 Experimental dynamic-stiffness coefficients and uncertainties at N = 6,000 rpm, P = 1379 kPa (200 psi)

N = 6,000 rpm P = 1379 kPa		Experimental Dynamic-Stiffnesses								Uncertainties							
f	f/N	Re(H_{xx})	Re(H_{yy})	Re(H_{xy})	Re(H_{yx})	Im(H_{xx})	Im(H_{yy})	Im(H_{xy})	Im(H_{yx})	Re(H_{xx})	Re(H_{yy})	Re(H_{xy})	Re(H_{yx})	Im(H_{xx})	Im(H_{yy})	Im(H_{xy})	Im(H_{yx})
[Hz]	[Hz/Hz]	[MN/m]								[MN/m]							
20	0.20	330.60	324.57	-103.22	-32.69	47.3	28.0	-12.37	-8.42	14.79	4.39	4.46	11.22	16.0	3.9	6.04	7.36
30	0.30	335.57	317.28	-107.17	-29.67	61.0	47.4	-14.13	-18.97	14.90	3.71	4.88	9.18	11.9	4.0	3.81	10.03
40	0.40	332.40	354.66	-97.21	-40.39	85.4	24.0	-21.01	-12.83	11.75	13.15	13.43	4.83	14.3	14.0	30.31	8.03
50	0.50	347.93	314.70	-113.62	-22.97	107.5	71.3	-25.62	-4.46	12.82	5.07	9.90	8.56	19.1	7.9	7.35	13.38
60	0.60	335.60	303.25	-111.35	-43.17	127.6	77.3	-40.46	-21.65	105.65	25.81	112.72	50.96	137.7	64.0	140.03	59.66
70	0.70	337.62	283.56	-96.58	-26.95	139.6	65.8	-27.49	-10.89	24.99	8.26	32.46	11.18	20.7	25.9	25.76	14.30
80	0.80	343.66	280.78	-100.13	-18.23	168.0	120.8	-47.96	-8.93	31.27	22.20	41.59	17.91	20.6	29.7	32.19	15.69
90	0.90	348.05	287.34	-98.46	-34.54	165.4	137.1	-20.49	-22.07	43.66	36.64	41.70	36.42	68.0	34.4	56.89	41.11
100	1.00	138.15	138.32	-92.99	66.10	137.4	114.4	158.48	-164.39	807.92	458.95	1007.61	682.26	797.7	767.8	411.32	649.28
110	1.10	350.13	306.61	-111.84	-38.57	211.6	167.5	-35.05	-37.04	51.15	51.59	13.86	54.89	48.6	74.9	38.97	44.46
120	1.20	360.72	310.52	-107.64	-29.86	232.1	180.8	-44.59	-28.38	54.61	41.37	48.33	73.95	57.3	42.5	41.55	80.78
130	1.30	346.18	289.77	-115.50	-32.51	252.0	168.6	-64.63	-17.87	33.14	26.04	28.52	37.47	29.8	33.1	68.90	31.44
140	1.40	358.79	314.77	-108.46	-26.29	254.5	221.4	-37.66	-38.55	14.17	14.34	24.15	11.37	16.5	30.5	24.08	21.08
150	1.50	355.73	301.34	-107.80	-18.55	271.3	234.9	-35.75	-35.85	11.83	12.55	9.70	11.67	20.8	31.8	25.50	25.00
160	1.60	340.34	276.39	-106.02	-17.88	280.9	231.9	-65.42	-32.27	18.08	31.27	15.52	12.17	23.2	28.1	28.05	23.83
170	1.70	343.04	355.82	-103.45	-31.60	296.2	215.5	-57.44	-33.02	27.66	46.46	28.25	29.66	21.8	21.9	35.41	17.53
180	1.80	346.72	330.01	-104.52	-18.24	315.4	254.6	-65.21	-50.38	57.04	70.66	69.52	59.34	98.3	73.7	70.73	80.91
190	1.90	339.00	323.26	-103.34	-15.08	300.4	304.0	-13.26	-42.06	61.43	68.77	39.86	57.65	54.8	138.2	140.34	50.54
200	2.00	105.47	59.43	251.17	148.42	-319.9	294.9	-111.84	470.95	630.55	1368.84	1764.83	539.56	3016.6	702.4	955.41	2298.19
210	2.10	323.79	308.37	-102.93	-7.58	326.2	329.8	-60.03	-48.16	100.84	90.36	103.27	88.75	84.1	61.1	93.23	61.67
220	2.20	340.80	284.06	-108.16	-25.72	346.2	302.4	-47.64	-39.21	47.45	20.99	46.79	30.86	70.7	40.9	49.18	50.61
230	2.30	332.45	339.25	-104.95	-17.13	352.2	349.0	-38.19	-56.98	32.50	12.43	21.24	21.73	37.7	23.4	40.66	32.85
240	2.40	331.23	345.59	-105.21	-23.03	347.9	316.3	-35.66	-55.78	29.10	12.21	33.00	25.14	17.2	16.4	11.30	15.64
250	2.50	328.59	333.96	-104.03	-21.08	355.0	307.4	-30.59	-51.02	13.52	14.41	20.97	12.97	9.5	9.1	20.69	5.75
260	2.60	318.13	342.51	-87.15	-23.27	361.3	334.8	-19.81	-44.60	16.34	11.88	13.05	16.31	20.6	12.5	27.30	19.07

Editor's note: Subsequent to publication, the author has noted the experimental dynamic-stiffness data, which are the basis for the rotordynamic coefficients, to be unreliable. To the author's knowledge, all static data (both experimental and theoretical) and the theoretical dynamic data are valid. Please reference the Texas A&M University Master's thesis of David M. Coghlan (Static, Rotordynamic, and Thermal Characteristics of a Four Pad Spherical-Seat Tilting Pad Journal Bearing with Four Methods of Directed Lubrication) for valid dynamic data for a spherical-seat tilting pad journal bearing. (2014)

Table 20 Experimental dynamic-stiffness coefficients and uncertainties at N = 6,000 rpm, P = 1896 kPa (275 psi)

N = 6,000 rpm P = 1896 kPa		Experimental Dynamic-Stiffnesses								Uncertainties							
f	f/N	Re(H_{xx})	Re(H_{yy})	Re(H_{xy})	Re(H_{yx})	Im(H_{xx})	Im(H_{yy})	Im(H_{xy})	Im(H_{yx})	Re(H_{xx})	Re(H_{yy})	Re(H_{xy})	Re(H_{yx})	Im(H_{xx})	Im(H_{yy})	Im(H_{xy})	Im(H_{yx})
[Hz]	[Hz/Hz]	[MN/m]								[MN/m]							
20	0.20	382.97	391.51	-97.30	-23.64	45.8	34.6	-13.46	-21.55	23.40	24.82	25.58	33.73	36.9	19.8	15.91	27.46
30	0.30	388.66	391.83	-99.92	-23.49	56.6	57.7	-12.15	-27.53	22.76	29.22	25.93	47.71	12.9	8.4	12.53	14.34
40	0.40	384.42	410.53	-81.47	-31.04	86.7	40.3	-19.97	-30.37	8.28	32.94	58.46	18.86	32.7	103.9	19.87	23.28
50	0.50	398.76	383.90	-95.07	-30.21	110.0	88.4	-19.70	15.33	44.59	49.26	32.09	55.89	46.8	42.0	47.32	77.06
60	0.60	393.88	389.26	-95.96	-46.08	153.0	98.0	-47.91	-27.37	197.98	83.62	179.30	45.44	181.5	129.1	202.73	102.15
70	0.70	355.53	381.33	-42.87	-41.81	155.0	123.2	-53.13	-57.74	129.81	184.24	513.33	140.35	159.0	512.1	258.52	130.18
80	0.80	394.76	383.65	-150.42	22.59	133.3	82.4	-71.01	-14.40	151.80	235.11	384.38	138.82	124.7	262.5	221.76	96.88
90	0.90	383.00	187.33	-78.91	-25.01	152.5	120.6	179.14	-31.21	557.89	423.56	515.09	341.33	384.2	505.0	505.35	536.83
100	1.00	269.70	178.35	-190.97	-41.84	247.9	36.1	208.52	-115.55	455.94	448.53	789.77	573.94	758.5	634.9	352.41	471.22
110	1.10	334.01	372.99	-56.22	-33.76	219.2	236.5	-36.01	-87.92	183.82	206.09	225.69	103.78	161.5	244.5	252.56	144.22
120	1.20	439.72	368.70	-105.21	-22.75	157.2	224.6	-5.13	-22.30	191.17	101.22	167.97	157.42	216.7	181.5	175.06	166.88
130	1.30	387.15	345.20	-167.25	-38.24	342.8	182.9	-63.90	-28.46	90.00	197.97	287.73	60.95	234.2	110.1	222.47	101.25
140	1.40	408.16	390.21	-96.20	-27.52	239.1	224.5	-11.09	-17.79	46.32	59.21	122.54	59.51	97.0	28.9	65.74	34.95
150	1.50	379.06	385.98	-85.66	-12.10	278.8	242.2	-45.10	-52.45	76.85	83.81	101.99	50.72	38.3	46.3	59.11	18.21
160	1.60	375.77	322.05	-87.91	-9.97	290.5	252.7	-66.79	-39.79	75.24	66.82	91.72	64.48	81.8	61.2	166.13	33.13
170	1.70	379.42	400.61	-83.45	-19.14	262.5	197.4	-40.48	-18.08	90.31	75.05	180.61	49.46	50.4	147.1	84.09	21.74
180	1.80	445.14	473.16	-121.50	-51.04	294.9	207.9	28.71	2.48	166.03	281.11	300.13	155.47	199.9	190.3	240.53	150.09
190	1.90	260.76	254.41	26.28	63.00	85.7	475.7	-190.66	191.65	452.62	881.61	1102.84	415.19	275.7	1131.3	1067.52	311.47
200	2.00	395.60	464.45	-162.66	-31.87	70.1	193.1	15.06	201.56	624.42	656.16	726.35	551.41	563.6	434.9	535.03	493.88
210	2.10	352.61	379.49	-72.09	20.38	330.1	308.7	-38.24	-27.98	149.58	160.72	171.20	140.80	152.3	99.0	183.83	153.25
220	2.20	375.04	350.15	-92.60	-27.30	332.1	310.7	-26.39	-24.81	74.47	94.59	107.72	21.69	81.8	54.4	53.39	133.39
230	2.30	374.75	402.66	-83.98	-12.72	359.4	383.2	-38.48	-69.87	94.22	118.77	90.94	49.10	64.1	89.7	58.32	38.19
240	2.40	376.75	416.57	-94.90	-24.07	348.6	335.2	-41.48	-61.66	36.67	28.35	39.15	35.12	61.7	115.1	34.01	52.89
250	2.50	366.96	411.77	-88.19	-11.94	358.3	318.8	-42.84	-54.31	37.00	65.00	53.79	22.06	38.4	86.8	60.51	45.99
260	2.60	365.62	426.30	-83.75	-20.48	361.3	348.7	-35.06	-37.59	20.97	88.67	49.73	13.25	64.4	67.8	43.56	25.73

Editor's note: Subsequent to publication, the author has noted the experimental dynamic-stiffness data, which are the basis for the rotordynamic coefficients, to be unreliable. To the author's knowledge, all static data (both experimental and theoretical) and the theoretical dynamic data are valid. Please reference the Texas A&M University Master's thesis of David M. Coghlan (Static, Rotordynamic, and Thermal Characteristics of a Four Pad Spherical-Seat Tilting Pad Journal Bearing with Four Methods of Directed Lubrication) for valid dynamic data for a spherical-seat tilting pad journal bearing. (2014)

Table 21 Experimental dynamic-stiffness coefficients and uncertainties at N = 8,000 rpm, P = 0

N = 8,000 rpm P = 0		Experimental Dynamic-Stiffnesses								Uncertainties							
f	f/N	Re(H_{xx})	Re(H_{yy})	Re(H_{xy})	Re(H_{yx})	Im(H_{xx})	Im(H_{yy})	Im(H_{xy})	Im(H_{yx})	Re(H_{xx})	Re(H_{yy})	Re(H_{xy})	Re(H_{yx})	Im(H_{xx})	Im(H_{yy})	Im(H_{xy})	Im(H_{yx})
[Hz]	[Hz/Hz]	[MN/m]								[MN/m]							
20	0.15	351.68	326.18	-110.02	-80.05	77.1	-72.16	-26.93	417.59	37.41	20.18	18.31	44.63	36.7	177.62	20.81	705.36
30	0.23	370.74	110.39	-119.65	657.45	64.7	-328.20	-21.33	1196.68	19.68	418.98	17.77	1376.60	20.3	788.69	10.35	2515.93
40	0.30	372.93	260.04	-129.56	164.52	103.0	-41.56	-23.31	236.28	13.31	123.62	24.72	355.37	21.0	137.75	50.95	467.08
50	0.38	351.38	581.00	-113.08	-864.87	124.0	44.6	-42.39	27.21	22.49	506.05	17.65	1737.15	20.8	46.3	18.52	12.72
60	0.45	353.71	241.77	-118.89	246.61	106.09	145.96	-29.75	-255.15	111.64	166.46	127.67	602.83	126.58	193.26	139.08	405.12
70	0.53	351.29	378.53	-128.54	-88.90	165.2	251.21	-35.98	-549.68	33.74	190.42	61.65	28.86	27.3	505.74	69.10	1166.95
80	0.60	370.87	300.30	-131.82	-56.53	180.8	10.68	-35.23	305.42	25.47	53.03	72.22	29.31	30.0	277.19	36.93	632.71
90	0.68	392.76	389.57	-138.67	-372.18	176.3	29.42	-42.00	23.05	27.84	234.13	61.29	743.23	32.8	157.85	41.90	64.11
100	0.75	342.00	316.60	-117.39	-91.04	169.8	249.22	-41.00	-406.51	41.13	26.79	57.69	37.13	34.3	300.01	52.57	720.44
110	0.83	367.60	286.36	-124.72	44.35	185.7	109.12	-31.12	146.04	46.13	30.78	88.28	144.06	45.1	179.01	56.80	440.98
120	0.90	353.01	289.99	-118.39	184.41	213.25	293.84	-23.96	-317.94	131.69	28.22	154.01	469.30	100.46	283.35	85.77	516.62
130	0.98	208.35	181.62	-54.65	305.34	-21.85	268.47	193.50	-139.71	795.20	625.89	801.24	461.45	605.54	575.79	760.27	634.82
140	1.05	343.28	316.70	-118.67	-22.36	253.73	253.5	-61.62	-315.35	86.02	228.92	140.13	61.88	165.51	55.4	204.04	538.01
150	1.13	347.69	311.85	-119.05	-73.38	254.6	220.3	-54.97	-38.57	67.35	93.13	76.07	24.48	74.6	77.1	88.85	46.09
160	1.20	346.20	348.89	-119.93	-62.07	277.3	94.11	-63.47	61.31	40.94	128.57	58.88	77.48	58.0	234.01	75.98	55.43
170	1.28	351.05	334.88	-123.88	-18.27	267.9	219.6	-51.08	-49.45	44.28	38.89	59.24	18.72	24.6	69.7	30.91	13.56
180	1.35	335.04	327.29	-120.71	-40.86	265.3	262.1	-43.50	-70.69	42.70	111.54	55.22	53.00	57.0	67.4	76.73	51.03
190	1.43	323.43	348.72	-120.05	-46.14	277.7	271.6	-40.42	-51.39	26.96	46.55	42.64	19.94	38.1	67.9	67.81	47.58
200	1.50	327.43	232.37	-127.18	20.65	289.7	260.3	-44.34	178.76	33.92	251.50	28.22	23.71	30.1	28.1	25.95	468.12
210	1.58	312.17	338.27	-139.46	18.48	321.9	304.9	-20.55	6.49	21.84	26.25	28.33	21.67	37.5	34.4	31.53	25.73
220	1.65	328.93	289.98	-134.83	5.32	287.7	298.4	-16.93	-20.76	32.94	181.32	21.05	27.42	30.6	39.9	47.54	40.42
230	1.73	299.04	376.60	-121.97	23.28	298.5	287.8	8.73	-81.22	47.38	43.03	55.67	25.19	25.6	52.8	61.95	26.53
240	1.80	302.14	300.63	-116.78	7.46	318.7	310.0	-1.25	28.38	62.57	218.66	53.38	70.23	53.6	65.1	73.99	31.35
250	1.88	279.33	377.61	-115.47	21.73	316.79	368.7	-39.82	60.15	63.12	78.18	57.97	57.04	106.13	74.2	170.44	36.84
260	1.95	234.79	-39.82	146.09	-128.82	358.42	54.03	381.58	92.66	670.59	672.94	832.19	647.75	586.29	611.54	347.97	791.82

Editor's note: Subsequent to publication, the author has noted the experimental dynamic-stiffness data, which are the basis for the rotordynamic coefficients, to be unreliable. To the author's knowledge, all static data (both experimental and theoretical) and the theoretical dynamic data are valid. Please reference the Texas A&M University Master's thesis of David M. Coghlan (Static, Rotordynamic, and Thermal Characteristics of a Four Pad Spherical-Seat Tilting Pad Journal Bearing with Four Methods of Directed Lubrication) for valid dynamic data for a spherical-seat tilting pad journal bearing. (2014)

Table 22 Experimental dynamic-stiffness coefficients and uncertainties at N = 8,000 rpm, P = 689 kPa (100 psi)

N = 8,000 rpm P = 689 kPa		Experimental Dynamic-Stiffnesses								Uncertainties							
f	f/N	Re(H_{xx})	Re(H_{yy})	Re(H_{xy})	Re(H_{yx})	Im(H_{xx})	Im(H_{yy})	Im(H_{xy})	Im(H_{yx})	Re(H_{xx})	Re(H_{yy})	Re(H_{xy})	Re(H_{yx})	Im(H_{xx})	Im(H_{yy})	Im(H_{xy})	Im(H_{yx})
[Hz]	[Hz/Hz]	[MN/m]								[MN/m]							
20	0.15	336.41	309.96	-110.75	-42.32	48.0	21.3	-13.50	5.33	11.58	8.69	18.66	23.08	35.1	12.6	14.68	22.41
30	0.23	337.99	307.39	-113.53	-32.49	61.2	46.6	-17.38	-29.03	7.67	11.28	13.34	19.67	17.1	12.8	14.31	17.95
40	0.30	339.59	319.68	-109.24	-36.49	88.4	31.6	-35.53	-5.52	15.78	7.12	29.48	11.41	27.6	24.9	38.25	14.45
50	0.38	346.63	309.18	-119.53	-33.08	103.4	58.1	-31.36	6.82	22.46	8.59	14.52	9.10	16.9	9.5	8.19	19.98
60	0.45	349.61	305.37	-120.65	-41.26	124.2	77.5	-35.77	-36.44	152.61	57.81	145.89	63.00	146.6	68.7	121.91	77.19
70	0.53	345.31	303.00	-119.23	-55.80	143.1	61.4	-53.85	-5.11	15.65	25.74	79.89	29.53	27.9	43.2	89.39	21.15
80	0.60	347.32	282.60	-133.79	-32.63	151.7	98.1	-32.72	0.34	18.36	19.15	37.35	13.87	17.3	22.0	35.91	14.23
90	0.68	351.78	303.00	-136.11	-30.36	164.7	110.2	-45.62	-11.12	21.82	13.74	40.91	18.01	34.0	17.0	31.84	33.34
100	0.75	348.49	302.76	-131.29	-54.23	176.5	122.5	-45.42	-27.41	19.88	28.81	37.40	20.69	37.5	19.4	36.06	19.76
110	0.83	345.01	302.19	-124.56	-34.84	186.7	150.5	-35.46	-43.63	25.44	14.14	26.16	33.83	39.0	38.0	38.88	34.01
120	0.90	381.18	304.08	-133.36	-78.64	259.5	166.5	-62.08	-47.50	134.06	66.05	62.51	119.92	154.0	74.2	82.83	94.74
130	0.98	17.29	232.83	-86.53	171.53	43.6	167.6	3.74	-219.54	556.35	542.61	856.54	489.20	602.6	707.3	755.96	410.82
140	1.05	345.03	301.28	-110.51	-40.67	213.3	222.7	-59.53	-48.92	114.76	65.02	48.46	53.54	77.9	64.3	94.14	99.20
150	1.13	353.44	299.58	-107.27	-51.87	259.5	223.1	-48.62	-45.10	56.72	18.77	31.55	27.08	54.5	43.6	49.08	55.22
160	1.20	346.23	277.43	-120.05	-28.15	270.4	200.8	-59.00	-14.39	46.89	27.61	34.97	31.52	27.6	26.9	57.78	31.12
170	1.28	332.78	339.34	-116.22	-30.21	273.9	191.2	-59.78	-51.96	14.91	27.18	28.21	31.89	43.4	25.8	24.86	31.21
180	1.35	338.47	308.27	-118.65	-27.77	278.1	209.4	-57.71	-44.46	81.46	17.55	36.45	12.47	69.6	58.5	87.92	72.07
190	1.43	325.52	337.80	-106.07	-32.89	295.4	264.6	-41.01	-62.29	16.45	36.21	20.57	12.25	32.2	29.2	39.39	25.88
200	1.50	336.52	292.54	-115.42	-25.11	310.7	219.8	-61.09	-42.87	35.56	16.46	16.45	17.13	25.5	15.2	22.92	27.15
210	1.58	329.62	289.67	-114.73	-13.59	307.4	270.7	-41.95	-32.52	24.83	25.59	22.79	21.84	28.8	18.8	23.10	21.26
220	1.65	328.28	252.35	-122.59	-20.04	327.7	279.2	-52.29	-55.76	52.89	20.55	18.66	37.50	35.8	23.1	28.20	29.89
230	1.73	308.89	289.56	-109.09	-28.39	319.1	306.2	-38.06	-51.39	45.39	10.98	24.46	45.76	28.5	44.9	48.14	29.39
240	1.80	312.86	287.43	-118.26	-12.96	337.6	293.3	-52.26	-50.15	39.04	19.22	68.27	25.13	58.3	30.9	34.27	49.86
250	1.88	319.14	286.40	-116.57	-16.98	338.6	322.1	-65.06	-49.83	56.92	33.50	111.03	45.45	82.7	106.4	141.19	65.14
260	1.95	146.86	190.99	66.36	96.32	242.9	89.4	247.57	66.11	528.94	353.33	419.06	442.90	620.1	399.4	475.85	540.94

Editor's note: Subsequent to publication, the author has noted the experimental dynamic-stiffness data, which are the basis for the rotordynamic coefficients, to be unreliable. To the author's knowledge, all static data (both experimental and theoretical) and the theoretical dynamic data are valid. Please reference the Texas A&M University Master's thesis of David M. Coghlan (Static, Rotordynamic, and Thermal Characteristics of a Four Pad Spherical-Seat Tilting Pad Journal Bearing with Four Methods of Directed Lubrication) for valid dynamic data for a spherical-seat tilting pad journal bearing. (2014)

Table 23 Experimental dynamic-stiffness coefficients and uncertainties at N = 8,000 rpm, P = 1379 kPa (200 psi)

N = 8,000 rpm P = 1379 kPa		Experimental Dynamic-Stiffnesses								Uncertainties							
f	f/N	Re(H_{xx})	Re(H_{yy})	Re(H_{xy})	Re(H_{yx})	Im(H_{xx})	Im(H_{yy})	Im(H_{xy})	Im(H_{yx})	Re(H_{xx})	Re(H_{yy})	Re(H_{xy})	Re(H_{yx})	Im(H_{xx})	Im(H_{yy})	Im(H_{xy})	Im(H_{yx})
[Hz]	[Hz/Hz]	[MN/m]								[MN/m]							
20	0.15	357.99	337.43	-109.87	-30.86	42.2	25.9	-10.80	-3.37	14.63	10.46	14.90	12.81	23.3	12.9	14.58	26.72
30	0.23	368.39	341.86	-116.07	-38.09	59.0	43.3	-13.79	-18.62	27.08	9.89	16.55	22.33	17.5	8.1	10.97	16.39
40	0.30	364.74	347.70	-106.28	-40.80	82.0	31.6	-21.26	-9.04	9.76	11.63	38.77	16.16	32.0	48.8	41.30	19.32
50	0.38	377.31	336.49	-119.48	-24.60	91.2	68.0	-22.40	-6.08	24.93	7.30	15.70	22.07	33.8	11.7	17.96	26.58
60	0.45	410.58	338.81	-110.93	-38.07	113.7	65.7	-20.77	-7.94	153.02	73.58	175.95	90.58	178.2	39.5	197.50	17.34
70	0.53	370.63	338.93	-112.59	-38.17	143.4	74.5	-22.66	-13.87	38.76	44.00	50.64	30.02	45.1	188.4	168.31	28.18
80	0.60	368.05	336.28	-129.33	-32.14	163.0	103.9	-53.28	-12.15	57.06	26.66	52.27	31.27	24.8	18.5	54.23	25.86
90	0.68	375.06	336.55	-114.45	-31.79	147.7	141.7	-43.35	-22.97	51.62	47.36	52.70	46.84	62.6	99.8	55.86	51.71
100	0.75	373.25	334.26	-120.89	-28.20	158.6	153.9	-50.13	-7.42	63.06	54.68	60.43	50.71	68.0	95.0	58.06	132.00
110	0.83	368.62	336.30	-121.58	-43.25	218.2	179.3	-60.11	-52.60	104.62	54.18	63.18	98.68	152.9	166.4	187.15	136.37
120	0.90	424.06	547.55	-54.69	-186.04	462.9	251.5	-358.58	-95.18	593.59	1071.83	314.72	1203.48	1862.5	401.8	1754.65	229.87
130	0.98	463.33	-81.38	-56.42	91.78	70.8	118.0	470.69	60.61	499.31	414.91	563.72	552.80	642.9	474.2	538.15	344.87
140	1.05	397.93	252.70	-147.28	-75.91	293.0	134.7	126.72	-56.80	523.08	687.29	726.03	614.34	746.0	563.8	675.62	548.60
150	1.13	371.64	326.76	-146.88	-19.14	233.2	187.7	28.71	-37.12	77.15	22.87	327.43	80.17	237.1	221.9	159.46	168.28
160	1.20	364.83	324.46	-107.81	-31.93	256.4	223.6	-65.88	-26.91	58.13	19.98	289.20	68.24	61.6	178.0	65.29	108.19
170	1.28	367.68	345.45	-119.22	-47.30	285.8	188.1	-56.01	-14.36	57.72	22.24	44.58	63.81	89.8	34.8	235.52	117.84
180	1.35	367.74	352.89	-117.51	-40.58	275.9	227.4	-54.97	-44.95	66.36	19.03	98.46	78.33	71.0	50.9	182.61	47.12
190	1.43	363.48	332.45	-98.46	-35.88	288.0	291.1	-38.86	-41.65	35.33	60.56	77.54	54.94	55.0	87.6	65.51	38.50
200	1.50	350.69	328.21	-115.21	-19.92	308.9	220.7	-60.28	-29.84	55.66	29.99	24.69	15.84	38.1	40.4	30.45	49.44
210	1.58	350.86	322.25	-115.22	-19.42	316.7	299.2	-46.18	-52.99	34.06	21.39	26.04	52.53	51.4	44.2	36.48	19.49
220	1.65	340.17	303.10	-111.95	-14.60	324.1	272.9	-46.35	-31.74	63.45	25.10	34.81	31.61	54.9	27.3	25.56	39.88
230	1.73	353.89	326.94	-110.11	-34.59	320.0	311.5	-36.61	-38.57	58.88	17.02	25.02	39.36	53.6	56.3	53.16	89.37
240	1.80	336.56	324.37	-104.61	-7.25	321.3	270.0	-37.75	-32.81	47.99	32.44	54.20	44.01	68.5	69.8	54.90	39.19
250	1.88	345.86	320.33	-93.20	-22.66	342.5	281.3	-25.05	-43.58	91.82	34.65	53.00	75.45	76.9	46.5	50.13	51.08
260	1.95	290.46	491.24	-225.28	57.19	318.7	478.0	-145.63	5.99	519.64	345.16	360.09	510.97	371.8	634.2	619.71	335.38

Editor's note: Subsequent to publication, the author has noted the experimental dynamic-stiffness data, which are the basis for the rotordynamic coefficients, to be unreliable. To the author's knowledge, all static data (both experimental and theoretical) and the theoretical dynamic data are valid. Please reference the Texas A&M University Master's thesis of David M. Coghlan (Static, Rotordynamic, and Thermal Characteristics of a Four Pad Spherical-Seat Tilting Pad Journal Bearing with Four Methods of Directed Lubrication) for valid dynamic data for a spherical-seat tilting pad journal bearing. (2014)

Table 24 Experimental dynamic-stiffness coefficients and uncertainties at N = 8,000 rpm, P = 1896 kPa (275 psi)

N = 8,000 rpm P = 1896 kPa		Experimental Dynamic-Stiffnesses								Uncertainties							
f	f/N	Re(H_{xx})	Re(H_{yy})	Re(H_{xy})	Re(H_{yx})	Im(H_{xx})	Im(H_{yy})	Im(H_{xy})	Im(H_{yx})	Re(H_{xx})	Re(H_{yy})	Re(H_{xy})	Re(H_{yx})	Im(H_{xx})	Im(H_{yy})	Im(H_{xy})	Im(H_{yx})
[Hz]	[Hz/Hz]	[MN/m]								[MN/m]							
20	0.15	396.28	398.52	-115.48	-36.03	45.4	19.5	-9.30	7.62	46.46	30.54	16.26	45.31	57.6	31.9	25.84	32.33
30	0.23	407.72	399.64	-120.24	-44.47	56.5	47.5	-10.43	-28.31	60.81	34.81	19.21	54.10	17.9	10.2	14.18	14.34
40	0.30	398.52	414.67	-110.40	-30.97	71.5	-1.7	-13.11	-3.65	22.09	38.56	32.62	31.61	48.7	132.4	33.07	57.11
50	0.38	403.48	393.01	-120.23	-15.93	95.0	73.0	-14.83	-7.38	33.68	44.66	15.67	18.04	57.8	22.2	22.85	27.94
60	0.45	410.58	396.43	-110.93	-42.57	113.7	65.7	-20.77	-7.94	153.02	82.14	175.95	90.20	178.2	39.5	197.50	17.34
70	0.53	392.21	365.27	-45.95	-21.51	120.1	74.5	-22.66	-7.71	62.87	178.32	184.85	78.34	71.4	188.4	168.31	26.61
80	0.60	407.50	350.52	-96.30	-21.34	158.7	97.3	-58.83	-0.51	80.79	127.82	63.20	56.63	53.7	54.1	131.94	42.90
90	0.68	402.78	393.15	-99.74	-32.22	154.1	141.7	-18.77	-35.90	105.87	88.15	60.56	64.96	95.6	99.8	129.49	121.95
100	0.75	411.44	369.10	-100.73	-29.73	173.9	153.9	-28.30	-7.42	157.68	133.06	82.36	109.38	94.9	95.0	137.61	132.00
110	0.83	405.00	394.06	-103.33	-63.06	218.2	179.3	-60.11	-52.60	156.97	189.09	206.96	144.52	152.9	166.4	187.15	136.37
120	0.90	424.06	547.55	-54.69	-186.04	462.9	251.5	-358.58	-95.18	593.59	1071.83	314.72	1203.48	1862.5	401.8	1754.65	229.87
130	0.98	463.33	-81.38	-56.42	91.78	70.8	118.0	470.69	60.61	499.31	414.91	563.72	552.80	642.9	474.2	538.15	344.87
140	1.05	397.93	252.70	-147.28	-75.91	293.0	134.7	126.72	-56.80	523.08	687.29	726.03	614.34	746.0	563.8	675.62	548.60
150	1.13	396.74	322.64	-146.88	2.96	233.2	187.7	28.71	-37.12	184.65	205.40	327.43	198.61	237.1	221.9	159.46	168.28
160	1.20	415.53	339.54	-107.81	-8.03	235.6	223.6	-66.00	-26.91	147.94	202.42	289.20	155.65	210.0	178.0	215.31	108.19
170	1.28	397.88	428.60	-106.81	-31.30	292.7	213.6	-56.01	-14.36	122.28	191.15	60.48	84.94	129.4	141.1	235.52	117.84
180	1.35	390.33	379.58	-110.05	-30.12	287.7	251.7	-54.97	-50.68	96.54	72.47	62.97	101.02	95.8	151.5	182.61	94.22
190	1.43	385.06	374.64	-129.69	-26.58	277.0	230.4	-30.00	-30.56	48.70	148.00	211.40	69.06	63.5	37.9	38.17	22.83
200	1.50	383.20	373.79	-106.36	-25.13	291.3	221.6	-45.39	-34.19	42.48	57.55	87.28	25.07	94.0	65.6	36.38	84.00
210	1.58	381.89	372.47	-107.52	-27.46	317.9	294.2	-48.56	-50.21	64.89	23.26	61.00	80.31	43.3	62.7	50.06	34.48
220	1.65	376.35	324.49	-105.88	-15.02	310.5	285.1	-43.91	-24.01	26.56	27.64	47.81	22.52	80.4	47.7	24.70	61.87
230	1.73	379.62	374.09	-105.75	-19.37	331.3	348.7	-42.40	-38.57	36.12	61.93	43.99	58.81	95.9	88.0	25.15	89.37
240	1.80	373.13	384.43	-102.90	-23.80	305.7	270.8	-18.32	-26.08	91.35	13.54	56.66	70.67	41.7	69.6	60.84	42.15
250	1.88	371.29	369.32	-103.35	-20.63	338.1	281.3	-25.05	-40.51	59.29	65.18	66.52	56.17	46.8	46.5	50.13	53.14
260	1.95	290.46	491.24	-225.28	57.19	318.7	478.0	-145.63	5.99	519.64	345.16	360.09	510.97	371.8	634.2	619.71	335.38

Editor's note: Subsequent to publication, the author has noted the experimental dynamic-stiffness data, which are the basis for the rotordynamic coefficients, to be unreliable. To the author's knowledge, all static data (both experimental and theoretical) and the theoretical dynamic data are valid. Please reference the Texas A&M University Master's thesis of David M. Coghlan (Static, Rotordynamic, and Thermal Characteristics of a Four Pad Spherical-Seat Tilting Pad Journal Bearing with Four Methods of Directed Lubrication) for valid dynamic data for a spherical-seat tilting pad journal bearing. (2014)

Table 25 Experimental dynamic-stiffness coefficients and uncertainties at N = 10,000 rpm, P = 0

N = 10,000 rpm P = 0		Experimental Dynamic-Stiffnesses								Uncertainties							
f	f/N	Re(H_{xx})	Re(H_{yy})	Re(H_{xy})	Re(H_{yx})	Im(H_{xx})	Im(H_{yy})	Im(H_{xy})	Im(H_{yx})	Re(H_{xx})	Re(H_{yy})	Re(H_{xy})	Re(H_{yx})	Im(H_{xx})	Im(H_{yy})	Im(H_{xy})	Im(H_{yx})
[Hz]	[Hz/Hz]	[MN/m]								[MN/m]							
20	0.12	406.32	343.44	-113.74	-52.68	64.3	1.7	-21.38	113.47	56.64	8.20	37.11	21.41	35.3	107.4	21.73	455.33
30	0.18	407.56	311.70	-118.15	99.56	57.3	-3.0	-16.53	161.01	38.48	232.52	20.85	38.86	37.6	372.1	20.27	1390.59
40	0.24	422.87	325.52	-125.99	24.93	81.0	15.7	-6.09	52.17	46.47	124.95	38.54	28.91	39.7	115.9	79.76	306.79
50	0.30	397.19	410.19	-118.94	-201.80	116.3	50.8	-31.37	11.23	24.69	361.72	27.52	35.28	54.1	21.2	18.18	19.24
60	0.36	374.06	341.64	-119.70	-65.93	85.6	104.6	13.21	-53.08	122.11	33.52	35.11	69.45	125.7	25.9	134.95	14.48
70	0.42	389.09	317.03	-116.07	-64.71	145.0	109.4	-11.52	-84.65	24.70	19.88	24.23	36.21	35.2	226.7	80.75	633.32
80	0.48	420.73	338.82	-119.38	-42.42	155.7	90.1	-29.69	62.44	43.02	37.33	42.56	23.40	34.2	126.7	38.97	354.76
90	0.54	437.45	338.54	-122.74	-64.99	165.8	95.0	-34.23	20.35	34.38	32.17	47.62	41.46	37.8	139.5	46.46	275.93
100	0.60	382.87	348.75	-116.05	-81.70	161.3	142.6	-29.67	-103.08	53.88	16.18	39.43	20.87	48.7	103.8	41.13	389.14
110	0.66	418.40	352.10	-123.18	-50.45	181.8	153.1	-44.21	-59.63	32.91	25.12	37.50	44.07	42.6	48.5	54.51	17.61
120	0.72	393.62	358.75	-110.67	-86.95	195.0	191.9	-41.81	-138.37	77.96	36.94	66.14	86.18	80.9	168.7	51.05	359.06
130	0.78	395.50	349.17	-113.95	-78.89	224.6	165.9	-28.24	-33.92	91.79	62.27	27.03	83.66	89.2	117.9	103.94	47.14
140	0.84	392.60	356.84	-118.28	-73.00	225.3	168.8	-50.97	-90.65	63.25	31.60	50.77	52.11	35.2	19.4	75.85	255.53
150	0.90	408.00	353.26	-121.27	-74.86	254.3	168.3	-69.36	-19.25	105.22	38.09	54.23	101.44	94.3	31.9	134.82	42.67
160	0.96	426.96	310.19	-114.08	-48.65	264.0	158.1	14.64	47.49	160.40	179.02	199.98	277.72	138.5	220.1	212.72	292.54
170	1.02	442.35	-23.52	-342.14	-40.04	262.1	-118.7	455.10	9.71	605.20	802.95	495.84	692.06	832.9	526.6	929.98	658.17
180	1.08	364.87	342.20	-137.40	9.40	223.1	215.9	-15.03	-69.79	299.06	378.74	363.27	181.34	192.7	342.8	396.60	375.74
190	1.14	343.74	326.40	-66.85	-29.46	271.6	212.7	-8.28	-41.28	87.33	287.27	191.87	159.36	146.3	45.8	246.67	22.92
200	1.20	353.42	359.03	-123.69	-20.02	287.7	225.8	-56.68	-23.38	78.76	130.19	102.89	94.38	76.4	40.4	72.14	37.43
210	1.26	359.22	337.85	-129.09	-14.06	301.4	254.9	-21.64	-18.63	48.65	11.92	55.91	73.83	33.9	33.9	30.52	26.28
220	1.32	345.71	345.21	-124.26	-25.68	283.7	248.2	-28.86	-31.01	41.83	125.27	32.46	45.24	43.1	27.8	60.71	32.62
230	1.38	327.21	365.29	-102.84	-20.78	280.3	260.9	-22.77	-29.53	27.05	54.02	42.74	27.90	36.8	48.5	36.89	15.93
240	1.44	313.19	372.15	-110.09	14.79	295.0	286.6	-25.32	-6.16	37.47	46.40	48.81	49.56	23.7	82.0	48.94	19.09
250	1.50	301.26	369.45	-142.74	5.61	303.0	284.3	-33.86	-0.02	19.36	41.18	32.72	44.91	37.3	27.5	51.41	10.98
260	1.56	193.29	388.11	-150.95	45.45	294.1	425.3	-22.32	113.33	139.60	215.23	167.90	188.45	90.2	360.5	95.54	745.65

Editor's note: Subsequent to publication, the author has noted the experimental dynamic-stiffness data, which are the basis for the rotordynamic coefficients, to be unreliable. To the author's knowledge, all static data (both experimental and theoretical) and the theoretical dynamic data are valid. Please reference the Texas A&M University Master's thesis of David M. Coghlan (Static, Rotordynamic, and Thermal Characteristics of a Four Pad Spherical-Seat Tilting Pad Journal Bearing with Four Methods of Directed Lubrication) for valid dynamic data for a spherical-seat tilting pad journal bearing. (2014)

Table 26 Experimental dynamic-stiffness coefficients and uncertainties at N = 10,000 rpm, P = 689 kPa (100 psi)

N = 10,000 rpm P = 689 kPa		Experimental Dynamic-Stiffnesses								Uncertainties							
f	f/N	Re(H_{xx})	Re(H_{yy})	Re(H_{xy})	Re(H_{yx})	Im(H_{xx})	Im(H_{yy})	Im(H_{xy})	Im(H_{yx})	Re(H_{xx})	Re(H_{yy})	Re(H_{xy})	Re(H_{yx})	Im(H_{xx})	Im(H_{yy})	Im(H_{xy})	Im(H_{yx})
[Hz]	[Hz/Hz]	[MN/m]								[MN/m]							
20	0.12	381.64	329.82	-128.76	-40.09	38.0	8.7	-6.85	22.44	48.34	6.85	26.42	22.15	48.3	21.0	17.31	15.36
30	0.18	381.37	330.81	-130.67	-37.92	54.0	42.8	-12.04	-23.52	34.31	10.09	19.82	65.25	50.8	18.1	23.57	25.37
40	0.24	379.82	327.03	-130.14	-27.13	67.3	14.6	-8.91	1.10	33.95	28.98	56.32	15.56	18.2	81.4	90.38	23.57
50	0.30	377.15	329.11	-124.12	-22.91	112.3	50.9	-28.89	-0.20	40.55	22.26	27.65	18.50	52.8	37.1	35.62	87.33
60	0.36	351.87	328.38	-116.30	-37.59	96.1	73.7	-17.17	-49.48	124.96	52.27	121.97	41.20	148.8	77.3	162.26	83.02
70	0.42	365.13	305.90	-110.61	-38.69	125.8	64.7	-32.94	-2.19	27.61	104.04	101.20	63.31	30.5	74.3	76.98	19.14
80	0.48	406.38	291.47	-136.68	-33.08	151.7	96.4	-34.21	-5.28	37.25	67.76	110.14	45.22	30.0	45.4	38.37	29.43
90	0.54	372.24	321.60	-128.98	-28.67	164.1	114.1	-22.84	-32.38	46.17	40.91	68.71	13.01	52.0	49.5	23.64	18.02
100	0.60	361.51	323.11	-120.59	-62.44	175.6	116.6	-38.03	-29.48	33.34	78.70	57.32	116.77	57.5	38.5	61.95	21.74
110	0.66	387.69	325.36	-136.32	-60.14	203.4	156.8	-39.64	-47.84	49.46	57.93	85.10	15.24	53.5	55.3	59.43	18.00
120	0.72	373.81	323.84	-109.01	-23.98	196.4	173.1	-35.43	-36.06	153.88	85.21	82.27	138.06	81.5	59.3	98.22	166.93
130	0.78	458.21	295.37	-152.41	-40.98	193.7	119.0	-21.19	41.55	179.11	169.50	202.47	52.08	127.8	176.2	246.78	95.12
140	0.84	361.60	344.78	-115.45	-20.04	193.6	194.6	-46.11	-45.64	132.62	147.83	120.46	118.93	127.0	125.9	173.41	156.40
150	0.90	417.77	323.38	-111.56	-121.26	333.8	213.4	-62.08	-46.53	252.82	285.28	390.63	362.52	502.6	377.7	403.08	290.89
160	0.96	648.90	-267.90	-200.25	22.08	108.4	-125.0	813.77	194.38	1854.29	1730.79	655.66	1189.39	2352.7	840.0	2390.29	1980.15
170	1.02	365.27	143.29	-157.16	109.21	91.7	93.0	220.46	-6.18	603.13	517.84	475.90	344.22	326.1	322.0	531.03	456.74
180	1.08	375.56	373.69	-109.49	-89.04	361.9	205.8	-79.26	-33.11	263.45	304.80	299.95	237.00	260.8	226.9	373.07	296.76
190	1.14	398.33	316.81	-114.91	-29.96	241.0	237.9	-3.26	-2.41	181.36	202.17	283.32	72.53	85.9	244.3	196.53	149.11
200	1.20	343.82	315.39	-107.23	-28.67	300.7	219.6	-63.34	-74.31	44.33	85.26	86.76	34.68	161.0	60.9	108.12	122.73
210	1.26	361.00	311.47	-118.96	-44.14	316.4	240.1	-46.91	-49.66	124.88	59.97	81.17	29.19	56.4	70.5	76.08	92.15
220	1.32	338.50	276.00	-122.09	-27.22	303.2	253.4	-46.62	-62.60	49.37	47.35	65.89	51.57	92.7	56.4	59.82	95.31
230	1.38	349.53	310.52	-111.82	-29.09	305.3	269.8	-30.84	-27.11	36.24	54.75	69.50	49.99	85.1	53.3	45.86	15.01
240	1.44	337.92	312.75	-112.09	-18.00	306.0	265.4	-42.90	-33.93	46.24	18.14	39.52	28.74	30.8	47.3	55.18	26.78
250	1.50	338.10	308.16	-120.86	-31.44	328.3	249.6	-46.51	-32.23	36.23	36.99	63.76	12.68	27.9	48.4	54.69	9.41
260	1.56	327.03	302.24	-100.53	-14.57	330.7	296.0	-29.77	-27.32	27.23	58.81	54.43	18.25	47.9	46.4	53.31	24.31

Editor's note: Subsequent to publication, the author has noted the experimental dynamic-stiffness data, which are the basis for the rotordynamic coefficients, to be unreliable. To the author's knowledge, all static data (both experimental and theoretical) and the theoretical dynamic data are valid. Please reference the Texas A&M University Master's thesis of David M. Coghlan (Static, Rotordynamic, and Thermal Characteristics of a Four Pad Spherical-Seat Tilting Pad Journal Bearing with Four Methods of Directed Lubrication) for valid dynamic data for a spherical-seat tilting pad journal bearing. (2014)

Table 27 Experimental dynamic-stiffness coefficients and uncertainties at N = 10,000 rpm, P = 1379 kPa (200 psi)

N = 10,000 rpm P = 1379 kPa		Experimental Dynamic-Stiffnesses								Uncertainties							
f	f/N	Re(H_{xx})	Re(H_{yy})	Re(H_{xy})	Re(H_{yx})	Im(H_{xx})	Im(H_{yy})	Im(H_{xy})	Im(H_{yx})	Re(H_{xx})	Re(H_{yy})	Re(H_{xy})	Re(H_{yx})	Im(H_{xx})	Im(H_{yy})	Im(H_{xy})	Im(H_{yx})
[Hz]	[Hz/Hz]	[MN/m]								[MN/m]							
20	0.12	383.48	356.62	-124.93	-39.84	50.1	18.9	-12.75	-2.39	31.32	11.06	20.40	34.27	68.9	13.7	35.00	15.70
30	0.18	386.68	354.32	-126.04	-39.31	49.6	42.6	-9.70	-20.95	38.92	8.97	24.09	28.93	20.2	14.6	14.23	15.27
40	0.24	388.78	351.51	-126.83	-29.52	80.4	22.6	-12.82	-11.61	28.03	12.88	33.26	16.49	41.7	85.5	83.92	22.50
50	0.30	405.45	348.37	-131.32	-23.27	90.0	58.2	-18.96	-15.22	37.93	22.35	25.73	15.35	58.3	27.4	30.97	17.66
60	0.36	395.70	348.33	-113.93	-42.55	117.4	79.2	-18.66	-26.51	154.78	79.18	171.35	66.27	131.4	65.7	125.28	60.75
70	0.42	403.38	345.72	-127.99	-32.94	127.4	71.5	-46.33	-8.21	60.58	134.12	124.99	39.83	44.4	83.5	169.54	12.60
80	0.48	404.14	345.68	-124.28	-22.55	152.6	100.3	-37.85	-12.22	50.32	31.63	55.23	39.10	25.3	47.6	39.81	26.12
90	0.54	392.34	345.53	-125.26	-30.63	149.3	120.4	-24.48	-29.37	46.64	47.87	59.36	28.11	78.5	33.2	63.55	24.28
100	0.60	393.98	345.02	-126.63	-35.40	154.2	118.8	-35.18	-6.09	64.08	50.57	74.24	39.58	47.0	38.2	49.25	68.67
110	0.66	388.65	344.49	-127.08	-56.65	201.1	157.1	-42.69	-32.65	58.29	25.99	79.45	44.06	69.8	74.4	61.45	19.81
120	0.72	430.94	343.24	-158.25	-68.98	183.6	157.8	-43.23	-29.62	163.30	73.98	147.17	142.20	93.3	126.9	81.66	120.20
130	0.78	393.41	307.09	-83.86	-27.71	241.4	180.9	-49.36	-19.28	195.61	166.77	215.82	97.36	202.2	216.4	314.86	155.10
140	0.84	440.36	389.85	-159.94	-45.45	227.1	166.1	-59.21	-0.67	192.50	195.25	119.83	180.71	176.3	139.2	246.29	139.69
150	0.90	476.62	436.34	-141.82	-94.29	311.0	222.7	-161.49	4.28	468.67	348.00	339.32	400.68	401.8	371.0	514.51	295.54
160	0.96	481.83	-0.08	-112.34	-13.79	194.5	60.0	378.79	44.54	594.51	248.29	704.46	712.96	849.7	540.8	338.61	339.41
170	1.02	777.95	48.63	-259.75	19.38	78.5	-47.0	367.79	345.05	1603.34	1004.46	1494.08	668.27	747.9	1498.0	1358.54	1438.18
180	1.08	373.58	376.79	-72.51	-61.54	325.9	243.0	-65.42	-59.77	151.04	211.52	239.32	231.07	264.1	216.8	306.39	103.81
190	1.14	384.07	345.90	-60.16	-46.79	299.0	296.3	-20.80	-27.68	101.78	237.86	246.99	189.25	206.7	269.2	249.36	100.29
200	1.20	368.26	334.62	-113.66	-25.10	282.8	231.4	-74.88	-30.35	143.66	45.03	103.21	80.30	83.3	107.4	90.64	143.94
210	1.26	365.15	333.02	-109.07	-26.87	307.3	254.6	-32.10	-46.74	71.77	44.74	69.29	44.27	89.6	78.9	73.80	23.44
220	1.32	356.11	316.97	-135.82	-21.40	309.3	242.1	-39.67	-24.50	82.99	19.35	64.46	43.08	59.9	45.8	54.78	96.22
230	1.38	374.32	328.62	-98.87	-33.02	309.3	276.4	-43.43	-19.37	65.97	71.30	45.70	37.11	53.4	43.9	45.68	52.39
240	1.44	350.65	340.47	-105.35	-24.35	307.1	266.0	-54.64	-25.94	38.41	8.36	60.51	47.92	54.5	73.1	42.38	18.46
250	1.50	358.33	328.23	-117.55	-33.63	333.0	263.3	-46.15	-29.47	28.14	38.15	21.96	34.20	29.2	63.9	47.85	21.81
260	1.56	328.07	322.79	-95.75	-8.16	334.8	290.8	-26.26	-20.40	51.88	59.62	28.52	17.12	46.1	50.1	45.89	40.46

Editor's note: Subsequent to publication, the author has noted the experimental dynamic-stiffness data, which are the basis for the rotordynamic coefficients, to be unreliable. To the author's knowledge, all static data (both experimental and theoretical) and the theoretical dynamic data are valid. Please reference the Texas A&M University Master's thesis of David M. Coghlan (Static, Rotordynamic, and Thermal Characteristics of a Four Pad Spherical-Seat Tilting Pad Journal Bearing with Four Methods of Directed Lubrication) for valid dynamic data for a spherical-seat tilting pad journal bearing. (2014)

Table 28 Experimental dynamic-stiffness coefficients and uncertainties at N = 10,000 rpm, P = 1896 kPa (275 psi)

N = 10,000 rpm P = 1896 kPa		Experimental Dynamic-Stiffnesses								Uncertainties							
f	f/N	Re(H_{xx})	Re(H_{yy})	Re(H_{xy})	Re(H_{yx})	Im(H_{xx})	Im(H_{yy})	Im(H_{xy})	Im(H_{yx})	Re(H_{xx})	Re(H_{yy})	Re(H_{xy})	Re(H_{yx})	Im(H_{xx})	Im(H_{yy})	Im(H_{xy})	Im(H_{yx})
[Hz]	[Hz/Hz]	[MN/m]								[MN/m]							
20	0.12	418.90	402.89	-125.03	-40.75	50.4	16.9	-15.86	-6.08	19.01	10.35	29.29	30.81	59.5	20.8	31.09	7.69
30	0.18	422.27	404.91	-129.44	-44.20	52.3	45.7	-9.83	-26.28	20.64	4.34	17.18	27.62	11.2	16.7	16.54	8.51
40	0.24	425.48	450.75	-123.79	-30.47	77.3	8.2	-24.32	-9.67	20.43	36.52	54.37	14.17	30.6	89.1	100.22	25.05
50	0.30	438.53	394.62	-136.66	-4.98	74.6	64.7	-14.20	-10.40	36.43	23.58	35.58	11.80	46.3	24.0	31.54	26.95
60	0.36	432.83	394.72	-126.66	-43.46	99.6	66.6	-15.64	-26.55	178.73	78.06	215.84	57.30	117.6	63.7	145.90	77.46
70	0.42	436.18	382.68	-144.48	-29.66	120.5	14.8	-12.40	14.05	48.58	61.93	166.16	18.99	28.8	109.9	146.24	10.74
80	0.48	427.72	350.15	-127.46	-24.12	150.2	86.6	-31.64	-10.54	32.46	45.99	103.56	18.11	30.9	45.9	59.96	12.86
90	0.54	430.24	386.62	-124.49	-28.61	144.7	111.8	-22.79	-27.22	47.26	45.34	78.49	19.92	67.9	50.6	40.74	17.94
100	0.60	436.35	384.03	-137.09	-24.56	150.4	103.7	-19.95	-5.28	55.04	36.74	74.87	43.53	49.4	44.3	42.81	27.79
110	0.66	422.05	381.72	-120.08	-53.14	174.7	158.8	-28.80	-30.17	42.99	60.66	84.75	49.02	58.6	59.6	63.32	24.93
120	0.72	432.58	382.27	-138.42	-50.06	195.8	160.2	-16.60	-3.88	90.26	81.41	105.31	77.66	100.6	94.5	78.72	109.94
130	0.78	421.09	353.11	-154.39	-41.42	254.4	139.7	-52.00	-5.25	130.18	167.22	170.09	102.66	157.4	163.5	245.93	98.94
140	0.84	435.75	399.43	-112.33	-36.94	224.9	200.9	-42.79	8.98	82.87	153.60	137.91	109.58	126.0	135.1	207.05	104.14
150	0.90	395.37	364.81	-86.45	-31.63	260.2	235.3	-27.17	-58.68	229.32	200.23	279.81	213.06	202.6	261.9	252.00	163.15
160	0.96	274.13	197.02	-301.70	238.58	-63.8	-6.3	230.79	-53.87	364.03	684.45	1215.03	720.82	1042.5	906.8	854.49	412.75
170	1.02	427.85	17.55	-193.57	129.35	76.0	20.3	421.01	13.99	711.44	607.76	243.89	401.56	575.5	210.8	645.80	752.84
180	1.08	372.73	386.49	-126.30	6.94	255.5	192.5	-3.91	-61.36	207.83	224.11	295.54	141.45	163.8	253.0	249.40	207.77
190	1.14	425.61	465.62	-142.88	-90.20	342.8	277.3	-98.23	-18.62	106.59	375.17	302.06	246.78	217.5	419.6	454.89	107.59
200	1.20	412.40	371.87	-109.98	-27.92	282.0	216.7	-35.59	0.42	92.79	64.33	84.60	108.76	115.9	86.7	87.73	98.82
210	1.26	388.43	375.59	-117.72	-25.13	288.3	238.4	-30.95	-55.36	60.37	79.53	91.13	83.99	66.5	35.5	22.60	67.49
220	1.32	399.23	353.51	-114.48	-22.39	293.9	260.9	-56.72	-9.43	58.57	34.34	62.77	63.03	78.1	38.3	80.66	76.47
230	1.38	388.46	371.06	-120.57	-27.01	322.3	292.7	-25.51	-28.19	49.39	42.48	51.40	66.19	61.8	35.9	15.69	34.66
240	1.44	384.00	370.63	-112.69	-30.56	301.1	280.6	-28.56	-22.56	46.11	37.32	59.40	45.53	42.8	21.3	34.10	37.84
250	1.50	373.42	365.00	-105.21	-16.31	316.4	276.8	-31.55	-33.52	16.10	65.65	54.73	27.88	28.5	35.1	13.37	10.79
260	1.56	374.26	367.97	-112.83	-3.89	323.7	298.2	-31.68	-1.76	23.78	73.77	56.09	42.01	56.4	27.0	31.21	59.81

Editor's note: Subsequent to publication, the author has noted the experimental dynamic-stiffness data, which are the basis for the rotordynamic coefficients, to be unreliable. To the author's knowledge, all static data (both experimental and theoretical) and the theoretical dynamic data are valid. Please reference the Texas A&M University Master's thesis of David M. Coghlan (Static, Rotordynamic, and Thermal Characteristics of a Four Pad Spherical-Seat Tilting Pad Journal Bearing with Four Methods of Directed Lubrication) for valid dynamic data for a spherical-seat tilting pad journal bearing. (2014)

Table 29 Experimental dynamic-stiffness coefficients and uncertainties at N = 12,000 rpm, P = 0

N = 12,000 rpm P = 0		Experimental Dynamic-Stiffnesses								Uncertainties							
f	f/N	Re(H_{xx})	Re(H_{yy})	Re(H_{xy})	Re(H_{yx})	Im(H_{xx})	Im(H_{yy})	Im(H_{xy})	Im(H_{yx})	Re(H_{xx})	Re(H_{yy})	Re(H_{xy})	Re(H_{yx})	Im(H_{xx})	Im(H_{yy})	Im(H_{xy})	Im(H_{yx})
[Hz]	[Hz/Hz]	[MN/m]								[MN/m]							
20	0.10	430.25	360.47	-137.22	-48.94	36.7	18.4	-9.62	0.22	53.24	3.38	23.52	30.54	38.6	9.8	25.05	25.06
30	0.15	417.01	374.17	-129.22	-51.80	50.8	35.0	-8.64	-19.33	35.73	8.84	20.48	10.92	20.5	11.5	12.84	16.50
40	0.20	416.53	363.02	-130.19	-45.10	65.2	20.2	-9.27	-8.18	16.47	9.33	40.79	10.37	19.3	24.3	37.19	10.40
50	0.25	424.32	363.46	-125.41	-41.44	87.6	46.0	-18.91	-7.85	43.16	5.38	25.38	20.00	36.4	9.8	19.32	12.36
60	0.30	417.04	353.57	-135.65	-48.56	114.3	59.7	-31.46	-28.16	138.21	63.47	133.32	59.47	148.7	86.6	160.99	74.27
70	0.35	433.62	323.17	-151.82	-40.94	128.1	41.5	-30.93	-8.67	19.82	29.35	36.00	20.58	31.1	32.8	43.60	15.42
80	0.40	438.76	335.02	-159.15	-37.21	138.1	99.3	-20.06	-21.36	16.06	10.47	24.18	18.28	15.2	31.8	21.40	17.50
90	0.45	432.73	338.79	-139.04	-37.11	152.8	91.4	-26.89	-22.21	26.98	3.91	21.12	12.92	22.8	11.8	25.04	11.73
100	0.50	418.96	349.27	-136.45	-49.90	160.4	101.7	-28.97	-29.83	37.67	9.50	33.33	20.08	19.7	18.8	15.38	25.72
110	0.55	423.38	352.25	-136.98	-44.77	178.4	135.4	-23.75	-37.37	16.08	16.47	16.46	19.26	26.4	10.1	23.13	19.36
120	0.60	421.95	354.20	-133.01	-40.64	207.0	148.3	-17.56	-37.33	57.73	46.94	55.16	69.78	76.1	37.5	52.07	44.07
130	0.65	419.66	354.48	-137.83	-46.22	211.5	109.3	-35.45	-25.70	25.57	8.48	30.89	42.06	30.9	25.8	34.27	42.84
140	0.70	409.90	358.73	-128.60	-48.09	214.4	166.2	-19.34	-42.71	23.74	10.14	18.03	19.84	28.2	22.3	22.67	23.80
150	0.75	420.59	357.33	-139.77	-50.63	229.7	168.3	-16.69	-30.01	37.27	20.47	35.80	32.36	29.8	25.1	27.28	29.09
160	0.80	412.10	359.64	-121.48	-40.96	236.1	143.9	-30.77	-32.87	30.02	26.78	38.05	39.39	31.5	37.6	39.72	27.41
170	0.85	382.39	365.37	-106.30	-51.40	256.0	178.3	-27.10	-42.86	53.63	7.69	34.20	52.24	42.8	43.2	41.79	43.02
180	0.90	391.47	355.70	-100.79	-36.43	242.9	211.4	-21.94	-47.28	43.56	43.29	65.93	40.33	64.9	81.1	54.56	80.62
190	0.95	382.40	340.11	-146.18	-56.56	296.5	200.2	19.09	-42.32	103.76	166.82	208.97	117.83	140.1	172.8	126.34	102.39
200	1.00	375.66	242.68	-120.74	211.17	7.0	168.4	106.22	28.86	315.10	298.55	339.92	175.91	161.5	269.6	277.38	264.06
210	1.05	362.74	359.99	-103.61	-56.99	313.5	264.2	-56.13	-51.42	103.54	39.15	93.85	130.80	121.8	92.7	97.75	97.30
220	1.10	341.82	351.66	-101.63	-36.25	285.9	236.3	-37.94	-48.37	52.88	33.00	45.25	50.21	58.0	38.8	63.80	51.34
230	1.15	349.15	364.52	-113.02	-41.34	292.1	239.1	-36.88	-23.66	25.78	32.95	23.26	29.74	37.1	18.9	37.34	27.78
240	1.20	334.58	361.31	-112.34	-22.38	285.6	228.0	-28.46	-17.03	33.45	7.80	38.65	26.50	20.1	22.4	19.89	17.52
250	1.25	321.55	356.39	-116.94	-23.08	295.8	234.9	-32.75	-17.73	10.90	6.08	20.80	11.90	16.2	21.6	17.60	12.75
260	1.30	289.55	371.23	-124.93	-22.60	290.8	290.0	-45.28	-0.04	38.48	11.94	37.92	20.45	29.4	72.2	38.66	20.17

Editor's note: Subsequent to publication, the author has noted the experimental dynamic-stiffness data, which are the basis for the rotordynamic coefficients, to be unreliable. To the author's knowledge, all static data (both experimental and theoretical) and the theoretical dynamic data are valid. Please reference the Texas A&M University Master's thesis of David M. Coghlan (Static, Rotordynamic, and Thermal Characteristics of a Four Pad Spherical-Seat Tilting Pad Journal Bearing with Four Methods of Directed Lubrication) for valid dynamic data for a spherical-seat tilting pad journal bearing. (2014)

Table 30 Experimental dynamic-stiffness coefficients and uncertainties at N = 12,000 rpm, P = 689 kPa (100 psi)

N = 12,000 rpm P = 689 kPa		Experimental Dynamic-Stiffnesses								Uncertainties							
f	f/N	Re(H_{xx})	Re(H_{yy})	Re(H_{xy})	Re(H_{yx})	Im(H_{xx})	Im(H_{yy})	Im(H_{xy})	Im(H_{yx})	Re(H_{xx})	Re(H_{yy})	Re(H_{xy})	Re(H_{yx})	Im(H_{xx})	Im(H_{yy})	Im(H_{xy})	Im(H_{yx})
[Hz]	[Hz/Hz]	[MN/m]								[MN/m]							
20	0.10	398.96	354.24	-139.58	-40.01	42.1	15.4	-12.55	8.00	44.91	8.27	21.40	20.18	33.9	16.6	14.29	33.53
30	0.15	398.31	367.52	-143.21	-40.47	48.2	35.2	-9.80	-24.10	19.42	6.02	10.65	18.57	23.3	8.9	12.19	27.39
40	0.20	406.94	349.59	-151.99	-22.54	69.5	15.6	-16.18	-11.90	24.76	12.41	46.82	20.61	20.6	26.4	45.98	15.65
50	0.25	414.45	351.33	-146.74	-24.02	85.8	43.7	-23.51	-0.44	28.83	6.17	20.31	17.92	23.6	13.3	17.16	15.75
60	0.30	428.16	335.90	-183.57	-30.46	78.9	51.3	-43.55	-49.70	111.53	42.25	103.67	51.62	109.7	47.2	121.91	43.15
70	0.35	405.12	313.08	-144.49	-34.92	121.8	41.5	-31.33	-4.16	32.60	17.64	46.63	12.56	15.8	39.7	38.57	33.24
80	0.40	414.82	303.89	-154.58	-17.53	133.1	105.4	-22.10	-22.17	20.26	13.52	28.10	15.53	14.3	12.0	22.12	21.04
90	0.45	408.18	334.29	-154.47	-29.78	133.6	98.2	-25.45	-43.44	20.27	19.25	18.70	24.40	30.8	16.2	23.11	23.18
100	0.50	408.39	333.94	-151.48	-56.60	157.0	92.5	-21.72	-7.93	22.10	10.51	15.34	18.76	19.6	16.0	15.48	18.35
110	0.55	403.08	338.92	-147.43	-45.34	168.4	136.8	-16.62	-44.95	13.66	10.65	20.19	17.27	14.5	10.4	16.24	11.93
120	0.60	411.15	331.04	-152.83	-43.70	196.4	135.2	-29.85	-39.10	37.31	56.92	49.51	23.20	66.6	26.6	41.53	50.47
130	0.65	403.05	313.39	-143.97	-29.15	208.2	107.8	-33.99	-20.19	15.07	6.10	24.95	33.08	20.9	32.1	29.42	35.39
140	0.70	403.89	343.70	-139.70	-50.02	215.1	162.8	-24.84	-28.68	21.30	9.64	15.70	8.79	16.9	18.0	24.06	25.86
150	0.75	393.04	320.56	-132.04	-33.32	221.1	180.0	-22.97	-26.58	18.77	14.72	13.56	14.54	15.5	15.1	22.07	24.70
160	0.80	388.21	319.73	-126.10	-21.02	225.9	189.4	-31.88	-44.92	14.30	8.03	20.87	21.85	19.7	16.7	30.36	27.65
170	0.85	397.97	371.28	-128.49	-50.94	240.0	155.9	-25.46	-30.84	27.78	16.77	28.97	23.18	22.8	24.7	26.94	25.62
180	0.90	389.13	375.73	-114.95	-42.60	258.1	175.2	-15.84	-36.71	67.26	14.36	63.93	17.19	50.0	53.2	55.73	55.40
190	0.95	385.55	330.91	-123.92	-33.86	246.8	223.6	-16.32	-25.87	58.09	66.91	92.68	22.13	63.3	82.1	112.05	65.11
200	1.00	81.99	361.64	-217.64	183.71	48.1	123.3	-56.72	-220.12	1408.34	674.04	795.57	738.06	1010.8	635.9	804.27	1155.53
210	1.05	372.59	322.84	-115.70	-28.39	262.4	220.7	-23.76	-48.12	78.99	40.53	44.63	16.80	55.1	31.2	66.80	55.12
220	1.10	366.27	279.53	-120.98	-38.85	288.0	229.3	-24.65	-24.60	48.14	14.48	40.07	30.00	55.8	23.7	29.14	42.56
230	1.15	351.88	322.55	-106.03	-30.25	288.3	252.5	-21.47	-34.31	18.27	15.46	20.03	25.91	34.4	11.8	19.26	20.88
240	1.20	343.49	330.40	-109.81	-41.54	296.8	238.8	-27.88	-26.01	33.87	6.75	8.07	15.87	19.6	11.1	20.09	16.95
250	1.25	341.03	312.64	-108.97	-35.14	297.6	230.7	-26.20	-27.25	17.24	10.83	9.21	9.82	6.2	10.9	27.10	15.49
260	1.30	326.77	312.54	-97.68	-33.63	308.5	266.2	-19.62	-21.05	30.64	15.63	14.72	16.59	14.5	8.2	13.17	13.96

Editor's note: Subsequent to publication, the author has noted the experimental dynamic-stiffness data, which are the basis for the rotordynamic coefficients, to be unreliable. To the author's knowledge, all static data (both experimental and theoretical) and the theoretical dynamic data are valid. Please reference the Texas A&M University Master's thesis of David M. Coghlan (Static, Rotordynamic, and Thermal Characteristics of a Four Pad Spherical-Seat Tilting Pad Journal Bearing with Four Methods of Directed Lubrication) for valid dynamic data for a spherical-seat tilting pad journal bearing. (2014).

Table 31 Experimental dynamic-stiffness coefficients and uncertainties at N = 12,000 rpm, P = 1379 kPa (200 psi)

N = 12,000 rpm P = 1379 kPa		Experimental Dynamic-Stiffnesses								Uncertainties							
f	f/N	Re(H_{xx})	Re(H_{yy})	Re(H_{xy})	Re(H_{yx})	Im(H_{xx})	Im(H_{yy})	Im(H_{xy})	Im(H_{yx})	Re(H_{xx})	Re(H_{yy})	Re(H_{xy})	Re(H_{yx})	Im(H_{xx})	Im(H_{yy})	Im(H_{xy})	Im(H_{yx})
[Hz]	[Hz/Hz]	[MN/m]								[MN/m]							
20	0.10	407.75	378.62	-140.95	-40.67	38.5	21.5	-15.70	-7.73	34.62	14.31	13.52	30.34	31.0	22.2	16.50	33.88
30	0.15	412.93	381.11	-144.71	-46.74	51.7	32.6	-9.33	-15.08	26.44	6.90	13.29	18.22	17.9	8.2	9.45	16.84
40	0.20	410.16	408.66	-138.30	-39.52	63.9	7.3	-17.95	-8.06	21.02	7.61	34.03	14.55	32.7	48.5	35.28	27.67
50	0.25	415.32	371.02	-143.37	-26.78	85.2	49.6	-17.27	-8.12	28.74	7.52	24.22	38.45	31.6	17.1	20.74	24.58
60	0.30	407.25	364.37	-148.63	-34.82	96.9	60.5	-12.05	-19.34	141.67	74.17	145.10	54.03	139.8	83.0	151.46	67.12
70	0.35	404.02	349.70	-147.16	-32.08	108.1	45.3	-16.74	-12.72	34.85	40.28	66.62	31.44	34.6	69.4	65.30	19.05
80	0.40	424.03	335.08	-152.14	-29.22	136.8	100.1	-25.72	-10.68	31.18	25.39	50.56	21.84	24.2	29.8	45.26	30.71
90	0.45	411.32	356.42	-151.37	-35.13	140.4	93.4	-14.32	-29.10	33.13	13.79	40.78	23.03	43.4	30.4	32.09	29.36
100	0.50	408.74	352.55	-137.76	-32.62	154.0	103.7	-21.13	-17.33	34.07	16.63	38.15	23.56	22.6	29.5	23.75	28.19
110	0.55	413.54	354.74	-138.36	-41.90	176.7	142.3	-27.21	-37.42	33.63	40.67	37.39	26.44	36.8	27.0	40.86	32.39
120	0.60	409.68	357.70	-133.69	-19.14	162.2	144.4	-23.82	-45.28	63.87	33.13	61.10	60.46	41.6	49.6	46.93	70.46
130	0.65	424.51	318.57	-151.80	-29.27	194.5	116.6	-12.13	-16.62	55.43	15.87	73.47	38.74	49.9	67.7	64.76	49.58
140	0.70	408.24	356.61	-121.20	-23.96	202.5	179.7	-28.24	-33.94	46.64	21.04	39.51	42.36	35.7	46.5	38.93	46.04
150	0.75	421.26	353.26	-124.07	-40.99	231.4	190.7	-33.06	-29.48	69.67	34.90	50.08	50.03	47.4	46.7	68.56	32.74
160	0.80	416.47	349.50	-157.79	-45.65	255.4	162.5	-50.47	-35.88	78.30	50.39	62.76	74.35	74.6	42.7	97.92	53.70
170	0.85	367.81	418.28	-132.69	-40.42	269.3	169.1	-70.66	-59.77	92.31	73.08	100.93	74.15	94.2	82.5	124.98	85.27
180	0.90	388.18	357.03	-127.78	-4.14	227.0	194.3	-54.31	-37.52	124.88	50.54	147.41	93.75	90.1	126.6	103.64	93.93
190	0.95	338.39	148.57	-158.05	78.28	170.9	163.2	218.76	-69.48	291.85	991.39	588.30	693.78	788.5	562.0	1090.45	342.43
200	1.00	615.90	214.44	205.31	269.33	-79.5	488.9	77.01	205.88	1472.96	460.82	2802.65	1784.13	2302.2	2440.5	655.16	1457.57
210	1.05	392.64	364.76	-177.92	-65.39	323.9	196.3	-30.54	-37.04	173.05	169.39	130.74	146.94	148.9	119.4	166.62	157.73
220	1.10	341.21	330.03	-116.24	-16.11	292.7	265.2	-54.12	-66.98	87.70	11.25	103.13	84.60	106.1	101.9	71.53	85.96
230	1.15	381.79	334.52	-124.51	-26.20	283.2	240.3	-6.92	-18.71	59.13	61.53	74.28	47.64	57.5	66.0	47.86	60.83
240	1.20	353.51	341.53	-97.78	-16.51	280.7	253.3	-25.12	-40.54	49.41	53.96	25.49	43.60	50.6	40.2	60.73	59.16
250	1.25	352.86	339.29	-99.81	-35.98	303.8	246.6	-31.99	-32.31	31.73	52.84	41.42	19.82	22.7	37.0	58.15	26.49
260	1.30	335.77	326.12	-97.15	-17.43	302.6	261.9	-10.39	-31.22	25.96	42.07	49.35	36.91	46.1	41.8	29.86	34.26

Editor's note: Subsequent to publication, the author has noted the experimental dynamic-stiffness data, which are the basis for the rotordynamic coefficients, to be unreliable. To the author's knowledge, all static data (both experimental and theoretical) and the theoretical dynamic data are valid. Please reference the Texas A&M University Master's thesis of David M. Coghlan (Static, Rotordynamic, and Thermal Characteristics of a Four Pad Spherical-Seat Tilting Pad Journal Bearing with Four Methods of Directed Lubrication) for valid dynamic data for a spherical-seat tilting pad journal bearing. (2014)

Table 32 Experimental dynamic-stiffness coefficients and uncertainties at N = 12,000 rpm, P = 1896 kPa (275 psi)

N = 12,000 rpm P = 1896 kPa		Experimental Dynamic-Stiffnesses								Uncertainties							
f	f/N	Re(H_{xx})	Re(H_{yy})	Re(H_{xy})	Re(H_{yx})	Im(H_{xx})	Im(H_{yy})	Im(H_{xy})	Im(H_{yx})	Re(H_{xx})	Re(H_{yy})	Re(H_{xy})	Re(H_{yx})	Im(H_{xx})	Im(H_{yy})	Im(H_{xy})	Im(H_{yx})
[Hz]	[Hz/Hz]	[MN/m]								[MN/m]							
20	0.10	432.99	411.65	-138.69	-41.04	30.1	18.8	-8.64	-5.25	28.66	7.34	15.85	24.67	40.7	18.4	20.49	43.75
30	0.15	436.29	412.54	-142.27	-43.31	46.9	36.9	-8.08	-16.63	34.86	6.71	19.26	31.18	15.1	10.3	7.35	17.15
40	0.20	427.97	420.61	-124.06	-36.43	63.7	21.0	-15.60	-7.66	23.96	29.07	40.64	20.04	30.1	64.6	30.03	15.20
50	0.25	432.82	404.64	-141.94	-17.89	91.0	57.5	-17.94	-7.36	27.23	14.31	36.52	39.34	31.5	17.8	11.57	22.09
60	0.30	441.14	396.11	-151.4	-39.86	93.2	66.3	-10.56	-27.04	159.46	71.33	193.4	79.61	93.7	82.7	130.28	72.71
70	0.35	423.61	390.76	-138.04	-35.67	106.2	38.0	-39.01	-12.70	45.79	122.24	125.69	29.00	33.0	96.6	95.25	33.18
80	0.40	438.73	383.59	-155.97	-28.20	140.1	76.7	-26.94	-4.45	30.43	48.00	87.42	28.39	30.0	46.7	45.85	25.02
90	0.45	425.42	390.48	-131.06	-41.17	146.7	99.9	-13.00	-27.59	33.12	67.38	62.28	24.38	48.6	46.5	43.81	46.94
100	0.50	429.85	388.52	-140.07	-36.09	159.6	100.5	-24.43	-8.97	35.00	41.78	58.29	28.36	34.6	31.0	40.55	29.39
110	0.55	438.38	392.39	-141.08	-41.70	170.1	119.8	-26.33	-18.46	37.96	49.36	58.33	29.85	29.3	23.3	43.57	20.22
120	0.60	414.49	378.98	-141.37	-41.39	185.8	162.0	-18.56	-38.61	99.72	41.29	55.26	64.91	63.4	88.2	41.68	107.95
130	0.65	432.30	385.46	-150.87	-17.42	197.1	129.3	-26.48	-16.80	53.69	68.28	57.60	57.23	86.3	80.5	148.42	22.48
140	0.70	419.24	387.71	-122.08	-24.35	202.3	150.1	-35.82	-40.15	71.16	50.95	58.45	48.74	46.9	34.4	94.72	76.22
150	0.75	448.00	384.07	-123.93	-24.93	220.0	197.8	-31.37	-18.00	91.91	61.59	94.22	78.26	66.9	96.9	105.38	30.05
160	0.80	442.70	370.83	-127.14	-27.78	232.7	196.1	-57.56	-18.59	136.67	72.50	162.43	77.34	81.5	147.6	163.53	105.64
170	0.85	401.19	423.46	-120.59	-55.97	279.8	169.7	-38.71	-44.56	123.43	171.33	275.56	154.30	168.3	239.2	157.65	113.99
180	0.90	392.04	408.47	-112.77	-15.42	252.6	179.8	-19.12	-49.64	169.13	259.86	230.10	178.45	222.4	189.9	252.58	164.25
190	0.95	449.50	112.93	-354.20	1.88	243.0	-33.0	299.03	3.87	264.36	364.45	636.15	589.27	596.2	592.1	295.57	243.02
200	1.00	240.12	252.05	-114.38	138.94	118.7	198.9	101.01	-162.34	488.18	444.82	483.50	379.02	468.8	406.8	484.91	456.33
210	1.05	443.92	419.54	-126.41	-54.30	311.7	261.1	-69.90	-2.67	276.09	346.19	295.74	263.65	237.1	288.5	347.18	246.39
220	1.10	366.37	327.79	-102.88	-22.34	311.5	274.0	-37.70	-66.36	148.54	166.34	156.79	119.50	149.3	128.1	159.38	148.95
230	1.15	392.48	398.14	-108.94	-14.36	297.2	271.4	-42.47	-24.65	70.50	160.62	88.88	104.86	104.9	89.2	139.56	83.50
240	1.20	364.17	371.10	-111.12	-12.37	276.6	262.2	-30.95	-44.52	73.07	29.72	98.02	52.02	48.0	66.5	31.87	87.47
250	1.25	376.92	367.82	-109.73	-29.62	300.9	248.0	-28.84	-26.29	35.97	72.59	87.01	40.91	33.3	65.3	31.79	33.50
260	1.30	349.31	364.28	-100.38	-16.97	305.2	264.3	-24.34	-37.63	52.09	76.07	69.88	33.57	49.7	64.3	22.42	68.66

Editor's note: Subsequent to publication, the author has noted the experimental dynamic-stiffness data, which are the basis for the rotordynamic coefficients, to be unreliable. To the author's knowledge, all static data (both experimental and theoretical) and the theoretical dynamic data are valid. Please reference the Texas A&M University Master's thesis of David M. Coghlan (Static, Rotordynamic, and Thermal Characteristics of a Four Pad Spherical-Seat Tilting Pad Journal Bearing with Four Methods of Directed Lubrication) for valid dynamic data for a spherical-seat tilting pad journal bearing. (2014)

Table 33 Experimental rotordynamic coefficients

N	P	K_{xx}	K_{yy}	K_{xy}	K_{yx}	C_{xx}	C_{yy}	C_{xy}	C_{yx}	M_{xx}	M_{yy}	M_{xy}	M_{yx}
[rpm]	[kPa]	[MN/m]				[kN·s/m]				[kg]			
4,000	0	264.09	209.75	-106.47	-44.67	207.25	227.88	–	–	–	-60.43	10.94	–
4,000	689	292.79	241.75	-111.33	-40.16	243.76	233.48	–	–	–	-31.35	–	–
4,000	1379	331.85	316.13	-109.21	-31.84	231.60	233.69	–	–	-14.73	-34.36	-10.03	–
4,000	1896	384.58	398.90	-58.16	-19.34	221.54	235.33	–	–	–	-38.68	–	–
6,000	0	308.65	260.04	-121.19	-63.99	177.19	236.95	–	–	–	-40.89	–	-30.62
6,000	689	308.57	286.51	-115.32	-34.59	214.31	209.95	–	-32.60	–	–	–	–
6,000	1379	340.31	314.83	-104.73	-25.87	212.22	219.72	–	-30.47	–	–	–	–
6,000	1896	381.68	398.17	-90.58	-24.48	215.29	212.18	–	–	–	–	–	–
8,000	0	369.66	327.89	-123.64	-89.04	177.36	216.27	–	–	29.74	–	–	-48.47
8,000	689	348.76	308.28	-121.26	-42.49	204.69	205.92	–	–	12.17	–	–	–
8,000	1379	373.10	332.94	-113.11	-30.44	207.91	202.87	–	-25.80	11.42	–	–	–
8,000	1896	403.54	387.42	-107.45	-27.45	204.90	198.18	–	–	12.40	–	–	–
10,000	0	416.26	342.41	-119.54	-82.70	162.70	168.90	–	–	40.89	-12.08	–	-34.06
10,000	689	382.80	328.71	-120.06	-32.79	187.58	175.69	–	–	19.82	8.78	–	–
10,000	1379	398.70	350.60	-119.78	-30.72	191.66	173.98	–	–	19.21	10.08	–	–
10,000	1896	435.95	393.53	-121.66	-31.61	187.50	184.84	–	–	21.28	12.16	–	–
12,000	0	439.68	356.49	-127.02	-41.84	173.20	166.44	–	–	46.28	–	–	–
12,000	689	417.98	331.03	-152.12	-35.59	177.61	166.62	–	–	29.31	–	-19.50	–
12,000	1379	421.34	366.96	-148.64	-31.96	176.19	165.91	–	–	28.03	14.26	-17.58	–
12,000	1896	441.22	388.97	-142.90	-29.65	175.40	168.36	–	–	27.82	–	-14.58	–

Editor's note: Subsequent to publication, the author has noted the experimental dynamic-stiffness data, which are the basis for the rotordynamic coefficients, to be unreliable. To the author's knowledge, all static data (both experimental and theoretical) and the theoretical dynamic data are valid. Please reference the Texas A&M University Master's thesis of David M. Coghlan (Static, Rotordynamic, and Thermal Characteristics of a Four Pad Spherical-Seat Tilting Pad Journal Bearing with Four Methods of Directed Lubrication) for valid dynamic data for a spherical-seat tilting pad journal bearing. (2014)

Table 34 Uncertainties of experimental rotordynamic coefficients

N [rpm]	P [kPa]	ΔK_{xx}	ΔK_{yy}	ΔK_{xy}	ΔK_{yx}	ΔC_{xx}	ΔC_{yy}	ΔC_{xy}	ΔC_{yx}	ΔM_{xx}	ΔM_{yy}	ΔM_{xy}	ΔM_{yx}
		[MN/m]				[kN·s/m]				[kg]			
4,000	0	5.26	18.55	4.72	12.84	24.98	49.87	–	–	–	13.12	3.73	–
4,000	689	6.61	11.94	3.70	6.56	23.86	25.84	–	–	–	9.10	–	–
4,000	1379	5.93	11.02	4.42	4.19	29.63	42.26	–	–	4.33	7.71	3.12	–
4,000	1896	12.68	15.05	8.97	5.06	28.46	28.35	–	–	–	9.64	–	–
6,000	0	8.29	10.71	6.85	11.86	29.19	29.83	–	–	–	6.73	–	8.60
6,000	689	5.92	5.67	3.74	4.18	19.04	21.92	–	9.70	–	–	–	–
6,000	1379	5.13	10.76	2.94	4.19	18.71	21.11	–	6.87	–	–	–	–
6,000	1896	7.51	11.26	4.56	5.99	22.71	26.15	–	–	–	–	–	–
8,000	0	8.50	19.45	4.13	19.83	19.19	23.27	–	–	6.96	–	–	13.93
8,000	689	4.87	4.52	5.78	5.55	13.65	20.51	–	–	3.90	–	–	–
8,000	1379	5.02	5.37	4.69	5.07	15.40	27.68	–	8.26	3.96	–	–	–
8,000	1896	3.76	9.68	4.32	4.46	16.31	28.93	–	–	2.75	–	–	–
10,000	0	11.22	3.92	4.15	14.71	17.71	11.50	–	–	9.45	3.30	–	10.88
10,000	689	7.98	1.62	5.52	5.90	18.51	12.33	–	–	5.69	1.17	–	–
10,000	1379	7.55	3.79	7.34	5.86	13.48	11.49	–	–	5.33	2.73	–	–
10,000	1896	6.56	5.45	5.88	6.53	12.84	11.64	–	–	4.90	3.81	–	–
12,000	0	7.92	4.24	7.41	4.33	18.80	17.15	–	–	6.28	–	–	–
12,000	689	5.71	7.14	4.22	4.54	13.65	16.12	–	–	4.53	–	3.28	–
12,000	1379	8.77	5.54	6.60	4.69	18.54	18.76	–	–	7.15	4.20	5.26	–
12,000	1896	8.97	8.01	5.90	5.26	18.79	12.54	–	–	7.41	–	4.82	–

Editor's note: Subsequent to publication, the author has noted the experimental dynamic-stiffness data, which are the basis for the rotordynamic coefficients, to be unreliable. To the author's knowledge, all static data (both experimental and theoretical) and the theoretical dynamic data are valid. Please reference the Texas A&M University Master's thesis of David M. Coghlan (Static, Rotordynamic, and Thermal Characteristics of a Four Pad Spherical-Seat Tilting Pad Journal Bearing with Four Methods of Directed Lubrication) for valid dynamic data for a spherical-seat tilting pad journal bearing. (2014)

Table 35 Theoretical rotordynamic coefficients

		Theoretical (XLTFPBrg Output)									Modified Stiffness	Modified Damping
N	P	$K_{xx}=K_{yy}$	K_{xy}	K_{yx}	$C_{xx}=C_{yy}$	C_{xy}	C_{yx}	$M_{xx}=M_{yy}$	M_{xy}	M_{yx}	$K_{xx}=K_{yy}$	$C_{xx}=C_{yy}$
[rpm]	[kPa]	[MN/m]			[kN·s/m]			[kg]			[MN/m]	[kN·s/m]
4,000	0	407.61	1.41	-0.29	881.48	-2.12	2.12	19.89	–	1.13	257.70	352.32
4,000	689	451.96	1.88	0.29	979.95	-1.06	3.23	16.33	–	1.25	274.74	362.12
4,000	1379	560.23	3.69	2.43	1214.96	2.56	6.88	12.44	–	1.58	311.32	375.18
4,000	1896	663.40	5.72	4.90	1460.61	6.51	10.84	–	–	2.03	338.64	380.60
6,000	0	549.49	1.84	-0.17	842.90	-1.86	1.85	27.83	–	1.65	307.97	264.78
6,000	689	583.24	2.31	0.35	903.67	-1.29	2.49	24.42	–	1.71	318.30	269.13
6,000	1379	661.30	3.76	1.94	1034.61	–	4.40	20.22	–	1.88	340.21	273.83
6,000	1896	741.22	4.32	3.92	1167.28	2.88	6.72	16.95	-1.29	2.05	360.19	275.64
8,000	0	678.08	2.04	-0.10	810.86	-1.51	1.51	38.81	–	1.93	344.60	209.42
8,000	689	705.32	2.50	0.36	852.33	-1.05	2.01	37.21	–	1.96	351.50	211.68
8,000	1379	766.81	3.65	1.58	938.87	–	2.98	35.27	–	2.05	366.13	214.04
8,000	1896	830.72	3.55	3.29	1027.75	1.70	4.81	33.77	-1.76	2.15	380.09	215.15
10,000	0	788.10	2.11	-0.08	766.24	-1.19	1.18	50.17	–	2.08	370.91	169.73
10,000	689	813.51	2.54	0.34	799.64	-0.88	1.52	49.56	–	2.10	376.45	171.23
10,000	1379	865.20	3.43	1.27	862.27	–	2.20	49.46	–	2.17	387.15	172.65
10,000	1896	920.56	3.05	2.89	928.91	1.26	3.70	49.37	-2.00	2.23	397.85	173.51
12,000	0	897.74	2.19	-0.04	740.05	-0.93	0.92	57.78	–	2.18	393.53	142.21
12,000	689	917.97	2.48	0.26	762.81	-0.75	1.13	58.03	–	2.21	397.37	142.94
12,000	1379	963.91	3.36	1.17	811.63	–	1.73	58.64	–	2.26	405.74	143.81
12,000	1896	1012.99	2.43	2.35	864.01	0.77	2.67	59.63	-2.13	2.30	414.19	144.45

Table 36 Uncertainties of theoretical rotordynamic coefficients

		Theoretical (XLTFPBrg)								
N	P	$\Delta K_{xx} = \Delta K_{yy}$	ΔK_{xy}	ΔK_{yx}	$\Delta C_{xx} = \Delta C_{yy}$	ΔC_{xy}	ΔC_{yx}	$\Delta M_{xx} = \Delta M_{yy}$	ΔM_{xy}	ΔM_{yx}
[rpm]	[kPa]	[MN/m]			[kN·s/m]			[kg]		
4,000	0	1.89	0.38	1.88	4.27	0.22	0.22	1.48	–	0.09
4,000	689	2.41	0.33	2.08	5.44	0.21	0.24	1.89	–	0.09
4,000	1379	3.38	0.23	2.62	7.72	–	0.27	2.65	–	0.10
4,000	1896	4.02	0.10	3.34	9.91	0.22	0.25	–	–	0.10
6,000	0	1.73	0.54	2.71	2.28	0.24	0.24	1.36	–	0.06
6,000	689	1.96	0.53	2.82	2.97	0.24	0.24	1.54	–	0.06
6,000	1379	2.55	0.48	3.08	4.31	–	0.25	2.00	–	0.07
6,000	1896	3.23	2.36	3.36	5.72	0.25	0.25	2.53	0.41	0.06
8,000	0	2.93	0.63	3.16	2.61	0.21	0.21	2.29	–	0.04
8,000	689	3.21	0.63	3.21	2.73	0.22	0.22	2.51	–	0.05
8,000	1379	3.88	0.60	3.36	3.05	–	0.21	3.04	–	0.05
8,000	1896	4.62	3.14	3.52	3.49	0.23	0.21	3.62	0.52	0.05
10,000	0	2.80	0.68	3.41	4.37	0.18	0.18	2.19	–	0.03
10,000	689	3.03	0.68	3.44	4.57	0.18	0.18	2.37	–	0.03
10,000	1379	3.56	0.67	3.55	5.08	–	0.18	2.79	–	0.03
10,000	1896	4.14	3.58	3.65	5.59	0.18	0.19	3.25	0.59	0.04
12,000	0	2.20	0.72	3.58	4.95	0.15	0.15	1.72	–	0.02
12,000	689	2.34	0.71	3.61	5.22	0.15	0.15	1.84	–	0.02
12,000	1379	2.68	0.71	3.70	5.71	–	0.15	2.10	–	0.02
12,000	1896	3.10	3.91	3.77	6.34	0.15	0.16	2.43	0.68	0.02

Table 37 r^2 values for experimental dynamic-stiffness coefficients

N	P	r^2 Values (Square of Pearson Product Moment Correlation Coefficient)							
[rpm]	[kPa]	Re($\boldsymbol{H}_{xx}$)	Re($\boldsymbol{H}_{yy}$)	Re($\boldsymbol{H}_{xy}$)	Re($\boldsymbol{H}_{yx}$)	Im($\boldsymbol{H}_{xx}$)	Im($\boldsymbol{H}_{yy}$)	Im($\boldsymbol{H}_{xy}$)	Im($\boldsymbol{H}_{yx}$)
4,000	0	0.34	0.88	0.72	0.15	0.95	0.89	0.40	0.08
4,000	689	0.46	0.74	0.17	0.44	0.96	0.95	0.07	0.49
4,000	1379	0.74	0.84	0.74	0.01	0.95	0.91	0.39	0.70
4,000	1896	0.72	0.86	0.51	0.16	0.96	0.96	0.42	0.61
6,000	0	0.66	0.93	0.41	0.75	0.90	0.96	0.34	0.07
6,000	689	0.48	0.39	0.00	0.54	0.98	0.97	0.01	0.81
6,000	1379	0.21	0.60	0.07	0.30	0.96	0.96	0.14	0.82
6,000	1896	0.50	0.49	0.14	0.26	0.97	0.96	0.57	0.44
8,000	0	0.78	0.71	0.00	0.77	0.95	0.89	0.09	0.02
8,000	689	0.62	0.59	0.07	0.50	0.98	0.96	0.51	0.64
8,000	1379	0.64	0.40	0.27	0.27	0.98	0.95	0.34	0.76
8,000	1896	0.85	0.75	0.13	0.25	0.98	0.95	0.56	0.60
10,000	0	0.79	0.82	0.04	0.74	0.96	0.97	0.00	0.06
10,000	689	0.78	0.94	0.33	0.20	0.97	0.99	0.47	0.33
10,000	1379	0.78	0.78	0.53	0.24	0.99	0.99	0.51	0.37
10,000	1896	0.80	0.74	0.55	0.42	0.99	0.99	0.57	0.29
12,000	0	0.90	0.18	0.44	0.41	0.95	0.95	0.54	0.03
12,000	689	0.88	0.51	0.87	0.00	0.97	0.95	0.11	0.11
12,000	1379	0.75	0.73	0.70	0.25	0.96	0.96	0.02	0.55
12,000	1896	0.76	0.64	0.70	0.44	0.96	0.99	0.56	0.42

Table 38 r^2 values for theoretical dynamic-stiffness coefficients

		r^2 Values (Square of Pearson Product Moment Correlation Coefficient)					
N	*P*	Theoretical (XLTFPBrg)					
[rpm]	[kPa]	Re($\boldsymbol{H}_{xx}$) =Re($\boldsymbol{H}_{yy}$)	Re($\boldsymbol{H}_{xy}$)	Re($\boldsymbol{H}_{yx}$)	Im($\boldsymbol{H}_{xx}$) =Im($\boldsymbol{H}_{yy}$)	Im($\boldsymbol{H}_{xy}$)	Im($\boldsymbol{H}_{yx}$)
4,000	0	0.97	0.96	0.96	1.00	0.94	0.94
4,000	689	0.93	0.96	0.97	1.00	0.81	0.97
4,000	1379	0.79	0.92	0.98	1.00	0.97	0.99
4,000	1896	0.51	0.52	0.99	1.00	0.99	1.00
6,000	0	0.99	0.99	0.99	1.00	0.91	0.91
6,000	689	0.98	0.99	0.99	1.00	0.82	0.95
6,000	1379	0.94	0.99	0.99	1.00	0.48	0.98
6,000	1896	0.88	0.98	0.99	1.00	0.96	0.99
8,000	0	0.98	1.00	1.00	1.00	0.89	0.90
8,000	689	0.97	1.00	1.00	1.00	0.80	0.94
8,000	1379	0.96	1.00	1.00	1.00	0.04	0.97
8,000	1896	0.94	1.00	1.00	1.00	0.90	0.99
10,000	0	0.99	1.00	1.00	1.00	0.88	0.88
10,000	689	0.99	1.00	1.00	1.00	0.80	0.92
10,000	1379	0.98	1.00	1.00	1.00	0.21	0.96
10,000	1896	0.97	1.00	1.00	1.00	0.89	0.98
12,000	0	0.99	1.00	1.00	1.00	0.87	0.87
12,000	689	0.99	1.00	1.00	1.00	0.81	0.90
12,000	1379	0.99	1.00	1.00	1.00	0.16	0.95
12,000	1896	0.99	1.00	1.00	1.00	0.82	0.98

Table 39 Static stiffness versus K_{yy} comparison

P [kPa]	*N* [rpm]	K_{yy} [MN/m]	$K_{yy,s}$ [MN/m]
0	4,000	209.75	231.63
0	6,000	260.04	235.34
0	8,000	293.13	295.43
0	10,000	342.41	294.07
0	12,000	352.31	749.23
689	4,000	241.75	248.28
689	6,000	281.06	200.20
689	8,000	308.28	255.82
689	10,000	328.71	324.84
689	12,000	341.64	321.98
1379	4,000	316.13	285.83
1379	6,000	297.16	329.80
1379	8,000	340.85	292.12
1379	10,000	350.60	276.44
1379	12,000	366.96	277.83
1896	4,000	398.90	246.81
1896	6,000	385.81	442.64
1896	8,000	399.76	665.75
1896	10,000	393.53	246.61
1896	12,000	399.99	182.85

APPENDIX B

DERIVATION OF EQUIVALENT PAD SUPPORT STRUCTURE STIFFNESS

To derive an effective value of pad support structure stiffness to place in series with the total bearing stiffness and damping about the coordinate axes, one begins with a free body diagram of the rotor attached to four springs (representing the pad support structures) acting at 45º-angles to the vertical (or loaded) axis, as shown in Fig. 53. An upward force, F, is applied to the rotor, causing a deflection δ_r (of the rotor).

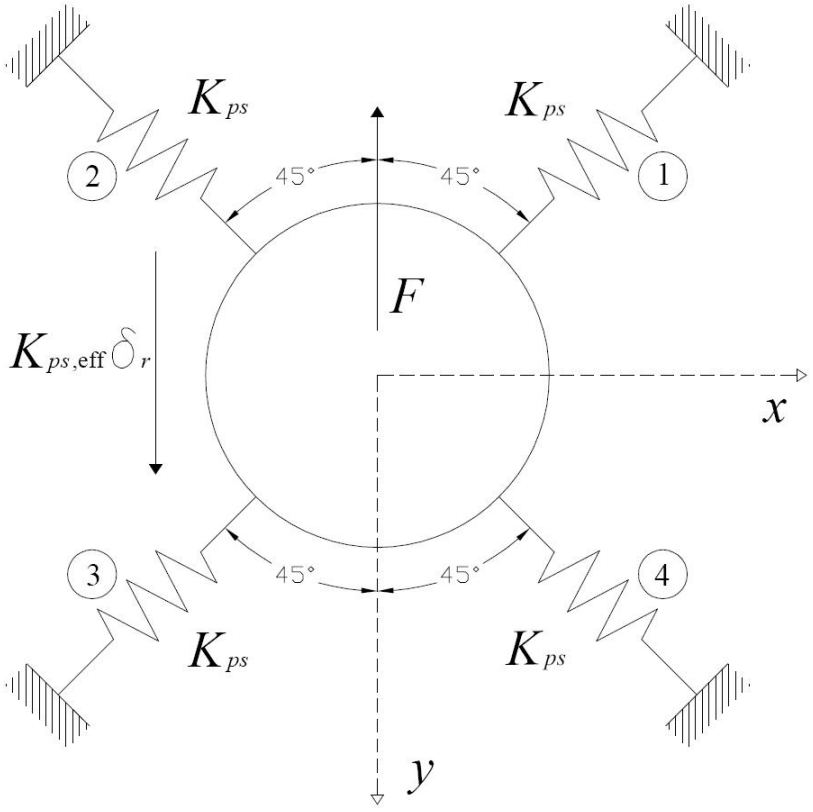

Fig. 53 Free body diagram of rotor connected to pad support springs

Summing forces about both axes gives

$$\begin{aligned} &\sum F_x = 0, \ \sum F_y = K_{ps,\text{eff}}\delta_r - F = 0 \\ &\therefore F = K_{ps,\text{eff}}\delta_r \end{aligned} \tag{39}$$

In Eq. (39), linearity is assumed since the rotor deflection is small compared to "length" of the springs—this length can be effectively represented by the distance between the journal center and the point of contact between the pivot and housing. Assuming each pad is initially loaded, each spring will displace a distance δ_{pi} (along its own axis) and will react with a force F_{pi} (also along its own axis) directly proportional to that displacement. Upon the assumption of small displacement, the angle that the i^{th} spring makes with the vertical, φ_i, can be assumed constant as the rotor is displaced. Figure 54 shows the relationships between (a) φ_i, δ_{pi}, and δ_r and (b) F_{pi}, its horizontal and vertical components, and φ_i.

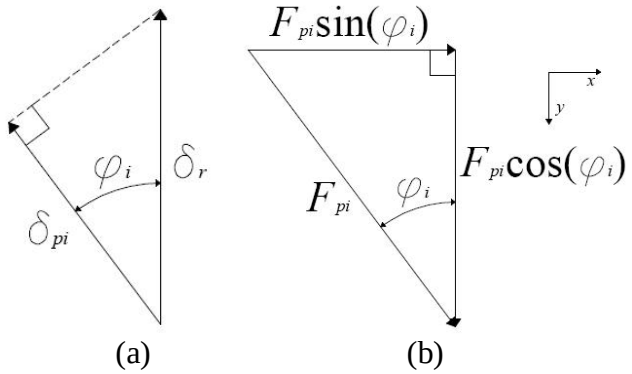

Fig. 54 Relationships between (a) φ_i, δ_{pi}, and δ_r and (b) F_{pi}, its horizontal and vertical components, and φ_i.

δ_{pi} is now easily related to δ_r as

$$\delta_{pi} = \delta_r \cos(\varphi_i) \tag{40}$$

Note that the relationships in Fig. 54 and Eq. (40) are valid for any angle φ_i, not just for the 45º-angles shown here. Summing forces in both directions, now using the individual spring contributions, gives

$$\begin{aligned} \sum F_x &= \sum_{i=1}^{M} F_{pi} \sin\left(\varphi_i\right) = 0 \\ \sum F_y &= \sum_{i=1}^{M} F_{pi} \cos\left(\varphi_i\right) - F = 0 \end{aligned} \tag{41}$$

for M springs. Making the substitutions $F = K_{ps,\text{eff}}\, \delta_r$ and $F_{pi} = K_{ps}\delta_{pi}$ yields

$$\begin{aligned} \sum_{i=1}^{M} F_{pi} \sin\left(\varphi_i\right) &= K_{ps} \sum_{i=1}^{M} \delta_{pi} \sin\left(\varphi_i\right) = 0 \\ \sum_{i=1}^{M} F_{pi} \cos\left(\varphi_i\right) &= K_{ps} \sum_{i=1}^{M} \delta_{pi} \cos\left(\varphi_i\right) = K_{ps,\text{eff}}\, \delta_r \end{aligned} \tag{42}$$

Substituting Eq. (40) into Eq. (42) nets

$$\begin{aligned} K_{ps}\delta_r \sum_{i=1}^{M} \sin\left(\varphi_i\right)\cos\left(\varphi_i\right) &= 0 \\ K_{ps}\delta_r \sum_{i=1}^{M} \cos^2\left(\varphi_i\right) &= K_{ps,\text{eff}}\, \delta_r \end{aligned} \tag{43}$$

$$\Downarrow$$

$$\begin{aligned} \sum_{i=1}^{M} \sin\left(\varphi_i\right)\cos\left(\varphi_i\right) &= 0 \\ K_{ps,\text{eff}} &= K_{ps} \sum_{i=1}^{M} \cos^2\left(\varphi_i\right) \end{aligned} \tag{44}$$

For the specific angles and number of springs in this case, Eq. (44) becomes

$$\sum_{l=0}^{3}\sin\left(\frac{\pi}{4}+\frac{\pi}{2}l\right)\cos\left(\frac{\pi}{4}+\frac{\pi}{2}l\right)=\frac{1}{2}-\frac{1}{2}+\frac{1}{2}-\frac{1}{2}=0$$
$$K_{ps,\text{eff}}=K_{ps}\sum_{l=0}^{3}\cos^2\left(\frac{\pi}{4}+\frac{\pi}{2}l\right)=\frac{1}{2}+\frac{1}{2}+\frac{1}{2}+\frac{1}{2}=2K_{ps} \quad (45)$$

Due to symmetry, this result is also valid in the horizontal direction.

To aid as a reference for future work, trigonometric identities can also be used to evaluate effective stiffness for the general case in which there are *M* springs separated by the angle $\varphi_s = 2\pi/M$. This configuration is shown in Fig. 55.

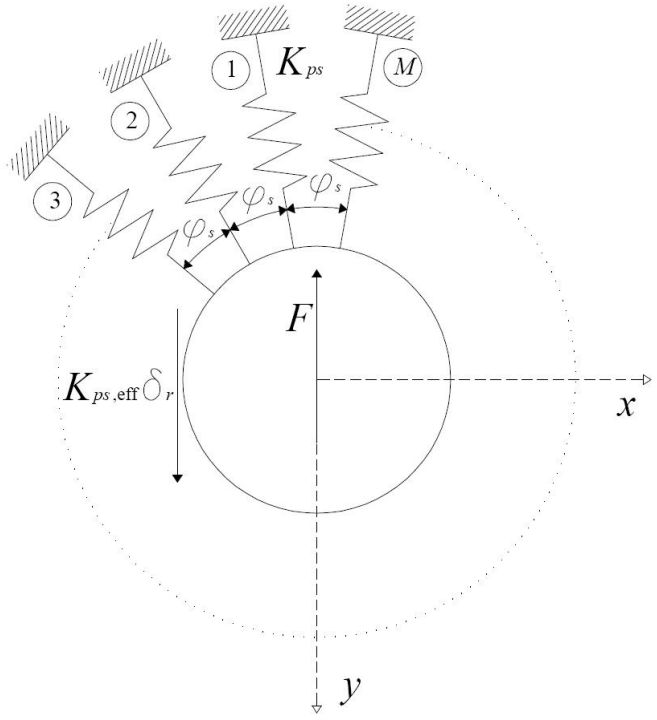

Fig. 55 General distributed spring configuration

If the first spring makes an angle φ_1 with the vertical (-*y*) axis, Eq. (44) is evaluated as follows:

$$\sum_{l=0}^{M-1} \sin\left(\varphi_1 + \frac{2\pi l}{M}\right) \cos\left(\varphi_1 + \frac{2\pi l}{M}\right) = 0$$
$$K_{ps,\text{eff}} = K_{ps} \sum_{l=0}^{M-1} \cos^2\left(\varphi_1 + \frac{2\pi l}{M}\right) = \frac{M}{2} K_{ps} \tag{46}$$

As long as there 3 or more springs surrounding the rotor, these results are valid in any direction. Hence, equivalent stiffness of a rotor surrounded by M (3 or more) equally spaced springs of stiffness K_{ps} will exhibit an equivalent stiffness $(M/2)K_{ps}$ to rotor displacement in any direction.

VITA

Name:	Joel Mark Harris
Address:	1100 White Bluff Rd., Warehouse 3, Redfield, AR 72132
Email Address:	jharr17@entergy.com
Education:	B.S. Mathematics, University of Central Arkansas, 2005
	M.S. Mechanical Engineering, Texas A&M University, 2008